

**INTEGRATED MULTIPHYSICS MODELING, TESTING AND
OPTIMIZATION OF FRICTION STIR WELDING OF ALUMINUM
ALLOYS**

by

Mohamadreza Nourani

B.A.Sc., Sharif University of Technology, Iran, 1999

M.A.Sc., Sharif University of Technology, Iran, 2001

PhD Candidate (No degree conferred), Sharif University of Technology, Iran, 2004

A THESIS SUBMITTED IN PARTIAL FULFILLMENT OF
THE REQUIREMENTS FOR THE DEGREE OF
DOCTOR OF PHILOSOPHY

in

THE COLLEGE OF GRADUATE STUDIES

(Mechanical Engineering)

THE UNIVERSITY OF BRITISH COLUMBIA

(Okanagan)

October 2013

© Mohamadreza Nourani, 2013

Abstract

The main objective of this work is the development of a novel integrated multiphysics modeling, testing, and optimization of friction stir welding (FSW) for aluminum alloys, and thereby facilitating a better understating of processing-microstructure-properties relationships in this relatively new welding technique. To this end, in this paper-based dissertation, first we review various models and optimization methods used in the field of FSW. Next, based on the current state-of-the-art and a validated 3D thermal model for aluminum 6061 along with a Taguchi design of experiments approach, we make a proposition that hot welds (with maximum temperature during FSW) have the lowest mechanical properties as opposed to cold welds. Using further experimental studies we also propose that another determining parameter in the resulting mechanical properties of FSW welds is the material flow around the tool which in very cold weld conditions may cause low mechanical properties due to low mechanical bonding.

Next, we develop and validate a novel two-dimensional Eulerian steady-state “integrated multiphysics” model of FSW of aluminum 6061 which did not exist earlier in the literature and can simultaneously predict temperature, shear strain rate, shear stress and strain fields over the entire workpiece. The model can additionally predict microstructural changes during and after FSW as well as residual stresses. In order to investigate the effect of different material constitutive equations on this integrated multiphysics model, we implement and compare most commonly used CFD (Computational Fluid Dynamics) and CSM (Computational Solid Mechanics) constitutive equations and show their similarities and differences. Using the same integrated multiphysics model, for the first time we also present a new semi-experimental approach to measure strain during FSW using visioplasticity.

Finally, we perform a comprehensive experimental study (tensile testing, Electron Back Scatter Diffraction, Scanning Electron Microscopy, and micro-hardness testing) on FSW of aluminum 6061 samples in order to further validate the developed numerical model and optimize the welding process parameters (tool rotation speed, weld speed and axial force). The experimental study also prove the above mentioned preposition on a correlation among the processing-microstructure-mechanical properties during FSW, especially when comparing the UTS of samples from cold and hot weld conditions.

Preface

The base of this thesis is on publication format, where chapters are based on published journal, peer reviewed conference and submitted (under review) articles as well as the ones that are ready for submission. Dr. Abbas S. Milani and Dr. Spiro Yannacopoulos co-supervised this dissertation and co-authored all of these publications.

The literature review (Chapter 2), thermal model and Taguchi optimization (Chapter 3) were published as journal article 1 (see publications section). I was responsible for the literature review, method development, programming, simulations and writing the article. Dr. Milani and Dr. Yannacopoulos reviewed the article.

The validation of the integrated multiphysics model (Chapter 4) has been sent for publication as journal article 6. I was responsible for model development, programming using Dr. Claire Yu Yan's guidance in Comsol software, simulations and writing the article. Dr. Milani and Dr. Yannacopoulos reviewed the article.

Some parts of the comparison of constitutive equations (Chapter 5) have been submitted for publication as journal article 7 and the rest has been accepted for publication in conference proceedings (article 8). I was responsible for the literature review, method development, programming, simulations and writing these articles. Dr. Milani and Dr. Yannacopoulos reviewed the article.

Some parts of the strain measurement and related modeling (Chapter 6) were published as journal article 3 and some parts as conference proceedings article 2. I was responsible for the literature review, method development, programming, simulations and writing the articles. Dr. Milani and Dr. Yannacopoulos reviewed the articles.

The microstructure model (Chapter 7) was published in conference proceedings as article 4. I was responsible for developing the model, writing the computer program under the guidance of Dr. Claire Yu Yan, simulations and writing the article. Dr. Milani and Dr. Yannacopoulos reviewed the article.

The residual stress model (Chapter 8) was published in conference proceedings as article 5. I was responsible for developing the model, writing the computer program under Dr. Claire Yu Yan's

guidance, simulations and writing the article. Dr. Milani and Dr. Yannacopoulos reviewed the article.

The experimental article (Chapter 9) is submitted as journal article 9. I was responsible for developing methodology, design of experiments, performing the tests (with the help of School lab technicians including Mr. Durwin Bossy and Mr. David Arkinstall), data analysis, and writing the article. Dr. Milani and Dr. Yannacopoulos closely guided me through data analysis and reviewed the article. Dr. Andre Phillion also provided valuable assistance and guidance through the SEM and EBSD tests.

Publications list (chronological order)

Article 1: Mohamadreza Nourani, Abbas S. Milani, Spiro Yannacopoulos, Taguchi optimization of process parameters in friction stir welding of 6061 aluminum alloy: a review and case study, Journal of Engineering, Volume 3, Issue 2, 2011, Pages 144-155.

Article 2: Mohamadreza Nourani, Abbas S. Milani, Spiro Yannacopoulos, A new approach to measure strain during friction stir welding using viscoplasticity, ASME International Mechanical Engineering Congress & Exposition, 11-17 Nov 2011, Colorado, USA.

Article 3: Mohamadreza Nourani, Abbas S. Milani, Spiro Yannacopoulos, On the experimental and numerical predictions of strain during friction stir welding: a case study on 7050 aluminum alloy, TSEST Transaction on Control and Mechanical Systems, Volume 1, No 6, 2012, Pages 259-263.

Article 4: Mohamadreza Nourani, Abbas S. Milani, Spiro Yannacopoulos, Claire Yan, Predicting grain size distribution in friction stir welded 6061 aluminum, The 9th International Symposium on Friction Stir Welding 15-17 May 2012, Huntsville, USA.

Article 5: Mohamadreza Nourani, Abbas S. Milani, Spiro Yannacopoulos, Claire Yan, Predicting residual stresses in friction stir welding of aluminum alloy 6061 using an integrated multiphysics model, The 9th International Conference on Residual Stresses (ICRS 9), 7-9 October 2012,

Garmisch-Partenkirchen, Germany (Conference Proceedings appeared in the Journal of Materials Science Forum, 768-769: 682-689, 2013).

Article 6: Mohamadreza Nourani, Abbas S. Milani, Spiro Yannacopoulos, Claire Yan, An integrated multiphysics model for friction stir welding of 6061 Aluminum alloy (submitted), 2013.

Article 7: Mohamadreza Nourani, Abbas S. Milani, Spiro Yannacopoulos, On the effect of different material constitutive equations in modeling friction stir welding: a review and comparative study on aluminum 6061 (submitted), 2013.

Article 8: Mohamadreza Nourani, Abbas S Milani, Spiro Yannacopoulos, A review of thermomechanical models of friction stir welding, accepted as invited article to Thermec 2013 Conference, 2-6 December 2013, Las Vegas, USA.

Article 9: Mohamadreza Nourani, Abbas S Milani, Spiro Yannacopoulos, Processing-microstructure-property relationship and experimental optimization of friction stir welding of aluminum 6061 (submitted), 2013.

Table of Contents

Abstract.....	ii
Preface.....	iii
Table of Contents.....	vi
List of Tables	ix
List of Figures	xi
Acknowledgments.....	xvii
Dedication	xviii
Chapter 1: Introduction	1
1.1 Research motivation	1
1.2 Research objectives and organization of the thesis	1
Chapter 2: Review of Metallurgical Aspects, Prediction and Optimization Models.....	4
2.1 Metallurgical aspects.....	5
2.2 Prediction models.....	7
2.3 Optimization models.....	8
Chapter 3: Thermal Model and Taguchi Optimization.....	12
3.1 Introduction	12
3.2 Setting up the Taguchi optimization problem	16
3.3 Results and discussion	18
3.4 Summary of findings.....	26
Chapter 4: Integrated Multiphysics Model and Validation.....	28
4.1 Introduction	28

4.2 Model description.....	31
4.3 Case studies.....	38
4.4 Results and discussion	42
4.5 Summary of findings.....	49
Chapter 5: Comparison of Constitutive Equations	51
5.1 Introduction.....	51
5.2 CFD and CSM constitutive equations	54
5.3 Implementing and comparing selected constitutive equations in a same FSW model.....	74
5.4 Results and discussion.....	75
5.5 Summary of findings.....	81
Chapter 6: Strain Measurement and Model	83
6.1 Introduction	84
6.2 Strain measurement using Visioplasticity method.....	87
6.3 Strain modeling using the integrated multiphysics model.....	92
6.4 Results and discussion	94
6.5 Summary of findings.....	97
Chapter 7: Microstructure Model	98
7.1 Introduction	98
7.2 Model description	99
7.3 Results and discussion.....	100
7.4 Summary of findings.....	103
Chapter 8: Residual Stress Model	104

8.1 Introduction	104
8.2 Model description	105
8.3 Results and discussion.....	107
8.4 Summary of findings.....	109
Chapter 9: Experimental Study	111
9.1 Introduction.....	112
9.2 Methods	112
9.3 Results and discussion	117
9.4 Summary of findings.....	143
Chapter 10: Conclusions, Contribution to Knowledge and Recommendations for Future Research.....	146
10.1 Conclusions	146
10.2 Summary of contributions to knowledge.....	147
10.3 Recommendations for future research.....	148
References	150
Appendix A: Polynomial functions tested for calculation of the adjusted maximum UTS...	186

List of Tables

Table 3.1- Temperature dependence of the shear yield strength of aluminum 6061 alloy.....	14
Table 3.2- Physical properties of aluminum 6061 alloy.....	14
Table 3.3- Typical FSW process parameters used in the Taguchi optimization model.....	16
Table 3.4- The Taguchi L ₉ design with three factors-each three levels, along with the obtained response values from the corresponding runs.....	18
Table 3.5- Peak temperature values (°C) in the full factorial search (the highlighted value indicates the optimum).....	22
Table 3.6- ANOVA results on the peak temperature response using the values of Table 3.4 (statistical confidence level: 95%).....	24
Table 3.7- ANOVA results on the HAZ distance to the weld line using the values of Table 3.4 (statistical confidence level: 95%).....	24
Table 4.1- Process parameters and material properties used in Case study 1.....	32
Table 4.2- Results of the mesh sensitivity analysis in the model with pin radius of 5 mm...	37
Table 4.3- Process parameters and material properties used in Case study 2	40
Table 4.4- Process parameters and material properties used in Case study 3	41
Table 4.5- Process parameters and material properties used in Case study 4.....	42
Table 5.1- Comparison of various thermomechanical models of friction stir welding.....	64
Table 6.1- Reported equivalent plastic strains in FSW of aluminum alloys and the related process parameters.....	85
Table 6.2- Process parameters and material properties used in the integrated multiphysics model of aluminum 7050.....	93
Table 6.3- Comparison of the strain values measured via the viscoplasticity-CAD approach and those predicted by the multiphysics model..	96
Table 7.1- Process parameters and material properties used in the model.....	100
Table 8.1- Process parameters and material properties used in the base multiphysics model.....	106
Table 8.2- Temperature-dependent properties of Aluminum 6061 alloy [11].....	107

Table 9.1- Friction stir welding process parameters used for different samples; Sample numbers are specified as 1n, 2n ,..., 9n and B2.....	114
Table 9.2- FSW maximum temperature at middle of the weld line on back plates of different tested samples	119
Table 9.3- Average axial force of the tool in the steady state phase of the FSW of samples.....	121
Table 9.4- Ultimate tensile strength of different FSW samples (Minimum, Maximum and Average).....	124
Table 9.5- The optimum regression constants obtained for model in Equation (9-2).....	125
Table 9.6- Adjusted Max UTS values using the regression model	127

List of Figures

Figure 1.1- Framework of the dissertation.....	3
Figure 2.1- Schematic of the FSW process	5
Figure 2.2- (a) Simulated temperature distribution in the cross-section of 6061-T6 aluminum alloy and (b) the measured and predicted hardness profiles at 1, 10 ⁴ , and 10 ⁷ seconds after FSW [15, 28].....	8
Figure 3.1- Boundary conditions of the FSW thermal model; due to symmetry, one plate is shown, also thermal insulation is set along the weld joint boundary; the upper and lower surfaces experience natural convection and surface-to-ambient radiation.....	14
Figure 3.2- Sample regions extracted from the simulation model having a temperature equal to or higher than 430 °C; (a) run# 9 and (b) the optimum solution (indicated in Table 3.4); tool moves from left to right.....	19
Figure 3.3- Main effect plots of the process parameters for the HAZ distance from the weld line (points are based on the values of run#1 to #9 in Table 3.4).....	19
Figure 3.4- Temperature distribution in (a) run# 9 and (b) the optimum solution (see also Table 3.4).....	20
Figure 3.5- Proportionality of the maximum temperature and the HAZ distance criteria in the FSW optimization problem under study.....	21
Figure 3.6- Contributions of the process parameters on the peak temperature.....	23
Figure 3.7- Contributions of the process parameters on the HAZ distance.....	23
Figure 3.8- Distribution of the surface heat flux (W/m ²) on the tool pin and shoulder for the optimum solution; tool moves from left to right.....	26
Figure 4.1- Schematic view of the model dimensions and boundary conditions.....	31
Figure 4.2- Schematic view of the weld speed and rotational velocity at pin surface.....	33
Figure 4.3- Constitutive behavior of aluminum 6061 based on Equation (4-10) with constants taken from [50].....	36
Figure 4.4- Effect of mesh size on minimum velocity value (m/s) which is defined as error during sensitivity analysis.....	37

Figure 4.5- Mesh size distribution and subdomains.....	38
Figure 4.6- Points where temperature was measured in the back of the aluminum plates during FSW.....	39
Figure 4.7- Temperature distribution around the pin in Case 1 using (a) our model, (b) the results in study [49]	43
Figure 4.8- Temperature distribution (K) along with the velocity field streamlines in Case 1 (using our model)	43
Figure 4.9- Comparison of temperature distribution during the experiment and the model of Case 2 at back of aluminum plate in two different points, (a) weld centerline (point 1) and (b) 25 mm from weld centerline (point 2) (Figure 4.6).....	44
Figure 4.10- (a) 2D strain distribution of Case 3 using the current model; (b) 3D strain distribution data from [44]; (c) Metallurgical processing zones during friction stir welding [57].....	46
Figure 4.11- Schematic a central streamline with four different regions around the pin in Case 4	47
Figure 4.12- Variation of the temperature and shear strain rate using different welding speeds and a constant rotational speed of 41.66 rev/sec [55]	47
Figure 4.13- Values of temperature (K) and shear strain rate (s ⁻¹) in different regions using our model with the weld speed of 13.33 mm/sec and rotational speed of 41.66 rev/sec and equivalent results from [55] (Figure 4.12).....	48
Figure 4.14- Shear strain rate distribution around the pin in the current model for case 4...	48
Figure 5.1- (a) Shear stress versus shear rate and (b) viscosity versus shear rate for different fluid-type materials [131]	55
Figure 5.2- Schematic of stress-strain curves in different solid mechanics-based material models (T is temperature and $d\varepsilon/dt$ is strain rate)...	58
Figure 5.3- Schematic of the true stress-true strain curve during (a) dynamic recovery, and (b) dynamic recrystallization [141].....	59
Figure 5.4- Effect of using different dynamic viscosity equations on shear stress around the pin	76

Figure 5.5- Effect of using different dynamic viscosity equations on shear strain rate and temperature around pin.....	77
Figure 5.6- Effect of using different dynamic viscosity equations on dynamic viscosity around pin.....	78
Figure 5.7- Effect of using different dynamic viscosity equations on maximum temperature on the weldline.....	78
Figure 5.8- The Effect of using different dynamic viscosity equations in the CFD model on the predicted torque on pin	79
Figure 5.9- The effect of applying CFD model results (namely the temperature, strain and strain rate distributions) from ZH flow stress model into JC flow stress, under different dynamic viscosity equations	80
Figure 5.10- Effect of applying temperature and strain rate results from CFD model-ZH flow stress into the CSM-JC flow stress model, both under the condition of zero strain around the pin.....	81
Figure 6.1- Schematic view of the location and shape of the marker used to calculate the equivalent plastic strain with tool tilt angle of 3 degrees. a) top view b) side section view	87
Figure 6.2- Section of the deformed discrete marker at mid-plane of the plate [25].....	88
Figure 6.3- Different steps to calculate the marker strain (a) the marker shape at mid-plane of the plate [25] (b) drawing the marker boundary points (c) calculating the area by CAD (d) simplifying the marker boundaries.....	89
Figure 6.4- Position of the original marker section at mid-plane of the plate before deformation (a'b'c'd') and the reduced area after a strain along the thickness (abcd), and along the streamlines (ABCD).....	90
Figure 6.5- Schematic view of original area of the marker section at mid-plane of the plate (a'b'c'd') and the reduced area after a strain along the thickness (abcd), and along the streamlines (ABCD).....	91

Figure 6.6- The position of corresponding points on the original marker boundaries at mid-plane of the plate (a'b'c'd') after deformation along the thickness direction (abcdefgh) and after deformation along the streamlines (ABCDEFGH).....	92
Figure 6.7- Streamlines and the magnitude of the velocity vectors around the pin in a multiphysics model of FSW [28].....	92
Figure 6.8- Strain distribution results of the marker along streamlines at mid-plane of the plate using COMSOL.....	94
Figure 6.9- The position of the marker at the strain field and streamlines of the integrated multiphysics model.....	96
Figure 7.1- Relationship between $1/T$ and $\ln D$ in an Al 6063 weld [3].....	99
Figure 7.2- Temperature distribution ($^{\circ}\text{C}$) via the multiphysics model with process parameters used in [4].....	101
Figure 7.3- Comparison of the multiphysics model results with temperature measurements at trailing edge of the weld centerline [4].....	101
Figure 7.4- The predicted distribution of grain diameter (μm) after FSW	102
Figure 7.5- The subgrain diameter at the region 8 mm behind the tool center during FSW.....	103
Figure 8.1- Comparison of the numerical model results with temperature measurements at trailing edge of the weld centerline in midplate.....	108
Figure 8.2- (a) longitudinal (x -component) and (b) transverse (y -component) residual stress distribution in the FSW process; model values are compared to measurements.	108
Figure 9.1- LowStir TM device (a), FSW test fixture (b) with two embedded thermocouples (c and d).....	113
Figure 9.2- Selected FSW tool pin and shoulder (dimensions in mm) made from tool steel.....	113
Figure 9.3- Tensile test sample perpendicular to the weld line in middle (dimensions in mm)	115

Figure 9.4- Temperature measurements of samples at middle of the weld line on back plates in different weld speeds and constant RPM=1000	117
Figure 9.5- Temperature measurements of samples at middle of the weld line on back plates in different weld speeds and constant RPM=1400.....	118
Figure 9.6- Temperature measurements of samples at middle of the weld line on back plates in different weld speeds and constant RPM=1800.....	118
Figure 9.7- Tool temperature of different samples during welding (for the process parameters in each sample refer to Table 9.1).....	119
Figure 9.8- Tool axial force of different samples during FSW with critical points of A, B, C, D, and E (for the process parameters in each sample refer to Table 9.1).....	120
Figure 9.9- Tool torque on different samples during FSW tests with critical points of A, B, C, D, and E. (for the process parameters in each sample refer to Table 9.1).....	121
Figure 9.10- Tool transverse force of different samples during FSW with points of A, B, C, D, and E (for the process parameters in each sample refer to Table 9.1).....	122
Figure 9.11- FSW samples with different process parameters of weld speed and tool RPM (excess material are shown with white stars).....	123
Figure 9.12- Tensile samples cut from FSW samples with different controlled process parameters (weld speed and tool RPM)	126
Figure 9.13- Main effects of process parameters based on the regression model on average process parameters: a) RPM main effect, b) weld speed main effect and c) axial force main effect	127
Figure 9.14- Percentage contributions of the FSW process parameters on the weld UTS (the axial force has been considered to be fixed at 6871.1 N).....	128
Figure 9.15- Visual inspection of fracture surfaces of the samples with maximum UTS values	130
Figure 9.16- Fracture zone under the tool pin in sample 7n (cold weld or 1000 RPM, 75 mm/min); notice the delaminated	

regions in vicinity of the weld line	131
Figure 9.17- Fracture zone under the tool's pin using sample 2n (1400 RPM, 45 mm/min) with the lowest average axial force; notice the delaminated regions in vicinity of the weld line	131
Figure 9.18- Fracture zone under the tool's pin of sample 3n (hot weld or 1800 RPM , 45 mm/min); notice the delaminated regions in vicinity of the weld line	132
Figure 9.19- Fracture surface of sample 5n (1400 RPM, 60 mm/min) with the highest UTS (X 28).....	133
Figure 9.20- Typical high magnification of fracture surface in sample 5n (1400 RPM, 60 mm/min) with the highest UTS (X 5000).....	134
Figure 9.21- Delamination in material under the tool's pin in sample 3n (1800 RPM, 45 mm/min) or hot weld (X 40).....	134
Figure 9.22- Distances between laminates at yellow circle in Figure 9.21 in higher magnification (X 500).....	135
Figure 9.23- Low ductility fracture in some regions of sample 3n or hot weld (X 5000)....	135
Figure 9.24- Brittle fracture in some regions of sample 3n or hot weld (X 5000).....	136
Figure 9.25- Inter-granular fracture in sample 3n (hot weld) with the lowest UTS (X 10000).....	136
Figure 9.26- Inter-granular fracture in sample 3n with high magnification (X 101000).....	137
Figure 9.27- Grain size distribution at mid thickness of the advancing side of the weld zones of sample 3n with the lowest UTS (hot weld) and the sample 5n with the highest UTS (see also Figure 2.1) a) The whole profile b) Higher magnification of the nugget zone and shear layer c) Higher magnification of shear layer and thermomechanically affected zone (TMAZ) d) Higher magnification of the thermomechanically affected zone (TMAZ), heat affected zone (HAZ) and base metal.....	139
Figure 9.28- Micro hardness (HV) and number of grains in a 77 micron horizontal line at different locations of samples 3n and 5n with the lowest and the highest UTS values respectively...	141

Acknowledgments

First I would like to thank my co-supervisors, Dr. Abbas S. Milani and Dr. Spiro Yannacopoulos. Their honesty, advise, constant support, inspiration, kind guidance, and patience were a key for my PhD. Thank you for everything you have done for me.

I would like to thank the members of my doctoral committee; Dr. Andre Phillion, Dr. Claire Yu Yan and Dr. Warren Poole for their accessibility, constructive suggestions, and recommendations.

My deepest thanks go to my wife and family. I cannot find any suitable words to fully describe and thank their endless support throughout my life. Their love and encouragement made this dissertation possible.

I would also like to acknowledge all agencies provided support for my PhD studies, including NSERC, MK Technolgies Inc., and University of British Columbia's PhD Tuition Fee Award, International Partial Tuition Scholarship, and Graduate Student Travel Award.

Dedication

This thesis is dedicated to my wife, *Mrs. Raheleh Ehsani Ardakani*, who gave birth to the miracle of our life, *Nika Nourani*, during my PhD studies in addition to all of her endless support.

Chapter 1: Introduction

1.1 Research motivation

Since its invention at the Welding Institute of UK in December 1991, there have been widespread applications of friction stir welding (FSW) in industries producing, e.g., airplanes fuselage, ship deck, automobiles BIW, and trains in chassis. In FSW a rotating tool consisting of a pin and a shoulder is pressed against the matched ends of two plates/parts to be welded, while traversing along the weld centreline. A specific aspect of this particular welding procedure is that the heat transfer is accomplished by the heat of deformation of material close to the tool and there is no need to melt the material (i.e., the weld is made in a solid state). The mass and heat transfers, however, highly depend on properties of the material and the welding process parameters including tool rotational speed and transverse speed as well as its geometry. The effect of welding parameters, design of tool, the multiphysics nature of the process, and the microstructure and mechanical properties of the weld have been under study only in recent years as FSW is a fairly new process and is developing rapidly. Therefore, a careful development and assessment of numerical models and experimental tools for this promising manufacturing process is deemed to be a key determinant for optimum application of FSW in related industries. In particular, there has been no “integrated multiphysics” modeling that can be tailored towards industrial applications by means of minimizing the cost and time of process optimization processes. In experimental studies of FSW there are also limited works studying the processing-microstructure-property relationships via a systematic design of experiments (DOE) approach. More details of background in each of the above areas will be presented in subsequent chapters.

1.2 Research objectives and organization of the thesis

Based on the above outlined research motivation on the numerical modeling, optimization, and experimental aspects of FSW, after a review of the underlying concepts and approaches in Chapter 2, we defined the objectives of this PhD thesis as follows:

Objective 1: Adapt a systematic Taguchi design of experiment method to perform process optimization, analysis of variance (ANOVA), calculation of main effects and the percentage

contribution of each process parameter (weld transverse speed, tool RPM and axial force), using a previously validated three-dimensional steady-state thermal model of FSW from the literature (Chapter 3).

Objective 2: Develop and validate a new, two-dimensional steady-state numerical model of FSW where different physics are coupled (multiphysics model) such as heat transfer, material flow (computational fluid dynamics or CFD) and structural mechanics (computational solid mechanics or CSM) (Chapter 4).

Objective 3: Review the most common constitutive equations used by other researchers in FSW modeling and subsequently study the effects of using some of these equations on the output of the multiphysics model for aluminum 6061 (Chapter 5).

Objective 4: Review the strain models of FSW and develop a new approach to measure strain in this dynamic process and compare the prediction results of the model from Objective 2 with measurements (Chapter 6).

Objective 5: Develop an integrated numerical model to predict the microstructure of FSW welds using the above multiphysics model outputs from Objective 2; hence arriving at an “integrated multiphysics” model of FSW where we can use process parameters during FSW and predict ‘post-process’ properties such as weld grain size (Chapter 7).

Objective 6: Extend the integrated multiphysics model of objective 2 to be able to predict residual stresses in FSW from the process model outputs (Chapter 8).

Objective 7: Establish an in-house FSW experimental test set-up along with related material characterization techniques to perform optimization and an in-depth investigation of processing-microstructure-property relationships of FSW of aluminum 6061, while re-evaluating capabilities of the multiphysics model in predicting experimental observations (Chapter 9). In doing so, we will also present a new approach via regression to eliminate the effect of variable axial force (uncontrolled noise factor) during optimization, analysis of variances (ANOVA), and calculation of main effects and percentage of contributions of FSW process parameters (Chapter 9).

In Chapter 10, we summarize the main conclusions of the dissertation by reviewing the key results and discussions of each chapter. We will also outline the limitations and discuss possible improvements for future research. Figure 1.1 summarizes the dissertation framework as related to each objective.

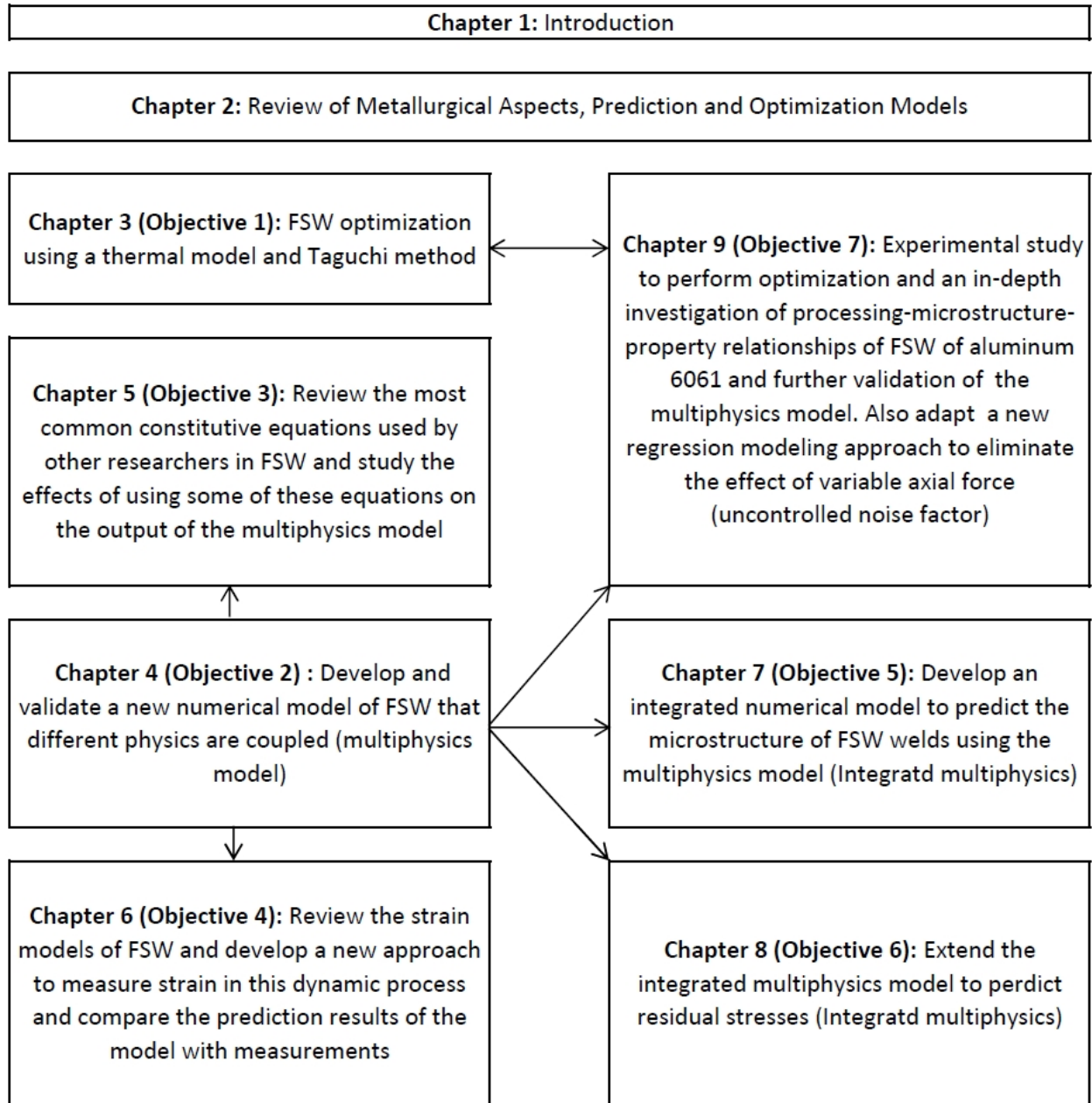


Figure 1.1- Framework of the dissertation

Chapter 2: Review of Metallurgical Aspects, Prediction and Optimization Models

The chapter has been published in some parts of **Article 1**: Mohamadreza Nourani, Abbas S. Milani, Spiro Yannacopoulos, Taguchi optimization of process parameters in friction stir welding of 6061 aluminum alloy: a review and case study, Journal of Engineering, Volume 3, Issue 2, 2011, Pages 144-155.

Overview: The chapter is intended to present basics of the friction stir welding (FSW) and give a review of its metallurgical aspects along with earlier works in the literature regarding prediction and optimization models. Further reviews will follow in the subsequent chapters as each corresponding topic and article from this thesis is presented. Namely, in Chapter 5 we will review CFD and CSM constitutive equations and compare various published thermomechanical models of FSW; in Chapter 6 we review strain models of FSW on aluminum alloys; and in Chapter 9 we review the experimental studies of FSW on different alloys.

Friction Stir Welding (FSW), a solid state joining method developed and patented by TWI Ltd., Cambridge, UK in 1991 [1], has particularly attracted a significant interest from aircraft and car manufacturers for joining high strength aluminum alloy components. Specific examples include the wrought 6000-series Al-Mg-Si (Cu) alloys that are commonly used in aircraft fuselage skin and automotive body panels, mainly due to their ability to be strengthened by artificial aging after forming. FSW has also been used to produce rocket shells, the panel of the cabin of aircrafts with stringers and beams, hollow panels of wagons, and pipes [2].

The basic concept behind FSW is simple: non-consumable rotating tool with a specially designed pin and shoulder is inserted into the abutting edges of the two parts to be joined and traversed along the line of joint (Figure 2.1).

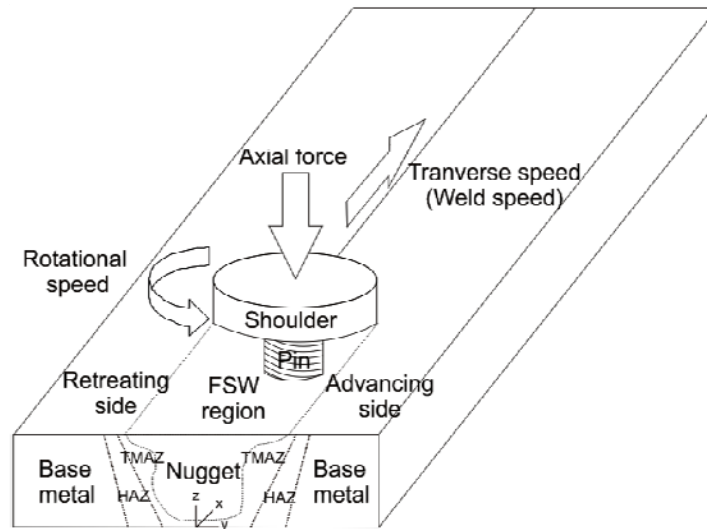


Figure 2.1- Schematic of the FSW process

The FSW tool primarily serves two functions: (a) heating the work piece, and (b) flowing the material to produce the joint. A detailed list of parameters controlling this joining process is given in [3] as follows:

1. Rotational speed (rpm)
2. Welding speed (mm/s)
3. Axial force (KN)
4. Tool geometry
 - (i) Pin length (mm)
 - (ii) Tool shoulder diameter, D (mm)
 - (iii) Pin diameter, d (mm)
 - (iv) Tool inclined angle ($^{\circ}$)
 - (v) D/d ratio of the tool

2.1 Metallurgical aspects

During friction stir welding, heating is accomplished by friction between the tool and the work piece and plastic deformation of the work piece. The localized heating softens the material

around the pin, and a combination of the tool rotation and translation leads to the movement of material from the front of the pin to its backside. As a result of this process a joint is produced in the 'solid state'. Because of various geometrical features of the tool, the material movement around the pin can be complex to study [4]. During the FSW process, the material undergoes intense plastic deformation at elevated temperature, resulting in the generation of fine and equiaxed dynamic- recrystallized grains [5-8]. Consequently, the fine microstructure in friction stir welds results in good mechanical properties (e.g., the tensile strength for FSW of Al 7039 plates is as high as 311 MPa while the base metal has a tensile strength of 383 MPa [9]).

FSW joints usually consist of four, as opposed to primarily three in "normal" welds, different regions as shown in Figure 2.1: (a) unaffected base metal; (b) heat affected zone (HAZ); (c) thermomechanically affected zone (TMAZ) and (d) friction stir processed (FSP) zone (nugget). The formation of these regions is affected by the material flow behavior under the action of the rotating non-consumable tool. The material flow behavior is predominantly influenced by the FSW tool profile, tool dimensions and welding process parameters [8, 10].

Frictional heat and plastic flow during FSW create fine and equiaxed dynamic-recrystallized grains in the stir zone (SZ) and elongated and recovered grains in the thermomechanically affected zone (TMAZ). The heat affected zone (HAZ) is often identified by means of only material hardness changes as there is no difference in grain structure compared to the base metal. This softened HAZ region can be characterized by the dissolution and coarsening of the strengthening precipitates during friction stir welding [11]. As an example, the precipitation sequence during aging of pseudobinary Al -Mg₂Si alloys has been characterized as follows: supersaturated solid solution → needle shaped precipitates (β'') → rod shaped precipitates (β') → β -Mg₂Si [11-13]. It is known that needle shaped precipitates correspond to coherent β'' phase, which contributes predominantly to the strength of 6000 series aluminum alloys. During prolonged aging, β'' needles are transformed into semi-coherent β' rod shaped precipitates. Coarsened precipitates and the associated loss of coherency lead to a diminished strengthening effect relative to the needle shaped precipitates [14]. Woo et al [15] showed a relation between the maximum temperatures experienced during FSW and the formation of SZ, HAZ and TMAZ.

2.2 Prediction models

Based on the physics involved (Section 2.1 of Chapter 2), prediction models of FSW should account for heat transfer, tool-part contact phenomenon, and the material plastic deformation. This makes detailed simulations of the process time consuming and complex [16]. A number of different FSW prediction models have been used in the literature by different research groups. The process thermal models were developed, e.g., by Colegrove et al. [17], Schmidt et al. [18], and Khandkar & Khan [19]. Computation fluid dynamics (CFD) models have been used, e.g., by Colegrove et al. [20], and Schmidt & Hattel [21]. Thermomechanical models of FSW have been used, e.g., by Chen & Kovacevic [22] and Schmidt & Hattel [23].

The most common approach reported on the prediction of FSW processes includes the thermal models, ranging from simple analytical models based on Rosenthal's solutions [24] to three-dimensional numerical models by Kovacevic et al. [25] and Schmidt et al. [26]. Traditionally the thermal models are either transient Lagrangian [25] or stationary Eulerian [26]. The first type allows finite plate dimensions to be used and the transient starting/stopping phases to be studied. The latter type has the advantage of fast solution time and the possibility of using a fine mesh close to the heat source (tool) [27]. The fully coupled Eulerian-Lagrangian approaches for this process are only recently under investigation.

Depending on a given study's objectives, the prediction models of FSW process may be used to investigate different mechanical/thermal/metallurgical properties of the weld. In the study by Myhr & Grong [28] a time-dependent model for determining the 'hardness' of a 6082-T6 aluminum alloy after an arbitrary thermal treatment, such as welding, is presented. In the T6 heat treated condition this alloy exhibits maximum attainable values of hardness and strength due to fine Mg_2Si precipitates. The model uses a relative fraction between 1 to X_d of these particles to interpolate between the maximum and the minimum possible hardness of the material. Heat treatment at an elevated temperature can decrease X_d and thereby the hardness [28-29]. Recently, Larsen et al. [30] proposed a hardness model for the optimization of friction stir welds following the work by Myhr & Grong [29], which could not predict the real hardness changes in the weld nugget because it did not consider dynamic recrystallization during the process. Another prediction of hardness minimum locations during natural aging in 6061-T6 aluminum alloy friction stir welds was carried out by Woo et al. [15]. In their model, the peak temperature

profiles were calculated for each characteristic region in the FSW (Figure 2.2): DXZ about 480–550 °C, TMAZ about 430–480 °C, and HAZ less than 430 °C. Thus, the critical temperature for the material to reduce its hardness was identified to be ~430 °C.

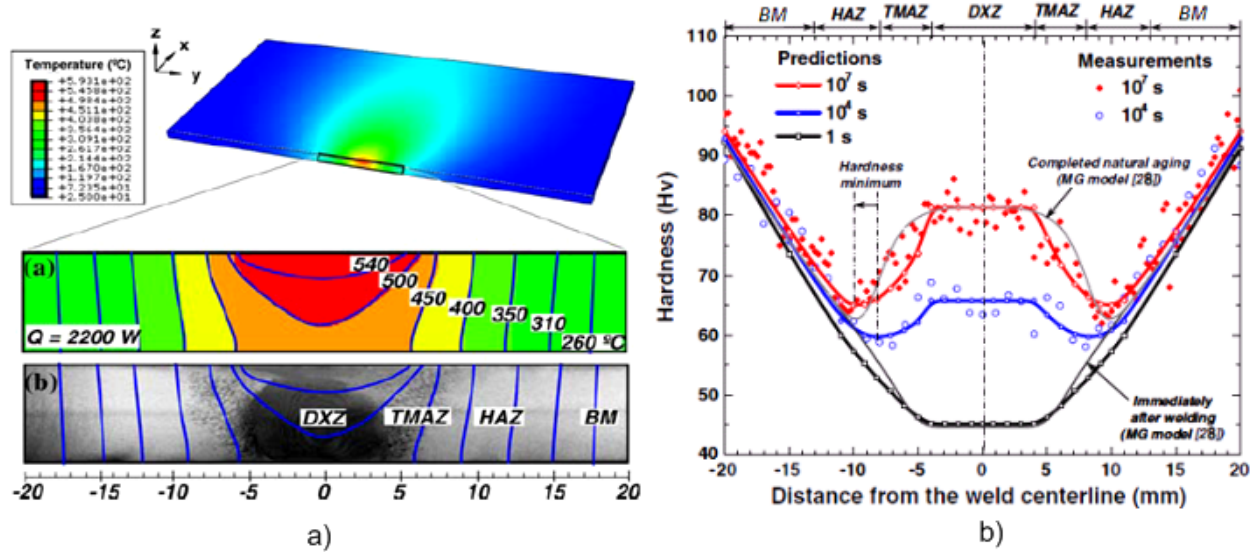


Figure 2.2- (a) Simulated temperature distribution in the cross-section of 6061-T6 aluminum alloy and (b) the measured and predicted hardness profiles at 1, 10^4 , and 10^7 seconds after FSW [15, 28]

2.3 Optimization models

The optimization problems considered in the literature for FSW, in general, are realized by considering a set of process parameters (in most cases, the translational welding speed and the rotational speed or heat input), and a few constraints and objective functions. The use of complex numerical models may become expensive and, in some cases, calculation of reliable analytic sensitivities of objective and constraint functions is prohibitive. While the real welding process is thermo-mechanically coupled in essence, purely thermal models have been among the least expensive models that provide important knowledge on the temperature distribution of a FSW process. Furthermore, they can be used as the first step of, for example, an uncoupled heat transfer, residual stress, microstructure or fatigue analysis [17, 18, 25-27].

Numerical techniques that are specifically developed to reduce the cost of expensive computer simulations are also available. These include the space and manifold mapping techniques developed by Bandler et al. [31] and Echeverria & Hemker [32]. In these techniques, a mapping between a high-level and low-level model is created and iteratively updated such that when applied to a coarse mesh, a good approximation of the true model is obtained during optimization. In Chapter 3, a similar space mapping technique for FSW [16] is used to convert the three dimensional heat flux due to the heat of deformation to an equivalent two dimensional (surface) heat flux (more details to follow in Chapter 3).

Nandan et al. [33] presented a genetic algorithm (GA) to determine an optimum set of four process parameters by minimizing the differences between their numerical model and experimental data. The parameters considered were the contact friction coefficient, the extent of sticking between the tool and the workpiece, the heat transfer coefficient at the bottom surface of the workpiece, and the amount of viscous dissipation converted into heat. The objective was to minimize the peak temperature and the time that temperature reaches above a critical limit. Tutum et al. [34] also used a genetic algorithm to solve a multi-objective optimization problem considering residual stress and the tool wear. In the study by Fratini & Corona [35], the steepest descent optimization method was used to maximize the strength of a friction stir welded lap joint using the welding speed and the tool rotational speed as process variables. The procedure was, however, purely experimental and objective function gradients were obtained using a forward finite difference approach. In the same study, in order to account for uncertainties during the experiments, several identical samples were tested at each set of variables and the final results showed an increase in the joint strength after the optimization. In the study by Gebhard & Zaeh [36], the authors established an empirical (second order polynomial) relationship between the tool temperature (response) and parameters of the welding including the rotational and transverse speeds. More specifically, the objective of the work was not optimization but rather the modeling and understanding of the FSW process by promptly predicting the effect of changes in welding parameters on the temperature response. In other case studies, trial and error approaches have been used to improve the welding process parameters. An example is given in the study by Shercliff et al. [37] where the welding speed was optimized such that the material in front of the tool was sufficiently softened to allow easy tool traversing. There have also been studies that

include trial and error methods for curve-fitting, e.g., the workpiece-backing plate heat transfer coefficient to reduce the difference in calculated and measured temperatures (Khandkar et al. [38] and Schmidt & Hattel [39]). Recently, Larsen proposed a systematic inverse modeling technique to estimate the workpiece-backing plate heat transfer coefficient in the FSW process [27] and Atharifar used a genetically optimized neural network system to optimize the process parameters in friction stir spot welding [40].

Jayaraman et al. [41] analyzed the effect of rotational and transverse speeds as well as the axial tool force on the tensile strength of the friction stir welded cast aluminum alloy A319. A full-factorial matrix was used to design the experiments. The Taguchi method has also been used for the optimization of the FSW process parameters using mechanical tests on tensile specimens (Lakshminarayanan et al. [9]) and for studying the impact resistance of dissimilar metal joints (Chen [42]).

The Taguchi optimization method is an efficient quality improvement tool that has been receiving attention in several engineering problems, owing to its simplicity and minimal optimization cost requirement based on the concept of orthogonal arrays. The use of trial and error, full factorial, and heuristic search methods such as GA for large-scale optimization problems can be prohibitive due to the high computation times associated with complex simulations/experiments. For instance, for an optimization with four variables and three levels each, a full factorial search would require a total of $3^4=81$ runs whereas the Taguchi L_9 orthogonal array only requires 9 runs to complete the optimization [43]. In a more intricate example, a process with 8 factors, each with 3 levels, would require 6561 ($=3^8$) experiments in order to test all possible factor combinations. With a Taguchi orthogonal array, only 18 experiments would be necessary, i.e., less than 0.3% of the original number. The method can also be used for screening purposes when the number of variables is high and the key parameters need to be identified before launching the final optimization routine. The main disadvantage of the Taguchi method, however, is that it assumes no interaction among design factors. Thus, it is critical to check the validity of the method for new applications using other methods such as full factorial design, follow-up (conforming) experiments, etc. The method has also been criticized in the literature for designing the product/process quality rather than correcting for poor quality,

however this aspect of the method would be more concerned when non-repeatability of process data (noise effect) is high [43].

Chapter 3: Thermal Model and Taguchi Optimization

This chapter has been published in some parts of **Article 1**: Mohamadreza Nourani, Abbas S. Milani, Spiro Yannacopoulos, Taguchi optimization of process parameters in friction stir welding of 6061 aluminum alloy: a review and case study, Journal of Engineering, Volume 3, Issue 2, 2011, Pages 144-155.

Overview: The chapter is intended to present a straightforward and computationally efficient methodology for optimizing the process parameters of friction stir welding (FSW) of 6061 aluminum alloy. In particular, it is shown how to minimize the heat affected zone (HAZ) distance to the weld line in the joined parts using a Taguchi design of experiments (DOE) optimization method and a temperature field finite element model. The peak temperature during the process has also been minimized. The Taguchi optimization is a statistical method developed to enhance the quality of manufactured products, and more recently applied to engineering, biotechnology, marketing and advertising. It is based on Orthogonal Array (OA) experiments which gives a reduced variance for the experiment with optimum settings of control parameters [1]. Since in the present work the method is used for the first time in relation to the HAZ objective function, an auxiliary full factorial search is conducted to ensure Taguchi's orthogonal design assumption for the FSW problem. Results will confirm that the method can be successfully used for minimizing both the HAZ distance to the weld line and the peak temperature, with a minimal number of simulation runs via orthogonal arrays. In addition, a new ANOVA analysis on the L_9 orthogonal array with three factors is performed and results indicate that among the parameters considered (i.e., the tool rotational speed, transverse speed, and the axial force), the most significant parameter on the weld quality is the rotational speed, followed by the axial force and transverse speed.

3.1 Introduction

As discussed in Section 2.1 of Chapter 2, the HAZ encompasses the weld region that undergoes softening (i.e., minimum hardness region of the welded part). Beyond the HAZ, no change in the base metal properties is expected. The HAZ is formed in a region which experiences minimum temperature rise during the friction stir welding process, causing dissolution and coarsening of

the strengthening precipitates in the joining alloy (see, e.g., [2] for FSW of 6061 aluminum alloy). The closer HAZ is to the weld center, the higher the possibility to merge the weld nugget with fine and equiaxed dynamic-recrystallized grains, and the lower the possibility of hardness decrease of the base metal. As a result, the quality of the welded part can be directly related to the size and position of the HAZ. In addition, one would physically expect that minimizing the HAZ size would affect the peak temperature that often occurs in the workpiece in the vicinity of the tool. The main objective of the present work is to show that using a Taguchi optimization procedure, the FSW process parameters (such as the tool transverse speed, rotational speed, and applied normal force) can be controlled in a way that both the HAZ distance to the weld line and the maximum (peak) temperature in the weld are minimized simultaneously. To this end, a case study is established via a thermal model in the COMSOL multiphysics package along with a set of reported experimental data in the literature on FSW of 6061 aluminum alloy (Section 3.1). Subsequently, the proposed optimization routine is presented and discussed in Sections 3.2 to 3.3. Using an adjusted ANOVA framework for the Taguchi's L_9 orthogonal array with three factors, it is also shown how each process parameter affects the HAZ distance to the weld line as well as the maximum peak temperature. Finally, the optimum levels of the process parameters are identified and validated using confirmation runs.

3.1.1 Case study

According to the study by Woo et al. [2], during FSW the regions experiencing the temperature of $\sim 430^\circ\text{C}$ are the locations of minimum hardness of the 6061 aluminum alloy because of the dissolution and coarsening of the strengthening precipitates (see also Figure 2.2-(b)). Hence, by decreasing the distance of this region to the weld line, the volume of the region with low hardness can be decreased as it will merge to weld nugget with fine and equiaxed dynamic-recrystallized grains with maximum hardness after aging. A steady-state heat transfer model of the FSW process is established in the COMSOL Multiphysics finite element package, where for modeling purposes a fixed tool approach [3] is employed by moving the workpiece towards the tool (Figure 3.1). The heat due to deformation in TMAZ and the tilt angle are not considered. The plates are long enough to ensure the steady-state condition (i.e., as the tool passes through the joint line, there is enough time for the welded regions behind the tool to come to the final

temperature equilibrium, resulting in a uniform temperature profile along the weld line). The aluminum alloy has temperature dependent yield strength as shown in Table 3.1, and constant physical and thermal properties that are given in Table 3.2 [4].

Table 3.1- Temperature dependence of the shear yield strength of aluminum 6061 alloy

Temperature (°C)	311	339	366	394	422	450	477	533	589	644
Yield stress (MPa)	241	238	232	223	189	138	92	34	19	12

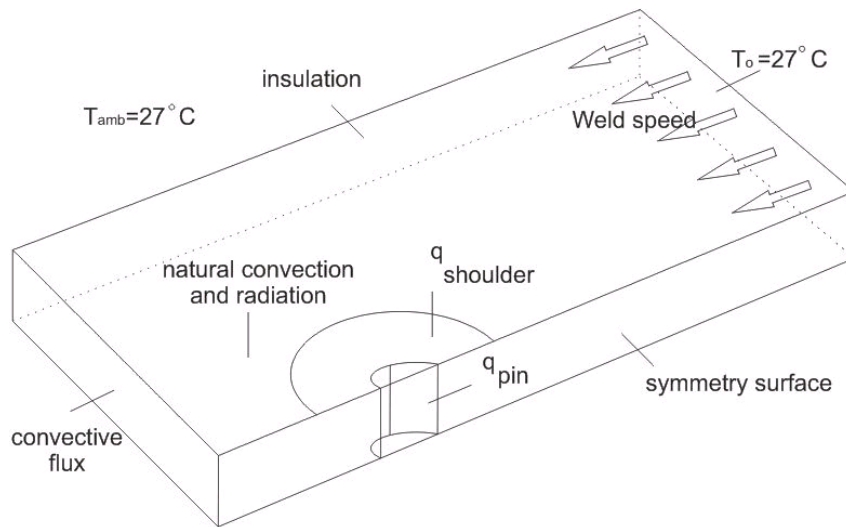


Figure 3.1- Boundary conditions of the FSW thermal model; due to symmetry, one plate is shown, also thermal insulation is set along the weld joint boundary; the upper and lower surfaces experience natural convection and surface-to-ambient radiation

Table 3.2- Physical properties of aluminum 6061 alloy

Thermal Conductivity, (W/mK)	$K = 160$
Density, (Kg/m ³)	$\rho = 2700$
Heat Capacity, (J/Kg-K)	$C_p = 900$

The FSW tool is made of steel with flat shoulder and cylindrical pin shapes. The thermal boundary conditions are illustrated in Figure 3.1. The model geometry is symmetric around the weld, allowing to model only one aluminum plate and half of the tool [5]. It is considered that according to the experimental study by Woo et al. [2], the temperature of 430 °C is the critical temperature that provides sufficient activation energy and kinetics for dissolution and coarsening of the strengthening precipitates during the process, thus causing the minimum hardness locations at the outer boundary of the HAZ (Figure 2.2).

Equation (3-1) describes the steady-state heat transfer in the plate where a convective term (right-hand side) is included to account for the effect of material movement.

$$\nabla \cdot (k \nabla T) + q = \rho C_p V_T \cdot \nabla T \quad (3-1)$$

q represents the rate of heat source per volume, V_T is the welding (transverse) speed.

The model simulates the heat dissipation due to the interaction among the tool's pin and shoulder with the workpiece (surface heat of friction and volumetric heat of deformation) as a surface heat flux (space mapping) in the tool pin and shoulder (Colegrove et al.) [5]:

$$q_{pin}(T) = \begin{cases} \frac{\mu}{\sqrt{3(1+\mu^2)}} r_p \omega \bar{Y}(T); T < T_{melt} \\ 0; T \geq T_{melt} \end{cases} \quad (3-2)$$

q_{pin} (W/m²) is the pin heat flux and μ is the friction coefficient between the pin and the workpiece, r_p denotes the pin radius, ω refers to the pin's angular velocity (rad/s), and $\bar{Y}(T)$ is the average shear yield stress of the material as a function of temperature, T . The latter function is approximated by an interpolation of experimental data given in Table 3.1. Equation (3-3) defines the local heat flux from the shoulder at the distance- r from the center axis of the tool (Colegrove et al.) [5]:

$$q_{shoulder}(r, T) = \begin{cases} (\mu F_n / A_s) \omega r; T < T_{melt} \\ 0; T \geq T_{melt} \end{cases} \quad (3-3)$$

F_n represents the normal force, A_s is the shoulder's surface area, and T_{melt} is the aluminum 6061 melting temperature (652 °C).

On the right side of the part (see also Figure 3.1), a constant temperature boundary condition is applied (Dirichlet boundary condition), whereas for the left side a convective flux boundary condition (Neumann boundary condition) is used (i.e., the flux created in that cross-section moves out of the domain by movement of the plate compared to the tool). The upper and lower surfaces of the aluminum plates lose heat due to natural convection and surface-to-ambient radiation. The corresponding heat flux expressions for these boundaries are [6]:

$$\begin{cases} q_{up} = h_{up} (T_0 - T) + \varepsilon\sigma (T_{amb}^4 - T^4) \\ q_{down} = h_{down} (T_0 - T) + \varepsilon\sigma (T_{amb}^4 - T^4) \end{cases} \quad (3-4)$$

Where h_{up} and h_{down} are the heat transfer coefficients for natural convection, T_0 is an associated reference temperature, ε is the surface emissivity, σ is the Stefan-Boltzmann constant, and T_{amb} is the ambient air temperature. In the current model, the following values are used: $h_{up} = 12.25$ W/(m²·K) and $h_{down} = 6.25$ W/(m²·K); $T_0=T_{amb}=27^\circ\text{C}$, and $\varepsilon=0.3$.

3.2 Setting up the Taguchi optimization problem

The nominal process parameters are chosen from reference [5] as follows: $\omega = 350$ rpm, the transverse speed $V_T = 1.72$ (mm/sec), and the axial force $F_n = 11$ kN, which produce the same peak temperature of 550 °C as reported in [5]. Next, we consider a ± 10 % variation around the nominal values to define two new levels for each of the above parameters as shown in Table 3.3.

Table 3.3- Typical FSW process parameters used in the Taguchi optimization model

Levels	Rotational speed (rpm)	Transverse speed (mm/sec)	Axial force kN
1	315	1.55	9.9
2	350	1.72	11
3	385	1.90	12.1

From a practical viewpoint, it is important to note that during numerical optimization one should not choose the FSW parameter ranges at extreme conditions (e.g., $\pm 50\%$ of the nominal/working condition), as they may correspond to failure modes in the actual weld as observed by Lakshminarayanan [7]:

- when the rotational speed is low, a wormhole at the retreating side of the weld nugget was observed, and it may be due to insufficient heat generation and insufficient metal transportation;
- when the rotational speed is high, a tunnel defect was observed and it is due to excessive turbulence caused by higher rotational speed;
- when the welding speed was low, a pin hole type of defect was observed due to excessive heat input per unit length of the weld and no vertical movement of the metal;
- when the welding speed was high, a tunnel at the bottom in the retreating side was observed due to insufficient heat input caused by inadequate flow of material;
- when the axial force was low, tunnel and crack-like defects in the middle of the weld cross section in the retreating side was observed since insufficient downward force causes no vertical flow of material; and
- when the axial force was increased beyond a threshold, a large mass of flash and excessive thinning were observed due to higher heat input.

In order to reduce the number of simulation runs ($3^3=27$), the Taguchi L_9 orthogonal design [8] (shown in gray in Table 3.4) is used to analyze the effect of each processing parameter (the rotational speed, the traverse speed, and the axial force) on the HAZ distance to the weld line of the friction stir welded joints. The ultimate goal is to minimize the distance of the points on the HAZ boundary having the critical temperature of $430\text{ }^\circ\text{C}$ from the weld center line (as explained in Section 3.1 of Chapter 3). Since there may be several points (a contour) having the same critical temperature in each run, the HAZ distance to the weld line is measured as the maximum distance of a location with $430\text{ }^\circ\text{C}$ on the mid plane to the weld line. For solving the finite element model in each run, 957 tetragonal normal elements (chosen through a mesh sensitivity

analysis on the temperature response) and the stationary linear direct UMFPACK solver were used with 1867 degrees of freedom [6].

3.3 Results and discussion

Table 3.4 shows the HAZ distance to the weld line in each of the nine runs dictated by the Taguchi L₉ design. The corresponding peak temperature for each case has also been included in the table. For illustrative purposes, the extracted regions of the weld having a temperature of 430 °C or higher for two samples runs are illustrated in Figure 3.2.

Table 3.4- The Taguchi L₉ design with three factors-each three levels, along with the obtained response values from the corresponding runs

Run#	Factor levels (as defined in Table 3.3)			HAZ distance to the weld line (mm)	Peak Temperature(°C)
	ω	V_T	F_n		
1	1	1	1	8.60	488.72
2	1	2	2	11.79	507.31
3	1	3	3	13.84	524.01
4	2	1	2	22.55	579.32
5	2	2	3	23.58	597.88
6	2	3	1	8.70	496.98
7	3	1	3	32.29	664.37
8	3	2	1	18.96	556.80
9	3	3	2	20.50	579.39
Optimum found	1	3	1	2.56	458.98

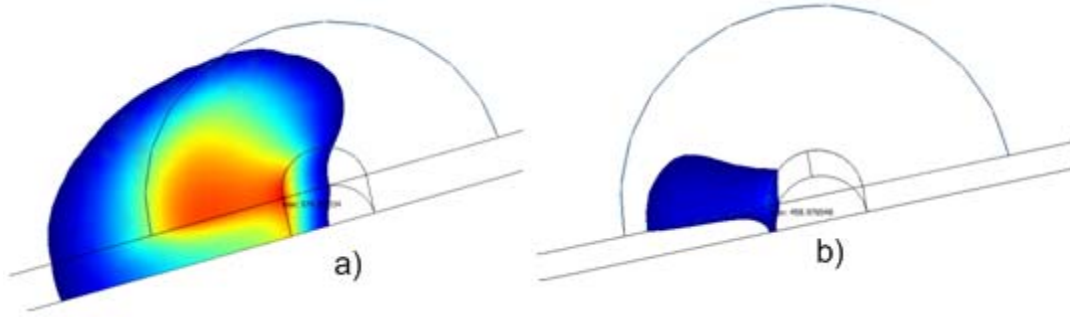


Figure 3.2- Sample regions extracted from the simulation model having a temperature equal to or higher than 430 °C; (a) run# 9 and (b) the optimum solution (indicated in Table 3.4); tool moves from left to right

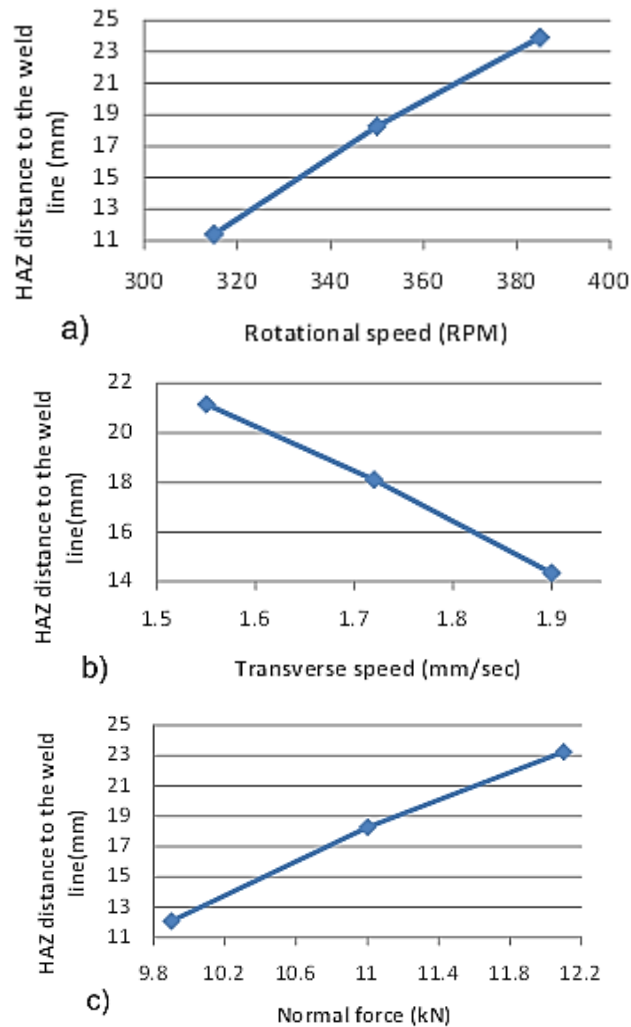
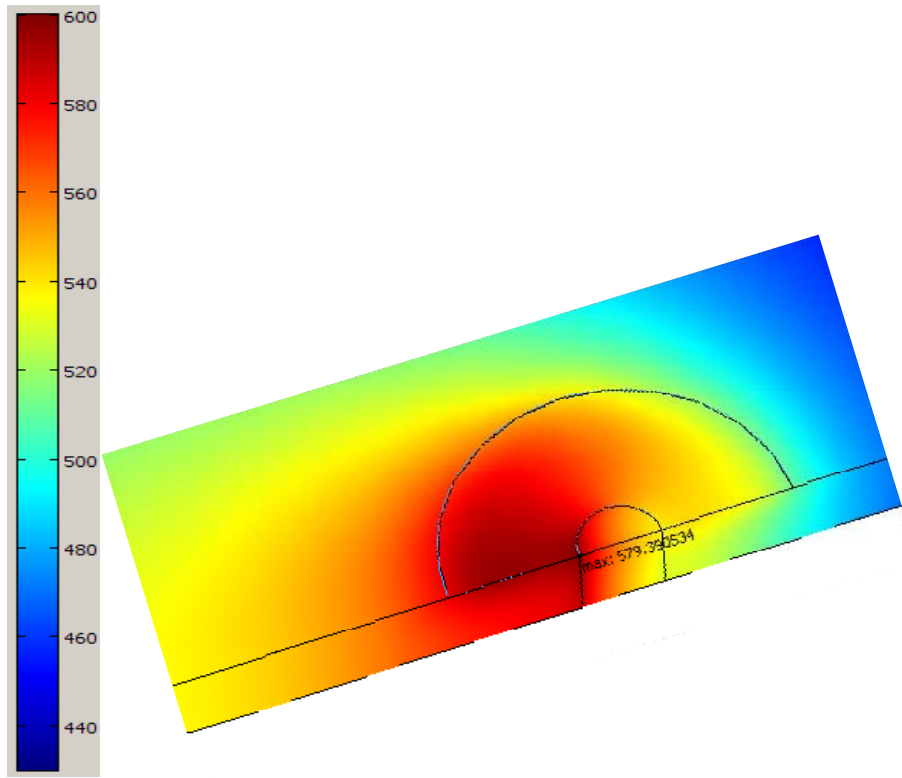
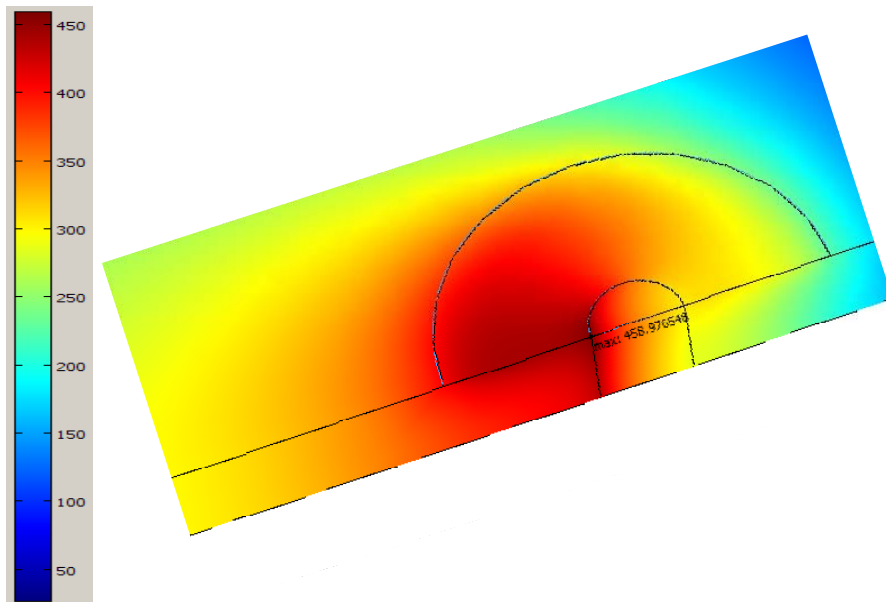


Figure 3.3- Main effect plots of the process parameters for the HAZ distance from the weld line (points are based on the values of run#1 to #9 in Table 3.4)



(a)



(b)

Figure 3.4- Temperature distribution in (a) run# 9 and (b) the optimum solution (see also Table 3.4)

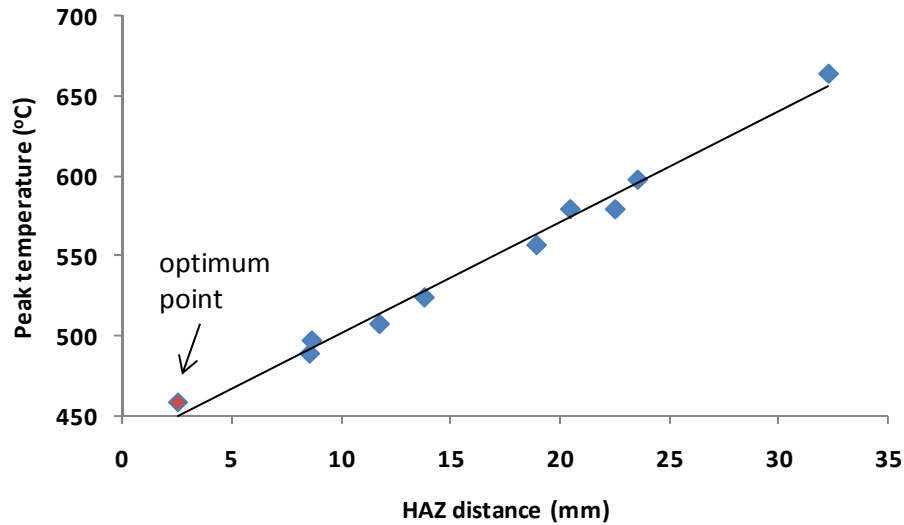


Figure 3.5- Proportionality of the maximum temperature and the HAZ distance criteria in the FSW optimization problem under study

By plotting the main effects according to the values of Table 3.4, it is readily seen from Figures 3.3 that according to the Taguchi method the lowest value of HAZ distance is achieved at the *lowest* level of rotational speed=315 RPM, the *highest* level of traverse speed=1.9 mm/sec, and the *lowest* level of axial force=9.9 kN. Note that this combination was not among the original nine runs in Table 3.4 but the method has been able to capture the optimum based on the (base) L_9 orthogonal array. To validate the solution, a new simulation was run at the aforementioned optimum levels and the results were obtained as follows.

- the peak temperature= 458.98 °C, and
- the distance of the HAZ from the weld center line= 2.56 mm

which are the lowest for both criteria when compared to the original L_9 runs in Table 3.4. It is seen that the minimization of HAZ distance criterion has automatically resulted in the minimization of the peak temperature criterion. The temperature distribution of the optimum solution is shown in Figure 3.4 and compared to run#9 for illustration purposes. The temperature distribution in Figure 3.4 between the two plates is symmetric as the effect of material movement around the tool is not considered in thermal models. Having a low peak temperature is occasionally referred to as cold FSW condition, which has been shown to yield higher formability

in aluminum 6061 as measured by the limited dome height (LDH) test [9]. The proportionality of the HAZ distance criterion and the peak temperature criterion is formally shown in Figure 3.5 using the optimization Pareto front. Finally, it is important to recall that the Taguchi method's assumption is that there are no significant interactions among design factors. While the above obtained optimum point implies the suitability of the method for the FSW problems, a full factorial design (i.e., with 3^3 runs) needs to be conducted to validate the assumption. Results of the full factorial search are shown in Table 3.5 (the highlighted value is the optimum response which is coincident with the Taguchi solution).

Table 3.5- Peak temperature values ($^{\circ}\text{C}$) in the full factorial search (the highlighted value indicates the optimum)

		F_n (kN)								
		9.9			11			12.1		
		V_T (mm/sec)			V_T (mm/sec)			V_T (mm/sec)		
		1.55	1.72	1.9	1.55	1.72	1.9	1.55	1.72	1.9
ω (RPM)	315	488.72	472.69	458.98	526.98	507.31	490.79	567.83	543.84	524.01
	350	533.64	513.58	496.98	579.32	554.54	533.94	625.30	597.88	573.05
	385	581.60	556.80	536.25	632.16	604.55	579.39	664.37	652.50	624.76

3.3.1 ANOVA analysis: Percentage contribution of the process parameters

Following the ANOVA scheme used for the L_9 Taguchi method in reference [7], the percentage contribution of each FSW process parameter on the peak temperature as well the HAZ distance to the weld line are calculated in the present case study. Detailed formulae of this analysis framework (which were not given in [7]) are included in Equations (3-5) to (3-13). The idea is that the original L_9 design is with four factors but here three factors are active. Thus, the effect of the fourth factor can be used to estimate a pooled error in the actual experiments. Subsequently, the sum of squares, SS , of the main factors should be adjusted to pure values, SS' (i.e., without reflecting the error). The analysis results are summarized in Tables 3.6 and 3.7, and graphically in Figures 3.6 and 3.7.

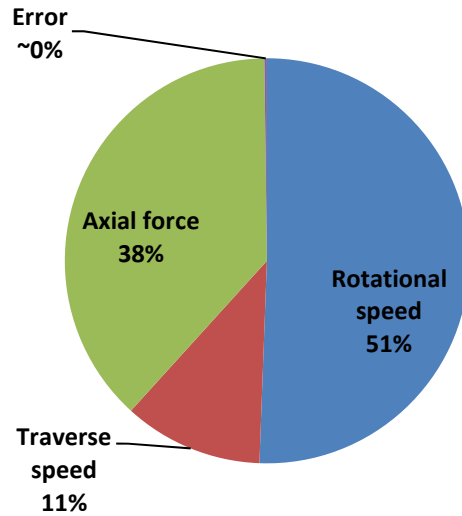


Figure 3.6- Contributions of the process parameters on the peak temperature

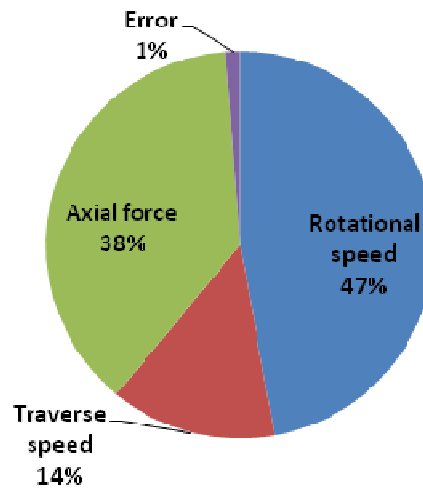


Figure 3.7- Contributions of the process parameters on the HAZ distance

The rotational speed has the highest contribution on both peak temperature and HAZ distance to the weld line. It has been reported in other studies that the tool rotational speed ω also has a maximum contribution on the resulting weld material properties such as tensile strength [7, 10]. This suggests that the FSW rotational speed is a key parameter to control welding process characteristics such as peak temperature and the HAZ distance to weld line as well as the

mechanical properties of the final welded part. By examining Equation (3-2) it can be seen that ω has a direct effect on the heat generation of the pin. In Equation (3-3) both ω and F_n (axial force) have effects on heat generation of the tool shoulder. Thus, between the two parameters, one would expect that ω has more influence on the process response, as shown in Figures 3.6 and 3.7. To scrutinize these effects further, in Figure 3.8 the distribution of surface heat fluxes on the pin and shoulder, q_{pin} and $q_{shoulder}$ according to Equation (3-2) and Equation (3-3) respectively, are presented for the optimum solution point as indicated in Table 3.4. According to Figure 3.8, the maximum heat flux in the shoulder is 80 % higher than that of the pin. Physically, the shoulder has higher radius compared to pin and the rotational speed of the tool causes a higher heat flux through the material shearing and frictional heat.

Table 3.6- ANOVA results on the peak temperature response using the values of Table 3.4
(statistical confidence level: 95%)

Source	SS	DOF	MS	F	P-value	SS'	%Contribution
ω	13158.06	2	6579.03	1036.71	0.0010	13145.37	51
V_T	2909.63	2	1454.82	229.25	0.0043	2896.94	11
F_n	9903.75	2	4951.88	780.31	0.0013	9891.06	38
Error	12.69	2	6.35	-	-	50.76	~0
Total	25984.14	8	12992.07	-	-	25984.14	100

Table 3.7- ANOVA results on the HAZ distance to the weld line using the values of Table 3.4
(statistical confidence level: 95%)

Source	SS	DOF	MS	F	P-value	SS'	%Contribution
ω	233.06	2	116.53	162.37	0.0061	231.62	47
V_T	69.71	2	34.86	48.57	0.0202	68.28	14
F_n	187.40	2	93.70	130.56	0.0076	185.96	38
Error	1.43	2	0.72	-	-	5.74	1
Total	491.61	8	245.81	-	-	491.61	100

Calculation of percentage contributions in the L₉ design with three active factors:

$$\bar{y}_L = \frac{1}{9} \sum_{i=1}^9 y_{L_i} \quad (\bar{y}_L \text{ is the total average response in the Taguchi design}) \quad (3-5)$$

$$SS_{Total} = \sum_{i=1}^9 (y_{L_i} - \bar{y}_L)^2 \quad (SS_{Total} \text{ is the total sum of squares}) \quad (3-6)$$

$$SS_{\omega} = 3 \sum_{i=1}^3 (y_{\omega_i} - \bar{y}_L)^2, SS_{V_T} = 3 \sum_{i=1}^3 (y_{V_{T_i}} - \bar{y}_L)^2, SS_{F_n} = 3 \sum_{i=1}^3 (y_{F_{n_i}} - \bar{y}_L)^2 \quad (3-7)$$

($y_{\cdot i}$ is the i -th level average response of the corresponding factor in the design)

$$SS_{Error} = SS_{Total} - SS_{\omega} - SS_{V_T} - SS_{F_n} \quad (\text{pooled error}) \quad (3-8)$$

$$MS_{Error} = \frac{SS_{Error}}{DOF_{Error}} = \frac{SS_{Error}}{2} \quad (\text{mean square error}) \quad (3-9)$$

$$F_{\omega} = \frac{MS_{\omega}}{MS_{Error}}, F_{V_T} = \frac{MS_{V_T}}{MS_{Error}}, F_{F_n} = \frac{MS_{F_n}}{MS_{Error}} \quad (\text{Fisher ratio}) \quad (3-10)$$

$$SS'_{\omega} = SS_{\omega} - DOF_{\omega} \times MSS_{Error} = SS_{\omega} - SS_{Error} \quad (\text{pure sum of square}) \quad (3-11)$$

Similarly,

$$SS'_{V_T} = SS_{V_T} - SS_{Error} \quad \text{and} \quad SS'_{F_n} = SS_{F_n} - SS_{Error} \quad (3-12)$$

$$\%Contribution_{\omega} = \frac{SS'_{\omega}}{SS_{Total}}, \%Contribution_{V_T} = \frac{SS'_{V_T}}{SS_{Total}}, \%Contribution_{F_n} = \frac{SS'_{F_n}}{SS_{Total}} \quad (3-13)$$

Remark: From a statistical standpoint, in the presence of interactions (which were not significant in this case study as shown), the ANOVA formulation outlined above on the Taguchi method with pooled error can be used to explore the main effect percentage contributions that one would identically obtain from a full factorial analysis. This means saving a significant amount of time to identify the process parameters effects by conducting only a fraction of a full factorial design (here 9 vs. 27 runs).

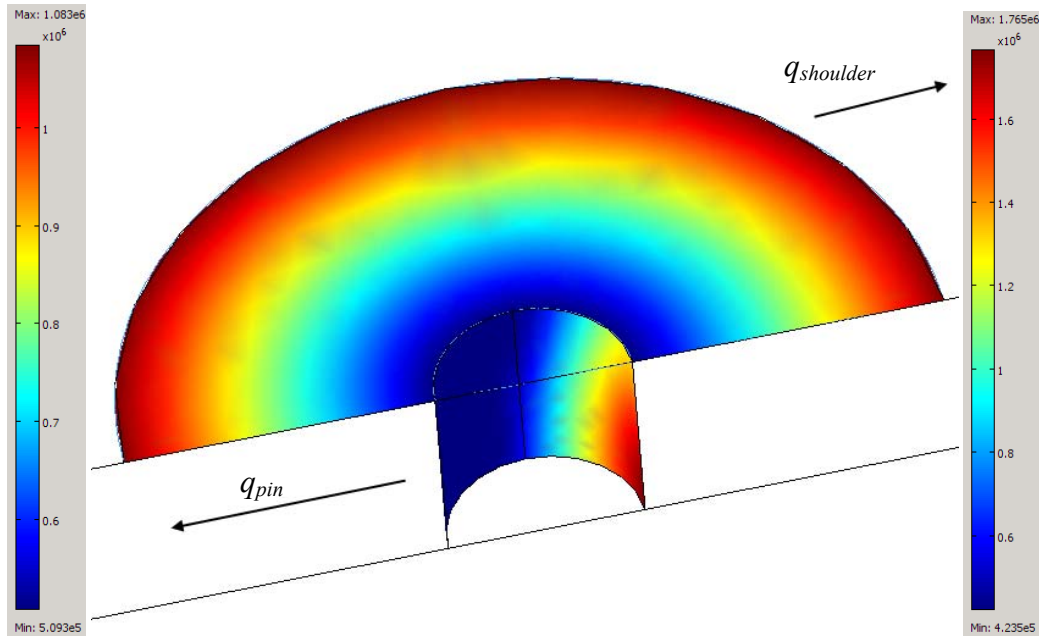


Figure 3.8- Distribution of the surface heat flux (W/m^2) on the tool pin and shoulder for the optimum solution; tool moves from left to right

3.4 Summary of findings

The Taguchi optimization of a FSW process was conducted on a temperature field for the 6061 aluminum alloy in Chapter 3. The (auxiliary 27 run) full factorial analysis of the process confirmed that the result of the Taguchi optimization is efficient and no significant interaction effects are present when the objective function comprises temperature field characteristics of the weld such as the HAZ distance to the weld line and/or the peak temperature in the workpiece. Contributions of the process parameters on both criteria were found to be comparable in the conducted case study; namely, the tool rotational speed showed the highest significance, followed by the normal force and the welding transverse speed. The variation of the rotational speed of the tool resulted in a 51% contribution on the HAZ distance to the weld line. The minimized peak temperature of $458.9\text{ }^\circ\text{C}$ (cold weld) in the case study indicated a 91°C temperature reduction from the nominal value of $550\text{ }^\circ\text{C}$ (hot weld). The ANOVA method of the Taguchi L_9 design and the full factorial analysis yielded similar parameter contributions.

While the application of optimization techniques on FSW reveals an increasing trend in the literature, it is important to recognize practical limitations of the process parameters. An example of such problem is excessive welding speed which can practically mean the risk of void creation in the weld line. Such phenomena cannot be modeled with, e.g., pure thermal or CFD models and a given optimizer may overestimate the practical range of the welding process.

Chapter 4: Integrated Multiphysics Model and Validation

This chapter has been submitted for publication as **Article 6:** Mohamadreza Nourani, Abbas S. Milani, Spiro Yannacopoulos, Claire Yan, An integrated multiphysics model for friction stir welding of 6061 Aluminum alloy (submitted), 2013.

Overview: The chapter presents a comprehensive ‘integrated multiphysics’ model of friction stir welding (FSW) where “multiphysics” theories, such as non-Newtonian incompressible fluid dynamics, conduction and convection heat transfer, and plain stress solid mechanics, have been coupled. Slip/stick condition between the tool and workpiece, friction and deformation heat source, the convection and conduction heat transfer in the workpiece, a solid mechanics-based viscosity definition, and the Zener-Hollomon- based rigid-viscoplastic material properties with a solidus cut-off temperature and empirical softening regime have been implemented. It is shown that the model is capable of simultaneously predicting the local distribution, location and magnitude of maximum temperature, strain, and strain rate fields around the tool pin which have been “integrated” to predict microstructure and residual stress of FSW later in Chapters 7 and 8, respectively. In order to validate each predicted process variable, the model has been applied to a set of published case studies and experiments on FSW of aluminum 6061.

4.1 Introduction

TWI Ltd. in 1991 developed Friction Stir Welding (FSW), which is a solid state joining method and has been patented [1]. FSW has different industrial applications and has considerable advantages compared to arc welding processes [2]. The main advantages of this process include:

- Mechanical properties of the weld are improved compared to other welding methods. Higher than 75% of joint efficiencies are reported for different materials.
- There is no need of shielding gases or filler materials as no melting happens in FSW. Because of the lower maximum temperature compared to conventional welding methods there is almost no distortion and solidification defects in FSW.
- There is no special training needed for FSW operators.
- There is huge cost reduction in FSW as no preparation or reworking is necessary.

- Energy consumption is reduced by 80% as there is no electrical current used in FSW.

Some of disadvantages of FSW are the tool cost and slower manufacturing speed.

Various numerical methods including the finite element, finite volume, finite difference, smooth particle hydrodynamics (SPH) and analytical methods are utilized in developing prediction models of FSW. The governing equations (analytical or coupled with process parameters) are based on thermal [3], thermomechanical fluid dynamics [4-7] or solid mechanics [8-15], conceptual [16], and kinematics [17] models, often developed in-house or built in conventional codes such as Abaqus, COMSOL, Fluent, Deform-3d, CTH, Forge3, Ansys, Nisa, Star-ccm, iStir, Stir3d, Fidap, Sysweld, Cosmos, Hickory, Thercast, Fastflo, LS-Dyna, Acusolve, Jmatpro and Weldsim. The solid mechanics models consider that material is solid during FSW and strain distribution is one of the model results. The fluid dynamics models usually consider a solid mechanics based definition of viscosity and non-Newtonian incompressible flow of the softened solid. They predict strain rate distribution and cannot predict strain distribution as a model result but there are some researchers who used some post processing techniques to compute strain on streamlines. Long et al [6] used a simple geometry based formulation to calculate engineering strains on different streamlines and Arora et al [7] estimated the accumulated strains experienced in the material by integrating strain rates over time along limited streamlines. In this multiphysics model we applied strain rate integration over time to compute plastic strains in all the points of fluid dynamics model for the first time which is based on a solid mechanics definition of viscosity.

The assumptions made during the simulation of FSW can affect the analysis results considerably. Some of the common assumptions are: 2D or 3D modeling, assigned values of the process parameters, coupled/semi-coupled or thermal-pseudo-mechanical relations between thermal and mechanical properties, Lagrangian/Eulerian or Arbitrary Lagrangian Eulerian (ALE) formulations, transient or steady state conditions, consideration of the welding material as a fluid or a solid, assigning the governing equations by means of rigid viscoplastic or elastic-viscoplastic material models (such as Zener-Hollomon, Johnson-Cook, Norton-Hoff, etc.) for the solid state or viscosity models (such as power law, Carreau, Perzyna, etc.) for the fluid state, temperature-dependent thermal properties of the material, tool/workpiece interface conditions (slip/stick) [18], and workpiece boundary conditions.

There exist other modeling approaches such as ‘integrated modeling’ [19-26] and ‘multiphysics modeling’ [27-33] that have been applied in more recent investigations for modeling forming processes. In the latter, it is necessary to use computer simulation to arrive to the optimized products and structures with a minimum cost and time. Now a days, complicated thermal processes such as welding and casting are studied using multiphysics models which contains both computational solid mechanics (CSM) and computational fluid dynamics (CFD) models. In studies on welding processes, multiphysics modelling has been used with optimization methods to find the needed properties of the final welds. Also, the integration of model outputs and prediction of some post process processing is a new research trend [34-39].

We recently reported some advantages of the integrated multiphysics modeling in directly predicting microstructure and residual stress *after FSW* based on the main process parameters (weld speed and rotational speed) [40, 41] which are discussed in Chapters 7 and 8 in details. There exist two regions in material flow *during FSW*; which some researchers call it “pin-driven flow” and “shoulder-driven flow”. These regions of material flow should properly join together to build a weld with no defect. In order to facilitate understanding the effect of parameters controlling these regimes during FSW, the main goal of this chapter is to present other results of the ‘integrated multiphysics’ model for simultaneously studying a multitude of variables of interest for a typical aluminum alloy. In multiphysics modeling, one uses different governing equations to predict the response variables in a deformation process (like strain, temperature, shear strain rate, etc); whereas in an integrated model, one uses the above main parameters to predict other (post-welding) parameters such as the weld microstructure and residual stresses [25]. The present model brings these two prediction routines together under a single comprehensive numerical analysis framework, thus facilitating the study of any combination of main and post-process parameters. To show the applicability of the model, in addition to comparing to in-house experimental measurements, prediction results are tested against a set of case studies from the literature focusing on strain, temperature, and strain rate fields.

4.2 Model description

4.2.1 General

In FSW a non-consumable tool with a specially designed pin and shoulder rotates and inserts into the contacting edges of the two plates to be joined and moves along it (Figure 4.1). When the plate is thick enough we may approximate a two dimensional flow in mid thickness of the plate and consider the shoulder as a remote heat source. The steady-state solution is a snapshot of the flow at an instant.

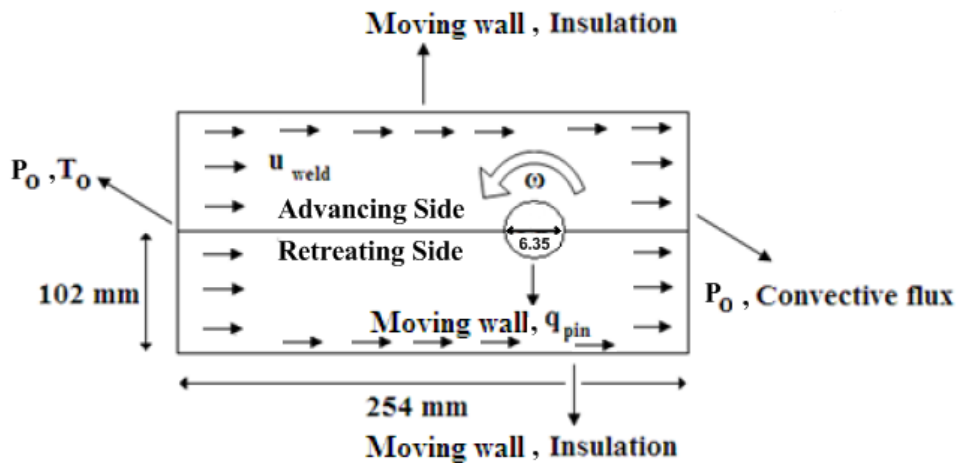


Figure 4.1- Schematic view of the model dimensions and boundary conditions

4.2.2 Fluid dynamics theory

To define the fluid-like behavior of the welding material around the pin, a set of governing equations assuming an incompressible flow has been used in the model as follows [42]:

$$\text{Continuity equation: } \nabla \cdot u = 0 \quad (4-1)$$

$$\text{Momentum equation (Navier-Stokes equation): } \rho(u \cdot \nabla)u = \nabla \cdot [-pI + \eta(\nabla u + (\nabla u)^T)] + F \quad (4-2)$$

$$\text{Dynamic viscosity: } \eta(T, \bar{\gamma}) = \frac{\bar{\tau}(T, \bar{\gamma})}{\bar{\gamma}} \quad (4-3)$$

where u is the velocity vector, ρ is the density, p is pressure, F is the volume force vector, $\bar{\tau}$ is the effective shear stress, $\bar{\gamma}$ is the effective shear strain rate, and η is the dynamic viscosity.

The dynamic viscosity in Equation (4-3), as opposed to a Newtonian fluid, may not be constant and can change by the shear flow stress and/or the shear strain rate (i.e., a non-Newtonian domain). This makes the coupled solution of partial differential equations highly non-linear. As shown in Figure 4.1, the pin is considered to rotate in its position (i.e., with no translational movement) and instead the plate moves from left to right. The inlet pressure at the left hand side of the plate and the outlet pressure at the right hand side of the plate are equal to ambient pressure as shown in Table 4.1. The upper and lower boundaries of the plate have moving-wall conditions equal to the weld transverse speed (u_{weld}). The outer boundaries of the plates are considered to be fixed and the material in contact with the pin is considered to accompany the pin during one rotation of the pin and then replaced by new material as the tool moves. This was based on a previous strain modeling study using experiments results via viscoplastic strain measurements during FSW [43]. It also complies with other evidence reported by Xu *et al* [44] that, there is a banded region in FSW, the thickness of the band or the space between the bands is equal to the tool progress in one pin rotation. we also noticed this in my experiments and it is shown in Figure 9-21 of Chapter 9.

Table 4.1- Process parameters and material properties used in Case study 1

Weld speed- u_{weld} (mm/s)	Rotational speed- ω (rev/s)	Pin radius- r_{pin} (mm)	Ambient pressure- P_o (KPa)	Ambient temperature- T_o (°C)	R (J/mol.K)	Friction coefficient- μ	δ
2.34 [52]	3.1 [52]	5 [52]	101	27	8.31451	0.4 [45]	0.65 [45]
α (1/MPa)	n	A (1/s)	Q (J/mol)	C_p (J/Kg K)	k (W/mK)	ρ (Kg/m ³)	Solidus (°C)
0.045 [54]	3.55 [54]	$2.41e^8$ [54]	145000 [54]	789.9+0.495 9T [52]	115.23+0.15 94T [52]	2700 [52]	582 [52]

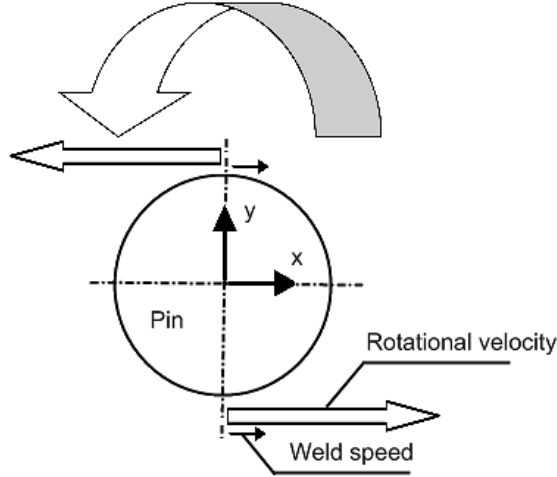


Figure 4.2- Schematic view of the weld speed and rotational velocity at pin surface

At the circularly shaped pin/plate interface (Figure 4.2), a rotating velocity boundary condition is applied with the stick coefficient (δ) equal to 0.65 [45]. The value was fitted by considering the torque measurement of the tool during FSW and its prediction by the model with different stick coefficients. The stick coefficient is initially defined as the ratio of tangential velocity of the material in contact with the pin to the tangential velocity of the pin periphery [5]:

$$\text{Stick coefficient [5]: } \delta = \frac{V_{\text{material in contact with pin}}}{V_{\text{pin periphery}}} \quad (4-4)$$

Considering a 2D model, the x and y components of the tangential velocity of the plate material are calculated using Equation (4-5) and (4-6):

$$\text{Velocity in } x \text{ direction: } u = -2\pi y\omega\delta - u_{\text{weld}}\delta \quad (4-5)$$

$$\text{Velocity in } y \text{ direction: } v = 2\pi x\omega\delta \quad (4-6)$$

where x and y are different positions of the pin based on the center of the coordinate system on the pin center, and ω is the pin rotational speed.

4.2.3 Heat transfer theory

The governing differential equation of conductive and convective heat transfer in a fluid during steady state conditions is as follows.

$$\text{Energy equation [46]: } \rho C_p \mu \cdot \nabla T = \nabla \cdot (k \nabla T) + q \quad (4-7)$$

where C_p is the specific heat capacity at constant pressure, T is temperature, k is thermal conductivity, q is internal heat source.

According to the thermal boundary conditions shown in Figure 4.1, the temperature at the left hand side of the plate is equal to ambient temperature (here 27 °C) and the right hand side of the plate has a convective heat flux temperature gradient. The upper and lower boundaries of the plate have insulation heat boundary conditions because of large dimensions of the plate compared to its thickness. The conductive heat transfer between the pin and plate is considered. The pin material is steel with the density of 7850 Kg/m³, the specific heat capacity of 475 J/KgK, and the thermal conductivity of 44.5 W/mK. Note that if heat transfer in the tool is not considered in the model, a lower value of temperature in the heading edge of the tool will be resulted. In majority of thermal models of FSW [18], the generation of heat is modeled from both plastic dissipation and frictional heat using a boundary condition of surface heat flux at the matrix-tool interface via Equation (4-8).

$$\text{Total heat flux [18]: } q_{pin} = \begin{cases} 2\pi r_{pin} \omega [\delta \bar{\sigma} + (1-\delta) \mu \bar{\sigma}] & T < Solidus \\ 0 & T \geq Solidus \end{cases} \quad (4-8)$$

where r_{pin} is the pin radius, ω is the tool rotational speed, δ is the stick coefficient, μ is the friction coefficient, and $\bar{\sigma}$ is the effective normal stress (flow stress).

4.2.4 Solid mechanics theory

Governing equations of a rigid viscoplastic material at elevated temperature were used in the model via Equations (4-9) to (4-13).

$$\text{Zener-Hollomon equation [47, 48]: } Z = \dot{\varepsilon} \exp\left(\frac{Q}{RT}\right) \quad (4-9)$$

$$\text{Flow stress [49]: } \bar{\sigma} = \begin{cases} \frac{1}{\alpha} \sinh^{-1}\left(\left(\frac{Z}{A}\right)^{1/n}\right) & T \leq \text{Solidus} - 50 \\ \frac{1}{\alpha} \sinh^{-1}\left(\left(\frac{Z}{A}\right)^{1/n}\right) \times \frac{\text{Solidus} - T}{50} & \text{Solidus} - 50 < T < \text{Solidus} \\ 0 & T \geq \text{Solidus} \end{cases} \quad (4-10)$$

$$\text{Equivalent strain rate: } \dot{\varepsilon} = \frac{\bar{\dot{\gamma}}}{\sqrt{3}} = \frac{2}{3} (\dot{\varepsilon}_{ij} \dot{\varepsilon}_{ij})^{\frac{1}{2}} \quad (4-11)$$

$$\text{Strain rate tensor: } \dot{\varepsilon}_{ij} = \frac{1}{2} \left(\frac{\partial u_i}{\partial x_j} + \frac{\partial u_j}{\partial x_i} \right) \quad (4-12)$$

$$\text{Equivalent Shear stress: } \bar{\tau} = \frac{\bar{\sigma}}{\sqrt{3}} \quad (4-13)$$

where Z is the Zener-Hollomon parameter, $\dot{\varepsilon}$ is the effective strain rate, Q is the temperature independent activation energy or self-diffusion energy, R is the gas constant, and α , A , and n are model constants determined by curve-fitting to hot deformation experimental data. Tello *et al* [50], for example, tested hot compression, measured the flow stress and determined the model constants of their materials. we also used strain rate integration over time to calculate plastic strain in all points of the model for the first time.

As stated earlier, friction stir welding is a solid state welding process. This has been verified by earlier microstructural studies after the process where no evidence of dendrite microstructure was seen [44]. Also there is no sharp decrease of transverse load during the process and hence the maximum temperature recorded during the process is normally below the solidus temperature of the material being welded. If a high volume of partial melting is introduced during FSW intentionally, it will generate a weld with low mechanical properties which is not desired. In order to implement the maximum temperature of solidus in the model, we consider that at a temperature equal or higher than solidus temperature, the flow stress (Equation (3-10)) is equal to zero, which in turn would cause no volumetric heat of deformation and surface frictional heat flux at material in contact with pin according to Equation (3-8). In practice, if localized melting

happens, the heat generation stops and the extra heat will be absorbed by the bulk material and the temperature decreases below the solidus temperature again. This would result in unwanted weld defects.

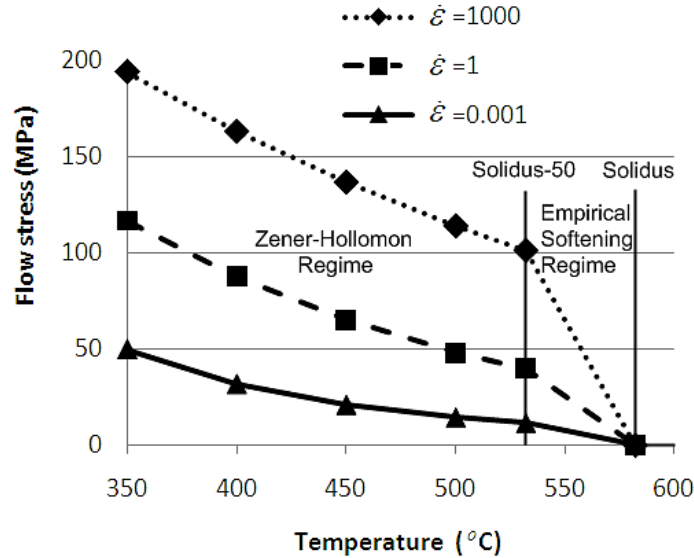


Figure 4.3- Constitutive behavior of aluminum 6061 based on Equation (4-10) with constants taken from [50]

As reported in [18, 49], there is an empirical softening regime at which the dynamic viscosity becomes almost zero when the temperature reaches near the solidus/ cut-off temperature. we consider a linear decrease of flow stress to zero as temperature increases under different strain rates in the neighboring region of 50 °C below the solidus temperature of aluminum 6061 (582 °C) as shown in Figure 4.3.

4.2.5 Mesh sensitivity analysis and solver selection

The optimum mesh size in the plate shown in Figure 4.1 was determined based on a sensitivity analysis on the value of minimum velocity from the CFD model. Triangular elements were used throughout the analysis and as shown in Table 4.2 and Figure 4.4, the error (calculated minimum velocity) remains almost constant and near zero when a ‘fine’ mesh is used. Hence, in order to have the minimum error and the lowest computational cost at the same time, we chose a mesh size between ‘fine’ and ‘finer’ in all subsequent cases. Also, in order to have more mesh size

control around the pin we divided the part domain into two subdomains as shown in Figure 4.5. In case studies 1 to 3 (details to follow in the next section) where there is a pin radius of 5 mm, the total number of meshes were 1758 with 116 boundary elements; and in case 4 where the pin radius is 2.22 mm we used the same number of boundary elements but smaller mesh size around the pin subdomain with a total number of 3132 elements. The chosen solver in COMSOL was UMFPACK with an error tolerance of 10^{-6} which yielded the best results. UMFPACK is a set of routines for solving non-symmetric sparse linear systems, $Ax=b$, using the “Unsymmetric Multi Frontal” method [51].

Table 4.2- Results of the mesh sensitivity analysis in the model with pin radius of 5 mm

Mesh type	Number of Elements	Solution time (sec)	DOF	Min velocity (m/s)	Iteration number
Extremely fine	40760	606.3	163880	5.120723e-5	30
Extra fine	10160	184.2	41080	1.88723e-5	42
Finer	6858	58.4	28136	4.828878e-5	22
Fine	1534	17.6	6328	3.290934e-5	25
Normal	1028	16.3	4272	3.672481e-4	32
Coarse	538	7.86	2272	3.465262e-4	25
Coarser	372	10.6	1592	2.856799e-4	40
Extra coarse	198	7.39	872	2.729464e-4	35
Extremely coarse	138	10.6	616	3.078724e-4	52

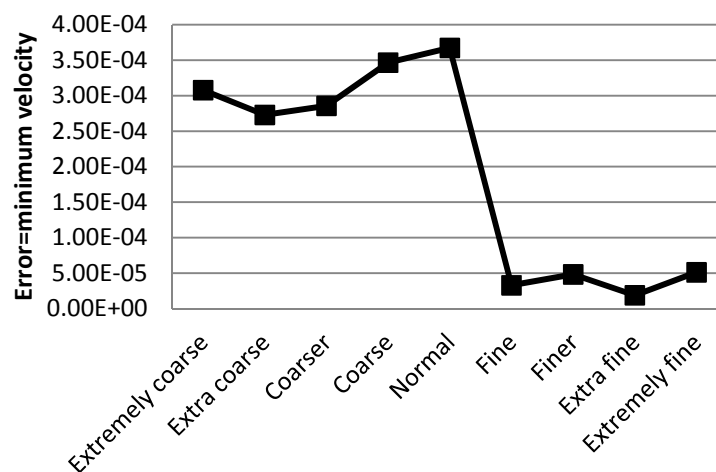


Figure 4.4- Effect of mesh size on minimum velocity value (m/s) which is defined as error during sensitivity analysis

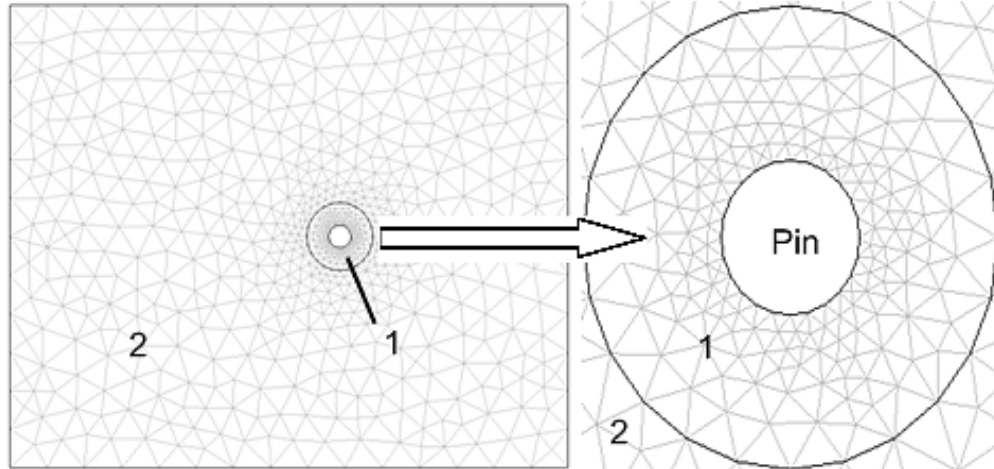


Figure 4.5- Mesh size distribution and subdomains

4.3 Case studies

In order to check the predictability of the model against temperature, strain, and strain rate fields via other published reports as well as our temperature measurements during FSW of aluminum 6061 alloy, four different cases with different process conditions were considered as follows.

4.3.1 Case study 1: Validation of the temperature field (compared to Long et al [52])

In this case, we try to reproduce the results of Long *et al* research [52] with the same process parameters and material properties as summarized in Table 4.1. In their 2D steady-state Eulerian model, heat generation was due to viscous dissipation in the material flow (fluid). Viscous dissipation and the increase of temperature were limited by a modification to the dynamic viscosity equation. It decreases rapidly within 50 °C above the solidus temperature of aluminum 6061 ($T_s \sim 582$ °C), i.e., simulating a sharp reduction in the viscosity in the transitional regime from the state of solid to the state of semisolid. This, in turn, prevents the model temperature to increase greater than the melting temperature [53]. A rigid-viscoplastic material behavior was used according to [54]. When this case was remodeled with our integrated multiphysics model, as explained in the previous section, a linear decrease of flow stress in Equation (3-10) to zero is

considered as the temperature decreases by 50 °C below the solidus temperature, which is slightly different from what was considered in the original model.

4.3.2 Case study 2: Validation of the temperature field (experimental temperature measurements)

In this case, we performed temperature measurements on two points on the back surface of the plates during FSW of aluminum 6061 plates with 6.5 mm thickness, as shown in Figure 4.6. The process parameters and material properties used in the model are summarized in Table 4.3.

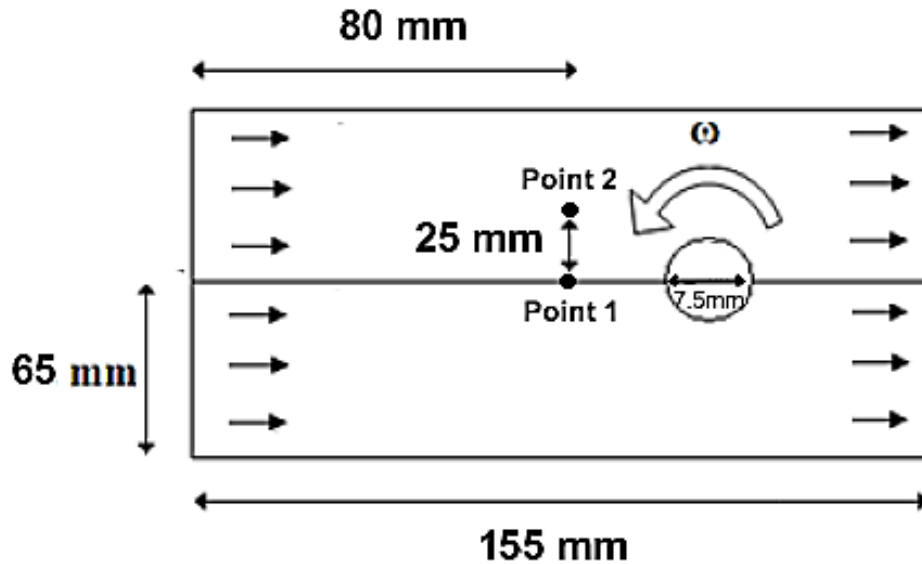


Figure 4.6- Points where temperature was measured in the back of the aluminum plates during FSW

Table 4.3- Process parameters and material properties used in Case study 2

Weld speed- u_{weld} (mm/s)	Rotational speed- ω (rev/s)	Pin radius- r_{pin} (mm)	Ambient pressure- P_o (KPa)	Ambient temperature- T_o ($^{\circ}\text{C}$)	R (J/mol.K)	Friction coefficient- μ	δ
0.75	1000	3.75	101	27	8.31451	0.4 [45]	0.65 [45]
α (1/MPa)	n	A (1/s)	Q (J/mol)	C_p (J/Kg K)	k (W/mK)	ρ (Kg/m ³)	Solidus ($^{\circ}\text{C}$)
0.045 [54]	3.55 [54]	$2.41e^8$ [54]	145000 [54]	900 [3]	160 [3]	2700 [3]	582 [3]

4.3.3 Case study 3: Validation of the strain field (compared to Xu et al [44])

In this case, we remodeled the work of Xu *et al* [44]. In their 2D and 3D steady-state arbitrary Lagrangian–Eulerian models, temperature values measured from an actual FSW process were used as input for the solid mechanics theory. Temperature values in the test were measured at mid thickness of the plate with thermocouples inserted in small holes in the plates. At the matrix-tool interface, the mechanical interaction was calculated from a friction contact model. Namely, the contact behavior at the matrix-tool interface was modeled by a modified Coulomb friction law. Temperature dependent elastic-plastic material properties were also used. In order to model the equivalent plastic strain distribution, they developed a 2D plane-strain model of the horizontal cross-section for the same in-plane model geometry as the 3D model. They concluded that, in general, a 2D plane strain model can provide a good estimate of the mechanical fields on the horizontal cross-section at half plate thickness. The same observation was noted when measuring a low strain in thickness direction compared to a high strain in streamlines direction via a combined viscoplasticity-CAD approach [43]. Here we use the same process parameters (Table 4.4) as in [44] and the rigid-viscoplastic material constants are employed according to Tello *et al* [50]. This material behavior would be more accurate compared to the one used by Sheppard *et al* [54] and would be closer to the actual hot deformation flow curves as described in [50].

Table 4.4- Process parameters and material properties used in Case study 3

Weld speed- u_{weld} (mm/s)	Rotation speed- ω (rev/s)	Pin radius- r_{pin} (mm)	Ambient pressure- P_o (KPa)	Ambient temperature- T_o (°C)	R (J/mol.K)	Friction coefficient- μ	δ
2.36 [44]	6.5 [44]	5 [44]	101	27	8.31451	0.4 [45]	0.65 [45]
α (1/MPa)	n	A (1/s)	Q (J/mol)	C_p (J/Kg K)	k (W/mK)	ρ (Kg/m ³)	Solidus (°C)
0.0165 [50]	5.33 [50]	1.63e ¹³ [50]	191000 [50]	900 [3]	160 [3]	2700 [3]	582 [3]

4.3.4 Case study 4: Validation of the shear strain rate vs. temperature (compared to Wang et al [55])

In this case we remodel the temperature and shear strain rate distribution of an Eulerian 3D model at mid thickness of the plate at a central streamline around the pin. In the original work of Wang *et al* [55], a stick boundary condition was assumed between the tool and the matrix (i.e., $\delta=1$). They used the rigid-viscoplastic material model according to Equation (4-10) with the same empirical softening regime explained in Section 4.2.4 of Chapter 4, in order to calculate the dynamic viscosity of the non-Newtonian hot deformed material. Once the flow rate has been calculated, the heat flux of the surfaces of the pin and the shoulder is calculated according to Equation (4-14).

$$\text{Total heat flux [55]:} \quad \dot{Q} = \sqrt{3} \mu \dot{\epsilon} r \omega \quad (4-14)$$

which is a product of the wall velocity and the shear stress at the surface. The Equation (4-14) is an empirical relation which was used to calculate the total heat flux on the tool.

An exact estimate of the thermal conductivity coefficient, which is temperature-dependent, is difficult to obtain as it can be sensitive to the material state and the amount of solute. Handbook

values usually have the equilibrium thermal conductivity which is not equal to the thermal conductivity in welding with short thermal cycles. As the volume of the material which is affected by high temperature at the heat affected zone (HAZ) is small, the use of conductivity values at room temperature may be reasonable [49]. The values of the process parameters and the material properties used for this case are given in Table 4.5.

Table 4.5- Process parameters and material properties used in Case study 4

Weld speed- u_{weld} (mm/s)	Rotation speed- ω (rev/s)	Pin radius- r_{pin} (mm)	Ambient pressure- P_o (KPa)	Ambient temperature- T_o (°C)	R (J/mol.K)	Friction coefficient- μ	δ
13.33 [55]	41.66 [55]	2.22 [55]	101	27	8.31451	0.4 [45]	0.65 [45]
α (1/MPa)	n	A (1/s)	Q (J/mol)	C_p (J/Kg K)	k (W/mK)	ρ (Kg/m ³)	Solidus (°C)
0.02416 [55]	4.70929 [55]	3.0197e ¹¹ [55]	168000 [55]	900 [3]	160 [3]	2700 [3]	570 [55]

4.4 Results and discussion

4.4.1 Case study 1 results (compared to Long *et al* [52])

The result of temperature distribution around the pin in Case 1 is shown in Figure 4.7 and compared with the original data from [52]. The two temperature fields show a similar distribution in Figure 4.7, while the minor difference in maximum temperature is due to different cut-off temperature values assumed in the two models. It should also be noted that in the present model (Figure 4.7-a) the tool moves from right to left and rotated counter-clockwise but in the work of Long *et al* (Figure 4.7-b) [52] the tool moved from left to right and rotated clockwise, though this does not have any effect in the magnitude of predictions. All 2D models in this thesis are based on the configuration in Figure 4.1 and for the sake of consistency we did not change the direction of tool rotation and its movement in the present case study. Using our multiphysics model, the velocity field streamlines along with the temperature distribution are also shown in

Figure 4.8. As seen in Figure 4.8, the maximum temperature is located at the backside of the pin after the material passes the pin and moves along the retreating side. As shown in streamlines of Figure 4.8, a shear layer exists around the pin which was proposed by Schneider *et al* [56].

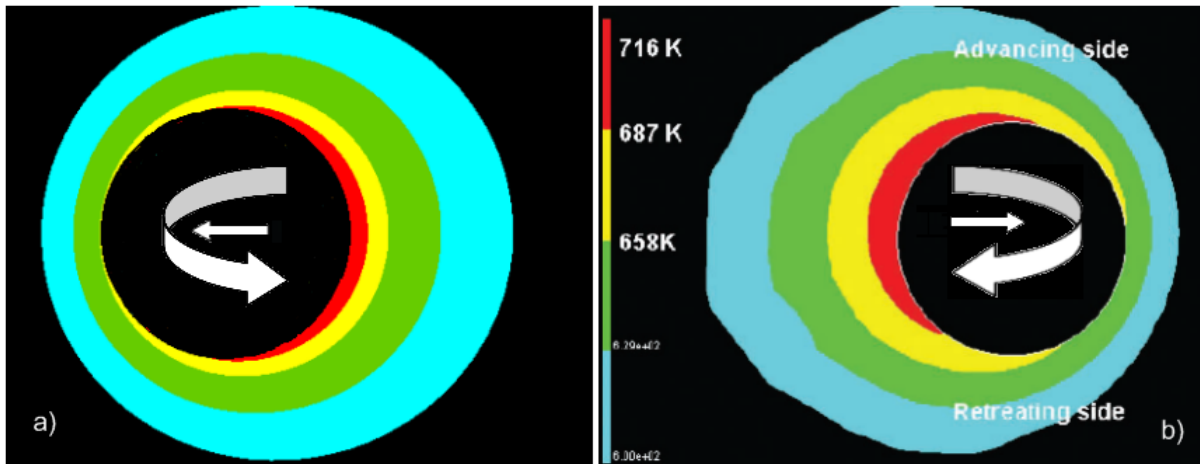


Figure 4.7- Temperature distribution around the pin in Case 1 using (a) our model, (b) the results in study [49]

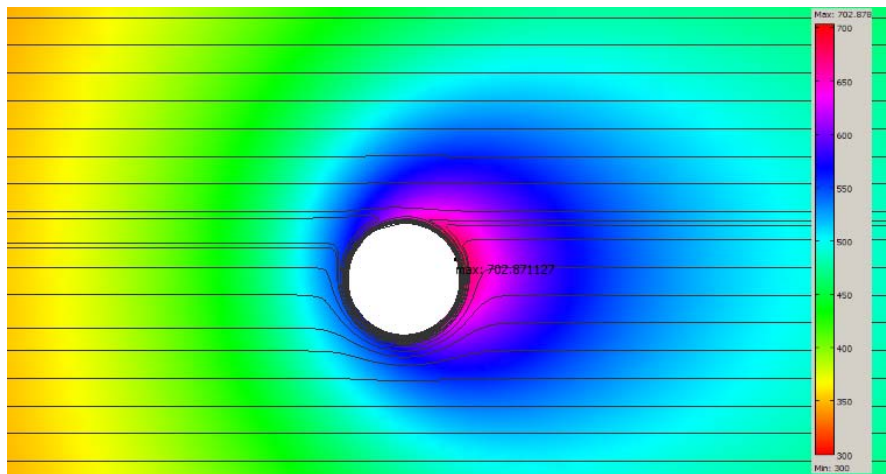


Figure 4.8- Temperature distribution (K) along with the velocity field streamlines in Case 1 (using our model)

We also examined the effect of using constant (temperature independent) thermal properties in the model and we noted that it generates a higher maximum temperature in the model. Also using the values of the thermo-mechanical model constants α , A , and n (Equation (4-10)) from the Sheppard *et al* study [54] generated a lower maximum temperature when compared to that of Tello *et al* [50].

4.4.2 Case study 2 results (Experimental temperature measurements)

The results of comparison of temperature distributions at points 1 and 2 (Figure 4.6) are shown in Figure 4.9 via the steady state model. They are plotted using the temperature changes with distance from the tool center, by considering the weld speed and converting temperature-time measurements to temperature-distance values. The model predicts a higher value of the peak temperature (about 30 °C difference compared to the measurement) and also a lower value in areas near the peak (~ 50 °C difference) which could be resulted due to the 2D modeling which does not consider heat generation from the shoulder.

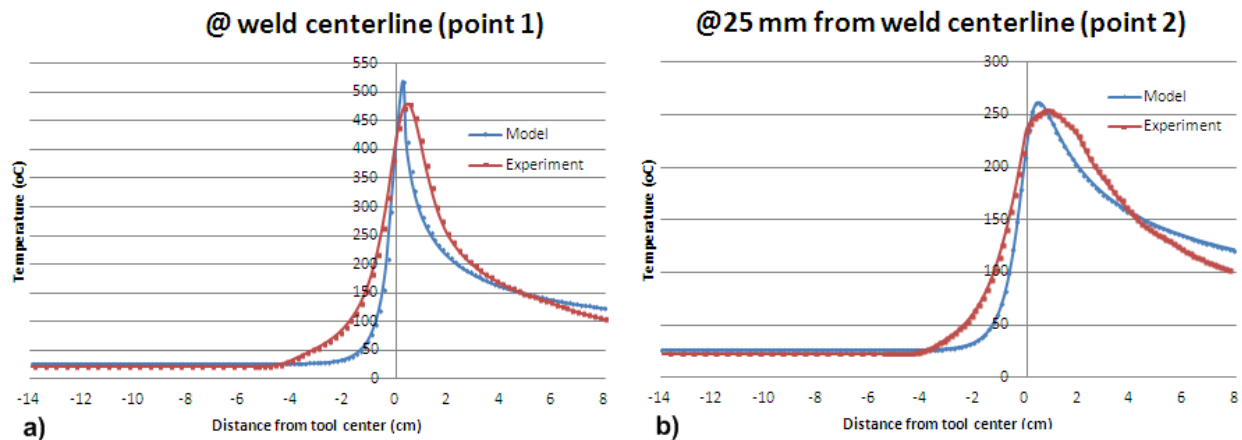


Figure 4.9- Comparison of temperature distribution during the experiment and the model of Case 2 at back of aluminum plate in two different points, (a) weld centerline (point 1) and (b) 25 mm from weld centerline (point 2) (Figure 4.6)

4.4.3 Case study 3 results (compared to Xu *et al* [44])

The result of strain distribution in Case 3 is shown in Figure 4.10-a and compared with the original results of Xu *et al* [44] (Figure 4.10-b) and a metalworking model from Arbegast [57] (Figure 4.10-c). The strain distribution at mid thickness of the plate in the present model (Figure 4.10-a) has almost the same strain distribution as in Figure 4.10-b. The maximum strain occurs in front of the leading edge of the pin which is estimated at 31.98 by our model. Near the pin there is almost the same/uniform high strain distribution. The maximum strain at mid thickness of the plate in Figure 4.10-b is about 30 [57]. Our model can also predict the formation of onion rings with space equal to advance per rotation as shown in Figure 4.10-a. There is a negative strain distribution around the pin in our model which complies with the forging zone in Figure 4.10-c. It also indicates the ring vortex generation around the pin as proposed by Schneider *et al* [56]. If the material is trapped in the shear layer, its deposit is delayed and may rotate with the pin more than one cycle. This can explain some of material flow behavior during FSW which has been reported by Colligan [58].

4.4.4 Case study 4 results (compared to Wang *et al* [55])

In case 4, the values of temperature (K) and shear strain rate (s^{-1}) are predicted in different regions of a central streamline around the pin (as marked in Figure 4.11). The original results from the research of Wang *et al* [55] with different weld speeds and a constant rotational speed are shown in Figure 4.12. The results of our model with the specified process parameters (weld speed of 13.33 mm/sec and the rotational speed of 41.66 rev/sec) are shown in Figure 4.13 as well as the results from the research of Wang *et al* using similar process parameters. Comparing the results, similar patterns and shear strain rate values are seen, while a temperature difference of about 20 to 40°C in different points exists, which should be the consequence of using different heat models in the two models. Our model predicts slightly less heat generation compared to the work of Wang *et al* [55] or maybe a slightly different thermal conductivity value is used for the plate and tool which in turn yields slightly lower temperature distribution at the leading edge of the tool (i.e., region 1 in Figure 4.11). Figure 4.14 shows the shear strain rate distribution around

the pin. The location of maximum shear strain rate is near the top of the advancing side of the pin.

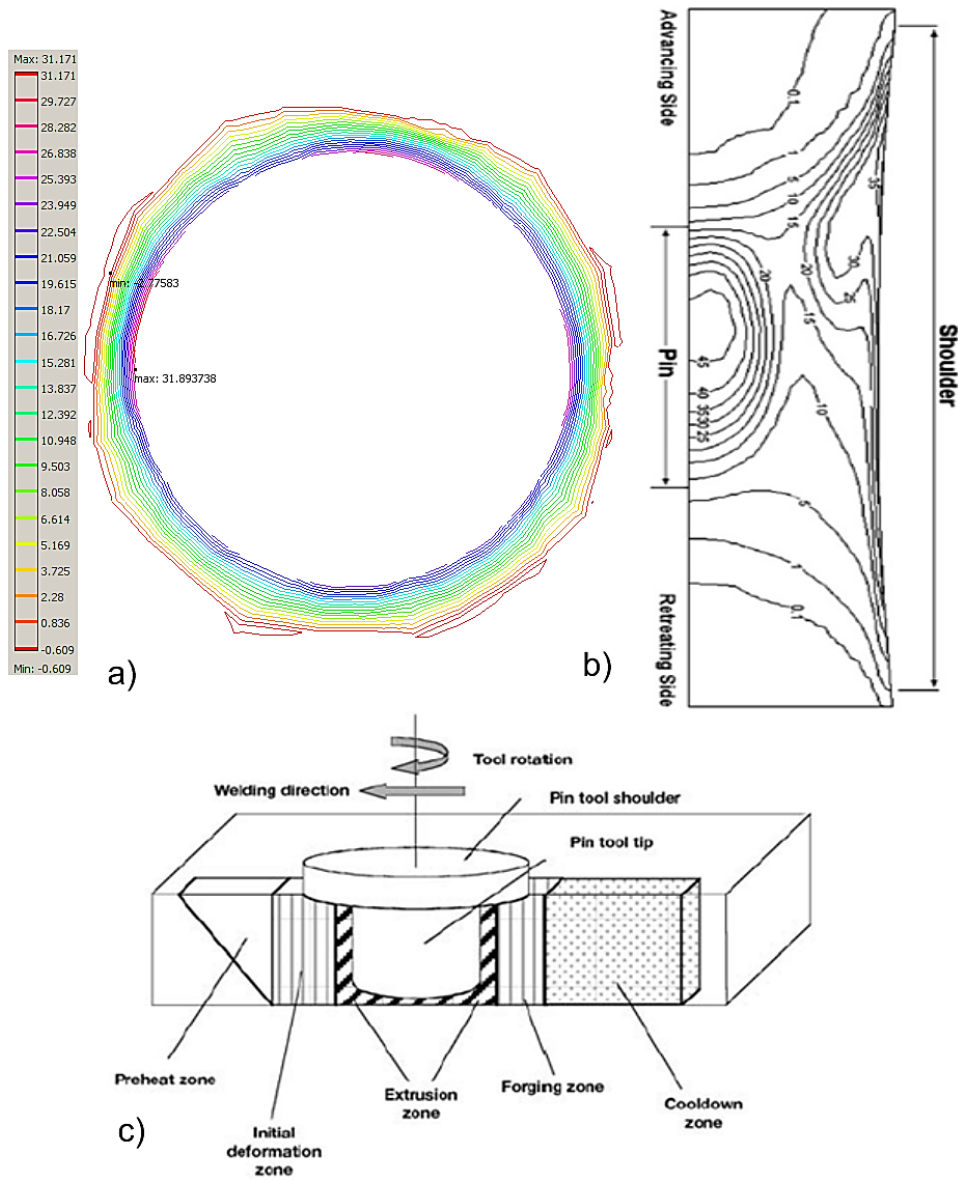


Figure 4.10- (a) 2D strain distribution of Case 3 using the current model; (b) 3D strain distribution data from [44]; (c) Metallurgical processing zones during friction stir welding [57]

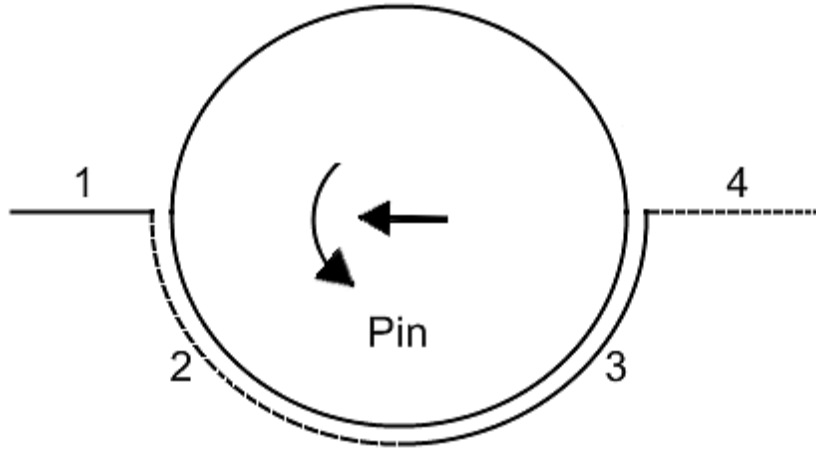


Figure 4.11- Schematic a central streamline with four different regions around the pin in Case 4

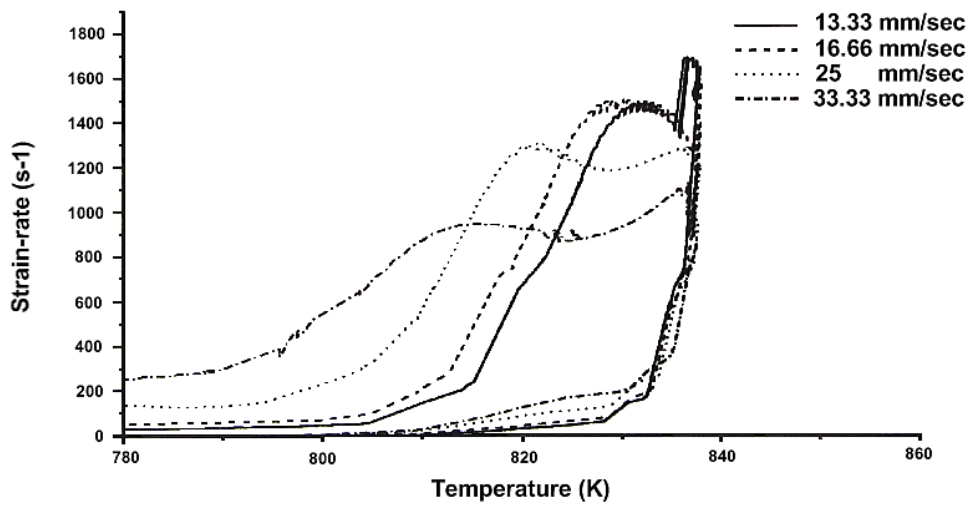


Figure 4.12- Variation of the temperature and shear strain rate using different welding speeds and a constant rotational speed of 41.66 rev/sec [55]

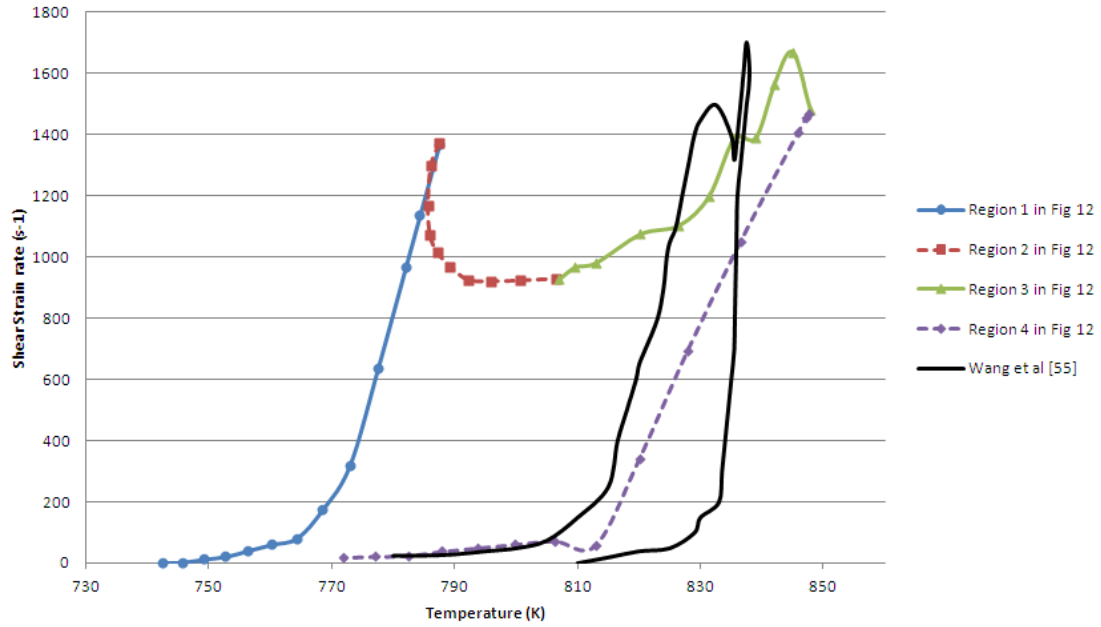


Figure 4.13- Values of temperature (K) and shear strain rate (s⁻¹) in different regions using our model with the weld speed of 13.33 mm/sec and rotational speed of 41.66 rev/sec and equivalent results from [55] (Figure 4.12)

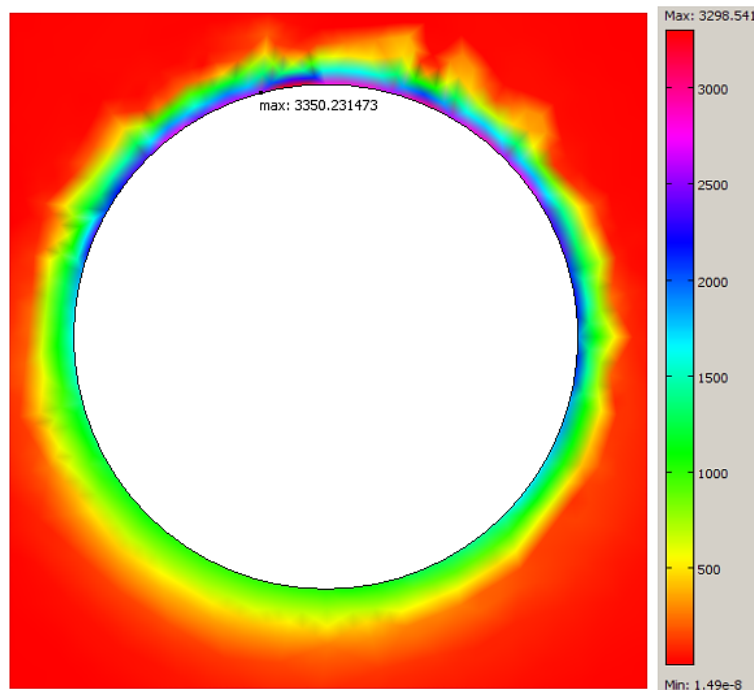


Figure 4.14- Shear strain rate distribution around the pin in the current model for case 4

4.5 Summary of findings

The developed integrated multiphysics model in Chapter 4 used different non-Newtonian incompressible fluid dynamics, conduction and convection heat transfer, and plain stress solid mechanics theories and physics to model FSW. It predicted strain at all points of the model for the first time compared to earlier CFD models which predicted strain only on limited streamlines. It can also predict the distribution of temperature, strain, and strain rate around the pin during friction stir welding as shown through four cases studies. The results of the developed model for aluminum 6061 agreed with the previously published data via different process parameters. Based on specific results in each presented case study we can conclude the following:

- 1- The maximum temperature during FSW is located at the backside of the advancing side of the pin after the material pass as the pin and moves along the retreating side.
- 2- The maximum strain during FSW in mid thickness of the plate occurs in front of the leading edge of the pin.
- 3- The generation of shear zone, forging zone and ring vortex around the pin can be well explained based on the numerical model results.
- 4- The pattern of temperature vs. shear strain rate is predictable in different regions of a central streamline around the pin. The maximum shear strain rate location is near the top of the advancing side of the pin.
- 5- If heat transfer in the tool is not considered in the numerical model, a lower value of temperature in the leading edge of the tool is resulted.
- 6- If constant thermal properties are used in the model, they generate higher maximum temperature compared to temperature dependent ones. Also using the values of a thermo-mechanical model constants (α , A , and n) from different literature references generated different maximum temperatures in the model. This indicates a necessity for further experimental-numerical studies in the field to arrive at a set of optimum model parameters that would equally perform under different processing conditions.

The model has also been successfully employed to predict the distribution of grain size and residual stress around the pin (to be presented in more details in Chapter 7 and Chapter 8). Combining the ‘integrated’ and “multiphysics” features under the same model is currently

deemed as the most advanced coupled modeling approach for FSW as it can predict the combination of main and post-process parameters under the same numerical tool.

Chapter 5: Comparison of Constitutive Equations

Versions of this chapter are to be published as **Article 7:** Mohamadreza Nourani, Abbas S. Milani, Spiro Yannacopoulos, On the effect of different material constitutive equations in modeling friction stir welding: a review and comparative study on aluminum 6061 (submitted), and **Article 8:** Mohamadreza Nourani, Abbas S Milani, Spiro Yannacopoulos, A review of thermomechanical models of friction stir welding, Thermec 2013, 2-6 Dec 2013, Las Vegas, USA (accepted as invited article).

Overview: In this chapter, first we review various thermomechanical approaches applied to modeling friction stir welding (FSW) along with different underlying constitutive equations employed by different researchers. Next, using a recently developed integrated multiphysics simulation model for FSW of aluminum 6061 (Chapter 4), the effect of using different constitutive equations on the prediction of process outputs, such as temperature, shear rate, shear strain rate, viscosity and torque, is studied under identical welding conditions. Based on the results of this comparative study, some very agreeable consistencies but also some disagreeable and alarming inconsistencies will be observed between outcomes of specific constitutive equations, indicating that they should be carefully chosen, identified, and employed in FSW simulations based on characteristics of each specific process and a given material.

5.1 Introduction

A key element of any selected FSW prediction model is the fundamental relation used to link the flow stress, temperature, strain, and strain rate values, which is commonly referred to as constitutive equation. The form of these equations closely depends on microscopic mechanisms of the plastic flow in crystalline materials, and their constants are obtained based on mechanical experiments such as hot tension, compression or torsion tests [1]. The reported FSW models can be categorized into three main groups as follows. Note that within all these categories, heat transfer for temperature predictions is an embedded formulation in the models.

5.1.1 Computational Solid Mechanics (CSM)-based models

CSM-based models have been extensively used in the literature [1-67] and consider that the material is solid during the welding process and the force equilibrium equation is expressed on the basis of continuum mechanics and the resulting partial derivative equations (PDE) are solved using in-house or commercial codes. The early models in this category have used a thermal model first to predict the temperature distribution in the welded parts and then in a segregated model they could predict the residual stress field [1]. In more recent models under this category, a coupled thermomechanical model is directly used to predict both the temperature distribution and the residual stress fields [65]. Nevertheless, it can be inferred that the main characteristic of the Solid Mechanics models is the computation of strain and residual stress distributions. Some of the commercial codes used in these models include Abaqus, Ansys, Forge3, and Deform3D.

5.1.2 Computational Fluid Dynamics (CFD)-based models

Under this category, some models directly use viscosity laws in simulation and some others are based on an equivalent dynamic viscosity definition from CSM models, also called solid mechanics based dynamic viscosity [3, 37, 43, 68-120]. For the latter, the Von-Mises flow stress was first used by Zienkiewicz et al. [121] in modeling viscoplastic deformation processes such as extrusion, rolling, deep drawing and stretching. Using in-house or commercial codes such as Fluent, in these models the momentum equilibrium equation (Navier-Stokes) is solved considering that the non-Newtonian material has different viscosity values equal to the ratio of shear stress to shear strain rate, whose value can vary in different regions of the deformation domain. Hence, the main characteristic of these models is the computation of strain rate, and they are most often not capable of predicting elastic strain and residual stress fields because of the incompressible flow assumption used. There are some few cases where a limited plastic strain has been predicted by CFD models using some post-processing techniques such as those presented by Reynolds et al. [3], Bastier et al. [87], Long et al. [105], and Arora et al. [118]. For instance, Long et al. [105] used a geometry-based formulation to calculate engineering strains on limited streamlines. Reynolds et al. [3], Bastier et al. [87], and Arora et al. [118] estimated the accumulated plastic strains in the material by integrating strain rates along limited streamlines.

5.1.3 Multiphysics (CSM-CFD) models:

There are models which use both CFD and CSM approaches to predict strains and residual stresses, along with flow characteristics: First they use a CFD approach based on the equivalent dynamic viscosity definition from CSM to predict temperature distribution and the shear stress near tool-material interface. Then, they employ the CSM approach to model elastic and plastic strains and residual stresses. The residual stresses are resulted from different elastic and thermal strains across the material domain before and after clamping release in the FSW set-up and complete cooling of plates. These models often use temperature dependent elastic moduli and thermal expansion coefficients [122-126]. If any solid-state phase transformation occurs after FSW with different lattice volume properties of the new phase compared to the parent phase, then transformation induced strains also needs to be considered in residual stress modelling; e.g., in FSW of carbon steels [127, 128]. The above explained categories of models are compared in Table 5.1 in more detail.

As explained in Chapter 4, we developed an integrated multiphysics model of FSW of aluminum 6061 [129] using Comsol. Regarding the ‘integrated’ feature of the model, it was continuously capable of predicting plastic strains and strain rates over the material domain during the process, followed by predicting the microstructure and residual stresses after the process within the same code. The strain components at different material points are calculated using the integration of strain rate over time on different flow streamlines. The heat transfer and CFD modules of the model use a viscoplastic material behaviour (fluid type constitutive equation) to find the temperature history, and subsequently it is used as a input in the CSM module with an elasto-viscoplastic constitutive material behaviour (solid type constitutive equation) to find residual stresses resulting from thermo-elastic strains at the end of the welding process after material cool down to ambient temperature and unclamping [126]. Finally it has been shown that using the same model, the weld material microstructure can be predicted by using empirical grain and subgrain size equations [130]. In Kocks-Mecking-Estrin (KME) or Hart’s constitutive models, the effect of dynamic recrystallization, grain growth and recovery on flow stress has been considered (more to be discussed in Section 5.2.2), but to the best of my knowledge no model has evaluated their effects on the strain softening and the strain distribution during FSW. In the next sections we review different material constitutive equations used most commonly by other

researchers (Section 5.2) and then we implement (Section 5.3) and compare (Section 5.4) them within the framework of the same FSW model in [129] for aluminum 6061. Concluding remarks regarding the optimal use of the selected constitutive equations are outlined in Section 5.5.

5.2 CFD and CSM constitutive equations

There are different constitutive equations defined for different materials based on the chosen modeling approach (CFD [131] or CSM [132]). Some of these constitutive equations have been previously used in modeling FSW processes, which are reviewed below.

5.2.1 CFD constitutive equations

The important point is that when a CFD approach is used, because it is assumed that the material is an incompressible fluid (based on the mass equilibrium equation), we cannot model elastic deformation. During the deformation of a plastic (or viscoplastic) solid, plastic strains are large enough that we can consider elastic strain to be negligible, then the material behaviour mimics an incompressible viscous flow (possibly non-Newtonian) along with the prescribed velocity boundary conditions. Different formulations for these problems are suggested in [133, 134, 121]. Kuykendall et al. [135] studied the effect of using some of such constitutive equations in stress-strain model of axial compression and compared them with data from experiments. They determined the model constants for Zener-Hollomon, Johnson-Cook and Kocks-Mecking-Estrin constitutive equations for aluminum 5083 and used them as input in a model developed for axial compression. Capabilities of the constitutive equations were compared with each other in capturing the strain hardening and saturation in the axial compression model and compared to experimental stress-strain curves.

There are different fluid-like material behaviors as shown in Figure 5.1. Generally, these include Newtonian, Bingham plastic, power law (dilatant or pseudoplastic) behavior, and structural. The structural fluids have a Newtonian behavior at very high and very low shear rates and have shear thinning or pseudoplastic properties between these two extremes [131].

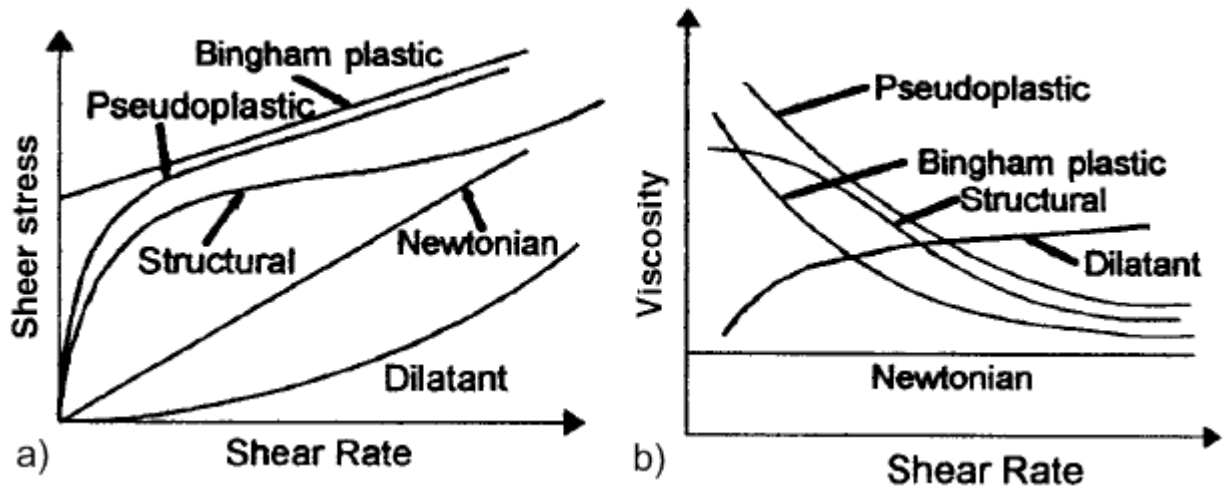


Figure 5.1- (a) Shear stress versus shear rate and (b) viscosity versus shear rate for different fluid-type materials [131]

General constitutive equations for the fluid-type materials should relate temperature (T), flow stress (σ), and strain rate ($\bar{\epsilon}$) or shear strain rate ($\dot{\gamma}$) to dynamic viscosity (η). It has been shown that the maximum temperature during FSW is solidus temperature, as this welding process is a solid state welding and there is a cut-off temperature (below the solidus temperature) at which the dynamic viscosity of material decreases dramatically. The dynamic viscosity becomes virtually zero when the temperature reaches the solidus temperature [104, 129].

5.2.1.1 Power law dynamic viscosity

The power law is an example of a generalized non-Newtonian fluid. If there is a linear relation between the logarithm of shear stress and the logarithm of viscosity then the viscosity of the material under a power-law can be represented as:

Power law dynamic viscosity:
$$\eta = m\dot{\gamma}^{n-1} \tag{5-1}$$

where two viscous rheological properties (model constants) are the consistency coefficient m , and the flow index n , For $n > 1$, the power law represents a shear thickening or pseudoplastic fluid. For $n < 1$, it is a shear thinning or dilatant fluid. When the value of n is equal to one then it describes a Newtonian fluid. Colegrove et al. [69] and Reynold et al. [3] used the above power-

law constitutive model in FSW modeling for the first time. Later, Reynolds et al. [3] presented a temperature dependent power law dynamic viscosity as:

$$\text{Temperature dependent power law dynamic viscosity: } \eta(T, \dot{\varepsilon}) = K \exp\left(\frac{T_0}{T}\right) \dot{\varepsilon}^{n-1} \quad (5-2)$$

5.2.1.2 Carreau model of dynamic viscosity

The Carreau model [136] has proven to be very effective for describing the viscosity of structural fluids. The constitutive equation under this model reads:

$$\text{Carreau model [136]: } \eta(\dot{\gamma}) = \eta_\infty + \frac{\eta_0 - \eta_\infty}{[1 + (\lambda^2 \dot{\gamma}^2)]^p} \quad (5-3)$$

where η_0 is the low shear limiting viscosity, η_∞ the high shear limiting viscosity, λ is a time constant, and p is the shear thinning index. Atharifar et al. [117] used the Carreau model for the first time in FSW modeling in the following form:

$$\text{Carreau model [117]: } \eta = \eta_\infty + (\eta_0 - \eta_\infty) \left[1 + (\dot{\gamma} \lambda \exp\left(\frac{T_0}{T}\right))^2\right]^{\frac{(m-1)}{2}} \quad (5-4)$$

where η_0 and η_∞ are zero and infinite shear viscosities respectively, $\dot{\gamma}$ is the shear strain-rate, λ is the time constant, T_0 is the reference temperature and m is the power law index for the non-Newtonian fluid.

5.2.1.3 Perzyna model of dynamic viscosity

The dynamic viscosity which is a function of temperature and strain rate can be derived from the ratio of the effective deviatoric flow stress to the effective strain rate by use of Perzyna's model of viscoplasticity [133] as presented by Zienkiewicz et al [134] and employed by Ulysse [70] in FSW modeling:

$$\text{Perzyna model: } \eta(T, \bar{\dot{\varepsilon}}) = \frac{\sigma(T, \bar{\dot{\varepsilon}})}{3\bar{\dot{\varepsilon}}} \quad (5-5)$$

However, in implementing this model one still required to use a constitutive equation for the effective flow stress, σ , versus effective strain rate, $\dot{\epsilon}$, which in turn is considered one of the equations for CSM approaches as will be discussed in Section 5.2.2.

5.2.1.4 Bendzsak-North model of dynamic viscosity

For some aluminum heat-treatable alloys, the Zener-Hollomon (Sellars-Tegart law) used in Perzyna dynamic viscosity equation provides a poor fit to isothermal, isostrain-rate data [71]. In this case it is preferable to interpolate the viscosity value at different temperature and strain rates numerically. An alternative approach has been adopted by Bendzsak et al. [68, 137, 138] who use an effective dynamic viscosity described at a given temperature by a heuristic material model which gives a moderate strain-rate sensitivity to the viscosity.

Bendzsak-North model:
$$\eta_a = \eta_0 \exp(-B\tau_{r\theta}) \quad , \tau_{r\theta} = 2\eta_0\dot{\epsilon} \quad (5-6)$$

where η_a is effective viscosity, η_0 is reference viscosity, B is material constant, $\tau_{r\theta}$ is shear stress and $\dot{\epsilon}$ is equivalent strain rate. Bendzsak et al. [70] used this constitutive model in FSW modeling for the first time.

5.2.1.5 Modified Bingham model of dynamic viscosity

Perfect yielding material behavior is known as Bingham fluid behavior as shown in Figure 5.1 and can be implemented by the following constitutive law [109]:

Bingham fluid:
$$\begin{cases} \bar{\tau} < \tau_0 : \dot{\gamma} = 0 \\ \bar{\tau} \geq \tau_0 : \bar{\tau} = \left(\frac{\tau_0}{\dot{\gamma}} + \eta\right)\dot{\gamma} \end{cases} \quad (5-7)$$

where $\bar{\tau}$ is the equivalent shear stress, τ_0 is the yield shear stress, $\dot{\gamma}$ is the equivalent shear strain rate and η is the dynamic viscosity.

Dorfler [109] introduced a modified Bingham equation for the first time in FSW modeling by using Papanastasiou approach [139] and also defining a new constant m (convergence parameter) to avoid numerical errors during simulations [109]:

Modified Bingham equation:
$$\bar{\tau} = \frac{\sigma(\dot{\gamma}, T)^m}{(\dot{\gamma} + h)^m} \cdot \dot{\gamma} \quad (5-8)$$

where the convergence parameter m is chosen as exponent in a way that the highly nonlinear term becomes eliminated for $m = 0$ and is fully effective for a value of $m = 1$. The constant h is used to achieve convergence when the shear rate is zero and is chosen very small so that it does not affect the accuracy of the model. Dorfler [109] used an empirical flow stress equation which will be explained in Section 2.2 as one of the solid mechanics-based flow stress constitutive equations. He also used a level set method to model material properties in dissimilar FSW. It is worth adding that there are other constitutive equations which have been developed in CFD but have not been used in FSW such as Ellis model, Sisko model, Meter model, Yasuda model [131], and also the formulation of Duvaut–Lions which is equal to the formulation of Perzyna [140].

5.2.2 CSM constitutive equations

Generally speaking, one can consider different solid mechanics-based material models during plastic deformation of a material. These include perfectly plastic, plastic, elastic-perfectly plastic, elastoplastic, perfectly viscoplastic, viscoplastic, elastic-perfectly viscoplastic and elastoviscoplastic as shown in Figure 5.2.

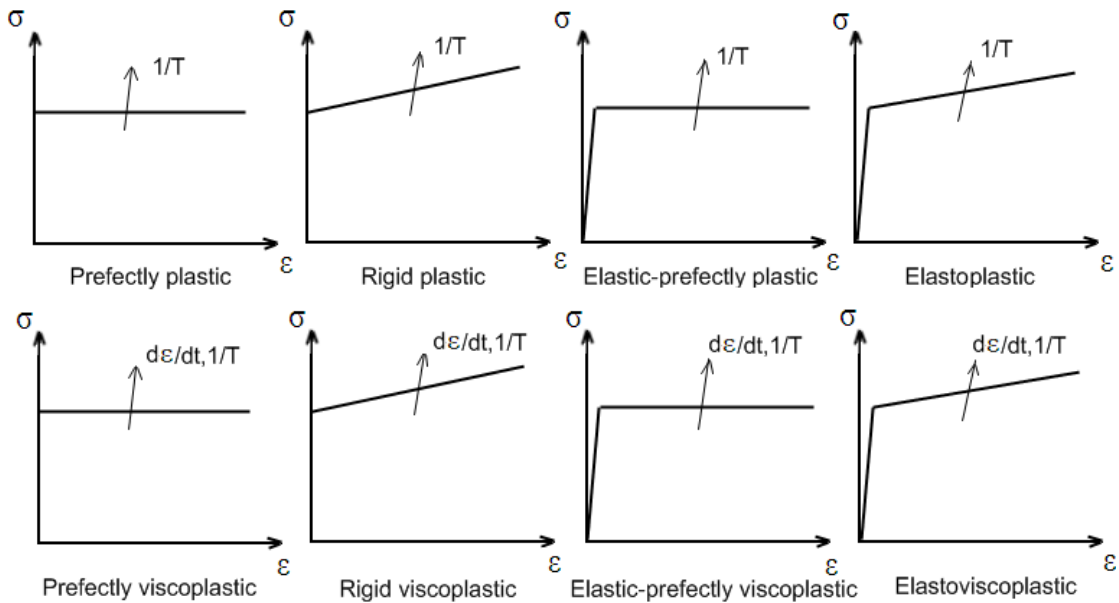


Figure 5.2- Schematic of stress-strain curves in different solid mechanics-based material models (T is temperature and $d\epsilon/dt$ is strain rate)

The material behavior during hot deformation can include dynamic recovery or dynamic recrystallization as shown in Figure 5.3 [141]. During dynamic recovery, stress reaches the steady state stress (saturation) and during dynamic recrystallization, first the stress increases to the peak stress and then reaches a steady state plateau where there is no change in stress value, but microstructural changes can be present.

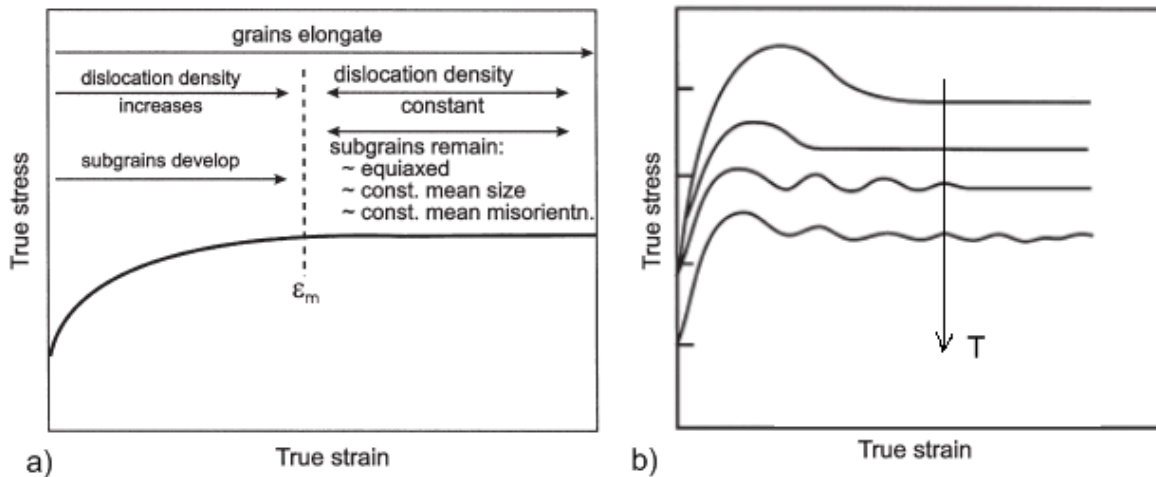


Figure 5.3- Schematic of the true stress-true strain curve during (a) dynamic recovery, and (b) dynamic recrystallization [141]

In general, CSM-based material constitutive relations in FSW models are aimed to link strain rate ($\dot{\epsilon}$), temperature (T) and sometimes strain (ϵ) to the equivalent flow stress (σ). Most commonly used models of this kind are reviewed below.

5.2.2.1 Zener-Hollomon (ZH) model or Sellars-Tegart law (Perfectly viscoplastic)

One may consider the flow stress of a solid during hot deformation to be equal to its dynamic recovery/recrystallization steady state stress which is independent of plastic strain. If the plastic deformation is high, we may also neglect the elastic deformation and consider the material behavior as perfectly viscoplastic as shown in Figure 5.2. The material flow stress can be correlated with the Zener-Hollomon parameter [142] (temperature-compensated strain rate) as proposed by Sellars and Tegart [143] and modified by Sheppard and Wright [144]:

Zener-Hollomon parameter [143, 144]:
$$Z = \dot{\varepsilon} \exp\left(\frac{Q}{RT}\right) \quad (5-9)$$

Zener-Hollomon flow stress model:
$$\sigma = \frac{1}{\alpha} \sinh^{-1}\left(\left(\frac{Z}{A}\right)^{1/n}\right) \quad (5-10)$$

where Z is the Zener-Hollomon parameter, $\dot{\varepsilon}$ is the effective strain rate, Q is the temperature independent activation energy which is equal to self-diffusion energy, R is the gas constant, and α , A , and n are model constants which are determined from hot deformation experiments. Tello et al. [145] recently reported more accurate model constants for some alloys compared to available experimental data. This CSM constitutive model has been extensively used in CFD models of FSW, which are essentially based on an equivalent dynamic viscosity definition from a CSM approach by means of Perzyna law [70] (Equation (5-5)).

5.2.2.2 Johnson-Cook model (Elastoviscoplastic)

The Johnson-Cook material model is an empirical equation in the following form [146]:

Johnson-Cook model [55]:
$$\sigma = [A + B(\bar{\varepsilon}^{pl})^n] \left(1 + C \ln \frac{\bar{\dot{\varepsilon}}^{pl}}{\dot{\varepsilon}_0}\right) \left[1 - \left(\frac{T - T_{ref}}{T_{melt} - T_{ref}}\right)^m\right] \quad (5-11)$$

where $\bar{\varepsilon}^{pl}$ is the effective plastic strain, $\bar{\dot{\varepsilon}}^{pl}$ is the effective plastic strain rate, $\dot{\varepsilon}_0$ is the normalizing strain rate (typically normalized to a strain rate of 1.0 s^{-1}) and A , B , C , m , n , T_{melt} and T_{ref} are material constants. Askari et al. [5] have been among early researchers who used this constitutive model in FSW, and more recently Grujicic et al. [48, 62, 66] employed a modified version of the Johnson-Cook constitutive equation considering the effect of grain size and dynamic recrystallization on the material flow stress.

5.2.2.3 Norton-Hoff model (Perfectly viscoplastic)

The Norton-Hoff material is a perfectly viscoplastic material law in which the stress is a power law function of the strain rate as follows.

Norton-Hoff model [148]:
$$\sigma = 2K(\sqrt{3}\bar{\dot{\varepsilon}})^{m-1} \dot{\varepsilon} \quad , K = K_0(\varepsilon_0 + \bar{\varepsilon})^n \exp\left(\frac{\beta}{T}\right) \quad (5-12)$$

Where, $\bar{\varepsilon}$ and $\bar{\dot{\varepsilon}}$ are the equivalent strain and the equivalent strain rate, m and n are the sensitivity indexes to strain rate and strain, respectively, and K_0 , ε_0 and β are material constants. If $m = 1$, the material is a Newtonian fluid with viscosity K . It is well known that the Norton-

Hoff law is an approximation to the Sellars-Tegart law, when the Zener-Hollomon parameter is smaller than A (material constant as shown in Equation (5-10)), i.e., when $Z \ll A$ [147].

The Norton-Hoff law has been widely used in metal forming process simulations, such as hot forging, where the material experiences high strain rate deformations at high temperatures. Fourment et al. [13] have used this constitutive model early in their FSW model, and more recently Assidi et al. [56] used the model with both K and m being functions of temperature.

5.2.2.4 Power law model (Rigid viscoplastic)

A temperature and strain rate dependent rigid-viscoplastic material power law model is defined as follows [22]:

Power law model:
$$\sigma = KT^A(\dot{\epsilon})^B(\bar{\epsilon})^C \quad (5-13)$$

where K , A , B and C are material constants calculated by regression of the experimental data. Buffa et al. [22] used this constitutive model in a FSW model in 2006.

The next two constitutive models, as opposed to the previous ones, are microstructurally motivated (with state variables) based on strain hardening of the forming material.

5.2.2.5 Kocks-Mecking-Estrin (KME) model (Rigid viscoplastic)

KME model is valid for pure materials in theory as it considers the effect of storage hardening and dynamic recovery softening mechanisms on dislocation density. It is a classic model in the literature for Al alloys which are strain hardened assuming that the plastic slope ($d\sigma/d\epsilon$) linearly changes with the flow stress in general situations for instance when precipitates are present. The KME model has the following expression for the flow stress σ_f as a function of the plastic strain ϵ_p , the dislocation storage rate θ and the recovery rate β : [149-155]:

KME model:
$$\frac{d\sigma_f}{d\epsilon_p} = \theta - \beta(\sigma_f - \sigma_y) \quad (5-14)$$

where σ_y is the material yield strength. The values of θ and β are obtained by a linear fit on the variation of the strain hardening rate $\frac{d\sigma_f}{d\varepsilon}$ with the true flow stress in plasticity (σ_{pl}). Equation (5-14) was identified by Voce empirically [152]. Simar et al. [67] used an extended KME constitutive model in FSW modeling, which accounts for dynamic precipitation and Orowan loop during the calculation of θ and β .

5.2.2.6 Hart's model (Rigid viscoplastic)

Dynamic recovery and hardening occur simultaneously during deformation and hence, any flow stress change is the result of both of these mechanisms by means of generation and annihilation of crystal defects such as dislocations. Hart [153] proposed a new constitutive equation which was later used by Eggert and Dawson [154, 155] in modeling of upset welding and by Forrest et al. [21] in FSW modelling. The simplified Hart's model considers the plastic stress (τ^p) and the viscous stress (τ^v) affecting the flow stress (σ) as follows [27, 33, 85]:

$$\text{Hart's model:} \quad \sigma = \tau = \tau^p + \tau^v \quad (5-15)$$

$$\tau^v = G \left(\frac{\bar{D}}{a} \right)^{1/M}, \quad a = a_0 \exp\left(-\frac{Q'}{RT}\right) \quad (5-16)$$

$$\tau^p = K \exp\left[-\left(\frac{b}{D}\right)^\lambda\right], \quad b = b_0 \left(\frac{K}{G}\right)^N \exp\left(-\frac{Q}{RT}\right) \quad (5-17)$$

where \bar{D} is the average value of deformation rate, T is temperature and K is strength. G , Q , Q' , M , N , λ , a_0 and b_0 are material constants identified from large deformation tests. During friction stir welding there is a high deformation rate around the tool's pin and accordingly Cho et al. [27] used an evolution equation to specify the strength's saturation value which is a function of temperature and strain rate. In their work K was also defined under a Voce-like saturation limit.

5.2.2.7 Dorfler empirical model

As strain values in material around tool during FSW is high and tension test gives limited strain value, the tensile test data may be suitable only to a limited extent for finding the parameters of a given constitutive model. To model the material behaviour under large deformations more

precisely, an empirical material model was introduced by Dorfler [109] based on experimental data from torsion test.

$$\text{Dorfler model: } \sigma(\dot{\varepsilon}, T) = a_a + b_a T + c_a T^2 - a_b (T - b_b) \ln(\dot{\varepsilon} + a_c + b_c T + c_c T^2) \quad (5-18)$$

σ is the flow stress, $\dot{\varepsilon}$ is the strain rate, T is the temperature and a_i, b_i, c_i are material constants. The empirical model factors have been worked out for strain hardened aluminum alloys as well as for precipitation hardened alloys and showed [109] good results for both alloy types. Dorfler [109] also compared his model with the Johnson-Cook constitutive model and showed that his model predictions are slightly lower compared to experimental stress-strain curves of two aluminum alloys, whereas the Johnson-Cook model results were quite higher compared to test data.

Hansel-Spittel is another constitutive model which has been used by Assidi et al. [56] in FSW modeling; however in that work the model generated a maximum temperature higher than the material melting point and hence they used the Norton-Hoff constitutive equation instead. There are other constitutive equations which have been developed in CSM approaches but have not, or rarely, been used in the FSW literature to date. These include: Bingham-Norton [132], Garvus [156], Zerilli-Armstrong (ZA) [157], Follansbee-Kocks (mechanical threshold stress model) [158], Mackawa [159], modified Johnson-Cook [160], Usui [161], Bammann-Chiesa-Johnson (BCJ) [162], Physics-based (PB) [163], Cowper-Symonds [164], Steinberg-Cochran-Guinan-Lund [165, 166] and Preston-Tonks-Wallace [167].

Finally, we would like to add that there are also some other early empirical equations for stress-strain response of materials, but the effect of strain rate is not considered in these models [168]:

$$\text{Ludwik equation [169]: } \sigma = \sigma_0 + k\varepsilon^m \quad (5-19)$$

$$\text{Hollomon equation [170]: } \sigma = k\varepsilon^n \quad (5-20)$$

$$\text{Swift equation [171]: } \sigma = k(\varepsilon + \varepsilon_0)^n \quad (5-21)$$

$$\text{Voce equation [172]: } \sigma = B - (B - A) \exp(-n\varepsilon) \quad (5-22)$$

$$\text{Levy-Mises equation (also called flow rules) [173]: } \frac{d\varepsilon_1}{\sigma'_1} = \frac{d\varepsilon_2}{\sigma'_2} = \frac{d\varepsilon_3}{\sigma'_3} = d\lambda \quad (5-23)$$

Table 5.1- Comparison of various thermomechanical models of friction stir welding

Authors [ref]	2D/3D	Steady state/time dependent	Software used	Coupled/Segregated	Heat source	Constitutive equation	Model output reported
Chao et al [1]	3D	Time dependent	In-house developed	Segregated	Frictional surface heat flux of tool	Table of temperature dependent mechanical properties with elastic, plastic and thermal deformation	Temperature, residual stresses, displacement
Dong et al [2]	3D	Time dependent	N/A	Coupled	Referred to a conventional friction and inertia welding process	Referred to a finite difference based weld pool dynamics model	Temperature, heat flux, equivalent plastic strain, contact pressure, flow field
Reynolds et al [3]	2D	Steady state	Abaqus/Fluent	Segregated	Prescribed temperature field around the pin/deformation heating	Rate-independent elastic-plastic material with temperature-dependent yielding behavior/non Newtonian power law shear stress	Interface position, specific weld energy, position of particles, strain, strain rate
Goetz et al [4]	2D	Time dependent	Deform	Coupled	Frictional surface heat flux of tool	Flow stress as a function of strain, strain rate and temperature	Point tracking, temperature, strain, tool temperature,
Askari et al [5]	3D	Steady state	CTH	Coupled	Heat of plastic work	Johnson-Cook	Temperature, flow stress, plastic strain rate, marker location
Dong et al [6]	3D	Time dependent	N/A	Coupled	Referred to a conventional friction and inertia welding process	Referred to a finite difference based weld pool dynamics model	Temperature, heat flux, equivalent plastic strain, contact pressure, flow field
Deng et al [7]	2D	Steady state	Abaqus	Segregated	Measured temperature values	Von Mises yield criteria with Temperature dependent mechanical properties with elastic and plastic deformation	Tangential velocity, marker positions
Heurtier et al [8]	3D	Steady state	In-house developed	Coupled	Plastic power	N/A	Path of material elements, strain, temperature
Xu et al [9]	3D	Steady state	Abaqus	Segregated	Measured temperature data	Von Mises yield criteria with temperature dependent mechanical properties and isotropic material with isotropic hardening	Tangential velocity, velocity, equivalent plastic strain
Chen et al [10]	3D	Time dependent	Ansys	Coupled	Friction between tool and plate	Temperature dependent mechanical properties with elasticity, plasticity and a kinetic hardening	Temperature, residual stresses, stresses
Guerdoux et al [11]	3D	Time dependent	Forge3 and TherCast	Coupled	Heat of deformation boundary heat flux	Hansel-Spittel	Temperature, velocity, vertical force
Chen et al [12]	3D	Time dependent	Ansys	Coupled	Frictional surface heat flux of tool	Table of temperature dependent mechanical properties with elastic, plastic and thermal strains	Temperature, principal stresses, longitudinal force, vertical force, lateral force
Fourmet et al [13]	3D	Time dependent	Forge3 and TherCast	Coupled	Heat of deformation boundary heat flux	Norton-Hoff	Temperature, velocity, vertical force

Authors [ref]	2D/3D	Steady state/time dependent	Software used	Coupled/Segregated	Heat source	Constitutive equation	Model output reported
McCune et al [14]	3D	Time dependent	Abaqus	Coupled	Surface heat flux calculated from total power input	Temperature dependent mechanical properties with elasticity, plasticity and an isotropic hardening	Temperature, residual stresses, stresses, residual distortions
Schmidt et al [15]	3D	Time dependent	Abaqus	Coupled	Frictional and plastic deformation surface heat flux	Johnson-Cook	Plunge forces, heat generation, temperature, velocity fields, strain
Zhu et al [16]	3D	Time dependent	Weldsim	Segregated	Frictional surface heat flux of tool calculated from total heat input energy	Von Mises yield criterion and the associated flow rule for temperature field/subsequent elastic-plastic material for residual stress	Temperature, longitudinal residual stress
Zhang et al [17]	2D	Time dependent	Abaqus	Segregated	Actual temperature values from practical FSW test	Rate-independent elastic-plastic material with temperature-dependent yielding behavior	Temperature, material flow, radial stress, shear stress, plastic strain, longitudinal residual stress
Schmidt et al [18]	3D	Time dependent	Abaqus	Coupled	Plastic dissipation resulted from sticking condition at tool-material contact interface	Johnson-Cook	Velocity, temperature, plastic strain, void formation, total heat generation, plunge force
Soundararajan et al [19]	3D	Time dependent	Ansys	Coupled	Friction between tool and plate	The temperature dependent material properties with thermal stress, elastic and plastic stress	Vertical forces, stresses, temperature,
Zhang et al [20]	2D	Time dependent	Abaqus	Segregated	Experimental temperature field	Temperature-dependent elastic viscoplastic material model with classic Von Mises criterion for the rate dependent material	Plastic strain, velocity, radial stress, circumferential stress, shear stress
Forrest et al [21]	2D	Time dependent	Hickory	Coupled	Simple convection model similar to friction model surface heat flux	Viscous element representing frictional forces and plastic element with an isotropic state variable representing resistance to dislocation motion	Streamlines, temperature, strain
Buffa et al [22]	3D	Time dependent	Deform	Coupled	Frictional and plastic deformation surface heat flux	Power law rigid-visco-plastic material model with Von Mises yield criterion and associated flow rule	Force, temperature, strain, material flow
Zhang et al [23]	2D	Time dependent	Abaqus	Segregated	Experimental temperature field	Temperature-dependent elastic viscoplastic material model with classic Von Mises criterion for the rate dependent material	plastic strain, velocity, radial stress, circumferential stress, shear stress
Buffa et al [24]	3D	Time dependent	Deform	Coupled	Frictional and plastic deformation surface heat flux	Power law rigid-viscoplastic temperature and strain rate dependent material model	Temperature, plastic strain, UTS, bonding line inclination
Buffa et al [25]	3D	Steady state	Deform	Coupled	Frictional and plastic deformation surface heat flux	Rigid-viscoplastic	Temperature, stress, strain, strain rate, material flow, vertical force, advancing force, Zener-Hollomon, grain size
Heurtier et al [26]	3D	Time dependent	In-house developed	Segregated	In the model material is first heated by the friction of the shoulder and then by the plastic strain	A temperature dependent rigid visco plastic material with a classical constitutive equation	Path of material flow, temperature, micro hardness

Authors [ref]	2D/3D	Steady state/time dependent	Software used	Coupled/Segregated	Heat source	Constitutive equation	Model output reported
Cho et al [27]	2D	Steady state	In-house developed	Segregated	Heat of deformation	Simplified Hart's model, yield condition and flow rule	Temperature, strength, streamlines, velocity, deformation rate, pole figure, ODF, texture
Zhang et al [28]	3D	Time dependent	Abaqus	Segregated	Measured temperature values from an actual test	Von Mises yield criterion and the associated flow rule with rate independent elastic-plastic	Temperature, equivalent plastic strain, radial velocity, tangent velocity, contact pressure
Zhang et al [29]	3D	Time dependent	Abaqus	Segregated	Actual temperature values from the practical FSW test	Von Mises yield criterion and the associated flow rule with rate independent elastic-plastic	Temperature, equivalent plastic strain, radial velocity, tangent velocity, velocity in Z direction
Zhang et al [30]	3D	Time dependent	Abaqus	Coupled	Surface heat flux calculated from frictional stress and slip rate	Von Mises yield criterion and the associated flow rule with rate independent elastic-plastic	Temperature, equivalent plastic strain with different axial pressures, material flow on different surfaces, energy dissipation, kinematic energy to internal energy ratio,
Jacquin et al [31]	3D	Steady state	In-house developed	Segregated	Different form of the friction dissipated power calculated from Tresca shear stress	Norton-Hoff	Flow lines, vortex velocity, dissipated power
Cho et al [32]	2D	Steady state	Fidap	Segregated	Heat of deformation	Simplified Hart's model, yield condition and flow rule	Strength, hardness, streamlines, texture
He et al [33]	3D	Steady state	In-house developed	Coupled	Viscous dissipation	Simplified Hart's model and Levy-Mises flow rule	Streamlines, temperature, strength, internal porosity
Cho et al [34]	2D	Steady state	In-house developed	Segregated	Heat of deformation	Simplified Hart's model, yield condition and flow rule	Strength, hardness
Cho et al [35]	2D	Steady state	In-house developed	Segregated	Heat of deformation	Simplified Hart's model, yield condition and flow rule	Pole figure, streamlines, velocity
He et al [36]	3D	Steady state	In-house developed	Coupled	Viscous dissipation	Simplified Hart's model and Levy-Mises flow rule	Temperature, streamlines, stress, porosity
Bastier et al [37]	3D	Steady state	Castem	Coupled	Plastic deformation surface heat flux	First step:Perzyna with Zener-Hollomon/second step: an adopted elastic-plastic and elasto viscoplastic model	Temperature, fraction of dissolved precipitates, residual displacements, residual stresses, yield stress (temperature and temperature-dissolved precipitates dependent)
Zhang et al [38]	3D	Time dependent	Abaqus	Segregated	Actual temperature values from practical FSW test	Inelastic deformation described by classical rate independent plasticity and inelastic rate of deformation described by inelastic flow rule	Von Mises stress, velocity around the pin with different weld speed and RPM, velocity in Z direction
Buffa et al [39]	3D	Steady state	Deform	Coupled	Deformation and frictional energy generated in the welding	Power law rigid-viscoplastic temperature and strain rate dependent material model	Temperature, strain, strain rate, welding forces

Authors [ref]	2D/3D	Steady state/time dependent	Software used	Coupled/Segregated	Heat source	Constitutive equation	Model output reported
Li et al [40]	3D	Time dependent	Abaqus	Coupled	Plastic strain energy dissipation and frictional energy dissipation	Johnson-Cook	Temperature, stress, velocity, tracer particles location and displacement, heat generation, tool force
Zhang et al [41]	3D	Time dependent	Abaqus	Coupled	N/A	Rate-independent elastic-plastic material with temperature-dependent yielding behavior	Plastic strain, temperature, material flow on different surfaces
Schmidt et al [42]	3D	Steady state	Comsol	Segregated (thermal-pseudo-mechanical)	Temperature dependent yield stress controls the frictional and plastic surface heat flux	Temperature dependent flow stress	Temperature, heat generation
Lorrain et al [43]	3D	time dependent/steady state	Abaqus/Fluent	Segregated	Friction at the tool-sheet interface and plastic work	Johnson-Cook/Perzyna	Stress, Strain rate, temperature, velocity
Buffa et al [44]	3D	Steady state	Deform	Coupled	Frictional forces work and by the deformation work	Power law rigid-viscoplastic temperature and strain rate dependent material model	Temperature, residual stresses, Zener-Hollomon parameter
Fratini et al [45]	3D	Steady state	Deform	Coupled	Friction forces and material deformation	Elastic-plastic rate dependent and temperature dependent material model	Temperature, strain, strain rate, average grain size
Zhang et al [46]	3D	Time dependent	Abaqus	Coupled	Frictional heat calculated from frictional stress times slipping rate	Temperature dependent and rate-independent constitutive model	Plastic strain, temperature, energy dissipation, external work, material flow patterns
Buffa et al [47]	3D	Steady state	Deform	Coupled	Plastic deformation and frictional conditions	Power law rigid-viscoplastic temperature and strain rate dependent material model	Temperature, strain, strain rate
Grujicic et al [48]	3D	Time dependent	Abaqus	Coupled	Work of plastic deformation and frictional sliding	Modified Johnson-Cook	Strength, plastic strain, velocity, tracer particles position, temperature, Von Mises residual stress, residual stresses, grain size
Zhang et al [49]	3D	Time dependent	Abaqus	Coupled	Frictional stress	Rate-independent elastic-plastic material with temperature-dependent yielding behavior	Temperature, plastic strain, external work, kinematic to internal energies ratio, material flow on different surfaces, residual stresses
Fratini et al [50]	3D	Time dependent	Deform	Coupled	Friction forces work and material deformation	Power law rigid-viscoplastic temperature and strain rate dependent material model	Temperature, accumulated strain, strain rate, average grain size
Gagner et al [51]	3D	Time dependent	Abaqus	Segregated	Frictional heat	Thermoelastic-plastic von Mises material with isotropic elasticity and temperature dependent linear kinematic hardening	Temperature, Von Mises stress, normal stress

Authors [ref]	2D/3D	Steady state/time dependent	Software used	Coupled/Segregated	Heat source	Constitutive equation	Model output reported
Buffa et al [52]	3D	Time dependent	Deform	Coupled	Plastic deformation and frictional forces	Rigid-viscoplastic temperature and strain rate dependent material model	Temperature, effective strain, tool force, advancing force
Hamilton et al [53]	3D	Time dependent	Abaqus	Coupled	Plastic strain energy dissipation and frictional energy dissipation	Johnson-Cook	Temperature, Von Mises stress, equivalent plastic strain, frictional and plastic dissipation energies, tracer particles location, particle displacement
Mukherjee et al [54]	2D	Time dependent	Abaqus	Segregated	Obtained from a model with fully sticking contact condition	Johnson-Cook	Temperature, tracer particles position, shear strain rate, equivalent plastic strain
Gemme et al [55]	3D	Time dependent	Forge3	Coupled	Plastic strain	Norton-Hoff	Temperature, torque, strain rate, power
Assidi et al [56]	3D	Time dependent	Forge3	Coupled	Coulomb's friction model	Hansel-Spittel/Norton-Hoff	Temperature, evaluation of contact area, normal stress, forces, error on forces and temperatures, equivalent strain
Azimzadegan et al [57]	3D	Time dependent	Abaqus	Coupled	Plastic deformation	Rigid-viscoplastic constitutive law with isotropic strain hardening	Temperature, equivalent plastic strain, hardness, deformation field, Von Mises stress
Moraitis et al [58]	3D	Time dependent	Ansys	Coupled	Heat produced due to material stirring (plastic deformation)	N/A	Velocity, temperature, Von Mises residual stress, displacement, residual stresses
Mendez et al [59]	3D	Steady state	In-house developed	Coupled	Plastic deformation	Power law behavior related to the Sellars and Tegart model (Zener-Hollomon)	Temperature, thickness of shear layer, shear stress, torque
Tutum et al [60]	2D	Time dependent	Ansys	Segregated	Rotational speed and the temperature dependent yield stress	Elasto-plastic mechanical model	Temperature, residual stresses
Nielsen et al [61]	3D	Time dependent	In-house developed	Coupled	N/A	Elastic-viscoplastic, but using a small strain rate hardening exponent to limit the viscous effect with Voce law hardening	Failure location
Grujic et al [62]	3D	Time dependent	Abaqus	Coupled	Frictional-sliding dissipation over an elementary contact surface area	Johnson-Cook	Equivalent plastic strain, temperature, spatial location of particles, residual stresses
Jamshidi Aval et al [63]	3D	Time dependent	Abaqus	Coupled	Friction and plastic deformation of the material	Temperature- and strain rate-dependent material law	Temperature, equivalent plastic strain, void formation, relation between yield strength and tensile strength
Jacquinet et al [64]	3D	Time dependent	Abaqus	Coupled	Frictional power and the plastic power	Power viscoplastic Arrhenius law, with non-linear strain rate sensitivity	Streamlines, vortex velocity, temperature, power dissipation, torque
Buffa et al [65]	3D	Time dependent	Deform	Coupled	Frictional and plastic deformation	Power law rigid-viscoplastic temperature and strain rate dependent material model	Temperature, residual stresses, computational times

Authors [ref]	2D/3D	Steady state/time dependent	Software used	Coupled/Segregated	Heat source	Constitutive equation	Model output reported
Grujicic et al [66]	3D	Time dependent	Abaqus	Coupled	Plastic deformation and friction-sliding	Johnson-Cook	Temperature, equivalent plastic strain, velocities, grain size
Simar et al [67]	3D	Pseudo steady state	Abaqus	Segregated	Frictional and plastic deformation surface heat flux	Kocks–Mecking–Estrin (KME) model	Temperature, microstructure, mechanical properties, damage model
Bendzsak et al [68]	2D axisymmetric	Steady state	In-house developed	Coupled	Viscous dissipation	Bendzsak-North model	Power, flow in radial direction, streamlines, flow patterns
Colegrove et al [69]	3D	Time dependent	Nisa	Segregated	Frictional surface heat flux	Power law dynamic viscosity	Temperature, velocity, pressure
Ulysse [70]	3D	Steady state	Fidap	Coupled	Plastic deformation	Perzyna dynamic viscosity with Zener-Hollomon flow stress	Temperature, axial and shear forces
Shercliff et al [71]	3D	Steady state	Nisa	Coupled	Frictional surface heat flux	Perzyna dynamic viscosity with Zener-Hollomon flow stress	Temperature, velocity, pressure, flow direction
Reynolds et al [72]	2D	Steady state	Fluent	Coupled	Viscous dissipation	Perzyna dynamic viscosity with Zener-Hollomon flow stress	Streamline, temperature, velocity, axial force, weld energy
Reynolds et al [73]	2D	Steady state	Fluent	Coupled	Viscous dissipation	Perzyna dynamic viscosity with Zener-Hollomon flow stress	Weld energy, temperature, axial force, streamlines
Colegrove et al [74]	3D	Steady state	In-house developed	Segregated	Isothermal temperature of 527 °C	Viscosity was found at a temperature near the solidus (527°C) from experimental stress versus strain rate data	Temperature, streamlines, weld power
Seidel et al [75]	2D	Steady state	Fluent	Coupled	Viscous dissipation	Perzyna dynamic viscosity with Zener-Hollomon flow stress	Streamlines, marker position, weld energy, longitudinal force, weld power, weld energy
Colegrove et al [76]	2D	Steady state	Fluent	Segregated	Isothermal temperature of 527 °C	Viscosity was found at a temperature near the solidus (527°C) from experimental stress versus strain rate data	Torque, traversing force, power
Colegrove et al [77]	2D	Steady state	Fluent	Segregated	Isothermal temperature of 527 °C	Viscosity was found at a temperature near the solidus (527°C) from experimental stress versus strain rate data	Temperature, traversing and down forces, streamlines, limiting shear stress and pin heat, deformation region size
Schmitter et al [78]	3D	Steady state	N/A	Coupled	Frictional surface heat flux	Perzyna dynamic viscosity with Zener-Hollomon flow stress	Temperature, velocity, Zener-Hollomon parameter

Authors [ref]	2D/3D	Steady state/time dependent	Software used	Coupled/Segregated	Heat source	Constitutive equation	Model output reported
Colegrove et al [79]	2D	Steady state	Fluent	Segregated	Isothermal temperature of 527 °C	Viscosity was found at a temperature near the solidus (527°C) from experimental stress versus strain rate data	Welding torque, Traversing force, down force, power, temperature, streamlines, shear stress, pin heat to total heat, deformation region size
Colegrove et al [80]	2D	Steady state	Fluent	Segregated	Isothermal temperature of 527 °C	Viscosity was found at a temperature near the solidus (527°C) from experimental stress versus strain rate data	Velocity, streamlines, material mixing model, surface velocity, shear stress, torque, traversing force
Colegrove et al [81]	2D/3D	Steady state	Fluent	Coupled	Material slip/viscous deformation	Interpolated experimental data/Johnson-Cook	Shear flow stress, temperature, velocity, strain rate, pressure, force, torque, particles position/ Temperature, velocity, strain rate, pressure, torque and traversing force, streamlines
Hirasawa et al [82]	2D	Time dependent	N/A	Segregated	Plastic flow	Spring model using particle method	Temperature, particles position
Schmidt et al [83]	2D	Steady state	Femlab	Coupled	In the case of sliding, heat is generated by frictional dissipation and in the case of sticking heat is generated by plastic or viscous dissipation	Power law dynamic viscosity	Streamlines, shear layer, velocity, shear rate
Colegrove et al [84]	3D	Steady state	Fluent	Coupled	Viscous dissipation	Perzyna dynamic viscosity with Zener-Hollomon flow stress	Velocity, deformation zones, streamlines, temperature, weld power, Traversing force
Nandan et al [85]	3D	Steady state	In-house developed	Coupled	Frictional dissipation surface heat flux	Perzyna dynamic viscosity with simplified Hart's flow stress	Velocity, heat generation rate, temperature, strain rate, viscosity, streamlines
Nandan et al [86]	3D	Steady state	In-house developed	Coupled	Frictional dissipation surface heat flux	Perzyna dynamic viscosity with Zener-Hollomon flow stress	Velocity, heat generation rate, temperature, strain rate, viscosity, iso viscosity surface
Bastier et al [87]	3D	Steady state	Castem	Coupled	Irreversible deformations	Perzyna dynamic viscosity with Zener-Hollomon flow stress	Temperature, material flow, shear stress, plastic strain, residual stresses
Crawford et al [88]	3D	Steady state	Fluent	Coupled	Sticking surface heat flux calculated from contact stress	Perzyna dynamic viscosity with Zener-Hollomon flow stress	Axial force, torque, temperature, viscosity
Foulvarc it et al [89]	3D	Steady state	SysWeld	Coupled	Friction heat dissipation	Power law dynamic viscosity	Velocity, temperature, streamlines

Authors [ref]	2D/3D	Steady state/time dependent	Software used	Coupled/Segregated	Heat source	Constitutive equation	Model output reported
Crawford et al [90]	3D	Steady state	Fluent	Coupled	Sticking surface heat flux calculated from contact stress	Perzyna dynamic viscosity with Zener-Hollomon flow stress	Axial force, torque, temperature, viscosity
Long et al [91]	2D	Steady state	Fluent	Coupled	Viscous dissipation with cut off temperature	Perzyna dynamic viscosity with Zener-Hollomon flow stress	Temperature, streamline, viscosity, axial force
Schmidt et al [92]	3D	Steady state	Comsol	Segregated	Temperature field varying linearly as function of radius ranging from 450oC the inner ring to 100 oC at the outer ring is prescribed	Power law dynamic viscosity	Tracer particles movement
Sato et al [93]	3D	Steady state	AcuSolve	Coupled	Volume heat (viscous dissipation)	Perzyna dynamic viscosity with power law flow stress of steady logarithmic creep strain rate	Temperature, torque
Owen [94]	2D	Steady state	Hickory	Coupled	Frictional and viscous heating	N/A	Temperature, velocity, stress
Tartakovsky et al [95]	2D	Steady state	SPH	Coupled	Viscous dissipation	Johnson-Cook without elastic deformation	Mixing patterns, temperature, accumulated strain, strain rate
Colegrove et al [96]	2D	Steady state	Fluent	Coupled	Viscous dissipation	Perzyna dynamic viscosity with Zener-Hollomon flow stress	Traversing force, flow stress, heat generation, temperature, velocity, pressure, deformation region size, power, strain rate, material condition
Crawford et al [97]	3D	Steady state	Fluent	Coupled	Sticking surface heat flux calculated from contact stress	Perzyna dynamic viscosity with Zener-Hollomon flow stress	Axial force, torque
Vuyst et al [98]	3D	Time dependent	Morfeo	Weak coupled	Plastic work (viscous dissipation)	Average viscosity and Norton-Hoff flow stress	Velocity, temperature
Alfaro et al [99]	2D	Time dependent	In-house developed	Coupled	Plastic deformation surface heat flux	Perzyna viscosity with power law flow stress	Temperature, strain rate
Vuyst et al [100]	3D	Time dependent	Morfeo	Weak coupled	Plastic work (viscous dissipation)	Average viscosity and Norton-Hoff flow stress	Velocity, temperature, strain, strain rate, position of the marker
Chen et al [101]	3D	Steady stae	Fluent	Coupled	Viscous dissipation in the fluid	Perzyna dynamic viscosity with Zener-Hollomon flow stress	Velocity, marker flow, temperature
Atharifar et al [102]	3D	Steady state	Fluent	Segregated	Plastic work surface heat flux (no slip conditions)	Carreau dynamic viscosity model	Temperature, lift force, velocity, dynamic viscosity, dynamic pressure
St-Georges et al [103]	3D	Steady state	CosmosFlow	Segregated	Mechanical energy	A hypothetic fluid which behaves as a viscose liquid at elevated temperatures and as a solid at low temperature	Tangential velocity, transverse material flow, vorticity, temperature

Authors [ref]	2D/3D	Steady state/time dependent	Software used	Coupled/Segregated	Heat source	Constitutive equation	Model output reported
Colegrove et al [104]	3D	Steady state	Fluent	Coupled	Frictional dissipation surface heat flux	Perzyna dynamic viscosity with Zener-Hollomon flow stress	Temperature, heat generation, material deformation condition, rotational flow diagram
Long et al [105]	2D	Steady state	Fluent	Coupled	Viscous dissipation with cut off temperature	Perzyna dynamic viscosity with Zener-Hollomon flow stress	Torque, nugget grain size, axial force, temperature, weld power, flow stress, streamlines, natural strain
Nandan et al [106]	3D	Steady state	In-house developed	Coupled	Viscous dissipation	Perzyna dynamic viscosity with Zener-Hollomon flow stress	Viscosity, temperature, fractional slip, friction coefficient, heat generation rate, temperature, strain rate, velocity, streamlines
Nandan et al [107]	3D	Steady state	In-house developed	Coupled	Interfacial and plastic deformation heat generation	Perzyna dynamic viscosity with Zener-Hollomon flow stress	Temperature, time span, torque, streamlines, concentration profile
Atharifar et al [108]	3D	Steady state	Fluent	Segregated	Plastic work surface heat flux (no slip conditions)	Carreau dynamic viscosity model	Streamlines, temperature, lift force, dynamic pressure, rake angle effects
Dorfler [109]	3D	Steady state	Comsol	N/A	N/A	Modified Bingham viscosity model with Dorfler empirical flow stress	Streamlines, interface location, tracer particles location
St-Georges et al [110]	3D	Steady state	CosmosFlow	Segregated	Mechanical energy	A hypothetic fluid which behaves as a viscose liquid at elevated temperatures and as a solid at low temperature	Transverse velocity, tangential velocity
Liechty et al [111]	3D	Steady state	Fluent	Coupled	Frictional dissipation surface heat flux	Perzyna dynamic viscosity with Norton-Hoff flow stress	Streamlines, pressure, shear stress, temperature
Schmidt [112]	3D	Steady state	Comsol	Coupled	Frictional and viscous dissipation surface heat flux	Power law dynamic viscosity	Temperature, heat generation, material flow, streamlines
Nandan et al [113]	3D	Steady state	In-house developed	Coupled	Interfacial and plastic deformation heat generation	Perzyna dynamic viscosity with Zener-Hollomon flow stress	Temperature, strain rate, viscosity, torque, time span, velocity, streamlines, pressure
Kumar et al [114]	3D	Steady state	JMatPro	Coupled	Viscous heating	Perzyna dynamic viscosity model with Hart's flow stress	Temperature, streamlines, strain rate, weld force
Kim et al [115]	3D	Steady state	Star-CCM	Coupled	Plastic dissipation	Perzyna dynamic viscosity model with rate-insensitive and incompressible rigid-perfect Von-Mises plastic	Temperature, material flow

Authors [ref]	2D/3D	Steady state/time dependent	Software used	Coupled/Segregated	Heat source	Constitutive equation	Model output reported
Lammlein et al [116]	3D	Steady state	Fluent	Segregated	Weld power	Perzyna dynamic viscosity with Zener-Hollomon flow stress	Temperature, velocity
Atharifar et al [117]	3D	Steady state	Fluent	Coupled	Frictional and viscous dissipation surface heat flux	Carreau dynamic viscosity model	Streamlines, temperature, axial force, dynamic viscosity, drag force, lift force, side force, moment, power
Arora et al [118]	3D	Steady state	In-house developed	Coupled	Interfacial and plastic deformation heat generation	Perzyna dynamic viscosity with Zener-Hollomon flow stress	Streamlines, strain rate, strain
Kim et al [119]	3D	Steady state	Star-CCM	Coupled	Plastic dissipation	Perzyna dynamic viscosity model with rate-insensitive and incompressible rigid-perfect Von-Mises plastic	Temperature, streamlines, strain rate, velocity, accumulated effective strain
Hilgert et al [120]	3D	Time dependent	Comsol	Coupled	Frictional and viscous dissipation surface heat flux	Perzyna dynamic viscosity with Zener-Hollomon flow stress/exponential strain rate function flow stress	Temperature, streamlines, torque
Nourani et al [129]	2D	Steady state	Comsol	Coupled	Frictional and viscous dissipation surface heat flux	Perzyna dynamic viscosity with Zener-Hollomon flow stress/elastic-viscoplastic flow stress	Temperature, strain, strain rate, streamlines, grain size/residual stresses

5.3 Implementing and comparing selected constitutive equations in a same FSW model

The integrated multiphysics FSW model considered for aluminum 6061 in the present work is adapted from [129], where details on different modules of the model can be found in Chapter 4. In brief, the model uses a 2D Eulerian multiphysics flow formulation. We neglected the elastic behavior and strain hardening of the aluminum alloy as there is high strain during FSW, i.e. we considered perfectly viscoplastic deformation without strain hardening and with fluid flow. The Perzyna viscosity law (Equation (5-5)) with the Zener-Hollomon flow stress equation (Equation (5-10)) and heat transfer equation were initially employed to model the flow stress of the material and provide the necessary temperature- and strain rate- dependent viscosity of the aluminum fluid. Also the Zener-Hollomon flow stress equation was used to define the pin heat flux. An empirical cut-off temperature (50 °C lower than solidus temperature) was applied to prevent temperature increase higher than solidus. The velocity boundary conditions are applied by defining a stick coefficient between the tool and workpiece. The model has been already validated using experimental data and other published models as discussed in [129]. The process conditions include a tool RPM of 186 and the weld speed of 2.34 mm/sec (Figure 4). In the next sections we aim to apply a set of selected constitutive equations reviewed in Section 2 to this FSW model of aluminum 6061 via the following implantations.

5.3.1 Applying different dynamic viscosity equations of aluminum 6061

As parameters of the dynamic viscosity equation of Carreau model (Equation (5-4)) are reported in Atharifar et al. [117], and the Zener-Hollomon flow stress (Equation (5-10)) model constants in Tello et al. [145], we used these two constitutive equations to develop Carreau and Perzyna dynamic viscosity (Equation (5-5)) models, respectively. Also we used the Zener-Hollomon flow stress to simulate the pin heat flux of the model, where we can predict temperature, shear strain rate, shear stress, viscosity and the applied torque around pin.

5.3.2 Identifying the power law viscosity model parameters for aluminum 6061

For comparison purposes, in the present work we determined the power law dynamic viscosity model parameters (m and n in Equation (5-1)) for aluminum 6061 near solidus by fitting the equation to Perzyna dynamic viscosity model response from [129] with the Zener-Hollomon flow stress. The fitted values of model parameters were $m=1.28 \times 10^7$ and $n=0.2$, with a

coefficient of determination of $R^2=0.99$. As a result, the (CFD based) power law model was also considered in the pool of compared constitutive models.

5.3.3 Applying Johnson-Cook flow stress equations in Perzyna dynamic viscosity model

In order to study the effect of using Johnson-Cook flow stress equation (Equation (5-11)) compared to Zener-Hollomon flow stress equation (Equation (5-10)) on the resulting flow stress around pin, we applied the temperature, strain and strain rate distributions obtained by the Zener-Hollomon equation (under different viscosity laws) into the Johnson-Cook flow stress equation with the latter model constants taken from the work of Lesuer et al. [174] for aluminum 6061.

In the next section, we will first compare the effect of using different CFD based constitutive equations (namely, the power law, Carreau, and Perzyna models) with Zener-Hollomon flow stress model to simulate the pin heat flux. Next, we will compare the predicted shear stress values using the Zener-Hollomon and Johnson-Cook equations with the same temperature, shear strain rate and strain distributions around the pin found via each of the power law, Carreau and Perzyna viscosity models.

5.4 Results and discussion

5.4.1 Effect of using different dynamic viscosity equations on CFD model results

The shear stress in the CFD model of FSW around the pin after using Perzyna, Carreau and power law dynamic viscosity equations are shown in Figure 5.4. In all the models in Figure 5.4 we use the Zener-Hollomon (ZH) flow stress to determine the tool's heat flux as discussed in [129]. It is clear that all models resulted in a comparable flow stress around the pin, however Carreau model shows the lowest shear stress compared to the other two models.

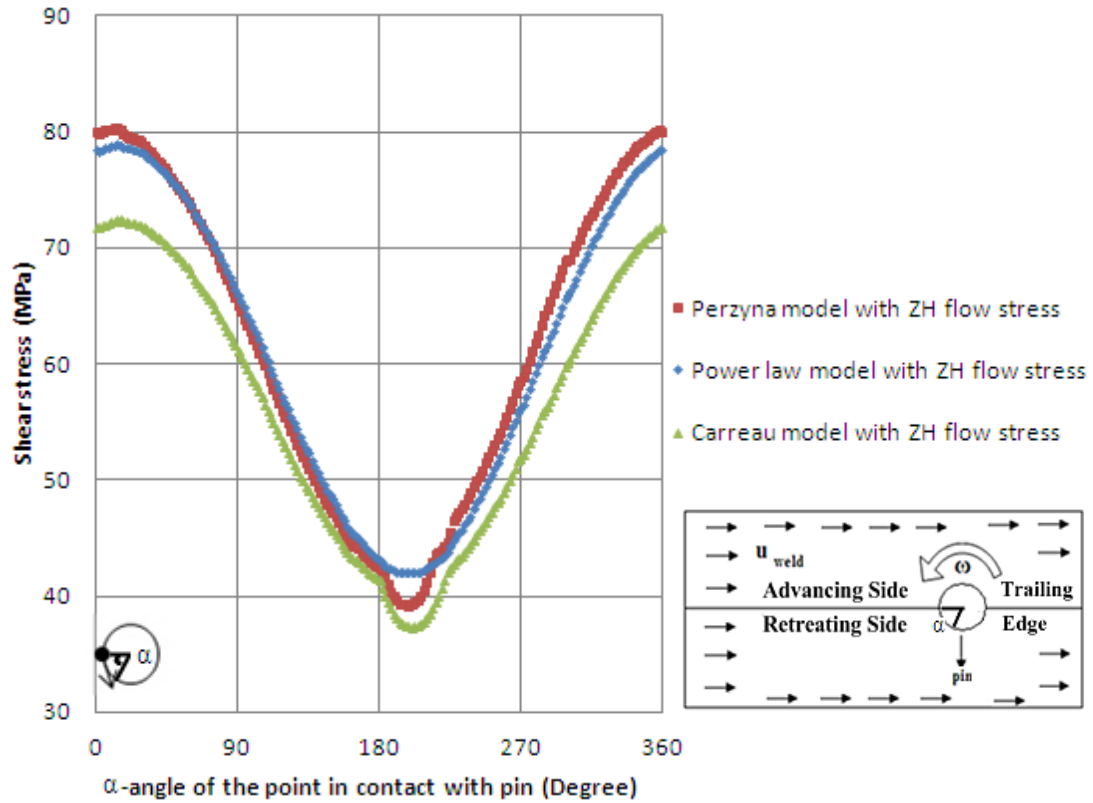


Figure 5.4- Effect of using different dynamic viscosity equations on shear stress around the pin

In Figure 5.5 the effect of different dynamic viscosity equations on the shear strain rate and temperature of points around the pin is shown. It is clear that the maximum temperature is somewhere between regions 2 and 3 and closer to region 3, i.e., in the trailing side of the pin (Figure 4) which is in agreement with earlier works [129]. Also the maximum shear rate occurs between regions 3 and 4 in advancing side of the plates. Apparently Carreau and power law models predict lower shear strain rates and temperature values compared to Perzyna dynamic viscosity model. Also they all result in a similar maximum temperature (about 540 °C) while the Carreau model predicts a slightly higher value.

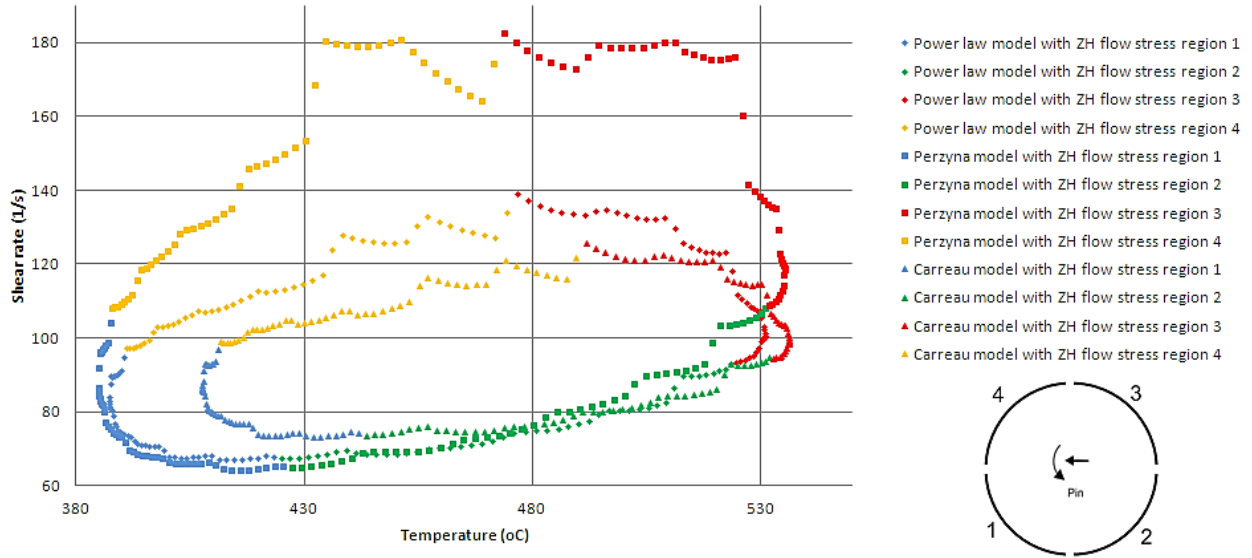


Figure 5.5- Effect of using different dynamic viscosity equations on shear strain rate and temperature around pin

In Figure 5.6, we notice that the effect of using different dynamic viscosity equations on resulting dynamic viscosity values around the pin is much more significant than the previous effects. As shown in Figure 5.6, Perzyna model with ZH flow stress predicts notably higher dynamic viscosity values compared to other dynamic viscosity models. Interestingly, however, they all show the same value at the point where the material temperature is equal to its solidus temperature. The difference would be due to the higher sensitivity of the Perzyna constitutive model to temperature and shear strain rate changes around the pin.

We also compared the resulting temperature distribution on the weld line after using different dynamic viscosity models in the CFD model which is shown in Figure 5.7. All of the models showed a very similar temperature distribution except for Carreau model at the leading edge (in front of the pin) which shows slightly higher temperatures.

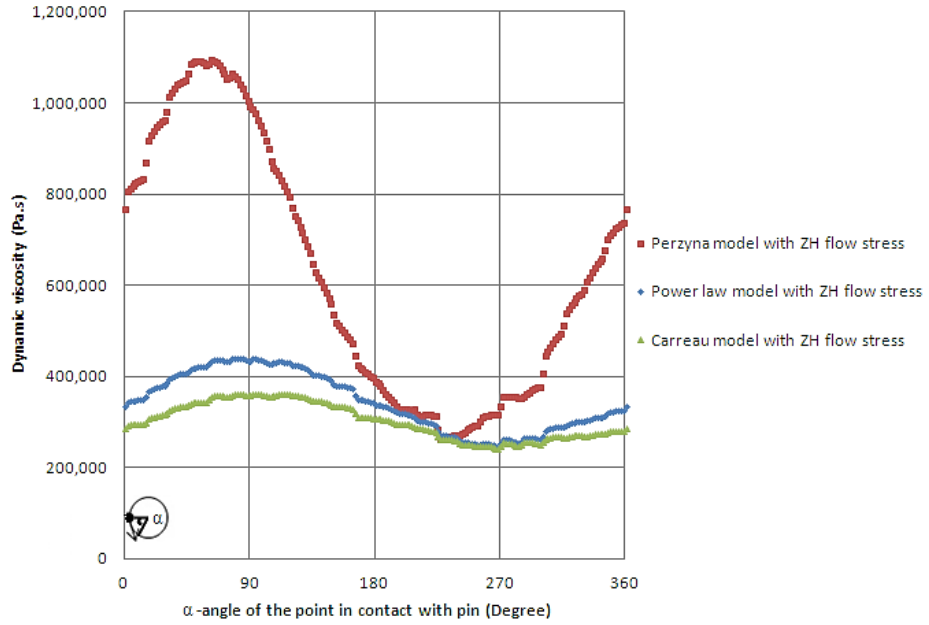


Figure 5.6- Effect of using different dynamic viscosity equations on dynamic viscosity around pin

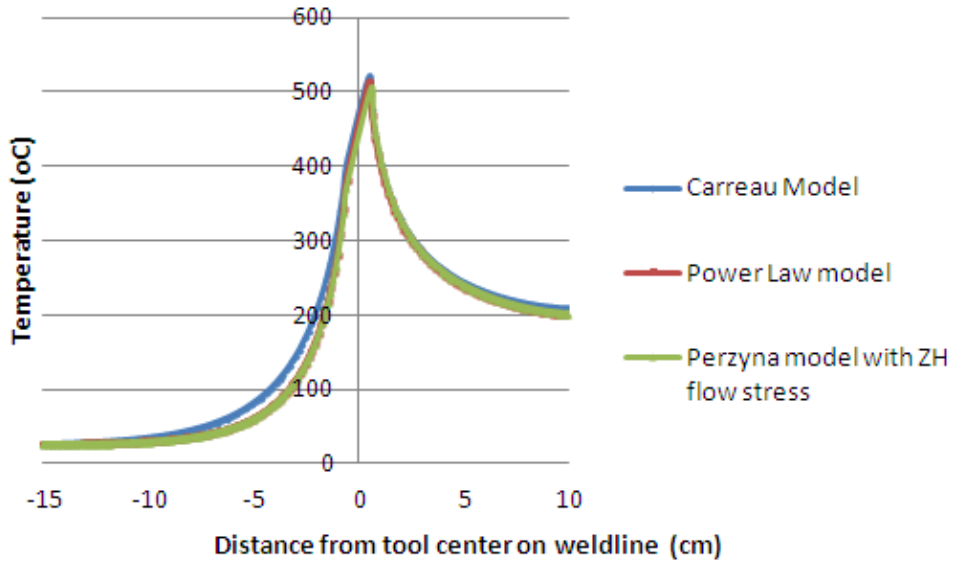


Figure 5.7- Effect of using different dynamic viscosity equations on maximum temperature on the weldline

Next, considering plates with 10 mm thickness, we calculated the resulting torque on the pin as shown in Figure 5.8. The predicted torque values are close to each other while in the Carreau model it is slightly lower compared to other two dynamic viscosity models.

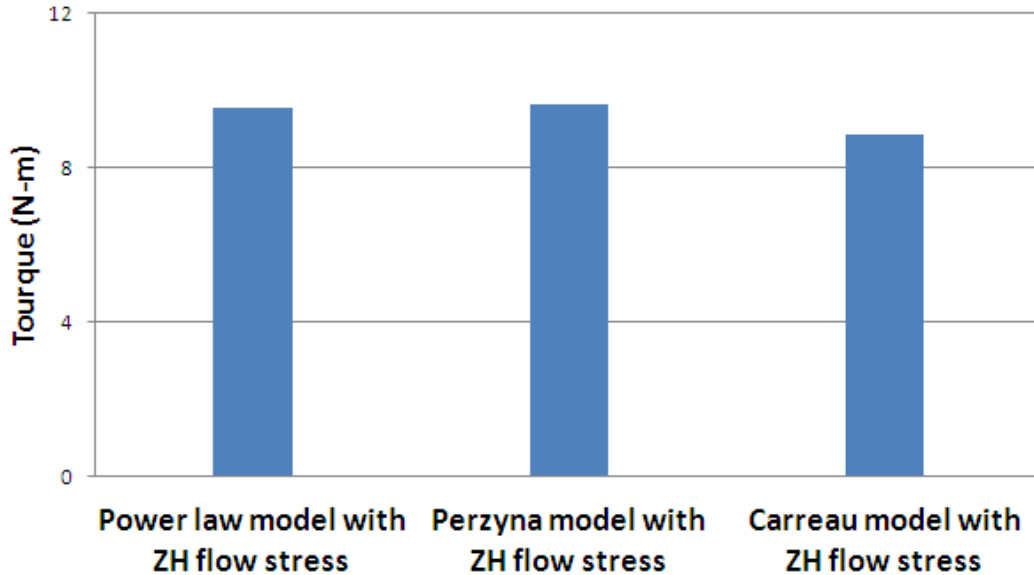


Figure 5.8- The Effect of using different dynamic viscosity equations on the resulted torque on pin

5.4.2 Effect of using different CSM flow stress equations

In order to compare the Johnson-Cook (JC) flow stress model to the Zener-Hollomon (ZH) flow stress model under similar CFD viscosity laws (power law, Carreau and Perzyna), we obtained the temperature, strain and strain rate distributions resulted from Zener-Hollomon model with each of the above viscosity models and applied them into the JC flow stress equation for aluminum 6061. The results are shown in Figure 5.9 (data from Figure 5.4 have been also added to Figure 5.9 for facilitating comparisons). As seen in Figure 5.9, using the JC flow stress model has resulted higher values of shear stress around the pin compared to the ZH flow stress model. Also when the JC model is used, the average value of shear stress around the pin is higher compared to that of the ZH model. This is because of high strain values during FSW around pin and its direct effect on the JC flow stress values, whereas the ZH flow stress is not strain dependent. This also suggests that the JC flow stress model may need some model tunings; for

example an application of different stick coefficient may be required to use in the JC model for FSW simulations when compared to the ZH flow stress model.

In order to understand exactly how much the deformation strains affects the JC flow stress model predictions, next we considered a strain state equal to zero around the pin by putting $B=0$ in Equation (5-11) and applied the values of temperature and strain rate resulting from the CFD model with the ZH flow stress into the JC flow stress equation. The idea is that strain softening happens in high temperatures around the FSW tool by dynamic recrystallization and hence the strain values in this region are annihilated. The results of this attempt are shown in Figure 5.10.

It is clear that the shear flow stress resulted in the CFD model using the JC flow stress (elastoviscoplastic model) with zero strain around pin becomes much closer to the ones that had been resulted from the ZH flow stress model (perfectly viscoplastic), specially in the trailing edge (as shown in Figure 5.4). The 2D multiphysics model can be effectively used as a baseline to study the effect of other constitutive model parameters and understand their differences regarding model predictions and underlying material behaviors.

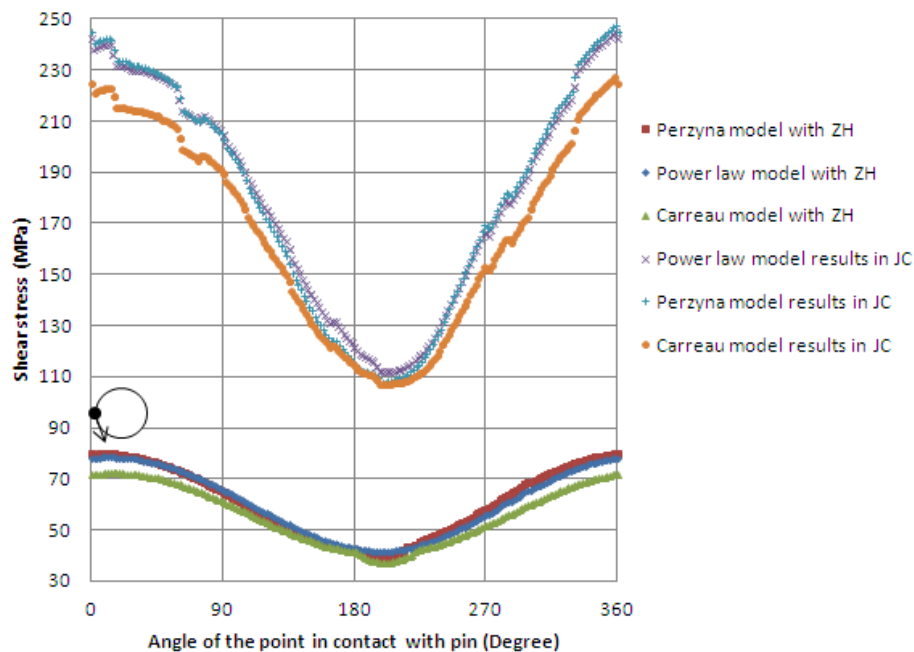


Figure 5.9- The effect of applying CFD model results (namely the temperature, strain and strain rate distributions) from ZH flow stress model into JC flow stress, under different dynamic viscosity equations

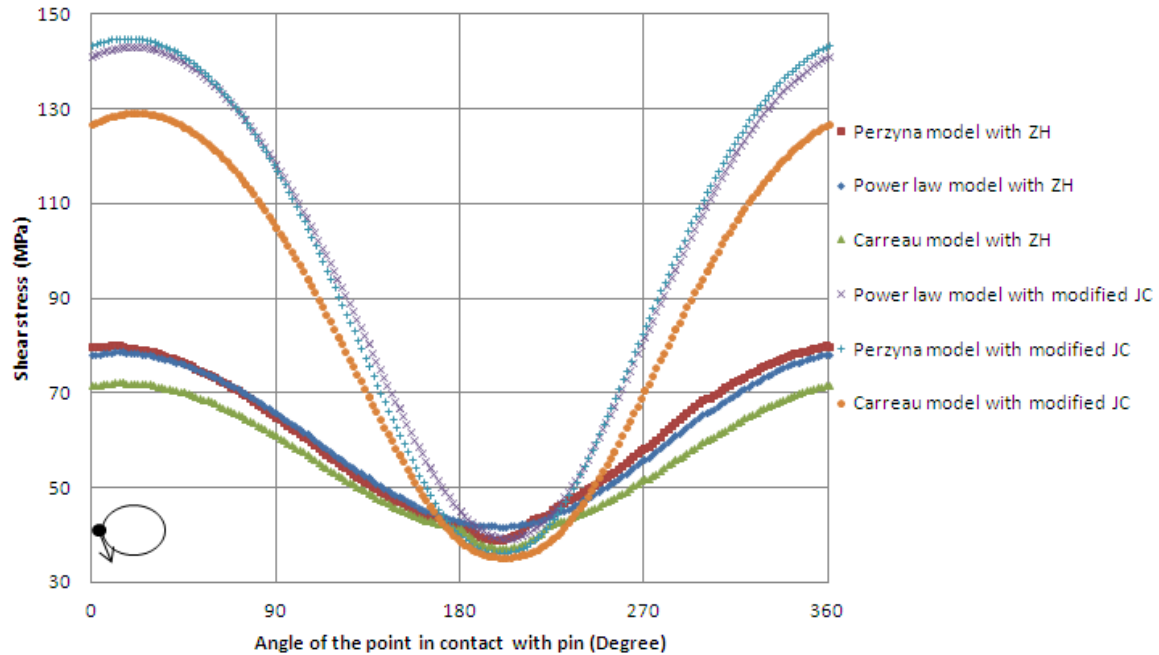


Figure 5.10- Effect of applying temperature and strain rate results from CFD model-ZH flow stress into the CSM-JC flow stress model, both under the condition of zero strain around the pin

5.5 Summary of findings

In Chapter 5, we studied the effect of using different types of constitutive equations in the previously validated multiphysics model of FSW, under the same welding conditions on aluminum 6061 sample. The following observations were found:

- 1- Using the CFD approach, all the three dynamic viscosity equations (power law, Carreau model and Perzyna model) on average yielded similar shear stress around the pin while the Carreau dynamic viscosity model predicted slightly lower values.
- 2- Comparing the CFD and CSM approaches, if we use the CFD approach's temperature, strain and strain rate predictions (using power law, Carreau model and Perzyna model) and import them in Johnson-Cook flow stress equation (CSM approach), the resulting shear stress around the pin is much higher with the Johnson-Cook's flow stress equation compared to the Zener-Hollomon flow stress.

- 3- The maximum temperature occurs in the retreating edge of the pin (between regions 2 and 3; Figure 5.5) during FSW.
- 4- The maximum shear strain rate occurs in the advancing side of the pin (between regions 3 and 4; Figure 5.5) during FSW.
- 5- Perzyna dynamic viscosity model generates higher shear strain rates compared to the power law and Carreau models.
- 6- All the three dynamic viscosity models (power law, Carreau model and Perzyna model) resulted in similar maximum temperatures however the Carreau model predicts a relatively higher minimum temperature.
- 7- The dynamic viscosity in all the three CFD models becomes closer in the areas where temperature is near the solidus temperature of the plates. In other weld regions, the Perzyna dynamic viscosity model predicted higher dynamic viscosity values.
- 8- The temperature distribution on the weld centerline and the required torque on the pin are predicted comparably using the three dynamic viscosity models. This means from a practical point of view, the external energy required to weld the material is independent of the underlying CFD constitutive models used for simulation.
- 9- The Johnson-Cook flow stress equation may need a different FSW model tunings, for example applying a different stick coefficient, in order to predict a comparable model performance to the Perzyna dynamic viscosity model in FSW simulations. At high temperatures, if we drop the strain components from the JC model, it predicts shear stresses close to the ones predicted via the CFD dynamic viscosity equations with the ZH flow stress. Advanced experimental set-ups are desired to directly compare and validate the performance of these widely used constitutive models in the FSW field.

Chapter 6: Strain Measurement and Model

Versions of this chapter have been published in **Article 2:** Mohamadreza Nourani, Abbas S. Milani, Spiro Yannacopoulos, A new approach to measure strain during friction stir welding using visioplasticity, ASME International Mechanical Engineering Congress & Exposition, 11-17 Nov 2011, Colorado, USA., and **Article 3:** Mohamadreza Nourani, Abbas S. Milani, Spiro Yannacopoulos, On the experimental and numerical predictions of strain during friction stir welding: a case study on 7050 aluminum alloy, TSEST Transaction on Control and Mechanical Systems, Volume 1, No 6, 2012, Pages 259-263.

Overview: During modeling of the friction stir welding (FSW) process, the prediction of strain range experienced by material is important as it affects the microstructure and mechanical properties of the final weld [1-7]. For aluminum alloys, this range has been reported very scarcely and/or scattered widely in the literature (the range of the maximum equivalent plastic strain has been reported to be from 2.4 to 184 [8-24]). A new approach is proposed in this chapter for measuring strain during friction stir welding using visioplasticity. In this approach, strains are calculated from changes in the boundaries of a small cylindrical Al- 30 % SiC composite marker mounted in the advancing side of mid-plane of adjacent plates during welding. The marker shape change is observed by a “stop action” (freeze-in) technique midway the process. COMSOL numerical modeling is then used to compute the strain distribution using the observed boundary changes compared to the initial marker boundaries. As an illustrative example, the method is applied to the results reported by London et al. [25] for the friction stir welding of 6.35 mm thick 7050 aluminum plates, welded with tool RPM of 350, welding speed of 1.69 mm/sec, tool pin diameter of 8 mm, tool shoulder diameter of 24 mm, and tool tilt angle of 3 degrees. A lower and upper bound of cumulative equivalent plastic strain of 14.1 and 20.3, respectively, are found to be in the neighborhood where the marker enters the severe deformation zone at mid-plane of plates in front of the leading edge of the pin.

6.1 Introduction

As measuring the strain and strain rate during the FSW process may not be directly possible, researchers often opt to use simulation methods to estimate the equivalent plastic strains in the workpiece. These strains are then validated by indirect measurable process quantities such as force, momentum, power, and temperature distribution. It is very important to note that some part or all of the variable strains generated during FSW may be relaxed due to the dynamic recrystallization in the weld nugget which has not been considered in the existing numerical models of strain during FSW up to date. Different modeling assumptions can cause scattered values of strain reported in the literature [8-24] (Table 6.1) for aluminum alloys. The maximum strain shown in Table 6.1 always occurs under the tool shoulder. In order to attain a conservative estimation of the strain induced during FSW quantitatively, a novel viscoplastic approach is recommended in this chapter following the work of London et al. [25] that only studied the material flow qualitatively.

Table 6.1- Reported equivalent plastic strains in FSW of aluminum alloys and the related process parameters

Reference	Code	Tool/workpiece interface	Material	Thickness (mm)	Normal force (KN)	Rotating speed (RPM)	Weld speed (mm/s)	Tilt angle (°)	Pin diameter (mm)	Shoulder diameter (mm)	Strain on mid-plane in front of leading edge of pin	Max strain
Schmidt <i>et al</i> [8]	Abaqus/Explicit	Slide	2024	3	18	400	2	1	6	18	111-122	133
Buffa <i>et al</i> [9]	Deform-3D	Shear friction	7075	3	4.75±0.75	1000	1.67	2	3	10	5.2	5.4
Heurtier <i>et al</i> [10]	Self developed	Kinematics model	2024	10	-	1003	2	0	6	12	8-10	18
Long <i>et al</i> [11]	Fluent	Stick	7050	9.5	-	152	1.27	2.5	10	28.6	6.8	8.2
Zhang <i>et al</i> [12]	Abaqus/Explicit	Slip (slip rate of 0.5 %)	6061	3	30 (MPa)	400	2	0	6	18	3.7-5 (FSW failed)	15
					70 (MPa)						27-41	165
					90 (MPa)						46-61	184
					150 (MPa)						70-94 (FSW failed)	282
Xu <i>et al</i> [13]	Abaqus	Modified Coulomb frictional law	6061	8.13	23.6	390	2.36	2.5	10	25.4	30	45
Zhang <i>et al</i> [14]	Abaqus/Explicit	Slip (slip rate of 0.5 %)	6061	3	-	400	2	0	6	18	36-48	145
							3				23-35	139
							4				8.9-11.9	35.6
Arora <i>et al</i> [15]	Self developed	$\delta=0.65^1$	2524	6.4	42.3	300	2.11	2.5	7.1	20.3	<2.5 ²	<6
Fratini <i>et al</i> [16]	Deform-3D	Shear friction	2139	3.2	-	1400	2.92	2	4	12	12	>12

¹ Ratio of linear velocity of material near the tool to linear velocity of the tool

² Von-Mises equivalent strain 0.133 mm below the top surface of FSW

Reference	Code	Tool/workpiece interface	Material	Thickness (mm)	Normal force (KN)	Rotating speed (RPM)	Weld speed (mm/s)	Tilt angle (°)	Pin diameter (mm)	Shoulder diameter (mm)	Strain on mid-plane in front of leading edge of pin	Max strain
Zhang <i>et al</i> [17]	Abaqus/Explicit	Slip (slip rate of 0.5 %)	6061	3	70 (MPa)	150	2.363	0	6	18	0.9-1.1 (FSW failed)	2.6
						240					28-42	167
						375					27-41	165
Azimzadegan <i>et al</i> [18]	Abaqus/Explicit	Coulomb friction model	1100	5	-	1500	1.67	3	6	20	31-35	44
Assidi <i>et al</i> [19]	Forge3	Friction model	6061	9.53	19±2.5	650	1.69	2.5	8	25.4	24-32	80
Hamilton <i>et al</i> [20]	Abaqus/Explicit	Contact pair with Coulomb friction	2024	3	9±2	477	2	0	5	14	1.5-1.65	2.4
Jamshidi Aval <i>et al</i> [21]	Abaqus/Explicit	Coulomb friction model	5086	5	-	900	2.5	1	3-6	20	46-57	69
Reynolds <i>et al</i> [22]	Fluent	No slip	2195	8.1	-	400	2	α	10	-	50.2	111
Reynolds <i>et al</i> [22]	Abaqus	Slipping/modified Coulomb law	6061	8.1	-	400	2	α	6.5	-	10	174/123
Xu <i>et al</i> [23]	Abaqus	Modified Coulomb law	6061	8.1	-	390	2.364	2.5	10	24.5	10	20
Goetz <i>et al</i> [24]	Deform	Coulomb law	1100	6.35	-	1000	1	-	6	25.4	5	5

6.2 Strain measurement using Visioplasticity method

In a conventional visioplasticity method during extrusion, strains are determined from changes in the shape of the flow lines as observed through the deformation of grids on an axial plane of the extrusion billet [26]. It cannot be directly used for FSW where there is the stirring of material by tool. In order to measure the strains during FSW, we can use discrete marker study in addition to a “stop action” or “freeze-in” technique. For the latter, it is also more convenient to use a retractable pin tool (RPT) where the pin can be removed from the shoulder conveniently. When the pin is near the marker, we can stop the process and remove the shoulder from the pin and workpiece and study the marker deformation before its separation and re-bonding by examining different sections of the plate.

Figure 6.1 shows the schematic view of the Al-30% SiC marker layout which is used to calculate the equivalent plastic strain on mid-plane in front of the leading edge of the pin.

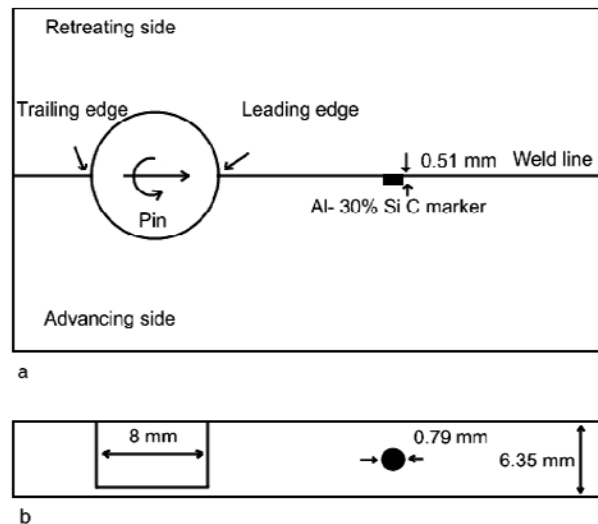


Figure 6.1- Schematic view of the location and shape of the marker used to calculate the equivalent plastic strain with tool tilt angle of 3 degrees. a) top view b) side section view

After sectioning the plate in different depths parallel to the top face, it was seen that the marker is stretched toward the top surface while elongated along the streamlines starting from the advancing side and deposited in the back of the pin through the retreating side [25]. The upward movement of the marker is because of a higher temperature near the shoulder which causes

lower flow stress and more flow localization. Figure 6.2 shows the section at mid-plane of the plate with the marker deformed by the tool and elongated along the streamlines around the pin.

In order to calculate the extent of marker strain in the thickness direction of the plate, first the area of the marker was calculated by drawing a line around the deformed marker boundary as shown in Figure 6.3. The ensuing area was 0.274 mm^2 . The original area of the marker on the mid-plane was 0.403 mm^2 . The strain along thickness causes a reduction of original area of the marker at mid-plane of the plate from 0.403 to 0.274 mm^2 .

The marker strain along the streamlines can be calculated if the original rectangle dimensions and the consequent deformed corners are known. We know the area of the deformed marker and we can consider an equivalent rectangle with the same length to width ratio as the original marker section on the mid-plane ($0.79/0.51=1.54$), and with the same area as the deformed marker (0.274 mm^2). This gives a length of 0.651 mm and a width of 0.421 mm as shown in Figure 6.4 (abcd). Figure 6.5 shows the original area of the marker section on the mid-plane (a'b'c'd') and consequent strain directions. The total strain can be decomposed into the strain along thickness and the strain along the streamlines. Next step to calculate the strain along the streamlines around the pin is correlating the initial marker corners after straining along the thickness (abcd) to those after the marker strain along the streamlines (ABCD). It is shown that rectangle (abcd) is translated by a longitudinal (L) and transverse (T) rigid body translation to a point where corner d coincides with corner D after deformation, without causing any strain at that point.

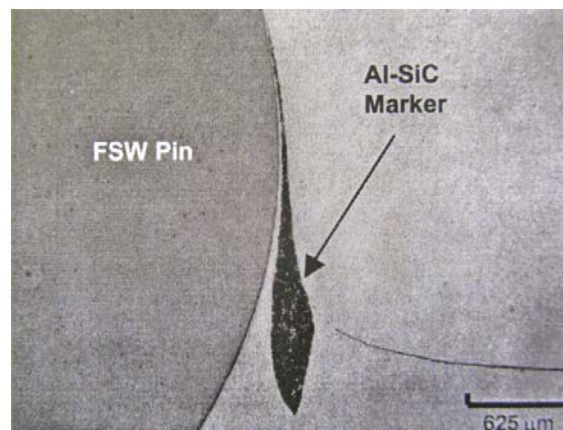


Figure 6.2- Section of the deformed discrete marker at mid-plane of the plate [25]

As shown in Figure 6.4, point B is on the faying surface between plates, which shows the streamline direction above the marker (black curved line). Points a and b should continue to be on the surface (streamline), thus their positions after deformation are points A and B. Because of the streamlines motion from Figure 6.4, points a and c which were initially in contact with the moving pin, enter the severe deformation zone and are indicated by A and C on the deformed marker. Point C is on a relatively longer streamline so it moves with a higher velocity compared to point A. That's why point C is higher than point A in Figure 6.4.

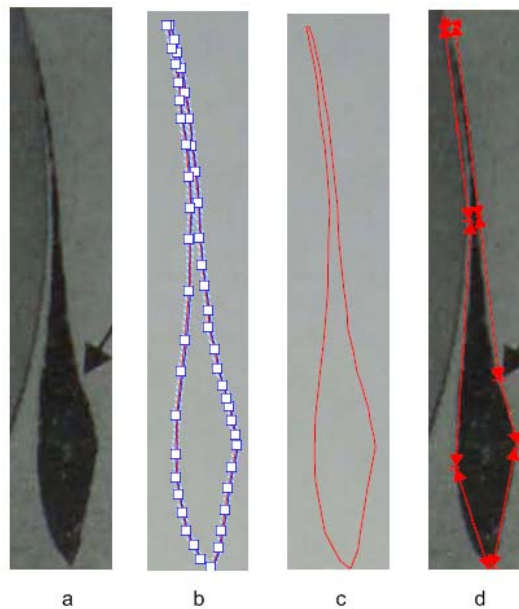


Figure 6.3- Different steps to calculate the marker strain

- (a) the marker shape at mid-plane of the plate [25] (b) drawing the marker boundary points (c) calculating the area by CAD (d) simplifying the marker boundaries

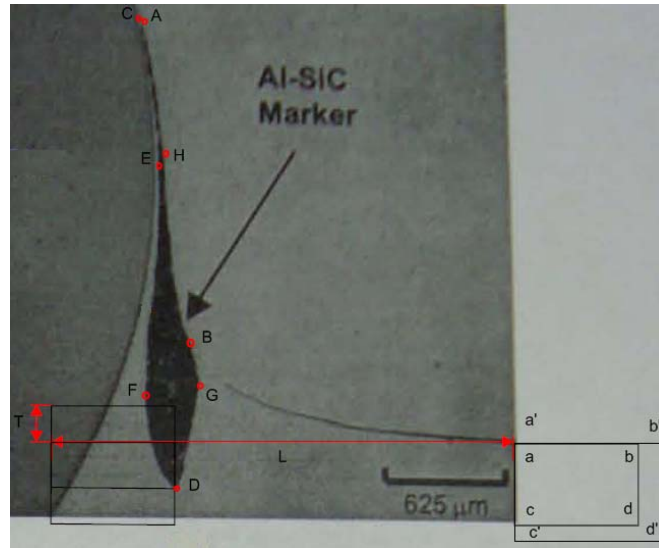


Figure 6.4- Position of the original marker section at mid-plane of the plate before deformation (a'b'c'd') and the reduced area after a strain along the thickness (abcd), and along the streamlines (ABCD)

In order to calculate the strain more accurately some additional points are selected on the deformed marker between the corners of A,B,C,D and named E,F,G,H. The area of (ABCDEFGH) is the same as (abcdefgh). The position of corresponding points on the marker before deformation is calculated considering a homogenous deformation as shown in Figure 6.6. The next step to estimate the strain of the marker in the direction of streamlines was the calculation of the equivalent plastic strain at its area using COMSOL. The transformations of the boundary points were implemented (using displacement-type boundary conditions) in a 2D plain strain model. In this model, a flow stress of 54 MPa for the aluminum 7050 at 673 K was used [27]. we also considered that points A and C are in the same position as another possibility. For the latter case, the model hardly converged and the average equivalent strain along the streamlines did not change considerably.

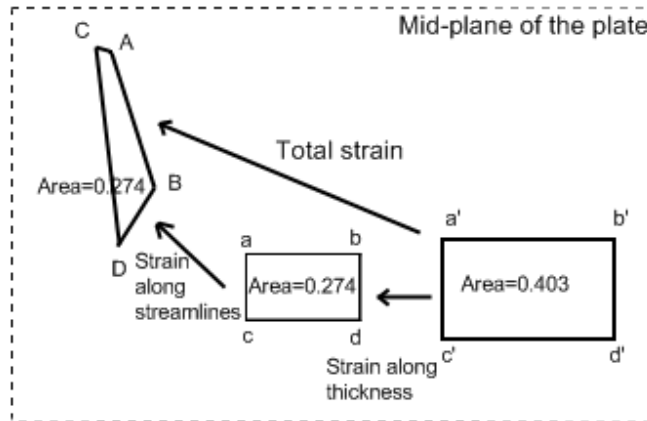


Figure 6.5- Schematic view of original area of the marker section at mid-plane of the plate ($a'b'c'd'$) and the reduced area after a strain along the thickness ($abcd$), and along the streamlines ($ABCD$)

The calculation of the strain normal to the streamlines was done considering the constant volume assumption during plastic deformation. Unlike the tensile strains along the streamlines and along the thickness, the strain normal to the streamlines is compressive. The equivalent plastic strain of the marker in the leading edge of the pin was calculated via the Von-Mises measure. As explained before in Chapter 4, a 2D steady-state Eulerian multiphysics finite element model of aluminum 6061 alloy [28], there is a semi-symmetric streamline distribution around the pin as shown in Figure 6.7. It shows that the marker after being stretched in the leading side of the pin and passing with a high velocity from the advancing side through the retreating side, is pushed back on the trailing side of the pin. The translational movement of the marker around pin with a high velocity through the retreating side is almost a rigid body rotation since the space between the streamlines and their length in the retreating side is almost the same for the marker position used. It also shows a rotation layer [29], which if the material is trapped in, its deposit is delayed and may rotate with the pin more than one cycle. It would not, however, cause any additional significant strain in the material. In order to calculate the cumulative equivalent plastic strain of the marker, we should add up the absolute values of the equivalent plastic strains in the leading and the trailing edges of the pin, which have the same value because of the semi-symmetric streamline distribution around the pin (Figure 6.7). Although we should note that the former is positive and the latter is negative.

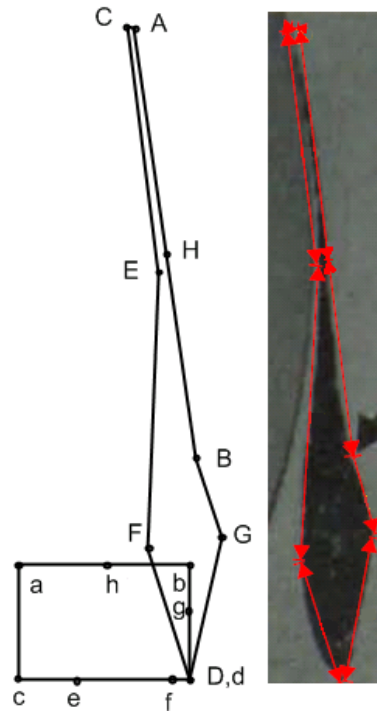


Figure 6.6- The position of corresponding points on the original marker boundaries at mid-plane of the plate (a'b'c'd') after deformation along the thickness direction (abcdefgh) and after deformation along the streamlines (ABCDEFGH)

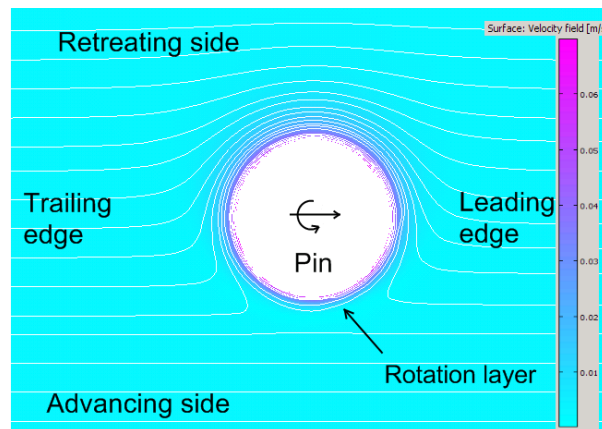


Figure 6.7- Streamlines and the magnitude of the velocity vectors around the pin in a multiphysics model of FSW [28]

6.3 Strain modeling using the integrated multiphysics model

We use the integrated multiphysics model we explained in Chapter 4 to find the strain distribution during FSW. In the model we applied strain rate integration over time to compute

plastic strains in all the points of fluid dynamics model for the first time which is based on a solid mechanics definition of viscosity. The main advantage of the multiphysics model is that, in addition to the strain field, it can provide a multitude of other process quantities including temperature, deformation rate, and flow stress distribution around the pin. Here the goal is to employ the previously developed model for strain prediction in FSW of aluminum7050, as compared to the experimental values via the visioelasticity-CAD (semi-experimental) approach outlined in Section 6.2 of Chapter 6. The process parameters and material properties used in the model are summarized in Table 6.2. The values of α , n , A , and Q can be considered the material constants in conjunction to governing Equations (4-9) and (4-10) in Chapter 4.

Table 6.2- Process parameters and material properties used in the integrated multiphysics model of aluminum 7050

Description (Unit)	Value
Weld speed- u_{weld} (mm/s)	1.69 [25]
Rotation speed- ω (rev/s)	5.83 [25]
Pin radius- r_{pin} (mm)	4 [25]
Ambient pressure- P_o (KPa)	101
Ambient temperature- T_o ($^{\circ}\text{C}$)	27
Ideal gas constant- R (J/mol.K)	8.31451
Friction coefficient- μ	0.4 [28]
Stick coefficient- δ	0.65 [28]
α (1/MPa)	0.0497 [27]
n	2.59 [27]
A (1/s)	$3.28e^5$ [27]
Q (J/mol)	123000 [27]
Heat capacity- C_p (J/Kg K)	860 [20]
Thermal conductivity- k (W/mK)	157 [20]
Density- ρ (Kg/m ³)	2830 [20]
Solidus ($^{\circ}\text{C}$)	488 [20]

6.4 Results and discussion

6.4.1 Strain measurement (semi-experimental viscoplasticity)

The strain of marker along thickness is found to be to 0.385. Figure 6.8 shows the strain distribution of the marker along streamlines results simulated using COMSOL. The average value of the strain distribution shown in Figure 6.8 was found to be 5.912. The maximum and minimum values of the strain are 8.603 and 2.725, respectively. These values are much higher than the strain along the thickness of the marker which shows the deformation is almost along the streamlines. Also we can notice that the left side of the marker which is in contact with the pin has a higher strain distribution and is decreased in the right side. The average and maximum values of the strain are used as the lower and upper bounds of strain along streamlines.

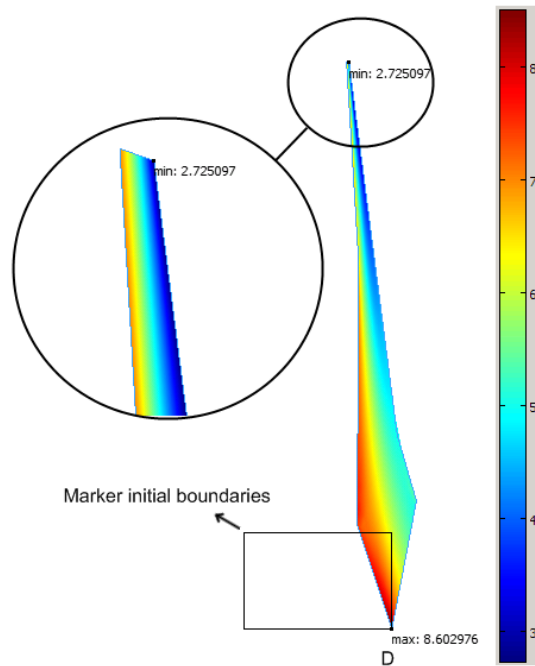


Figure 6.8- Strain distribution results of the marker along streamlines at mid-plane of the plate using COMSOL

The strain normal to the streamlines is calculated considering that the sum of the three principal strains should be equal to zero (i.e., no volume change during plastic deformation).

The lower and upper bounds of the total strain in the marker on mid-plane in front of the leading edge of the pin are 7.059 and 10.163, respectively based on Von-Mises measure.

As mentioned before the same amount but compressive strains occur in the trailing edge of the pin during the back deposit of the marker. Subsequently, the lower and upper bounds of the cumulative equivalent plastic strain of the marker are found to be 14.118 and 20.326, respectively. It should be noted that in order to compare the results of the equivalent strains on the mid-plane in front of the leading edge of the pin in the models of Table 6.1 with those obtained in this work; we chose only the models with comparable process parameters (material type, pin diameter, tool rotation speed, transverse speed, etc). The literature process parameters which are comparable to our runs are highlighted in Table 6.1. Among these, the simulated strain results reported by Zhang *et al* (27 to 41) [12] are the nearest to the results in this study (14.1 to 20.3). The average strain in Zhang *et al* model is 34 [12] for aluminum 6061 and for 7050 it is found to be 17.2. According to Tello *et al* [27] the flow stress of 7050 at the maximum temperature during the FSW process (673K) [30] is about 54 MPa and for 6061 at 739 K [31] it is about 28 MPa. Thus, as one would expect, the strain reported by Zhang *et al* [12], for almost similar process parameters of 6061 with a flow stress ~50% lower than 7050, is 50% higher compared to 7050 results that are reported in this work.

6.4.2 Strain modeling (Integrated multiphysics model)

Figure 6.8 showed the strain distribution results of the marker along streamlines at mid-plane of the plate using the semi-experimental approach in Section 6.4.1 of Chapter 6. The maximum strain of 8.603 occurs at point D. The measured values of strain at the points of A, B, C, D, E, F, G, and H (see also Figure 6.6) are included in Table 6.3. Figure 6.9 shows the position of the marker at the strain field and streamlines of the integrated multiphysics model. As can be seen in this figure, the streamlines are not symmetric and the maximum strain of 34.394 is located near the streamline with the maximum curvature. The position of the marker used to measure strain is also shown in Figure 6.9. While the numerical model could predict the strain distribution all around the pin, the experimental approach was limited to the discrete points of the marker. One-to-one comparison of strain values at these points via the two approaches are given in Table 6.3.

Table 6.3- Comparison of the strain values measured via the viscoplasticity-CAD approach and those predicted by the multiphysics model

Point (Figure 6.6)	Measured strain (Figure 6.8)	Modeled strain (Figure 6.9)	Difference (%)
A	2.725	2.394	12.1
B	4.972	4.605	7.4
C	6.987	5.350	23.4
D	8.603	7.547	12.3
E	6.628	5.164	22.1
F	7.453	6.686	10.3
G	4.986	3.442	30.9
H	3.980	2.784	30

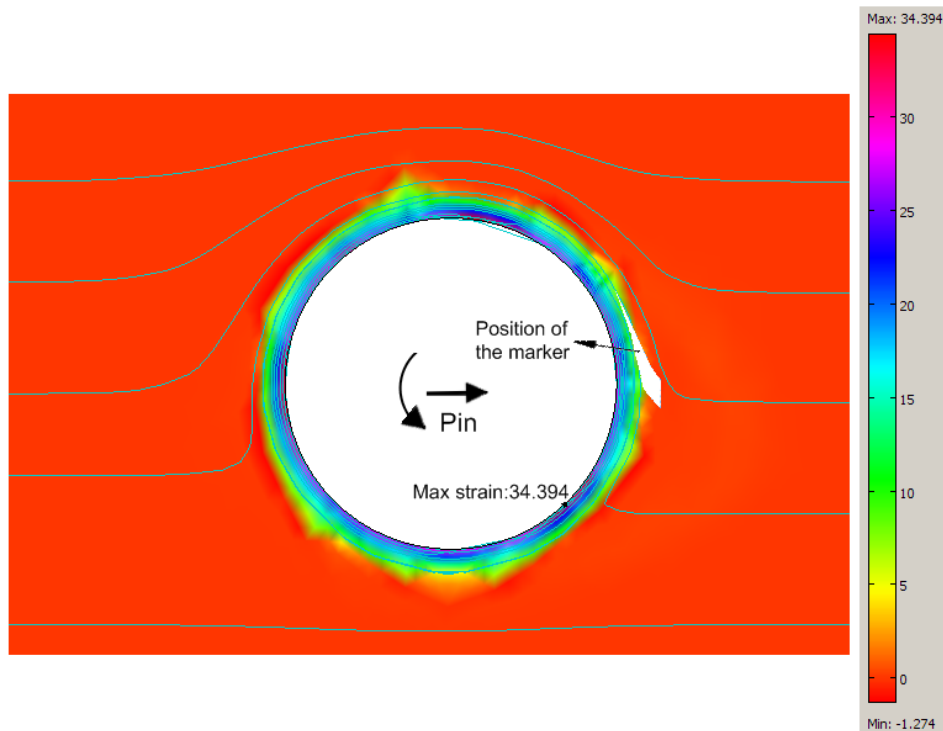


Figure 6.9- The position of the marker at the strain field and streamlines of the integrated multiphysics model

6.5 Summary of findings

For FSW of aluminum alloys, the range of reported values of maximum strain in the literature via numerical models varies largely (from 2.4 to 184). On the other hand, a direct measurement of strain during FSW is practically impossible, due to the stirring of the material near the tool. In this chapter, a new semi-experimental approach by means of viscoplasticity with the “stop action”/ “freeze-in” technique, followed by a CAD procedure, was developed to map the material flow lines and measure the strain at discrete points. As a result, the performance of numerical models can be tested against the experimental values via the aforementioned approach. The difference between the measured strain values and those obtained from the integrated multiphysics model (developed for the FSW of aluminum 7050 with a tool RPM of 350, welding speed of 1.69 mm/sec, and tool pin diameter of 8 mm) was between 7.4 to 30.9 %. Some high differences between the numerical and experimental values at specific points of the workpiece may be due to the use of Al-30% SiC marker in the experiments, which has different deformation properties (e.g., different flow stress) compared to the main weld alloy, and/or due to errors in the assumed positions of points C, E, G, and H in the semi-experimental approach.

The numerical model predicted the maximum strain of 34.394. As it was shown in Table 6.1, Assidi et al. had similarly predicted strain values between 24-32 in the workpiece mid-plane in front of leading edge of the pin during the FSW of aluminum 6061 with the same welding speed and pin diameter, but the tool RPM of 650. Further experimental work is deemed necessary using different aluminum alloys, different marker materials, different process parameters, and/or marker detection procedures to verify the performance of different 2D or 3D multiphysics models against measured strain values. The accuracy of the method can also be increased using, e.g., 3D Computed Tomography to measure marker deformation more accurately. It is believed, although the current FSW numerical model may not fully comply with actual experimental conditions (due to three dimensional interaction between the marker and weld material), it can be used to estimate an expected range of strain, the location of maximum strain, etc, which can affect the ensuing mechanical properties and microstructure of the final weld, as well as, the optimization of experimental techniques.

Chapter 7: Microstructure Model

This chapter has been published in our **Article 4:** Mohamadreza Nourani, Abbas S. Milani, Spiro Yannacopoulos, Claire Yan, Predicting grain size distribution in friction stir welded 6061 aluminum, The 9th International Symposium on Friction Stir Welding 15-17 May 2012, Huntsville, USA

Overview: The base model developed and verified in Chapter 4 was to capture the effect of friction stir welding (FSW) process parameters on the local distribution, the maximum value and location of temperature, strain rate, strain, and flow stress around the pin during the process. In the model, a non-Newtonian flow mode of the CFD theory, general heat transfer mode of the heat transfer theory, and the plain stress mode of the structural mechanics theory were coupled in COMSOL. In this chapter, using this previously developed multiphysics model, the temperature distribution during FSW, the post-welding grain size distribution, and the local subgrain size distribution around the pin during FSW in the mid-plate thickness are predicted, hence arriving at an ‘integrated’ multiphysics FSW model.

7.1 Introduction

The grain size distribution of FSW of 6061 aluminum alloy affects its tensile strength [1]. Although numerous researches have been done to model the FSW, there are limited results to relate the process parameters to weld microstructure. This chapter is intended to use a previously developed multiphysics model (Chapter 4) and predict the local subgrain size distribution during welding and post-weld grain size distribution around the pin in the mid-plate thickness. In doing so, two empirical subgrain and grain size models are employed from the literature. Results will be compared to a set of reported experimental data on FSW of 6061 aluminum alloy.

7.2 Model description

We used the multiphysics model explained in Chapter 4 and a set of empirical models for microstructure prediction during and after FSW, as follows:

$$\text{Subgrain size during FSW [2]: } d^{-1} = 1.75 + 0.244 \times \log\left(\dot{\epsilon} \exp\left(\frac{156000}{RT}\right)\right) \quad (7-1)$$

$$\text{Grain size after FSW [3]: } \ln(D) = -5.8576e3 \times 1/T + 10.397 \quad (7-2)$$

where d is the subgrain diameter or Low Angle Grain Boundary (μm) and D is the grain diameter or High Angle Grain Boundary (μm). Equation (7-1) shows the subgrain diameter during FSW at high temperature [2] and Equation (7-2) shows the grain diameter after FSW and grain growth for aluminum 6063 (which is assumed to be close to that of aluminum 6061). The latter equation is derived based on a curve fitting of Figure 7.1 which shows the relation between the maximum temperature of the process thermal cycle and the generated grain size in the weld region [3].

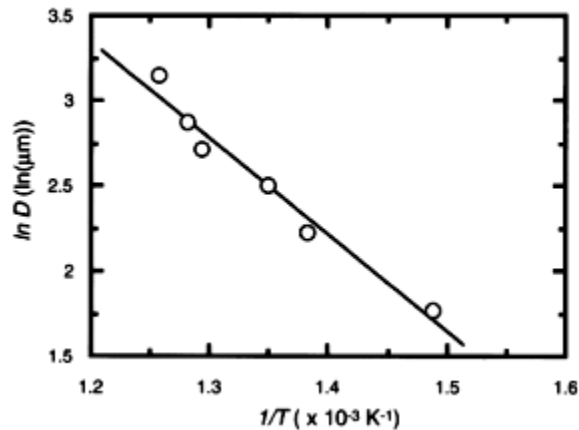


Figure 7.1- Relationship between $1/T$ and $\ln D$ in an Al 6063 weld [3]

In order to run the model and compare the results with some existing experiments on 6061 aluminum alloy, we employed the process parameters similar to those experienced by Woo *et al* [4-6]: a pin diameter of 6.35 mm, a rotational speed of 156 RPM, and the weld speed of 0.42 mm/s. In [4], the temperature distribution at the trailing edge of the weld centerline during FSW was first evaluated using neutron diffraction at the midplane of the plate, and then in [5] the average grain size after FSW as a function of distance from the weld centerline at the midplane was obtained using high-resolution micro-beam X-ray diffraction. Finally, in [6], the average subgrain size 8 mm behind the tool center at the midplane of 6061 aluminum alloy during FSW was determined using high-resolution X-ray diffraction measurements. The values of employed process parameters and material constants are summarized in Table 7.1.

Table 7.1- Process parameters and material properties used in the model

Weld speed- u_{weld} (mm/s)	Rotational speed ω (rev/s)	Pin radius- r_{pin} (mm)	Ambient pressure- P_o (KPa)	Ambient temperature T_o (°C)	R (J/mol.K)	Friction coefficient μ	δ
0.42 [4-6]	156 [4-6]	3.175 [4-6]	101	27	8.31451	0.4 [7]	0.65 [7]
α (1/MPa)	n	A (1/s)	Q (J/mol)	C_p (J/Kg K)	k (W/mK)	ρ (Kg/m ³)	Solid us (°C)
0.0165 [8]	5.33 [8]	$1.63e^{13}$ [8]	191000 [8]	789.9+0.4959T [9]	115.23+ 0.1594T [9]	2700 [10]	582 [10]

7.3 Results and discussion

7.3.1 Temperature distribution during FSW

The obtained temperature distribution via the multiphysics model is shown in Figure 7.2.

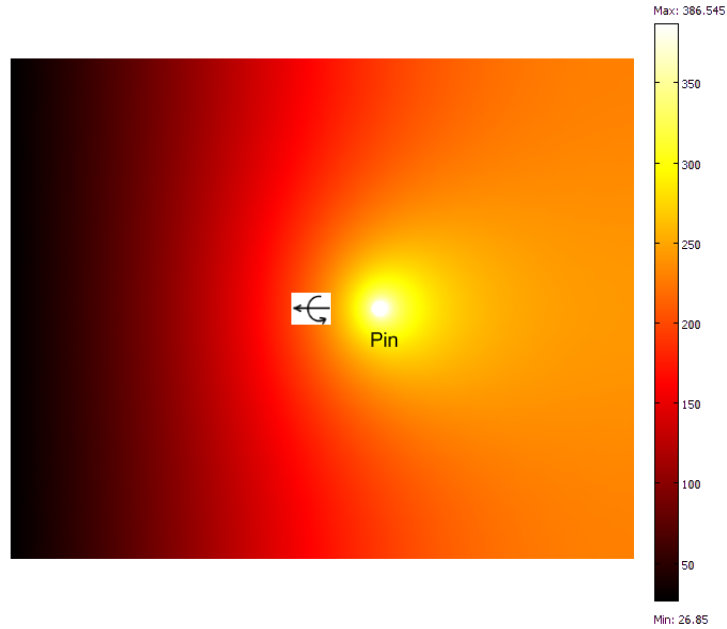


Figure 7.2- Temperature distribution ($^{\circ}\text{C}$) via the multiphysics model with process parameters used in [4]

The maximum temperature measured in [4] at midplane was $362\ (^{\circ}\text{C})$ with an accuracy of $\pm 15\ (^{\circ}\text{C})$. The maximum temperature predicted in our numerical model is $386\ (^{\circ}\text{C})$ which showed a good agreement with the measured data. In order to further examine the model prediction, we compared the modeled temperature distribution with measurements in [4] at the trailing edge of the weld centerline during FSW, as shown in Figure 7.3 which shows a good agreement.

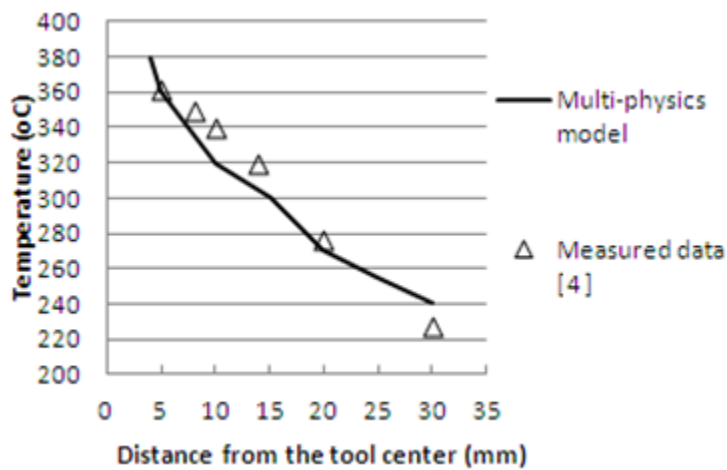


Figure 7.3- Comparison of the multiphysics model results with temperature measurements at trailing edge of the weld centerline [4]

7.3.2 Grain diameter distribution after FSW

The average grain diameter (μm) distribution after FSW as a function of distance from the weld centerline at the midplane is shown in Figure 7.4.

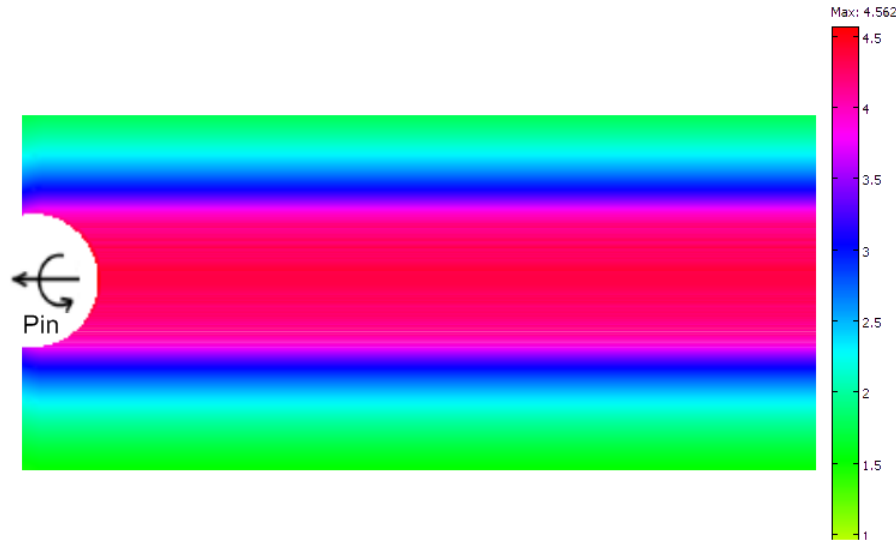


Figure 7.4- The predicted distribution of grain diameter (μm) after FSW

Note that in Figure 7.4 the grain size distribution is shown after dynamic recrystallization (DRX) and grain growth (based on Equation (7-2)). The average grain size predicted at nugget ($4.56\mu\text{m}$) is close to the average of $5\mu\text{m}$ which was measured in [5]. The model predicts a lower DRX grain size at the thermo-mechanically affected zone (TMAZ) compared to the nugget zone, which can be created by the lower temperature at TMAZ causing a lower static grain growth after FSW. It supports previous findings in [11] that the cell size (grain size) at nugget was reported to be larger than the cell size in TMAZ. When we studied the grain size distribution of our FSW experiments at the midplane we also found similar behavior in grain size distribution which is explained in more details in Section 9.3.5 of Chapter 9.

7.3.3 Subgrain diameter during FSW

As shown in Figure 7.5, the model predicted a subgrain size of about 135 to 145 nm at a region about 8 mm behind the tool center during FSW using Equation (7-1). The predicted range is

close to the average measured value of 160 nm at the same location in [6]. It has also been observed that after FSW the average subgrain size in the above position is ~180 nm [6].

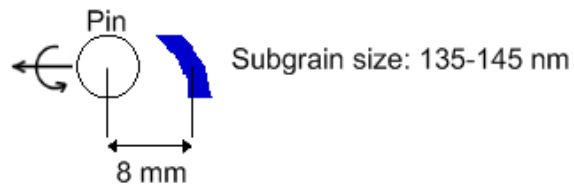


Figure 7.5- The subgrain diameter at the region 8 mm behind the tool center during FSW

7.4 Summary of findings

The developed integrated multiphysics model was applied to the FSW of aluminum 6061 using a set of process parameters and material properties similar to those employed in the process parameters similar to those experienced by Woo *et al* [4-6]: a pin diameter of 6.35 mm, a rotational speed of 156 RPM, and the weld speed of 0.42 mm/s. The model successfully predicted the temperature distribution at the trailing edge of the weld centerline during the process. The microstructure predictions were close to what was measured in [4] and it was found that:

- 1- The average grain size in the weld nugget is 4.56 μ m.
- 2- A smaller grain structure is present at TMAZ compared to the nugget zone.
- 3- The average subgrain size at a region about 8 mm behind the tool center during the process is 135-145 nm.

The model can be used in future studies to optimize the process parameters and arrive at desired mechanical properties based on FSW microstructure predictions.

Chapter 8: Residual Stress Model

Parts of this chapter has been published in **Article 5:** Mohamadreza Nourani, Abbas S. Milani, Spiro Yannacopoulos, Claire Yan, Predicting residual stresses in friction stir welding of aluminum alloy 6061 using an integrated multiphysics model, The 9th International Conference on Residual Stresses (ICRS 9), 7-9 Oct 2012, Garmisch-Partenkirchen ,Germany.

Overview: In this chapter first we use the multiphysics model of in Chapter 4 to find temperature history of FSW. Next, the predicted thermal history during the process by the model is used as input for an elasto-visco-plastic analysis to estimate the local residual stresses distribution due to variable thermal and elastic strains in the sample resulted from temperature difference during cooling, temperature dependent thermal expansion coefficient and temperature dependent elastic modulus after cooling to room temperature and unclamping of the work piece. Finally, the predicted longitudinal and transverse residual stresses are verified by comparing to experimental data.

8.1 Introduction

Regarding residual stress analysis of FSW, earlier experimental investigations include the work of Woo et al. 2006 [1], who used the well-established technique of spatially resolved neutron strain scanning to measure residual stresses in the retreating side of plates at different depths. In their work, 306 x 306 x 6.5 mm³ commercial 6061-T6 Aluminum alloy plates were welded during the experiment. Forty points were measured 1.26 mm above the middle of the plate, along the middle of the plate thickness (z), and 1.26 mm below the middle of the plate. These points were called ‘face’, ‘center’, and ‘root’, respectively. The processing parameters included a 12.4 MPa compressive pressure; 1250 rpm rotating speed; and 4.7 mm/s traveling speed. A tool with 6.35 mm pin diameter, 19.05 mm shoulder diameter and with 6.23 mm pin depth was used for the FSW experiments.

Numerical modeling of FSW has its own difficulties because of the presence of high amount of deformations during the process. A considerable part of the strain and deformation is relaxed by dynamic recrystallization in the nugget because of the existence of high temperature and strain

rate at the same time which has not been considered in the existing strain models. By using Lagrangian frame during modeling, high amount of deformations cause severe distortion of meshes and make it necessary to use continuous adaptive remeshing, which in turn can cause numerical divergences/errors [2]. Consequently, for models having severe deformation an Arbitrary Lagrangian Eulerian (ALE) method is typically recommended to minimize the errors caused by distortion of meshes. The ALE method let us define the contact of the part and the tool a Lagrangian formulation while having an Eulerian formulation for the boundaries. Because of the difficulty of working with mesh distortion, researchers using a Lagrangian method do not consider the material flow and consider the distortion and residual stress in FSW resulted from thermal expansion. The temperature distribution is usually modeled using a thermal analysis with a surface heat flux [3] or a CFD model, which considers the effect of material movement on temperature gradient [4]. Hence, an Eulerian method is easier to use because of the high material deformation in FSW where the material is not stuck to the mesh but flows through it. In Eulerian method, there is no problem with mesh distortion as in a Lagrangian method and it has been used earlier for thermomechanical simulations in drawing and rolling processes [5].

In this chapter, the two-dimensional Eulerian multiphysics model of Chapter 4 has been employed and extended (by means of integrating to an elasto-visco-plastic post analysis) to predict residual stresses during the FSW of 6061-T6 Al alloy as measured by Woo et al. 2006 [6].

8.2 Model description

Friction stir welding is a solid state welding process. This has been verified by earlier microstructural studies after the process where no evidence of dendrite microstructure was seen indicating that no melting takes place during the process [7]. Also there is no sharp decrease of transverse load during the process and, hence, the maximum temperature recorded is normally below the solidus temperature of the material being welded. If we introduce a high volume of partial melting during FSW intentionally, it would generate a weld with low mechanical properties. In order to implement the maximum temperature of solidus in the model, we consider that at temperature equal or higher than solidus the flow stress is equal to zero (Equation 4-10 in

Chapter 4), which in turn would cause no volumetric heat of deformation and surface frictional heat flux at the material in contact with the pin according to Equation 4-8 in Chapter 4. In practice, if a localized melting occurs, the heat generation stops and the extra heat is absorbed by the bulk material and the temperature decreases below the solidus again. This would result in unwanted weld defects, however minor. For more details of the multiphysics model please refer to Chapter 4. The employed process parameters and material properties are summarized in Table 8.1.

Table 8.1- Process parameters and material properties used in the base multiphysics model

u_{weld} (mm/s)	ω (RPM)	r_{pin} (mm)	P_o (KPa)	T_o ($^{\circ}\text{C}$)	R (J/mol.K)	μ	δ
4.7 [1]	1250 [1]	3.175 [1]	101 [1]	27 [1]	8.31451	0.4 [8]	0.65[8]
α (1/MPa)	n	A (1/s)	Q (J/mol)	C_p (J/Kg K)	k (W/mK)	ν	Solidus ($^{\circ}\text{C}$)
0.0165 [9]	5.33 [9]	$1.63e^{13}$ [9]	191000 [9]	789.9+0.4959 T [10]	115.23+0.159 4T [10]	0.35 [11]	582 [10]

After a coupled thermo-visco-plastic analysis was performed via the multiphysics model as explained in Chapter 4 to provide the material thermal history during the process, it was used as an input for a subsequent elasto-visco-plastic analysis, with cooling and keeping clamp constraints, followed by final cooling to ambient temperature and unclamping the work-piece. The related governing equations are comprised of:

$$\text{Force equilibrium equations (i, j = 1, 2):} \quad \sigma_{ij,j} + P_j = 0 \quad (8-1)$$

$$\text{Linear decomposition of strain tensor:} \quad \varepsilon_{ij}^{\text{total}} = \varepsilon_{ij}^{\text{elastic}} + \varepsilon_{ij}^{\text{plastic}} + \delta_{ij}\varepsilon^{\text{thermal}} \quad (8-2)$$

$$\text{Hooke's constitutive law:} \quad \sigma_{ij} = C_{ijkl}^{\text{elastic}} \varepsilon_{kl}^{\text{elastic}} = C_{ijkl}^{\text{elastic}} (\varepsilon_{ij}^{\text{total}} - \varepsilon_{kl}^{\text{plastic}} - \delta_{kl}\varepsilon^{\text{thermal}}) \quad (8-3)$$

$$C_{ijkl}^{\text{el}} = \frac{E}{1+\nu} \left[\frac{1}{2} (\delta_{ik}\delta_{jl} + \delta_{il}\delta_{jk}) + \frac{\nu}{1-2\nu} \delta_{ij}\delta_{kl} \right]$$

$$\text{Small strain theory: } \varepsilon_{ij}^{total} = \frac{1}{2}(u_{i,j} + u_{j,i}) \quad (8-4)$$

$$\text{Thermal strain: } \varepsilon^{thermal}(T_1 \rightarrow T_2) = \int_{T_1}^{T_2} \alpha' dT \quad (8-5)$$

where P_j is the body force of any point in the plate, σ_{ij} is the stress tensor, ε_{ij} is the strain tensor, δ_{ij} is Kronecker delta, C_{ijkl} is the 4th order elasticity tensor, E is the Young's modulus, ν is the Poissons's ratio, $u_{i,j}$ is displacement vector and α' is the thermal expansion coefficient. The plastic strain calculation was according to the J2 (second deviatoric stress invariant) flow assumption using a temperature and strain rate dependent Von-Mises yield criteria [12]. The elastic part of the elasto-visco-plastic material behavior of Aluminum 6061 was based on the temperature-dependent Young's modulus as shown in Table 8.2, and its visco-plastic proof stress was resulted from Equation (4-10) in Chapter 4.

Table 8.2- Temperature-dependent properties of Aluminum 6061 alloy [11]

Temperature ($^{\circ}\text{C}$)	25	37.8	93.3	148.9	204.4	260	315.6	371.1	426.7
α' -Thermal expansion coefficient (1/K)	22	23.45	24.61	25.67	26.6	27.56	28.53	29.57	30.71
ρ -Density (Kg/m^3)	2700	2685	2685	2667	2657	2657	2630	2620	2602
E-Young's modulus (GPa)	68.9	68.54	66.19	63.09	59.16	53.99	47.48	40.34	31.72

8.3 Results and discussion

First let us use the base multiphysics model to compare the results of the temperature distribution at the trailing edge of the weld centerline in midplate (back of the tool) with the experimental measurements by Woo et al 2007 [13]. As shown in Figure 8.1, there is a good agreement between the measured temperature and the model prediction.

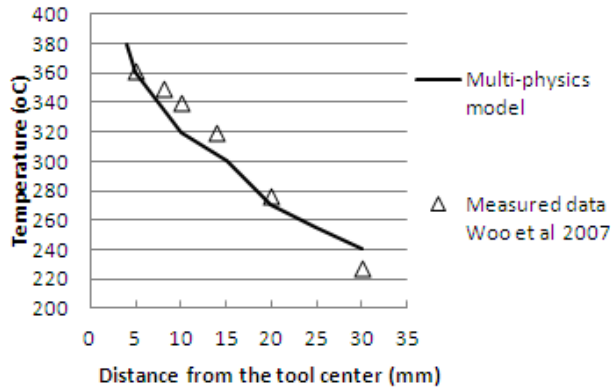


Figure 8.1- Comparison of the numerical model results with temperature measurements at trailing edge of the weld centerline in midplate.

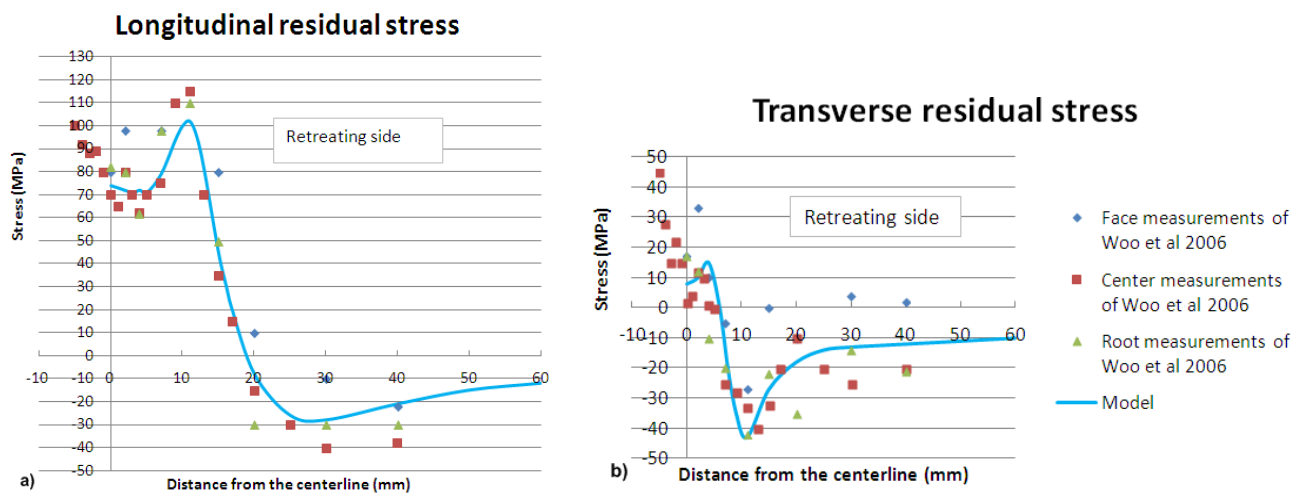


Figure 8.2- (a) longitudinal (x -component) and (b) transverse (y -component) residual stress distribution in the FSW process; model values are compared to measurements.

Next, in Figures 8.2 (a) and (b), respectively, the predicted longitudinal and transverse residual stresses of the integrated multiphysics model are shown along with the corresponding values experimentally obtained by Woo et al. 2006 [1]. It can be observed that the tensile longitudinal

stress profile changes into compressive stress beyond the HAZ and TMAZ boundary and the tensile transverse stress profile becomes compressive beyond the nugget zone (recall also Figures 2.1 in Chapter 2). The yield stress of the alloy in room temperature is about 276 MPa [14], and from Figure 8.2 (a) it is seen that the maximum value of the longitudinal residual stress during the studied FSW process is less than half of this value.

In order to explain a reason for the residual stress changes with location it is important to know the precipitation sequence of the alloy which affects the hardness. The precipitation sequence of these heat treatable aluminum alloys is as follows: solid solution \rightarrow GP \rightarrow β'' \rightarrow β' or Q phase \rightarrow β -Mg₂Si or Q phase. For the T6 temper aluminum 6061 (solution heat treated and then artificially aged), the weakest zone after FSW is generated by the formation of the coarse Q phase and its precipitation on dispersoids in the boundary of HAZ and TMAZ [15], and as shown in Figure 8.2 (a) the longitudinal residual stress is switched from tension to compression in this area. The weld nugget which forms a solid solution during FSW, is softer than the base metal because of the small β'' and Q hardening precipitates [15] and generates a softening-induced depression in the residual stress curve in the center of the weld as seen in Figure 8.2.

8.4 Summary of findings

The enhanced integrated numerical modeling of friction stir welding of Aluminum 6061 based on a prior computational model presented in Chapter 4 was studied in Chapter 8. In particular, the aim in this chapter was to predict the material flow and the temperature history during the process and subsequently the residual stress field after performing FSW, cooling to room temperature and unclamping the workpiece. The simulated temperature and stress profiles demonstrated a good match with those measured in earlier experiments from the literature. The numerical simulation for residual stress prediction consisted of the following steps:

- First, the multiphysics model based on a thermo-visco-plastic with non Newtonian incompressible constitutive model is used to predict the temperature gradient and the material movement around the pin.

- The second step is to use the thermal history from the first step as an input for a subsequent elasto-visco-plastic analysis with cooling history and keeping clamp force, followed by cooling to ambient temperature and unclamping.

Relying on the results of the presented case study in this chapter, some conclusions may be drawn as follows:

- The tensile longitudinal stress profile changes into compression beyond the HAZ and TMAZ boundary, whereas the tensile transverse stress profile becomes compressive beyond the nugget zone.
- The maximum value of the longitudinal stress peak is less than half of the yield stress at room temperature.
- The residual stress variation with location (distance from the weld centerline) can be related to the precipitation sequence of the alloy.

Chapter 9: Experimental Study

Parts of this chapter have been submitted for publication as **Article 9:** Mohamadreza Nourani, Abbas S Milani, Spiro Yannacopoulos, Processing-microstructure-property relationship and experimental optimization of friction stir welding of aluminum 6061 (submitted), 2013.

Overview: In this chapter, after addressing earlier experimental studies on FSW of different alloys, we name the test equipment and procedures used to optimize the FSW process parameters and produce an aluminum 6061 weld with an optimum ultimate tensile strength (UTS) given a FSW tool type. we assembled a complete FSW experimental set-up at our Manufacturing Shop at School of Engineering, UBC Okanagan, to be able to measure temperature at multiple points of welding plates as well as the FSW tool axial force, transverse force (weld force), torque and temperature under different combination of process parameters. After performing a set of FSW tests based on a full factorial design of experiment (DOE), we used X-ray and ultrasonic tests to study if there is any failure in the welded samples. Two tensile samples were then cut from each weld coupon underwent tensile testing. Using statistical analysis tools, we studied the main effects and contribution percentage of the process parameters on the measured UTS from tensile tests, while proposing a new methodology to cope with the effect of ‘variable’ axial force as it was an uncontrollable factor during FSW tests. Samples with the highest and lowest UTS values were then selected and examined in more details by comparing their fracture surfaces using SEM (Scanning Electron Microscope) as well as their grain size distributions using EBSD (Electro Back Scattered Diffraction) and micro hardness (Vickers method) at their mid-thickness on the advancing side of FSW. Finally, based on the experimental results of this chapter and the modeling results in the previous chapters, we explained why such typical mechanical properties (UTS and micro hardness) are found to notably vary between the best and worst samples, while correlating them to the material microstructure and process parameters.

9.1 Introduction

There have been numerous experimental studies on friction stir welding of similar and dissimilar alloys. Namely, the FSW of similar alloys have been studied on aluminum alloys [1], aluminum matrix composites [2], magnesium [3], copper [4], ferrous [5], nickel [6] and titanium [7] alloys. On dissimilar alloys, the earlier FSW studies include different aluminum-aluminum [8], aluminum-steel [9], aluminum-lithium [10], aluminum-magnesium [11], titanium-stainless steel [12], aluminum-stainless steel [13], aluminum-copper [14], aluminum-titanium [15], and different steel-steel [16] alloys. Most researchers in the category of experimental studies have investigated the weld hardness, mechanical properties such as ultimate tensile strength, microstructure, fatigue properties and residual stresses [17]. Some have also studied the texture [18] or corrosion [19] of the weld.

9.2 Methods

9.2.1 FSW test equipment

We used the LowStirTM device for FSW tests with a CNC milling machine as shown in Figure 9.1. The LowStirTM device has the following specifications:

- Axial force (F_z) up to 50 kN
- Transverse force or weld force (F_{xy}) up to 25 kN
- Torque (M_z) up to 100 Nm
- Rotational speed up to 3000 rpm
- Weld speed is limited by the feed rate of our CNC milling machine which is from 0.5 to 20 mm/sec.

Among provided tool types by the manufacturer (MX-TriflatTM and MX-TrifluteTM), the selected FSW tool consisted of the Mx-TrifluteTM pin and the single spiral scrolled shoulder with dimensions shown in Figure 9.2. For welding, we used 155 x 65 x 6.5 mm³ aluminum 6061-T6 plates with their weld lines parallel to the rolling direction.



Figure 9.1- LowStir™ device (a), FSW test fixture (b) with two embedded thermocouples (c) and (d)

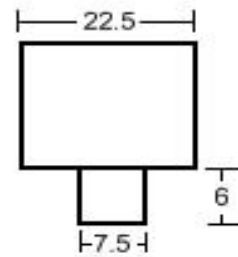


Figure 9.2- Selected FSW tool pin and shoulder (dimensions in mm) made from tool steel

9.2.2 Design of experiments

We chose different process parameters (RPM and weld speed) for different FSW samples according to Table 9.1, according to limitations of the supplied torque and speed of the existing CNC milling machine. We originally attempted to keep the axial force to be constant in different samples during FSW tests by choosing a fixed penetration of 0.1 mm of the shoulder inside the plates. However, it was hard to maintain a fully constant axial force between different welding tests with the open-loop axial force control test set up. Hence, the variation of normal force had to be dealt with in the subsequent statistical analysis.

Table 9.1- Friction stir welding process parameters used for different samples; Sample numbers are specified as 1n, 2n ,..., 9n and B2

Weld Speed	Tool Rotational Speed		
	1000 RPM	1400 RPM	1800 RPM
45 (mm/min)	1n	2n	3n
60 (mm/min)	4n	5n	6n
75 (mm/min)	7n	8n	9n
As Received (i.e., parent material)	B2		

For all the tests the tool plunge rate was 15 mm/min, tool dwell time was 10 seconds, the weld length was 125 mm that started and ended 15 mm far from the edges of the plates, and the tool exert rate was 15 mm/min.

For tensile testing, we water-jet cut the samples perpendicular to the weld line according to subsize specimen dimension of ASTM E8-M standard as shown in Figure 9.3. For each friction stir welding coupon (i.e., under a specific combination of process parameters) we machined two tensile samples for repeatability purposes.

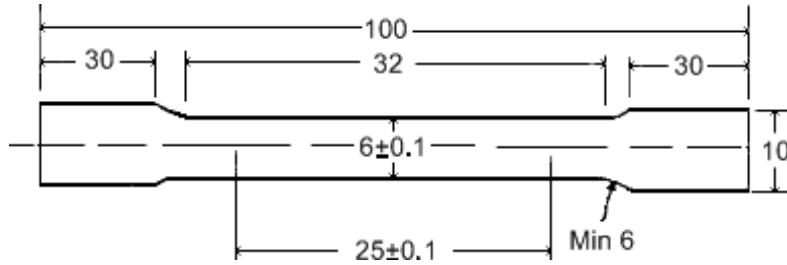


Figure 9.3- Tensile test sample perpendicular to the weld line in middle (dimensions in mm)

9.2.3 Temperature and force measurements

During FSW experiments, the temperatures of two points at the back of the plates were recorded as shown in Figure 4.6 using K type thermocouples and a Fourier DBSA720 data acquisition system. Also the tool axial force, transverse force, torque, and temperature were recorded during the tests using the wireless data transferring capability of the LowStir™ device.

9.2.4 X-ray and ultrasonic of FSW welds

All the welded plates were examined using X-ray or ultrasonic inspections by a certified inspector at Kelowna Flightcraft Company, BC. Subsequently, the tensile specimens were cut from regions where there were no failure indications in the weld. For ultrasonic inspection, ASTM E164-08 standard was used.

9.2.5 Tensile tests

We used Instron 3385H tensile test machine with a maximum load capacity of 250 kN at a speed of 2.5 mm/min. After tensile tests in all welded samples, we chose the samples with the highest and lowest UTS values for further examinations as follows.

9.2.6 Scanning electron microscope (SEM) of fracture surfaces

We used Tescan Mira3 XMU Field Emission Scanning Electron Microscope in order to study the morphology/fracture surfaces of selected tensile samples with the highest and lowest UTS values.

9.2.7 Microstructure study with electron back scattered diffraction (EBSD)

We used Oxford AZtecHKL EBSD system in order to study the grain size distribution on mid plane of the advancing side of the samples with the highest and the lowest UTS values. For preparation of EBSD samples, we cut the weld cross section from the weld line and mounted the advancing sides of them. Subsequently, we used a StruersTM polishing and electro-polishing machines to polish the samples. For the latter, first we used a 320 μm sand paper for 60 seconds and then a polishing mat with 100 μm Al_2O_3 suspension for 20 seconds and 10 μm diamond paste with sand paper for 30 seconds. In electro-polishing, we used A_2 solution in the manual mode with a voltage of 12 V for 15 seconds. The A_2 solution composition was as follows:

- Distilled Water (90 ml)
- Ethanol (Ethyl Alcohol) (730 ml)
- Ethylene glycol monobutyl ether (100 ml)
- Perchloric Acid (78 ml)

The perchloric acid had to be added to the mixture of ethanol, ethylene glycol monobutyl ether, and water immediately before use.

The scanned region at each time frame had a 1350 X 400 μm^2 area. In each subsequent frame, we moved the beam 1250 μm toward the next point in order to have a 100 μm overlap between the images, which we later merged/stitched to form a continuous image of the grain size distribution on the mid plates of two samples with the highest and the lowest UTS. we also counted the number of grains at each EBSD frame on 3 points (two sides and the middle point) within a 77 μm horizontal line.

9.2.8 Micro hardness study

We used Ualitest QV-1000 micro hardness test equipment with 500 grams force and 15 seconds dwell time in order to measure the Vickers micro hardness in 0.5 mm intervals on the mid plane of the advancing side of the weld cross section of two samples with the highest and the lowest UTS.

9.3 Results and discussion

9.3.1 Temperature and force measurements

In this section we discuss the results of temperature measurements for validation of the developed integrated multiphysics model as was also briefly referred to in Figure 4.9 of Chapter 4. Here we present the entire obtained temperature test data at the middle of the back of plates on the weld line of ‘all’ samples, along with the corresponding tool axial force, transverse force, and torque and measurements under different processing conditions.

Figures 9.4 to 9.6 compare the temperature measurements at point 1 in the back of each plate (as marked in Figure 4.6) under different weld speed and tool RPMs of 1000, 1400 and 1800. As seen from these figures, the maximum temperature of point 1 in the plates is reduced by increasing the weld (transverse) speed given a tool RPM.

Also the maximum temperature of point 1 in different samples is evaluated in Table 9.2, which shows that this FSW output variable is increased by increasing the tool RPM given a weld speed. The highest maximum temperature of 519 °C has occurred in the sample 3n (hot weld) and the lowest maximum temperature of 407 °C is in sample 7n (cold weld), which are highlighted in red and green colors, respectively. The difference between these two extreme temperatures is 112 °C.

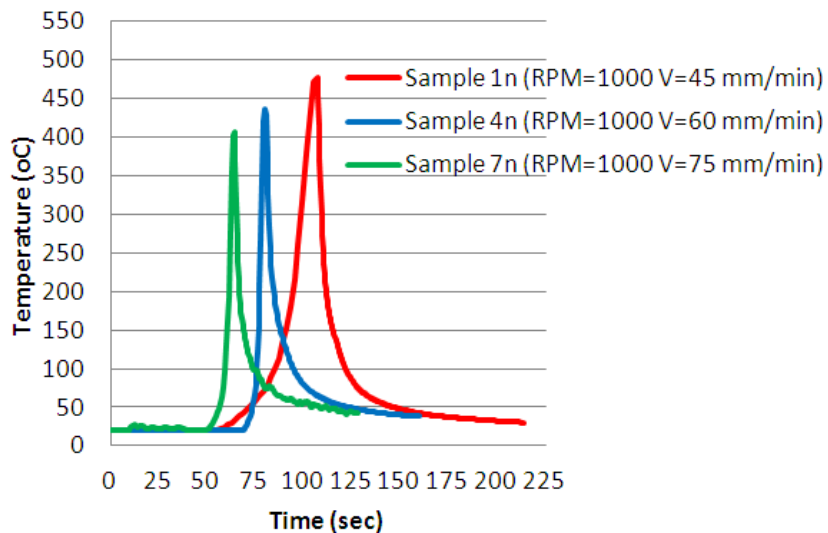


Figure 9.4- Temperature measurements of samples at middle of the weld line on back plates at different weld speeds and a constant RPM=1000

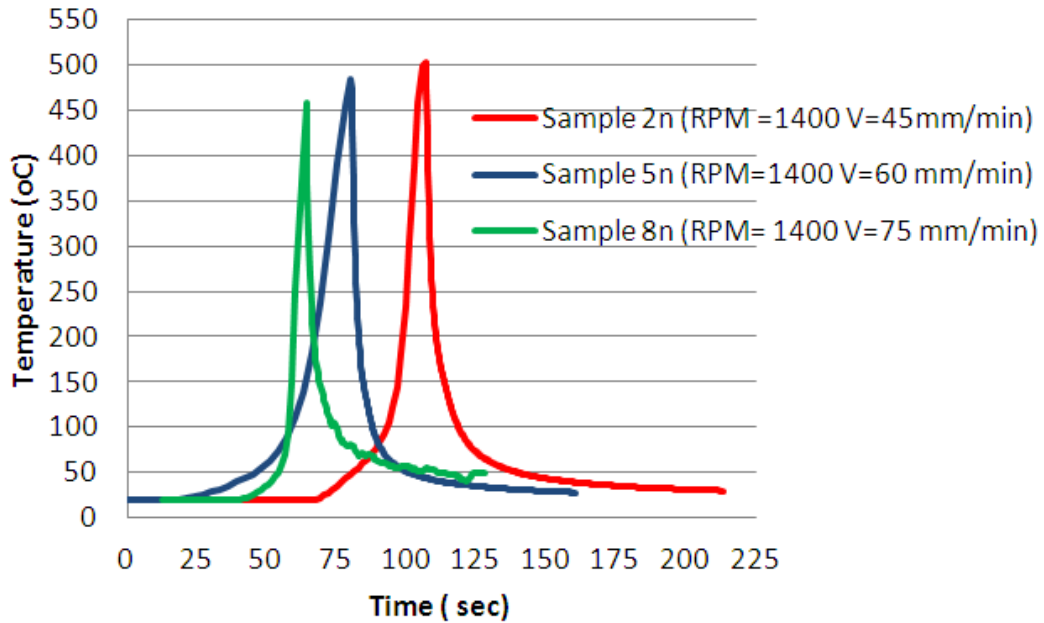


Figure 9.5- Temperature measurements of samples at middle of the weld line on back plates at different weld speeds and a constant RPM=1400

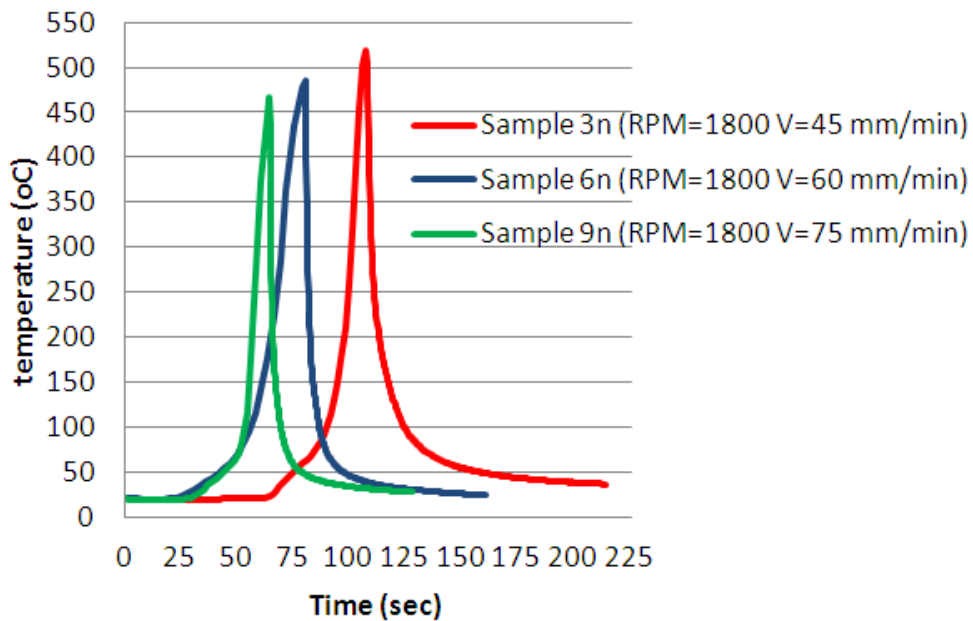


Figure 9.6- Temperature measurements of samples at middle of the weld line on back plates at different weld speeds and a constant RPM=1800

Table 9.2- FSW maximum temperature at middle of the weld line on back plates of different tested samples

Maximum temperature (°C)	1000 RPM	1400 RPM	1800 RPM
45 (mm/min)	476	502	519
60 (mm/min)	438	484	485
75 (mm/min)	407	441	467

In Figure 9.7, we also measured the tool temperature in different samples at far end of the tool shaft from the weld zone (somewhere near point (a) in Figure 9.1). Results reconfirm that samples 3n and 7n correspond to the hot weld and cold weld states, respectively.

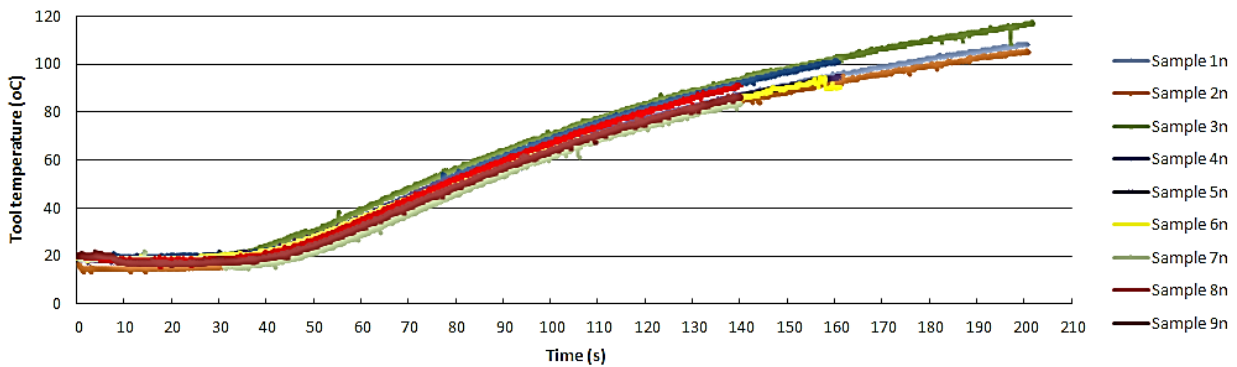


Figure 9.7- Tool temperature in different samples during FSW tests (for the process parameters in each sample refer to Table 9.1)

Figure 9.8 shows the tool axial force of different samples. We notice that the highest axial force during steady state phase of the curves (point D) belongs to sample 7n (cold weld or 1000 RPM, 75 mm/min) and the lowest axial force has occurred in sample 3n (hot weld or 1800 RPM, 45 mm/min). There are 5 critical points in the axial force curve during FSW as noted in Figure 9.8 as A, B, C, D and E. Point (A) shows the maximum axial force when the tool’s pin starts the plunge inside the plates. Point (B) is the point when the tool’s shoulder reaches the fixed penetration of 0.1 mm inside the plates during the plunge phase. Point (C) is the end of dwell phase when the plates are hot enough to start the FSW after 10 seconds of dwell time. Point (D) is when the FSW reaches the steady state conditions and point (E) is when the tool starts exiting

the plates. A-B is called plunge phase, B-C is called dwell phase, C-D is called welding phase and D-E is called exist phase. As seen in Figure 9.8, it is hard to keep a constant axial force in test samples using an open loop force control system of FSW set-up (despite a fixed penetration of 0.1 mm). The source of this noise in the axial forces can be one or all of the following items:

- 1- the tool wearing during the process which changes the reference point during tool set up,
- 2- operator's error,
- 3- plates thickness tolerances,
- 4- vibration effects, and
- 5- formation of different excess material from weld zone (flash) during FSW.

One may use a closed-loop control system which changes the tool penetration inside the plates in order to keep a constant axial force during FSW tests. The average axial forces in steady state phase of the response curves are reported in Table 9.3. The highest average axial force is generated in sample 5n and the lowest value is seen in sample 2n (1400 RPM, 45 mm/min), which are highlighted in green and red colors, respectively.

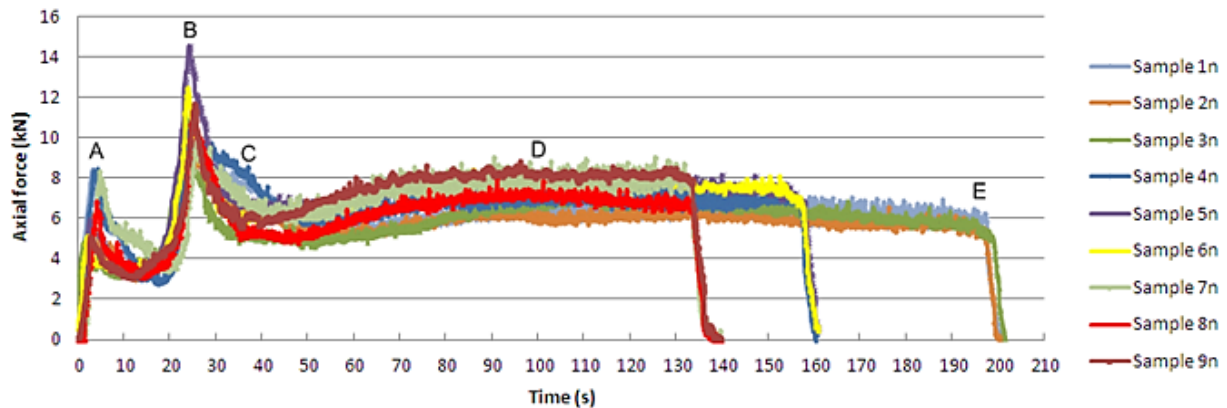


Figure 9.8- Tool axial force on different samples during FSW tests with critical points of response curves marked as A, B, C, D, and E (for the process parameters in each sample refer to Table 9.1)

Table 9.3- Average axial force of the tool in the steady state response phase of the FSW samples

Average axial force (kN)	1000 RPM	1400 RPM	1800 RPM
45 (mm/min)	6.33	6.08	6.19
60 (mm/min)	7.10	7.70	7.14
75 (mm/min)	7.14	6.64	7.52

Figure 9.9 shows the tool torque in different experiments during FSW with the same critical points of A, B, C, D and E as in Figure 9.8. The highest torque is seen in sample 7n (cold weld or 1000 RPM, 75 mm/min) and also sometimes in sample 4n (second cold weld or 1000 RPM, 60 mm/min). The lowest torque belongs to sample 3n (hot weld or 1800 RPM, 45 mm/min). Also when the RPM is increased under a constant weld speed, the torque is decreased which is because of the increase in heat input during FSW.

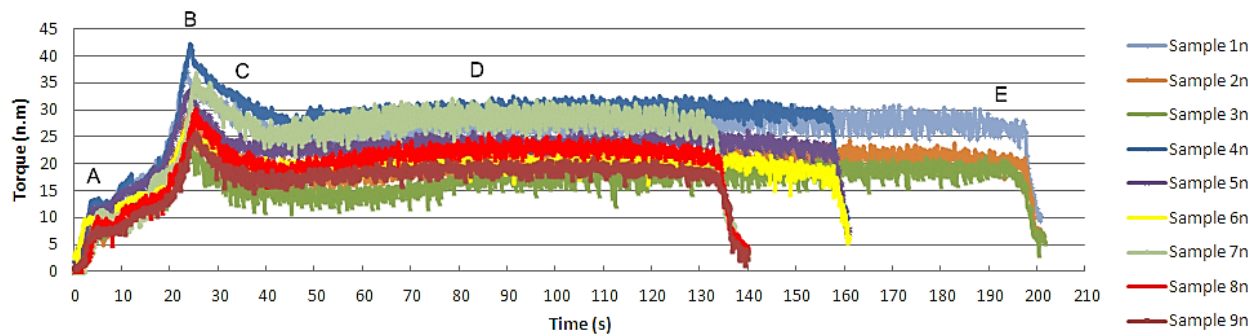


Figure 9.9- Tool torque on different samples during FSW tests with critical points of A, B, C, D, and E (for the process parameters in each sample refer to Table 9.1)

Figure 9.10 shows the measured transverse force of different samples during FSW tests. The minimum transverse force is seen in sample 4n and the maximum transverse force belongs to samples 6n and 9n with the highest RPM, and sometimes to samples 7n (cold weld) and 1n. The highest transverse force in samples 6n (1800 RPM, 60 mm/min) and 9n (1800 RPM, 75 mm/min) or 7n can be a result of higher excess material from the weld (flash) or higher material flow stress during the process. The distance between two consecutive transverse force peaks in Figure 9.10 is equal to the time of one advance per rotation.

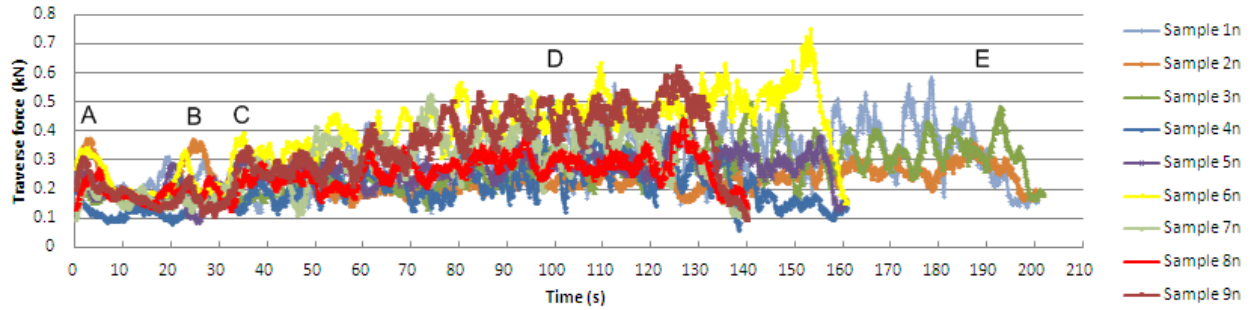


Figure 9.10- Tool transverse force on different samples during FSW tests with critical points of A, b, C, D, and E (for the process parameters in each sample refer to Table 9.1)

9.3.2 X-ray and ultrasonic

After completing the FSW experiments, we performed X-ray and ultrasonic tests on the welded samples to see if there is any evidence of failure on the weld regions. Figure 9.11 shows the samples after the FSW experiments. The samples 1n (1000 RPM, 45 mm/min), 6n (1800 RPM, 60 mm/min) and 9n (1800 RPM, 75 mm/min) had some areas with lack of diffusion. Sample 9n has had the highest lack of diffusion. If we examine Figure 9.11 it is clear that the samples 3n (1800 RPM, 45 mm/min), 6n and 9n with the highest tool RPM values and sample 5n with the highest average axial force have had high volume of excess material from the weld zone (flash). It is interesting that in samples 1n, 6n and 9n which showed the failure in X-ray and ultrasonic tests we saw a relatively higher transverse force during FSW (Figure 9.10) which can be a result of higher excess material from the weld zone (flash).

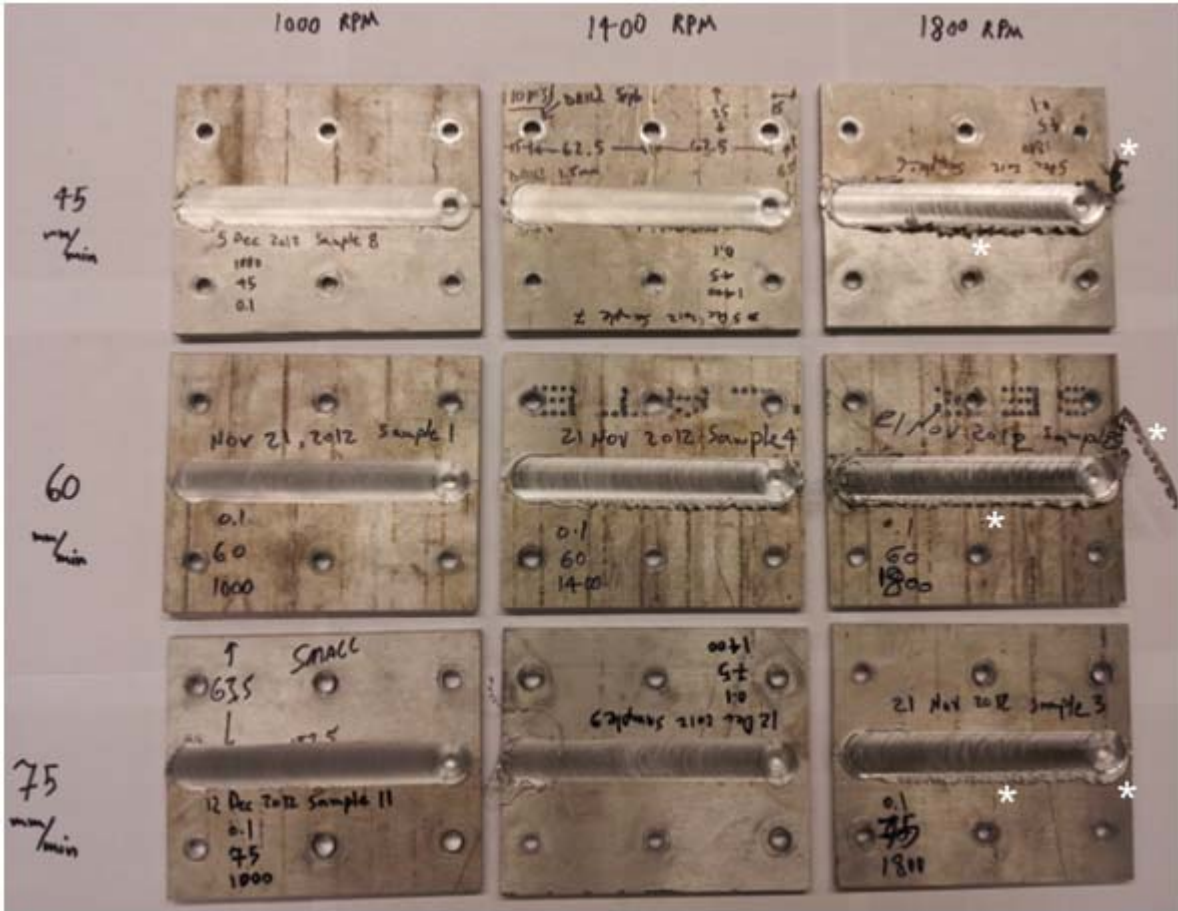


Figure 9.11- FSW samples with different process parameters of weld speed and tool RPM (the excess material is shown with white stars)

9.3.3 Tensile tests

After cutting two tensile samples from each FSW plate (Figure 9.12) as well as the as received plate, we did tensile tests and compared the ultimate tensile strength (UTS) of different samples. The originally received 6061-T6 plate showed a UTS of 348.2 MPa. The highest UTS in the FSW samples had a UTS equal to 0.76 of the as received plate. The lower UTS of welded samples compared to the parent metal is a result of overaging in heat treatable aluminum alloys such as Al 6061 (due to the heat during welding and its effect on precipitates' size and distribution as explained in Section 2.1). The values of UTS of different samples are summarized in Table 9.4. The minimum UTS belongs to sample 3n (hot weld or 1800 RPM, 45 mm/min) and

the maximum UTS is seen in both samples 5n (1400 RPM, 60 mm/min with the highest average axial force as seen in Table 9.3) and 4n (1000 RPM, 60 mm/min the second cold weld, see Table 9.2) with a small difference in the UTS of the latter two samples. Bases on the theory we explained in Chapter 3, one should expect to see the lowest UTS in the hot weld (sample 3n) which is conformed with the results of Table 9.4, and also the highest UTS in the cold weld (sample 7n or 1000 RPM, 75 mm/min) which is not the case here; however, sample 4n was the second cold weld sample and is among those with the highest UTS. It is resulted from the low mechanical bounding in the very cold weld of 7n as shown in Figure 9.16.

Table 9.4- Ultimate tensile strength of different FSW samples (Minimum, Maximum and Average)

UTS (MPa)	1000 RPM			1400 RPM			1800 RPM		
	Min	Ave	Max	Min	Ave	Max	Min	Ave	Max
45 (mm/min)	180.6	193.1	205.7	187.1	197.6	208.2	158.2	164.3	170.5
60 (mm/min)	219.7	220.6	221.6	224.1	224.4	224.7	166.6	181.5	196.4
75 (mm/min)	205.9	209.4	212.9	173.0	175.3	177.6	200.2	202.5	204.9

9.3.3.1 Factor effect analysis

In order to statistically estimate the effects of controlled process parameters (namely RPM and weld speed) on the UTS of the FSW samples, first it is necessary to eliminate the effect of variable (uncontrolled) axial forces during FSW tests. To this end, we used a regression method and tried different second order polynomials with up to eight different constants (given that we had nine data points/FSW configurations) and found the best polynomial fit to predict maximum UTS values in Tables 9.3 and 9.4. In doing so, we tested 27 different forms (see Appendix A) of the general second order polynomial shown in Equation (9-1).

A general form of a 2nd order polynomial with three variables:

$$Y = a+bX_1+cX_2+dX_3+eX_1^2+fX_2^2+gX_3^2+hX_1X_2+iX_1X_3+jX_2X_3 \quad (9-1)$$

X_1 is the weld speed in mm/min, X_2 is the tool RPM and X_3 is the average axial force in Newton (N) from Table 9.3.

We used the max UTS values (instead of min values in Table 9.4) based on the best performance of the weld obtained under each process condition (i.e., a maxi-max design strategy). There may have also been outliers in the min UTS values because of inclusions or failure in the received plates, hence causing a wide difference between the two repeats of the UTS values ranging from 0.1 to 30 MPa as seen in Table 9.4. The highest coefficient of determination (R^2) of 0.955 was achieved when Equation (9-2) was used as the regression polynomial for UTS values, given nine data points:

Best fitting polynomial with the given nice data points:

$$Y = a+bX_1+cX_2+dX_3+bX_1^2+cX_2^2+dX_3^2+eX_1X_2+fX_1X_3+gX_2X_3 \quad (9-2)$$

The values of fitted model constants are included in Table 9.5.

Table 9.5- The optimum regression constants obtained for model in Equation (9-2)

a	b	c	d	e	f	g
213.78834	-0.15400	-0.000095	-0.000016	-0.001180	0.00298	0.000043

Next, using the above regression model we re-calculated/predicted the value of UTS at each given combination of RPM and weld speed, considering the corresponding constant (average) axial force. Results of the predictions are shown in Table 9.6, where the recalculated UTS values are called ‘adjusted’ UTS hereafter. It is interesting that both samples 5n (1400 RPM, 60 mm/min) and 4n (1000 RPM, 60 mm/min) now demonstrate literally the same highest UTS values (marked in green). This is again in accordance with the theory we proposed in Chapter 3 about the cold weld condition and its positive effects on mechanical properties of FSW using a thermal model where the material flow and mechanical bonding were not included.

reduce the UTS of the FSW samples. The reason of low UTS in FSW samples with a cold process condition is high viscosity and low mechanical bonding between material layers which rotate with tool and are deposited on the trailing edge. Generally speaking, the trends of main process factors in Figures 9.13 (a), (b) and (c) show that there are optimum values to set the FSW process in order to get the highest UTS in weld samples among the tested points through the DOE analysis. In the current experimental space, the global maximum UTS is reached when RPM=1400, Weld speed=60 mm/min (1 mm/sec) and Axial force=7.14 kN, which is the closest condition to that of samples 5n.

Table 9.6- Adjusted Max UTS values using the regression model

Adjusted Max UTS (MPa)	1000 RPM	1400 RPM	1800 RPM
45 (mm/min)	181.5	189.1	166.0
60 (mm/min)	226.4	226.9	196.8
75 (mm/min)	202.1	195.4	170.2

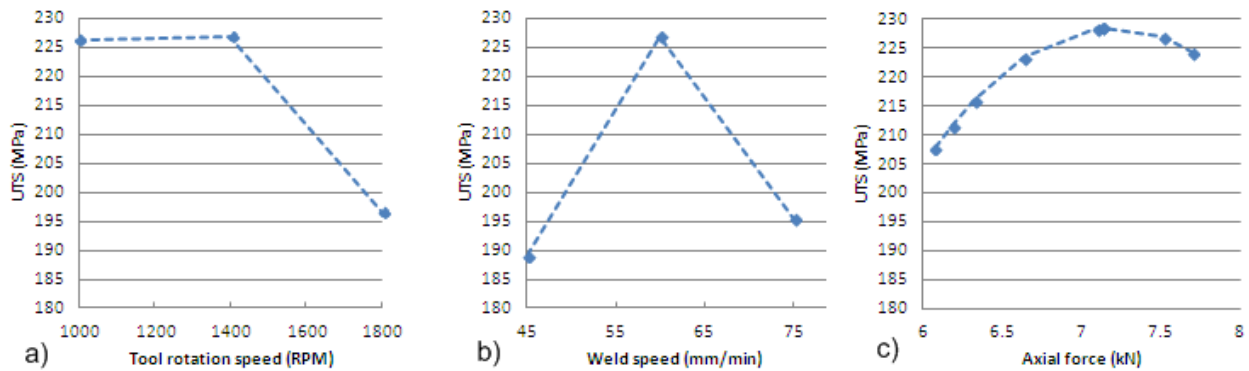


Figure 9.13- Main effects of process parameters based on the regression model on average process parameters: a) RPM main effect, b) weld speed main effect and c) axial force main effect

(Sample calculation note: in each main factor plot above the remaining two factors were set at their averages. For instance, in order to plot Figure 9.13.a we fixed the average weld speed and grand average axial force in Equation (9-2) and varied the values of three levels of tool RPM.)

Finally, we calculated the percentage of contribution of each process parameter using Equation (3-13 in Chapter 3), along with their interaction effects, based on the adjusted UTS values considering the average value of the process parameters with the same total average of axial force for all the FSW samples (total average axial force= 6871.1 N). Results are shown in Figure 9.14.

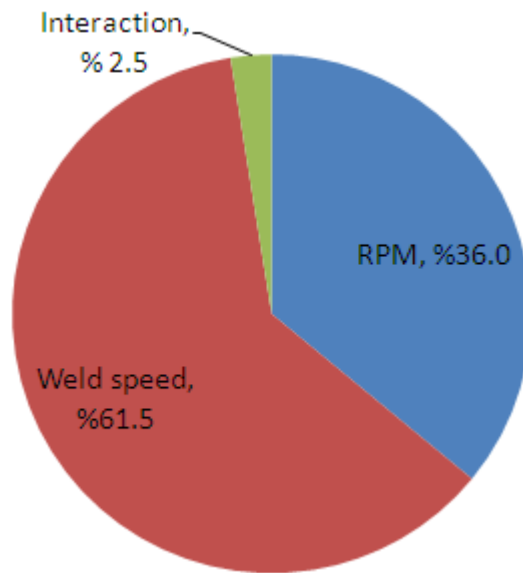


Figure 9.14- Percentage contributions of the FSW process parameters on the weld UTS (the axial force has been considered to be fixed at 6871.1 N)

9.3.4 Examination of fracture surfaces

We examined the fracture surfaces of all the FSW samples as shown in Figure 9.15. we noticed that all the samples with low UTS values had an S-shape fracture surface (samples 3n or 1800 RPM, 45 mm/min and 8n or 1400 RPM, 75 mm/min) and all the samples with high UTS values had a ductile fracture surface with a necking region (samples 4n or 1000 RPM, 60 mm/min and 5n or 1400 RPM, 60 mm/min). It was also interesting that the entire samples from the same weld fractured at the same location with a similar fracture surface, indicating uniform weld properties along the weld line.

If we study the fracture surfaces of tensile samples after tensile tests in more details we notice that the material in the weld zone under the tool's pin has delaminated in sample 7n (cold weld 1000 RPM, 75 mm/min) (see Figure 9.16) as a result of very low temperature (see Table 9.2), high viscosity and low mechanical bonding of the material, which flows around the tool and merges again in the retreating edge of the tool during one rotation of the FSW tool. We see that the delamination happens in sample 2n (1400 RPM, 45 mm/min) too (see Figure 9.17) which has had the lowest average axial force during FSW (see Table 9.3) and a relatively high maximum temperature (see Table 9.2). The delamination also happened in sample 3n (1800 RPM, 45 mm/min) which had the highest temperature during welding and a relatively low axial force (Tables 9.2 and 9.3), probably because of the formation of thicker layers of aluminum oxide which prevent mechanical bonding of the material during FSW in addition to the lack of sufficient contact force effect from a relatively low axial force of the tool (Figure 9.18).

Next, we performed microstructural analysis on the sample 5n (1400 RPM, 60 mm/min) with the highest UTS (highest average axial force) and sample 3n with the lowest UTS (hot weld) using Scanning Electron Microscope (SEM).

In sample 5n, we studied 5 different points of the fracture surface as marked in Figure 9.19. All over the sample we saw tiny cups and cones which are representatives of ductile fracture with micro void formation and coalescent as shown in Figure 9.20.

In sample 3n, as we saw before in the macro-level visual inspection of the tensile samples after fracture, the delamination of material under the tool pin has occurred (see both Figure 9.18 and Figure 9.21). When we examined this delamination by SEM we noticed as shown in Figure 9.22 that it also happens in other regions under the tool pin after tensile test fracture, with a uniform distance of the laminated layers equal to the advance-per-rotation of FSW; which is 25 $\mu\text{m}/\text{rotation}$ ($45/1800=0.025$ mm). Figure 9.22 is at the intersection of the continuation of an opened delamination and the fracture surface on sample 3n after tensile testing fracture as marked by a yellow circle in Figure 9.21. The yellow parallel lines in Figure 9.22 were drawn with an equal distance of 0.025 mm which coincided with the tiny delaminated layers. In some regions of sample 3n, we saw low ductility fracture with very small cups and cones compared to sample 5n as shown in Figure 9.23. Also in some regions of sample 3n (hot weld) we noticed the brittle fracture surfaces with cleavage as shown in Figure 9.24. In brittle fracture regions there were

some areas which we could see the inter-granular crack propagation and a sudden fracture evidence (see grains in Figure 9.25 and Figure 9.26).



Sample 1n



Sample 2n



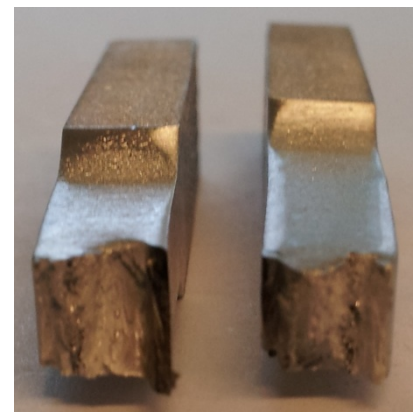
Sample 3n



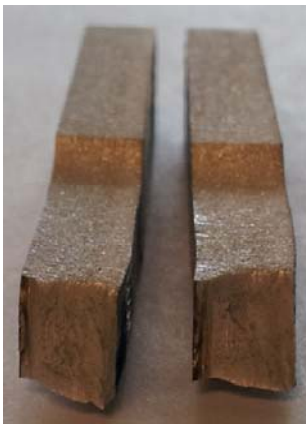
Sample 4n



Sample 5n



Sample 6n



Sample 7n



Sample 8n



Sample 9n

Figure 9.15- Visual inspection of fracture surfaces of the samples with maximum UTS values



Figure 9.16- Fracture zone under the tool pin in sample 7n (cold weld or 1000 RPM, 75 mm/min); notice the delaminated regions in vicinity of the weld line



Figure 9.17- Fracture zone under the tool pin using sample 2n (1400 RPM, 45 mm/min) with the lowest average axial force; notice the delaminated regions in vicinity of the weld line



Figure 9.18- Fracture zone under the tool pin in sample 3n (hot weld or 1800 RPM, 45 mm/min); notice the delaminated regions in vicinity of the weld line

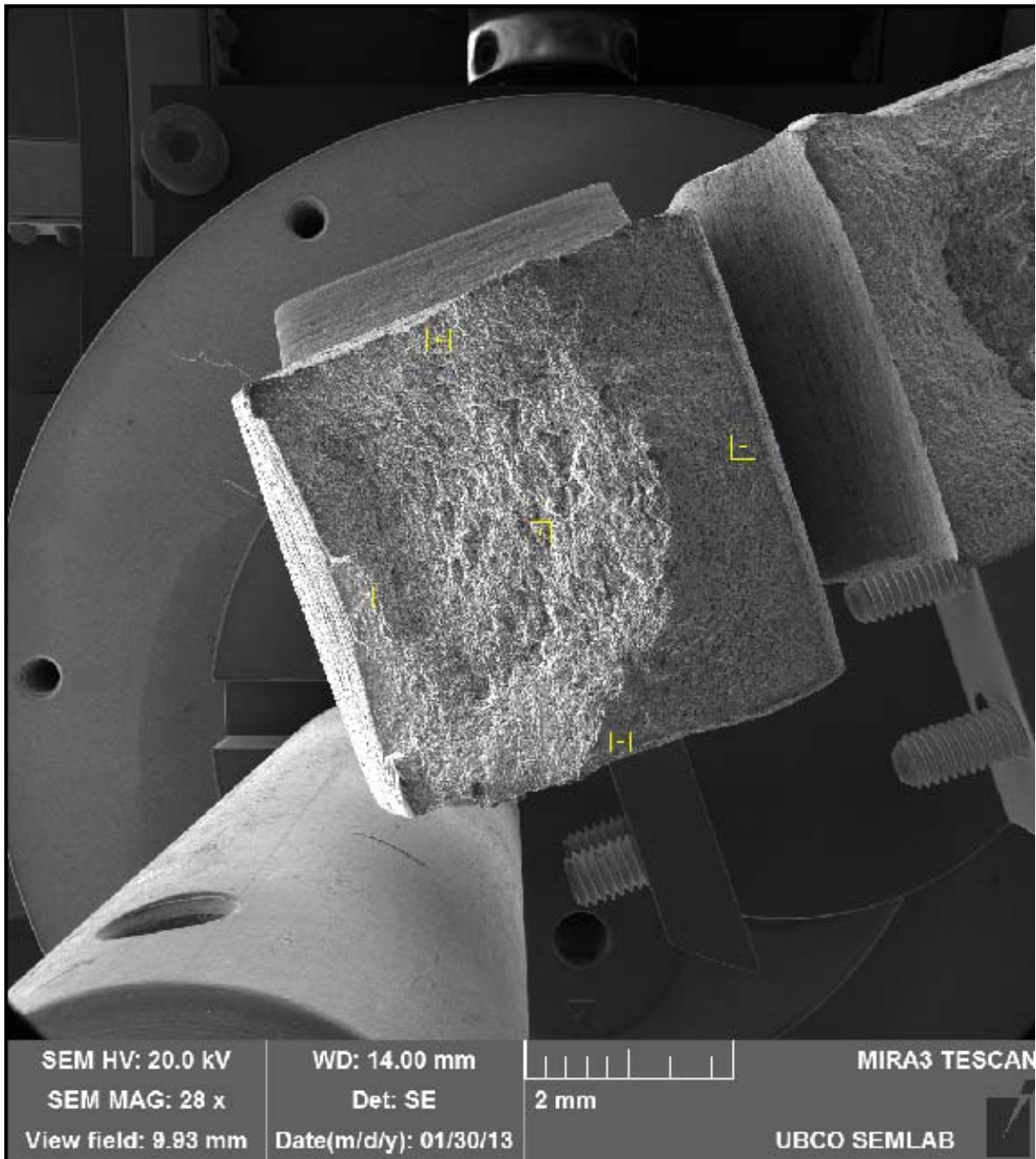


Figure 9.19- Fracture surface of sample 5n (1400 RPM, 60 mm/min) with the highest UTS (X 28)

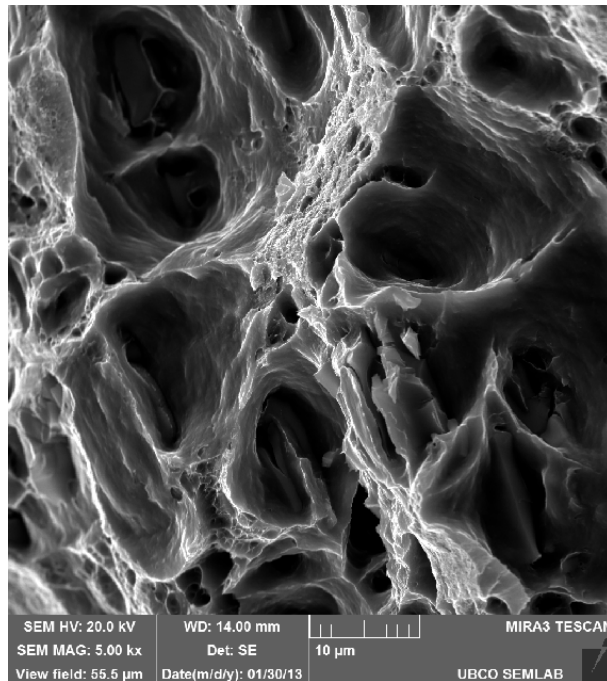


Figure 9.20- Typical high magnification of fracture surface in sample 5n (1400 RPM, 60 mm/min) with the highest UTS (X 5000)

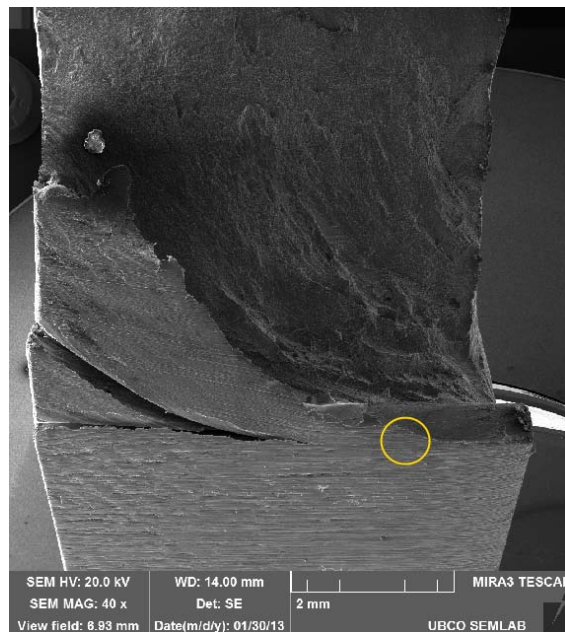


Figure 9.21- Delamination in the material under the tool pin in sample 3n (1800 RPM, 45 mm/min) or hot weld (X 40)

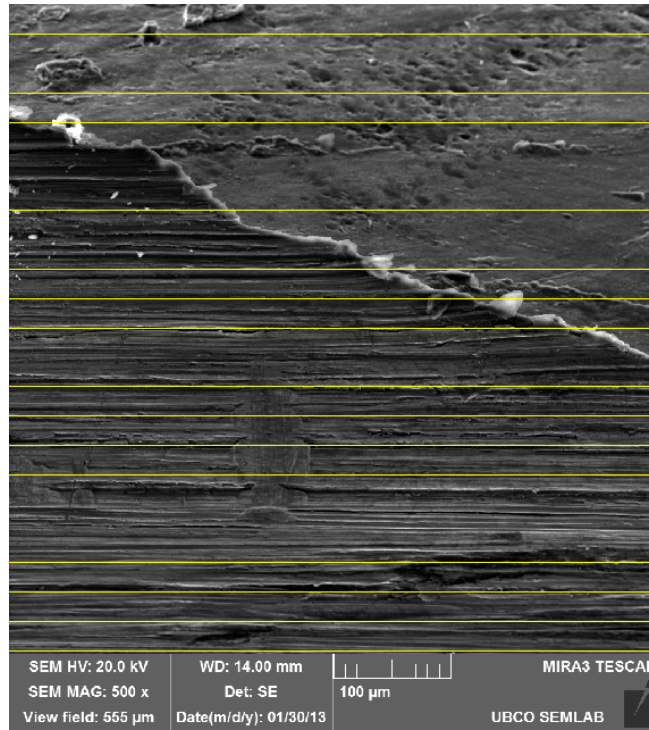


Figure 9.22- Distances between laminates at yellow circle in Figure 9.21 using higher magnification (X 500)

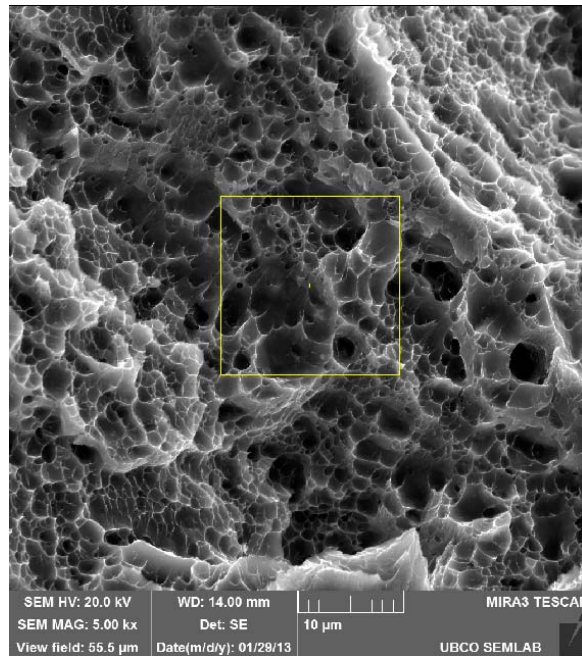


Figure 9.23- Low ductility fracture in some regions of sample 3n or hot weld (X 5000)

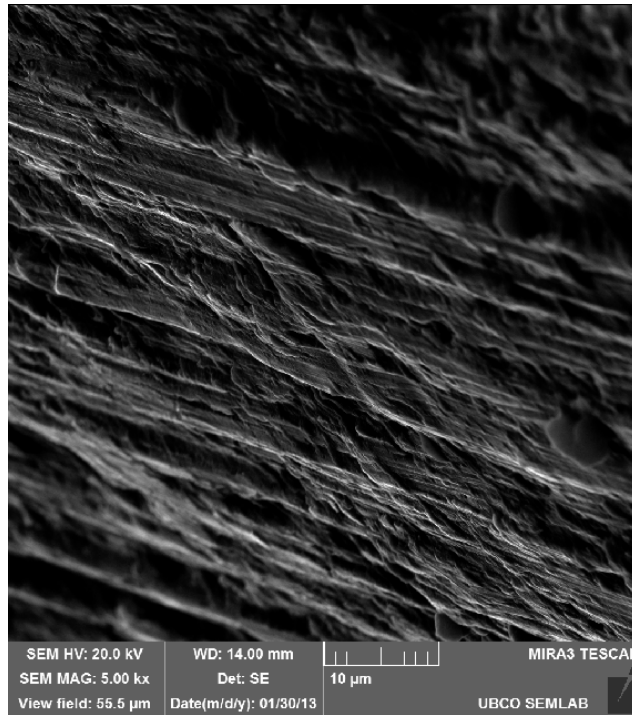


Figure 9.24- Brittle fracture in some regions of sample 3n or hot weld (X 5000)

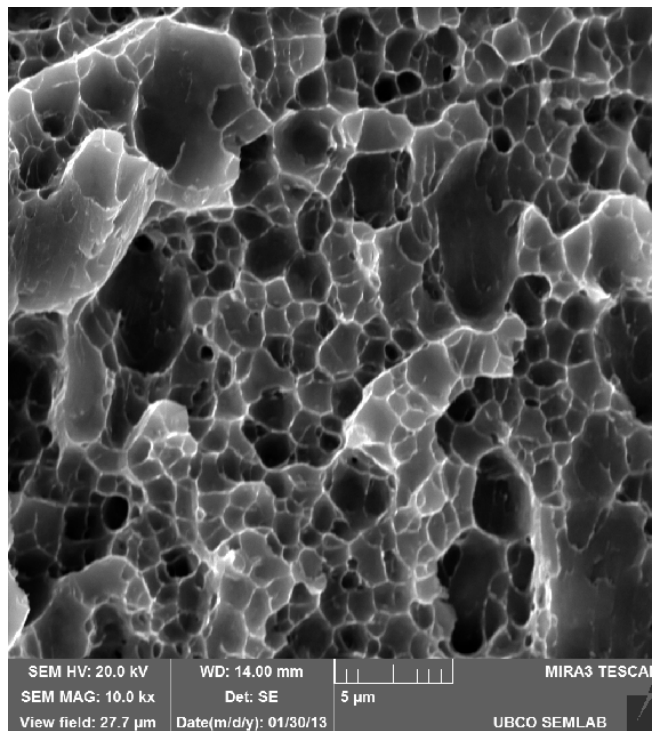


Figure 9.25- Inter-granular fracture in sample 3n (hot weld) with the lowest UTS (X 10000)

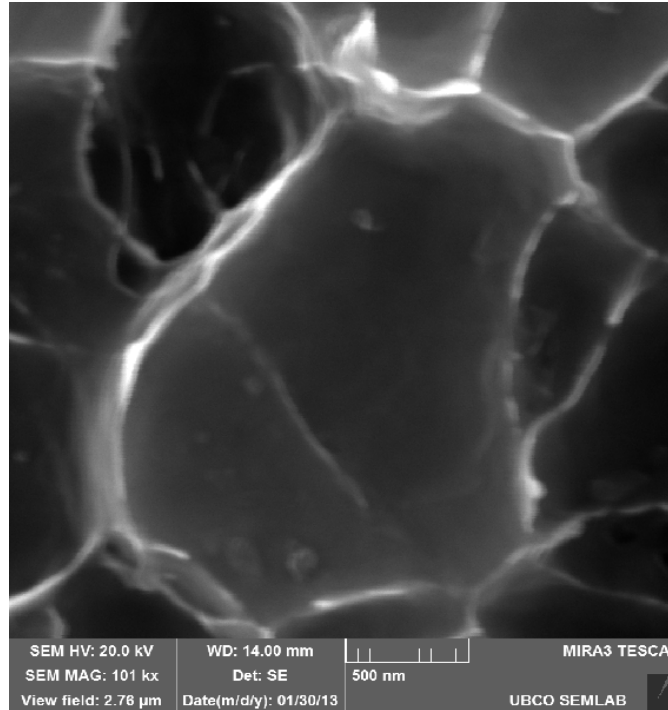


Figure 9.26- Inter-granular fracture in sample 3n with high magnification (X 101000)

9.3.5 Electron Back Scattered Diffraction (EBSD)

We studied the grain size at mid thickness of the advancing side of the weld zone in sample 3n (1800 RPM, 45 mm/min) with lowest UTS (hot weld) and sample 5n (1400 RPM, 60 mm/min) with highest UTS and axial force. Namely, we compared the grain size distribution of these two samples in Figure 9.27.

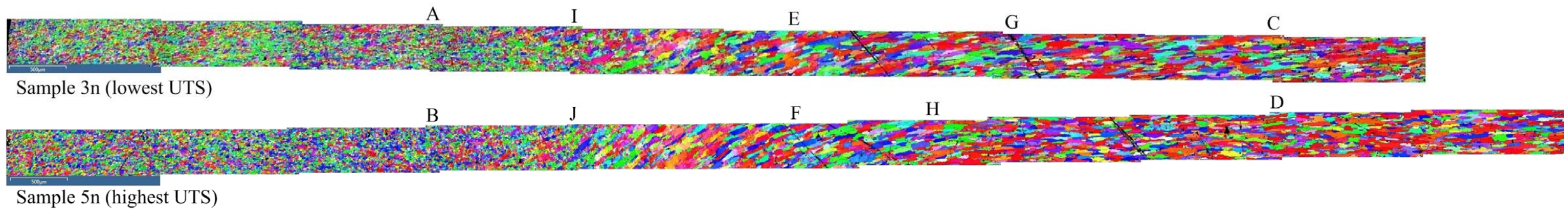
In Figure 9.27 (a) we show the x-coordinates of some important regions of interest. Points A and B are at the tool's pin location (nugget zone), points C and D are at the tool's shoulder location, points E and F are at the middle points between the pin and the shoulder, points G and H are where the directional grains do not exist anymore (TMAZ ends and HAZ start) and points I and J are where the directional grains start to form (TMAZ start) in samples 3n and 5n, respectively. For a more general view please see Figure 2.1 of Chapter 2.

In Figure 9.27 (b) we can see that there is a relatively uniform Dynamic Recrystallized (DRX) grain size distribution in the nugget zone in both samples and this average is higher in sample 3n

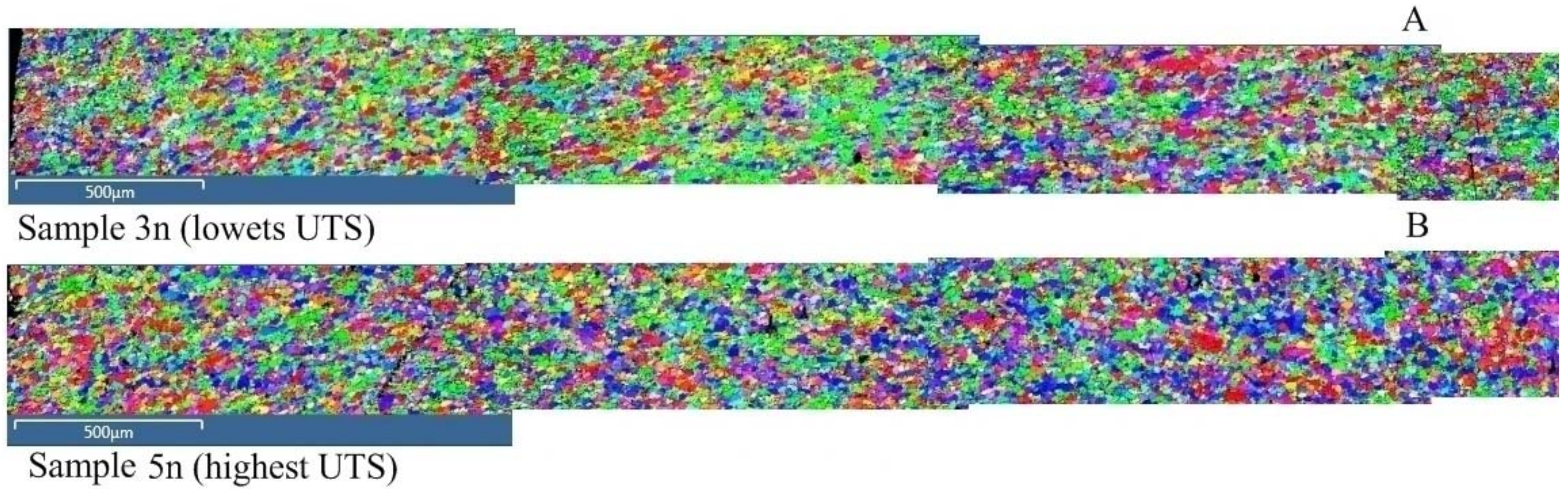
with the highest maximum temperature during FSW that is similar to what was shown in Figure 7.1 of Chapter 7. In the right hand side of points A and B where the tool's pin has not physically passed through the plate during FSW (but has been very close to it), there is a very low grain size region compared to the nugget zone in the left hand side of these points. The same behavior was predicted in the microstructure modeling of aluminum 6061 in Figure 7.4 of Chapter 7 using our developed integrated multiphysics model.

In Figure 9.27 (c) we can clearly see the very low grain size in A-I and B-J regions which are near the tool's pin from left hand side, followed by I-G and J-H regions with directional grains (TMAZ) in the right hand side. The A-I and B-J regions are shear zones (or rotation zones) with the same size of 1.35 mm in both samples 3n and 5n, which have had different maximum temperatures of 519 °C and 484 °C, respectively, during FSW (see Table 9.2). This narrow region is where the material has a high rotation speed around the tool which is defined using the stick coefficient (δ) and the tool rotation speed in our developed integrated multiphysics model as discussed before for Equation (4-4) in Chapter 4. If the material is trapped in the shear layer, its deposit is delayed and may rotate with the pin more than one cycle which causes a higher strain rate and more grain refinement during Dynamic Recrystallization (DRX). It is important to notice that the shear layers have the same thickness in both hot and relatively cold samples. We earlier discussed the shear layer (or rotation layer) in more details in Figure 4.8 (Chapter 4), Figure 6.7 (Chapter 6) and Section 4.4.3. It is also interesting that the length of TMAZ region in sample 3n (hot weld) with maximum temperature of 519 °C is higher than sample 5n with maximum temperature of 484 °C. Also the directional grain in TMAZ of sample 3n (hot weld) are more towards the horizon line compared to sample 5n (relatively cold weld).

In Figure 9.27 (d) we can see that the Heat Affected Zone (HAZ) starts after the end of directional grains in the TMAZ. The size of grains in HAZ regions near TMAZ are increased compared to the base metal grains which are at the right hand side of the figure. The grain growth in the HAZ of sample 3n (hot weld) is higher compared to sample 5n (relatively cold weld).



a)



b)

Figure 9.27- Grain size distribution at mid thickness of the advancing side of the weld zones of sample 3n with the lowest UTS (hot weld) and sample 5n with the highest UTS (see also Figure 2.1)

(a) The whole profile

(b) Higher magnification of the nugget zone and shear layer

(c) Higher magnification of shear layer and thermomechanically affected zone (TMAZ)

d) Higher magnification of the thermomechanically affected zone (TMAZ), heat affected zone (HAZ) and base metal

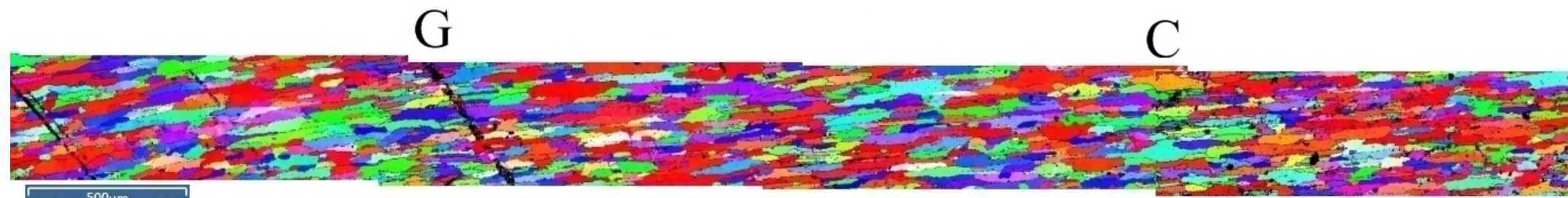


Sample 3n (lowest UTS)

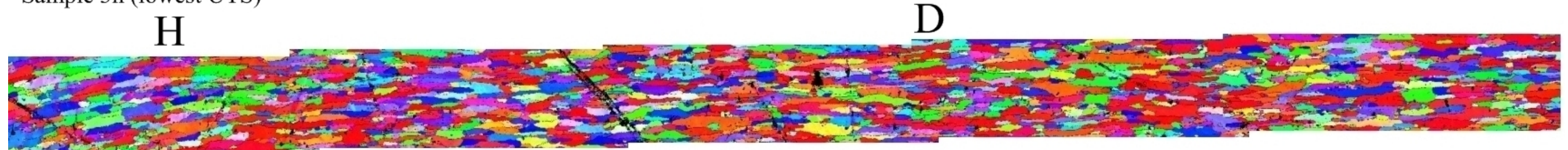


Sample 5n (highest UTS)

c)



Sample 3n (lowest UTS)



Sample 5n (highest UTS)

d)

Figure 9.27- continued

9.3.6 Micro hardness and number of grains

We measured the micro hardness (HV) distribution and also counted the number of grains on a length of 77 micron (horizontal line) at different points of samples 3n (1800 RPM, 45 mm/min) and 5n (1400 RPM, 60 mm/min). Results are shown in Figure 9.28.

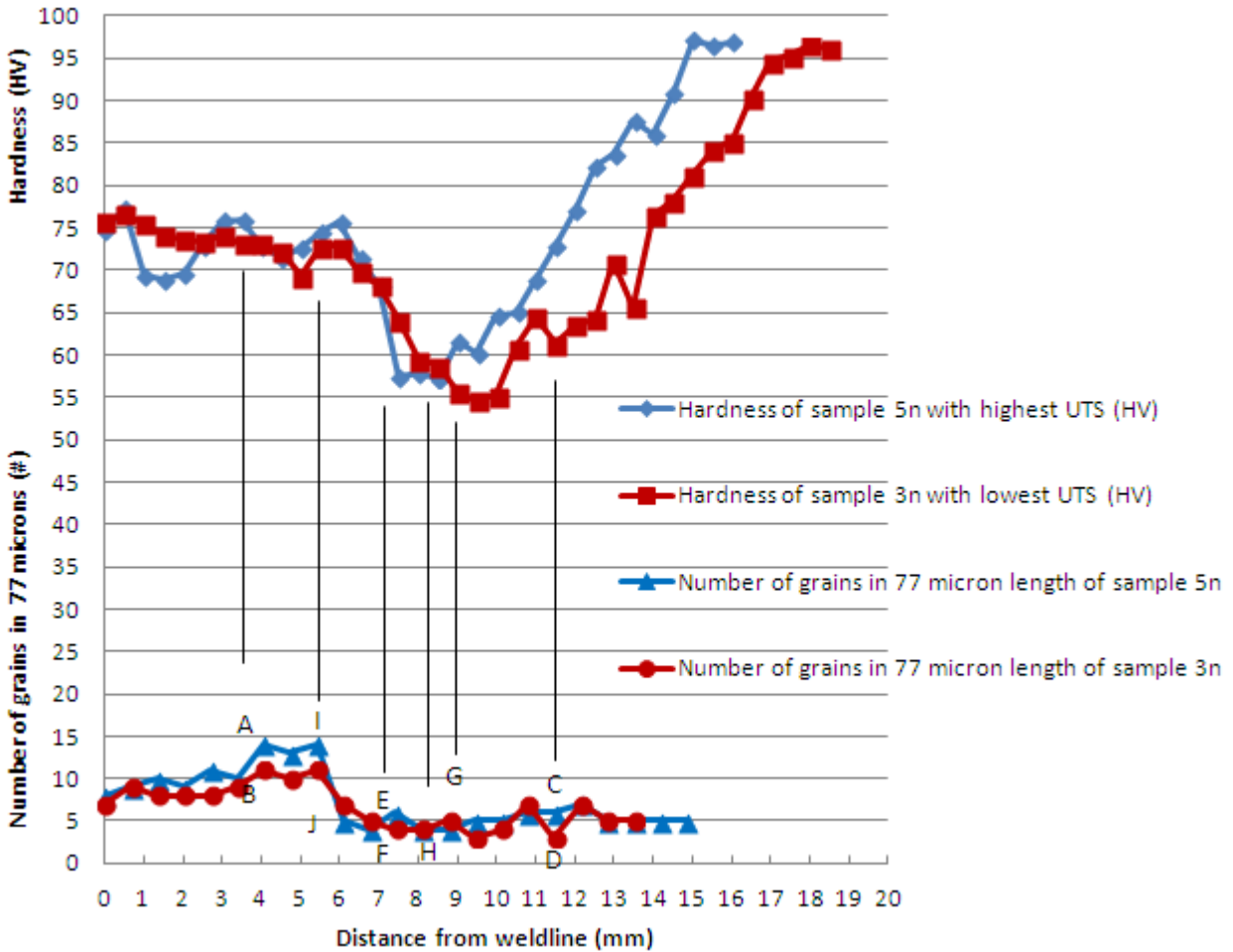


Figure 9.28- Micro hardness (HV) and the number of grains in a 77 micron horizontal line at different locations of samples 3n and 5n with the lowest and the highest UTS values, respectively

In Figure 9.28, in the nugget zone (left hand side of points A and B), we can see that the number of grains is higher in sample 5n compared to sample 3n (hot weld). In other words, sample 5n

(relatively cold weld) has had a lower average grain size in the nugget zone compared to sample 3n (hot weld), which would have been resulted from the lower temperature during dynamic recrystallization and grain growth in sample 5n (relatively cold weld). Relatively higher values of hardness are also noticed in sample 5n compared to sample 3n in the nugget zone.

In the regions A-I and B-J in Figure 9.28, we can notice the evidence of shear layers (rotation layer) in samples 3n and 5n, respectively. More specifically, in these regions again the grain size of the sample 5n is lower compared to the sample 3n which also causes a higher hardness in sample 5n. Also in both samples in the middle of shear layer, the number of grains decreases or the average grain size increases, causing a decrease in the corresponding micro hardness.

In regions I-G and J-H, we can see the thermomechanically affected zone (TMAZ) of samples 3n and 5n, respectively, with the directional grains with larger sizes compared to the base metal; indicating the occurrence of grain growth in TMAZ during FSW. In the TMAZ region of sample 3n, near its shear zone still some dynamic recrystallization happens which causes a lower grain size as compared to sample 5n in the same region. Looking at the right hand side of the TMAZ we see that the directional grain size in sample 5n (highest UTS and relatively cold weld) becomes smaller compared to sample 3n (hot weld). The total length of the TMAZ of sample 3n (I-G) is higher than the one in sample 5n (J-h) (I-G \approx 3.75 μ m and J-H \approx 3.12 μ m).

The minimum hardness in both samples happens at the interface of TMAZ and heat affected zone (HAZ) where both samples have similar grain size values. This shows the effect of precipitates size, coherency to matrix and their distribution on the formation of the minimum hardness location. we also showed in Chapter 3 that the minimum hardness location is located at the interface of TMAZ and HAZ. The minimum hardness of sample 5n (relatively cold weld) is higher than the one in sample 3n (hot weld) where it occurs at a closer location to the weld line compared to sample 3n. The latter observation also complies with the idea we proposed in Chapter 3 that the lower the peak temperature and the HAZ distance to the weld line, the lower the hardness decrease of the FSW samples. In Addition, we noticed in Section 9.3.4 that if the FSW weld is very cold, the low mechanical bounding deteriorates the mechanical properties of FSW samples. In both regions of HAZ which are very close to TMAZ, we can see the grain growth in both samples 3n and 5n in Figure 9.28, while the extent of grain growth is higher in sample 3n (hot weld) due to the higher maximum temperature during FSW.

Finally, when we inspect the right hand side of the HAZ in both samples 3n and 5n in Figure 9.28, no grain growth happens and their grain sizes become equal to that of the base metal. The steep hardness increase from the HAZ toward the base metal region is the result of the FSW heat and its effect on the precipitates size, coherency to matrix and distribution as explained in Chapter 2 Section 2.1 (metallurgical aspects). The base metal hardness is recovered in higher distances to the weld line in sample 3n (hot weld) compared to sample 5n (relatively cold weld) as a result of higher maximum temperature in sample 3n during FSW.

9.4 Summary of findings

Based on the experimental results and discussions of Chapter 9 we drew the following findings:

- 1- The maximum temperature is reduced by increasing the weld speed under a constant tool RPM during FSW.
- 2- The maximum temperature is increased by increasing the tool RPM under a constant weld speed during FSW.
- 3- The highest axial force during steady state phase of FSW occurs in sample 7n (cold weld or 1000 RPM, 75 mm/min) and the lowest axial force occurs in sample 3n (hot weld or 1800 RPM, 45 mm/min).
- 4- The highest torque is seen in sample 7n (cold weld) and also occasionally in sample 4n (second cold weld). The lowest torque happens in sample 3n (hot weld).
- 5- When the RPM is increased with a constant weld speed, the torque is decreased during FSW.
- 6- The highest UTS in the FSW samples had a UTS equal to 0.76 of the as-received plate.
- 7- The minimum transverse force is seen in sample 4n (1000 RPM, 60 mm/min) and the maximum transverse force belongs to samples 6n (1800 RPM, 60 mm/min) and 9n (1800 RPM, 75 mm/min) with the highest RPM and sometimes to samples 7n (cold weld or 1000 RPM, 75 mm/min). The highest transverse force in samples 6n (1800 RPM, 60 mm/min) and 9n (1800 RPM, 75 mm/min) or 7n (1000 RPM, 75 mm/min) may have been resulted from higher excess material from the weld (flash) or a higher material flow stress during FSW, respectively.

- 8- The time distance between two consecutive transverse force peaks is equal to the time of advance per rotation during FSW.
- 9- The samples 3n (1800 RPM, 45 mm/min), 6n (1800 RPM, 60 mm/min) and 9n (1800 RPM, 75 mm/min) with the highest tool RPM values and sample 5n with the highest average axial force had a high volume of excess material from the weld zone (flash).
- 10- In samples 1n (1000 RPM, 45 mm/min), 6n (1800 RPM, 60 mm/min) and 9n (1800 RPM, 75 mm/min) which had the lack of diffusion failure, a relatively higher transverse force during FSW was seen, which would be due to the higher excess material from the weld zone (flash).
- 11- The minimum UTS belonged to sample 3n (hot weld or 1800 RPM, 45 mm/min) and the maximum UTS is seen in both samples 5n (1400 RPM, 60 mm/min with highest average axial force) and 4n (second cold weld or 1000 RPM, 60 mm/min) with small difference in UTS.
- 12- Based on the regression model at the same average axial force, both samples 5n (highest average axial force) and 4n (second cold weld) showed literally the same highest UTS values.
- 13- There are optimum values to set the FSW process parameters in order to get the highest UTS in the weld. If one exceeds the optimum processing window, it can reduce the weld mechanical properties.
- 14- All the samples with low UTS values had an S-shape fracture surface (samples 3n and 8n) and the samples with high UTS values had a ductile fracture surface with necking region (samples 4n and 5n).
- 15- When the temperature is very low or very high or axial force is very low during FSW, the material under the tool's pin in the weld zone after tensile test fracture showed the delamination which is a result of low mechanical bounding between layers of material rotating around the pin and forming the weld.
- 16- Based on the SEM studies on fracture surfaces after tensile tests, sample 5n with the highest UTS and axial force values had a ductile fracture surface and sample 3n (hot weld) with the lowest UTS had both low ductility and brittle fracture surfaces.

- 17- There is a relatively uniform Dynamic Recrystallized (DRX) grain size in the nugget zone in both samples 3n (hot weld) and 5n (relatively cold weld) and on average it is higher in sample 3n having a higher maximum temperature during FSW.
- 18- Shear layer had the same thickness in both sample 3n (hot weld) and 5n (highest UTS and axial force) equal to 1.35 mm. Note that grain size in sample 3n (hot weld) was smaller compared to sample 5n (relatively cold weld). In the middle of both shear layers, there are slightly larger grains.
- 19- The length of TMAZ region in sample 3n (hot weld) is higher compared to sample 5n (relatively cold weld). Also the directional grains in the TMAZ of sample 3n are more towards the horizon line compared to sample 5n.
- 20- The sizes of grains in HAZ near TMAZ are increased in both samples 3n and 5n, while the increase is more significant in sample 3n (hot weld).
- 21- In the TMAZ of sample 3n near its shear zone still some dynamic recrystallization happens and causes a lower average grain size compared to sample 5n in the same position. Looking at the right hand side of the TMAZ, we noted that the directional grain size in sample 5n (relatively cold weld) becomes smaller compared to sample 3n (hot weld).
- 22- The total length of TMAZ of sample 3n (hot weld) is higher than the one in sample 5n (relatively cold weld).
- 23- The minimum hardness in both samples 3n and 5n happens at the interface of TMAZ and heat affected zone (HAZ). The precipitates size and their distribution cause the hardness decrease.
- 24- The minimum hardness of sample 5n (relatively cold weld) is higher than the one in sample 3n (hot weld) and it happens at a closer location to the weld line compared to the sample 3n.
- 25- In border regions of HAZ close to TMAZ, the grain growth happens in both samples 3n and 5n where the amount of grain growth is higher in sample 3n (hot weld) due to the higher maximum temperature during FSW.
- 26- The base metal hardness is recovered at higher distances to the weld line in sample 3n (hot weld) compared to sample 5n (relatively cold weld) due to higher maximum temperature in sample 3n (hot weld).

Chapter 10: Conclusions, Contribution to Knowledge and Recommendations for Future Research

10.1 Conclusions

Recalling Figure 1.1, in this dissertation we researched on a range of FSW topics with the main goal of developing a novel integrated multiphysics modeling (Chapter 4), testing (Chapter 9), and optimization (Chapter 3 and Chapter 9) approach for aluminum alloys and arriving at a better understating of processing-microstructural-properties relations in this relatively new welding process (Chapter 9). To this end, we defined a set of sub-objectives as outlined in Chapter 1 and discussed in the subsequent chapters. From the presented adjusted ANOVA formulation for L₉ Taguchi optimization of a thermal model of FSW on aluminum 6061 alloy, it was shown that there are no interactions between processing parameters (tool RPM, transverse speed, and normal force) and hence the Taguchi method may be reliably and efficiently used for optimization of FSW processes (Chapter 3). Contributions of the process parameters on both HAZ distance to the weld line as well maximum temperature criteria showed that the tool rotational speed has normally a very high effect, followed by the normal force and weld speed.

Next to the above optimization model (Chapter 3) along with a set of in-house experiments (Chapter 9), we correlated the mechanical properties of the weld material during and after FSW to the process parameters. Accordingly, we found that hot weld conditions result in the lowest mechanical properties and the relatively cold welds show the highest mechanical properties. In a very cold weld, usually the lack of mechanical bonding due to the material high viscosity causes failure and in turn, lowers mechanical properties in the final weld. Accordingly, it was shown that there is a limited window of processing parameters in which optimum weld properties during FSW may be reached. Among other specific experiential observations, we found that the base metal hardness is recovered at higher distances to the weld line in hot welds compared to cold welds (Chapter 9).

In this thesis, we also developed a novel 2D integrated multiphysics model which can simultaneously predict temperature, strain and strain rate at mid thickness of the welding plates

during FSW (Chapter 4) as well as post-process properties such as the material microstructure (grain size) (Chapter 7) and residual stresses after FSW (Chapter 8). In support of earlier numerical and experimental studies, it was found that the maximum temperature during FSW occurs at the backside of the advancing side of the pin, while the maximum strain during FSW in mid thickness of the plate occurs in front of the leading edge of the pin. The maximum shear strain rate location was near the top of the advancing side of the pin. It was also shown that if the heat transfer in the FSW tool is not considered during modeling, a lower bound of temperature distribution in the leading edge of the tool will be resulted (Chapter 4). From residual stress prediction of the intergraded model, among other detailed results listed in the preceding chapters, it was the most interesting to notice that the longitudinal stress distribution changes from tensile into compression beyond the HAZ and TMAZ boundaries, whereas the tensile transverse stress profile becomes compressive beyond the nugget zone (Chapter 8). A comparison of different CFD- and CSM-based constitutive equations in the model showed that even though in the literature several constitutive equations are used for the same process model, they can result in different results in terms of particular variables of interest (Chapter 5). In particular, it was found that The Johnson-Cook and Zener-Hollomon constitutive equations can yield significantly different flow stress predictions.

We also developed a new approach to measure strain during FSW which can measure the strain during welding with acceptable accuracy (Chapter 6). The approach was based on viscoplasticity with a “stop action” or “freeze-in” technique, followed by a CAD procedure to map the material flow lines and measure the strain at discrete points. In particular it was deemed that there is a need for such measurement techniques since the range of reported values of maximum strain in the literature via numerical models varies very inconsistently.

10.2 Summary of contributions to knowledge

- In Chapter 3 we developed formulas of adjusted ANOVA to be applicable to the Taguchi L9 method with three FSW process variables.
- In Chapters 4, 7 and 8 we developed a novel “integrated multiphysics” model which can predict the strain as well as temperature, strain rate and stress over the entire workpiece

domain using a CFD-CSM approach. The model can also predict post-process properties such as residual stresses and weld grain size.

- In Chapter 5 for the first time we investigated the effect of using different constitutive equations on the FSW model predictions.
- In Chapter 6 we developed a CAD-visioplasticity approach to measure strain during FSW and compared it with my integrated multiphysics model.
- In Chapter 9 we proposed a regression approach to eliminate the effect of variable axial force (uncontrolled noise factor) during optimization, analysis of variances (ANOVA) for the first time in FSW optimization research and demonstrated a theory about the hot and cold weld conditions and its effect on mechanical properties of the final weld.

10.3 Recommendations for future research

Below are recommended directions that may be pursued to further the research conducted in this thesis.

1. Here we developed and validated a 2D integrated multiphysics model of FSW. For future research, a 3D integrated multiphysics model can be developed and studied in conjunction to experimental data, especially on FSW of thick plates or parts with irregular geometries.
2. In this study we considered a constant (average) axial force during FSW experimental analysis. The effect of variable axial force during welding on weld properties may be studied in future.
3. Strain measurement during FSW can be studied with more experiments and the effect of dynamic recrystallization on strain distribution after welding can be studied in more detail.
4. The effect of using different tool shapes of weld properties can be studied further.
5. The internal state variables modeling can be implemented in the current integrated multiphysics model in order to predict the local properties of weld during or after FSW (such as flow stress and strain). In such a method the effect of changes in dislocation density, grain size, precipitates size and distribution during FSW on the final weld properties can be considered.
6. The integrated multiphysics modeling and experimentation of dissimilar plates can be studied.

7. More experiments and in-situ weld studies can be set up in order to study the effect of different process parameters on material flow and relative velocity of material and tool during FSW.
8. Transition Electron Microscope (TEM) experiments can be performed in different regions of weld samples to study the effect of process parameters on the dislocation density, precipitates' size and distribution after welding.

References

References of Chapter 2

- [1] W.M. Thomas, E.D. Nicholas, J.C. Needham, M.G. Murch, P. Temple-Smith, C.J. Dawes, Friction Welding. Cambridge, UK: The Welding Institute TWI (1991) Patent Application No 91259788.
- [2] M.M. Shtrikman, Current state and development of friction stir welding Part 3, *Welding International*, 22 (2008) 806–815.
- [3] S. Vijayan, R. Raju, Process parameter optimization and characterization of friction stir welding of aluminum alloys, *International Journal of Applied Engineering Research*, 3 (2008) 1303–1316.
- [4] B. London, M. Mahoney, B. Bingel, M. Calabrese, D.Waldron, High strain rate superplasticity in thick section 7050 aluminum created by friction stir processing, *Proceedings of the Third International Symposium on Friction Stir Welding*, Kobe, Japan, 27–28 September, 2001.
- [5] C.G. Rhodes, M.W. Mahoney, W.H. Bingel, R.A. Spurling, C.C. Bampton, Effects of friction stir welding on microstructure of 7075 aluminum, *Scripta Materialia*, 36 (1997) 69-75.
- [6] G. Liu, L.E. Murr, C.S. Niou, J.C. McClure, F.R. Vega, Microstructural aspects of the friction-stir welding of 6061-T6 Aluminum, *Scripta Materialia*, 37 (1997) 355-361.
- [7] K.V. Jata, S.L. Semiatin, Continuous dynamic recrystallization during friction stir welding of high strength aluminum alloys, *Scripta Materialia*, 43 (2000) 743-749.
- [8] S. Benavides, Y. Li, L.E. Murr, D. Brown, J.C. McClure, Low-temperature friction-stir welding of 2024 aluminum, *Scripta Materialia*, 41 (1999) 809-815.
- [9] A.K. Lakshminarayanan, Process parameters optimization for friction stir welding of RDE-40 aluminum alloy using Taguchi technique, *Transactions of Nonferrous Metals Society of China*, 18 (2008) 548-554.
- [10] Y. Chen, H. Liu, F. Jicai, Friction stir welding characteristics of different heat-treated-state 2219 aluminum alloy plates, *Materials Science and Engineering A*, 420 (2006) 21–25.
- [11] W.B. Lee, Evaluation of the microstructure and mechanical properties of friction stir welded 6005 aluminum alloy, *Materials Science and Technology*, 19 (2003) 1513-1518.

- [12] H.W.I. Phillips, The Constitution of Alloys of Aluminium with Magnesium, Silicon and Iron, *Journal Institute of Metals*, 72 (1946) 151-227.
- [13] J. Zhang, Z. Fan, Y. Q. Wang, B. L. Zhou, Equilibrium pseudo-binary Al-Mg₂Si phase diagram, *Materials Science and Technology*, 17 (2001) 494–496.
- [14] D.L. Zhang, L. Zheng, The quench sensitivity of cast Al-7pct Si-0.4pct Mg alloy *Metallurgical and Materials Transactions A*, 27A (1996) 3983–3991.
- [15] W. Woo, H. Choo, P. J. Withers, Z. Feng, Prediction of hardness minimum locations during natural aging in an aluminum alloy 6061-T6 friction stir weld, *Journal of Materials Science*, 44 (2009) 6302–6309.
- [16] A.A. Larsen, M. Bendsøe, J. Hattel, H. Schmidt, Optimization of friction stir welding using space mapping and manifold mapping—an initial study of thermal aspects, *Structural and Multidisciplinary Optimization*, 38 (2009) 289–299.
- [17] P. Colegrove, M. Painter, D. Graham, T. Miller, 3-dimensional flow and thermal modelling of the friction stir welding process, *Proceedings of the 2nd International Symposium on Friction Stir Welding*, Gothenburg, Sweden, 2000.
- [18] H. Schmidt, J. Hattel, J. Wert, An analytical model for the heat generation in friction stir welding, *Modelling and Simulation in Materials Science and Engineering*, 12 (2004) 143–157.
- [19] M. Khandkar, J. Khan, Thermal modeling of overlap friction stir welding for al-alloys, *Journal of Materials Processing and Manufacturing Science*, 10 (2001) 91–105.
- [20] P. Colegrove, H. Shercliff, P. Threadgill, Modelling and development of the trivex (TM) friction stir welding tool, *Proceedings of 4th International Symposium on Friction Stir Welding*, Park City, 14–16 May 2003.
- [21] H. Schmidt, J. Hattel, CFD modelling of the shear layer around the tool probe in friction stir welding, *Proceedings of Friction Stir Welding and Processing III*, TMS, San Francisco, 13–17 February 2005.
- [22] C. Chen, R. Kovacevic, Finite element modeling of friction stir welding—thermal and thermomechanical analysis, *International Journal of Machine Tools and Manufacture*, 43 (2003) 1319–1326.
- [23] H. Schmidt, J. Hattel, A local model for the thermomechanical conditions in friction stir welding, *Journal of Materials Processing and Manufacturing Science*, 13 (2005) 77–93.

- [24] D. Rosenthal, The theory of moving sources of heat and its application to metal treatments, Transactions of the A.S.M.E., November 1946.
- [25] V. Soundararajan, S. Zekovic, R. Kovacevic, Thermo-mechanical model with adaptive boundary conditions for friction stir welding of Al 6061, International Journal of Machine Tools and Manufacture, 45 (2005) 1577-1587.
- [26] H.B. Schmidt, J.H. Hattel, Modelling in friction stir welding. Scripta Materialia, 58 (2008) 332-337.
- [27] A.A. Larsen, Process optimization of friction stir welding based on thermal models, PhD Dissertation, Department of Mathematics, Technical University of Denmark, June 2009.
- [28] O.R. Myhr, Ø Grong, Process modelling applied to 6082-T6 aluminium weldments-I. Reaction kinetics, Acta Metallurgica et Materialia, 39 (1991) 2693-2702.
- [29] O.R. Myhr, Ø Grong, Process modelling applied to 6082-T6 aluminium weldments-II. Applications of model, Acta Metallurgica et Materialia, 39 (1991) 2703-2708.
- [30] A.A. Larsen, M. Stolpe, J. Hattel, H. Schmidt, Optimization of Hardness in Friction Stir Welds, 8th World Congress on Structural and Multidisciplinary Optimization, Lisbon, Portugal, 1-5 June 2009.
- [31] J. Bandler, Q. Cheng, S. Dakroury, A. Mohamed, M. Bakr, K. Madsen, J. Søndergaard, Space mapping, The State of the Art. IEEE Transaction on Microwave Theory and Techniques, 52 (2004) 337–361.
- [32] D. Echeverria, P. Hemker, Manifold mapping: a two-level optimization technique, Computing and Visualization in Science, 11 (2008) 193-206.
- [33] R. Nandan, B. Prabu, A. De, T. Debroy, Improving reliability of heat transfer and materials flow calculations during friction stir welding of dissimilar aluminum alloys, Welding journal, 86 (2007) 313–322.
- [34] C.C. Tutum, J.H. Hattel, Optimisation of process parameters in friction stir welding based on residual stress analysis: a feasibility study, Science and Technology of Welding and Joining, 15 (2010) 369–377.
- [35] L. Fratini, V. Corona, Friction stir welding lap joint resistance optimization through gradient techniques, Journal of Manufacturing Science and Engineering, 129 (2007) 985–990.

- [36] P. Gebhard, M. Zaeh, Empirical model for the tool shoulder temperature during friction stir welding, Technische Universitt Mnchen, Institute for Machine Tools and Industrial Management, 2007.
- [37] H. Shercliff, M. Russell, A. Taylor, T. Dickerson, Microstructural modeling in friction stir welding of 2000 series aluminium alloys, *Mecanique & Industries*, 6 (2005) 25–35.
- [38] M. Khandkar, J. Khan, A. Reynolds, Input torque based thermal model of friction stir welding of al-6061, Proceedings of the 6th International trends in welding research conference, 15-19 April 2002, Pine Mountain, GA.
- [39] H. Schmidt, J. Hattel, Thermal modelling of friction stir welding, *Scripta Materialia*, 58 (2008) 332–337.
- [40] H.Atharifar, Optimum parameters design for friction stir spot welding using a genetically optimized neural network system, 224 (2010) 403-418.
- [41] M. Jayaraman, R. Sivasubramanian, V. Balasubramanian, A.K. Lakshminarayanan, Optimization of process parameters for friction stir welding of cast aluminium alloy A319 by Taguchi method, *Journal of Scientific & Industrial Research*, 68 (2009) 36–43.
- [42] T. Chen, A Study on Dissimilar FSW Process Parameters in Aluminum Alloy and Low Carbon Steel, International Conference on Smart Manufacturing Application, KINTEX, Gyeonggi-do, Korea, 9-11 April 2008.
- [43] K. Ranjit Roy, A primer on the Taguchi method, 2nd edition, Society of Manufacturing Engineers, 2010.

References of Chapter 3

- [1] K. Ranjit Roy, A Primer on the Taguchi Method, 2nd Edition, Society of Manufacturing Engineers, Michigan, 2010.
- [2] W. Woo, H. Choo, P. J. Withers, Z. Feng, Prediction of hardness minimum locations during natural aging in an aluminum alloy 6061-T6 friction stir weld, *Journal of Materials Science*, 44 (2009) 6302–6309.
- [3] M. Song, R. Kovacevic, Thermal modeling of friction stir welding in a moving coordinate and its validation, *International Journal of Machine Tools & Manufacture*, 43 (2003) 605–615.

- [4] H. Baker, Metal Handbook, Vol. 2, Properties and Selection: Nonferrous Alloy and Pure Metals, 9th edition, American Society for Metals, Ohio, 1979.
- [5] P. Colegrove, M. Painter, D. Graham, T. Miller, 3-dimensional flow and thermal modelling of the friction stir welding process, Proceedings of the 2nd International Symposium on Friction Stir Welding, Gothenburg, Sweden, 2000.
- [6] Heat transfer module-Model library of Comsol 3.4, October 2007.
- [7] A.K. Lakshminarayanan, Process parameters optimization for friction stir welding of RDE-40 aluminum alloy using Taguchi technique, Transactions of Nonferrous Metals Society of China, 18 (2008) 548-554.
- [8] K. Ranjit Roy, A primer on the Taguchi method, 2nd edition, Society of Manufacturing Engineers, 2010.
- [9] D.M. Rodrigues, A. Loureiro. C. Leitao, R.M. Leal, B.M. Chaparro, P. Vilaca, Influence of friction stir welding parameters on the microstructural and mechanical properties of AA 6016-T4 thin welds, Materials and design, 30 (2009) 1913-1921.
- [10] M. Jayaraman, R. Sivasubramanian, V. Balasubramanian, A.K. Lakshminarayanan, Optimization of process parameters for friction stir welding of cast aluminium alloy A319 by Taguchi method, Journal of Scientific & Industrial Research, 68 (2009) 36–43.

References of Chapter 4

- [1] W.M. Thomas, E.D. Nicholas, J.C. Needham, M.G. Murch, P. Temple-Smith, C.J. Dawes, Friction Welding. Cambridge, UK: The Welding Institute TWI Patent Application No 91259788, 19991.
- [2] M.M. Shtrikman, Current state and development of friction stir welding Part 3. Welding International, 22 (2008) 806–815.
- [3] M. Nourani, A.S. Milani, S. Yannacopoulos, Taguchi optimization of process parameters in friction stir welding of 6061 aluminum alloy: a review and case study, Engineering, 3 (2011) 144-155.

- [4] P. Colegrove, H. Shercliff, P. Threadgill, Modelling and development of the Trivex (TM) friction stir welding tool, Proc. 4th International Symposium on Friction Stir Welding, TWI Ltd., Park City, (CD-ROM), 2003.
- [5] H. Schmidt, J. Hattel, CFD modelling of the shear layer around the tool probe in friction stir welding, Proc. of Friction Stir Welding and Processing III, K. V. Jata *et al*, eds., TMS, San Francisco, (2005) 225-232.
- [6] T. Long, W. Tang, A.P. Reynolds, Process response parameter relationships in aluminium alloy friction stir welds, Sci. Tech. Weld. Join., 12 (2007) 311-318.
- [7] A. Arora, Z. Zhang, A. De, T. Debroy, Strains and strain rates during friction stir welding, Scrip. Mater., 61 (2009) 863-866.
- [8] C. Chen, R.Kovacevic, Finite element modeling of friction stir welding-thermal and thermomechanical analysis Inter. J. Mach. Tool. Manuf., 43 (2003) 1319-1326.
- [9] H. Schmidt, J. Hattel, A local model for the thermomechanical conditions in friction stir welding, Model. Sim. Mater. Sci. Eng., 13 (2005) 77-93.
- [10] L. Fratini, G. Buffa, D. Palmeri, Using a neural network for predicting the average grain size in friction stir welding processes, Comp. Struc., 87 (2009) 1166-1174.
- [11] Z. Zhang, H.W. Zhang, Numerical studies on controlling of process parameters in friction stir welding, J. Mater. Proc. Tech., 9 (2009) 241-270.
- [12] T. Azimzadegan, S. Serajzadeh, Thermo-mechanical modeling of friction stir welding, Int. J. Mater. Research, 101 (2010) 390-397.
- [13] M. Assidi, L. Fourment, S. Guerdoux, T. Nelson, Friction model for friction stir welding process simulation: calibrations from welding experiments, Inter. J. Mach. Tool. Manuf., 50 (2010) 143-155.

- [14] R. Hamilton, D. Mackenzie, H. Li, Multi-physics simulation of friction stir welding process, *Eng. Comput.*, 27 (2010) 967-985.
- [15] H.J. Aval, S. Serajzadeh, A.H. Kokabi, Theoretical and experimental investigation into friction stir welding of AA 5086, *Inter. J. Adv. Manuf. Tech.*, 52 (2011) 531-544.
- [16] K.J. Colligan, R.S. Mishra, A conceptual model for the process variables related to heat generation in friction stir welding of aluminum, *Scrip. Mater.*, 58 (2008) 327-331.
- [17] P. Heurtier, M.J. Jones, C. Desrayaud, J.H. Driver, F. Montheillet, D. Allehaux, Mechanical and thermal modelling of friction stir welding, *J. Mater. Proc. Technol.*, 171 (2006) 348-357.
- [18] J.H. Hattel, H. Schmidt, C. Tutum, Thermomechanical modelling of friction stir welding. *Trends in Welding Research, Proceedings of the 8th International Conference*, ASM, Stan A. David Ed., 1-10, 2009.
- [19] D. Radaj, Integrated finite element analysis of welding residual stress and distortion. *The Proceedings of the 6th Mathematical Modelling of Weld Phenomena*, 469-485, 2002.
- [20] S.W. Williams, P.A. Colegrove, H. Shercliff, P. Prangnell, J. Robson, P. Withers, Integrated modelling of the friction stir welding process. *The Proceedings of the 6th International Symposium on Friction Stir Welding*, 1-10, 2006.
- [21] N. Kamp, P.A. Colegrove, H.R. Shercliff, J.D. Robson, Microstructure – property modelling for friction stir welding of aerospace aluminium alloys. *The Proceedings of the 8th International Symposium on Friction Stir Welding*, 1-20, 2010.
- [22] C. Gallais, A. Denquin, Y. Bréchet, G. Lapasset, Precipitation microstructures in an AA6056 aluminium alloy after friction stir welding: Characterisation and modelling. *Materials Science and Engineering A*, 496 (2008) 77-89.
- [23] J.H. Hattel, Integrated modelling in materials and process technology. *Materials Science and Technology*, 24 (2008) 137-149.

- [24] E. Hersent, J.H. Driver, D. Piot, C. Desrayaud, Integrated modelling of precipitation during friction stir welding of 2024-T3 aluminium alloy. *Materials Science and Technology*, 26 (2010) 1345-1352.
- [25] A. Simar, Y. Bréchet, B. de Meester, A. Denquin, C. Gallais, T. Pardoën, Integrated modeling of friction stir welding of 6xxx series Al alloys: Process, microstructure and properties. *Progress in Materials Science*, 57 (2012) 95-183.
- [26] Z. Feng, X.-L. Wang, S.A. David, P.S. Sklad, Modelling of residual stresses and property distributions in friction stir welds of aluminium alloy 6061-T6. *Science and Technology of Welding & Joining*, 12 (2007) 348-356.
- [27] C. Mapelli, L. Bergami, Simulation of the inverse extrusion of brass rod by the coupling of fluid mechanical, thermal and ALE modules. *The Proceedings of the COMSOL Users Conference, Milan*, 1-6, 2006.
- [28] T.D. Vuyst, O. Magotte, A. Robineau, J.-C. Goussain, L. D'Alvise, Multi-physics simulation of the material flow and temperature field around FSW tool. *The Proceedings of the 6th International Symposium on Friction Stir Welding*, 1-19, 2006.
- [29] D. Deloison, F. Marie, B. Guerin, B. Journet, Multi-physics modelling of bobbin-tool friction stir welding – simulation and experiments. *The Proceedings of the 7th International Symposium on Friction Stir Welding*, 1-12, 2008.
- [30] R. Lopez, B. Ducoeur, M. Chiumenti, B.D. Meester, C.A.D. Saracibar, Modeling precipitate dissolution in hardened aluminium alloys using neural networks. *International Journal of Material Forming*, 1 (2008) 1291-1294.
- [31] T.D. Vuyst, V. Madhavan, B. Ducoeur, A. Simar, B.D. Meester, L.D. Alvise, A thermo-fluid / thermo-mechanical modelling approach computing temperature cycles and residual stresses in FSW. *The Proceedings of the 7th International Symposium on Friction Stir Welding*, 1-19, 2008.

- [32] R. Hamilton, D. MacKenzie, H. Li, Multi-physics simulation of friction stir welding process. *Engineering Computations*, 27 (2010) 967-985.
- [33] D. Jacquin, B.D. Meester, A. Simar, D. Deloison, F. Montheillet, C. Desrayaud, A simple Eulerian thermomechanical modeling of friction stir welding. *Journal of Materials Processing Tech.*, 211 (2011) 57-65.
- [34] M. Crumbach, M. Goerdeler, G. Gottstein, L. Neumann, H. Aretz, R. Kopp, Through-process texture modelling of aluminium alloys. *Model. Simul. Mater. Sci. Eng.*, 12 (2004) S1- S18.
- [35] A. Bellini, J. Thorborg, J.H. Hattel, Thermo-mechanical modelling of aluminium cast parts during solution treatment. *Model. Simul. Mater. Sci. Eng.*, 14 (2006) 677–688.
- [36] A. Kermanpur, P.D. Lee, S. Tin, M. McLean Integrated model for tracking defects through full manufacturing route of aerospace discs. *Mater. Sci. Technol.*, 21 (2005) 437–444.
- [37] Ch.-A. Gandin, Y. Brechet, M. Rappaz, G. Canova, M. Ashby, H. Schercliff, Modelling of solidification and heat treatment for the prediction of yield stress of cast alloys. *Acta Mater.*, 50 (2002) 901–927.
- [38] O.R. Myhr, O. Grong, H.G. Fjaer, C.D. Marioara, Modelling of the microstructure and strength evolution in Al-Mg-Si alloys during multistage thermal processing. *Acta Mater.*, 52 (2004) 4997–5008.
- [39] A. Lundback, H. Alberg, P. Henrikson, Simulation and validation of TIG-welding and post weld heat treatment of an Inconel 718 plate. *The proceeding of the Mathematical modelling of weld phenomena 7*, (H. Cerjak *et al.* ed.), Graz, Technical University of Graz, 683–696, 2005.
- [40] M. Nourani, A.S. Milani, S. Yannacopoulos, C. Yan, Predicting grain size distribution in friction stir welded 6061 aluminum, *The 9th International Symposium on Friction Stir Welding*, Huntsville, USA , 1-9, 2012.

- [41] M. Nourani, A. S. Milani, S. Yannacopoulos, C. Yan, Predicting residual stresses in friction stir welding of aluminum alloy 6061 using an integrated multiphysics model, Submitted to the 9th International Conference on Residual Stresses (ICRS 9), Garmisch-Partenkirchen, Germany, 2012.
- [42] H.K. Versteeg, W. Malalasekera, An introduction to computational fluid dynamics the finite volume method, Longman Scientific & Technical, New York, 1995.
- [43] M. Nourani, A.S. Milani, S. Yannacopoulos, A new approach to measure strain during friction stir welding using viscoplasticity, Proc of ASME Conference, Denver, 1-7, 2011.
- [44] S. Xu, X. Deng, A study of texture patterns in friction stir welds. *Acta Materialia*, 56 (2008) 1326-1341.
- [45] H. Atharifar, D. Lin, R. Kovacevic, Numerical and experimental investigations on the loads carried by the tool during friction stir welding, *J Mater Eng Perform*, 339-350, 2009.
- [46] R. Lewis, P. Nithiarasu, K. Seetharamu, Fundamentals of the finite element method for heat and fluid flow, John Wiley & Sons, Ltd, New York, 2004.
- [47] C.M. Sellars, W.J.M. Tegart, On the mechanism of hot deformation. *Acta Metall.*, 14 (1966) 1136–1138.
- [48] T. Sheppard, D. Wright Determination of flow stress: Part 1 constitutive equation for aluminum alloys at elevated temperatures. *Met. Technol.*, 6 (1979) 215–223.
- [49] P.A. Colegrove, H. R. Shercliff, R. Zettler, Model for predicting heat generation and temperature in friction stir welding from the material properties. *Science and Technology*, 12 (2007) 284-298.
- [50] K. Tello, A. Gerlich, P. Mendez, Constants for hot deformation constitutive models for recent experimental data, *Sci Tech Weld Join*, 15 (2010) 260–266.

- [51] P. Wriggers, *Nonlinear Finite Element Methods.*, Springer-Verlag Berlin Heidelberg, Germany, 2008.
- [52] T. Long, A.P. Reynolds, Parametric studies of friction stir welding by commercial fluid dynamics simulation. *Science And Technology*, 11 (2006) 200-209.
- [53] T.U. Seidel, A.P. Reynolds, Two-dimensional friction stir welding process model based on fluid mechanics. *Science And Technology*, 175-184, 2003.
- [54] T. Sheppard, A. Jackson, Constitutive equations for use in prediction of flow stress during extrusion of aluminum alloys. *Materials Science and Technology*, 13 (1997) 203-209.
- [55] H. Wang, P. A. Colegrove, H.M. Mayer, L. Campbell, J.D. Robson, Material constitutive behaviour and microstructure study on aluminum alloys for friction stir welding. *Advanced Material Research*, 89-91 (2010) 615-622.
- [56] J. Schneider, R. Beshears, A.C. Nunes, Interfacial sticking and slipping in the friction stir welding process. *Materials Science and Engineering A*, 436 (2006) 297-304.
- [57] W.J. Arbegast, Modeling friction stir joining as a metal working process, in *Hot deformation of aluminum alloys*, ed. Z. Jin. TMS Warrendale, 2003.
- [58] K. Colligan, Material flow behavior during friction stir welding of aluminum. *Welding Journal*, 78 (1999) 229-237.

References of Chapter 5

- [1] Y.J. Chao, X. Qi, Thermal and thermo-mechanical modeling of friction stir welding of aluminum alloy 6061-T6, *J. Mat. Process. Manuf. Sci.* 7 (1998) 215–233.
- [2] P. Dong, F. Lu, J.K. Hong, Z. Cao, Analysis of weld formation process in friction stir welding, *Proceedings of the First International Conference on Friction Stir Welding*, TWI, Thousand Oaks, 1999.

- [3] A. Reynolds, X. Deng, T. Seidel, S. Xu, Recent advances in FSW process physics, Proceedings of the International Conference of Joining of Advanced and Specialty Materials, TWI, St. Louis, 2000.
- [4] R.L. Goetz, K.V. Jata, Modeling friction stir welding of titanium and aluminum alloys, in: V. Jata, et al. (Eds.), Friction Stir Welding and Processing, TMS, Warrendale, 2001, pp. 35-42.
- [5] A. Askari, S. Silling, B. London, M.W. Mahoney, Modeling and analysis of friction stir welding processes, in: V. Jata, et al. (Eds.), Friction Stir Welding and Processing, TMS, Warrendale, 2001, pp. 43-54.
- [6] P. Dong, F. Lu, J.K. Hong, Z. Cao, Coupled thermomechanical analysis of friction stir welding process using simplified models, Sci. Technol. 6 (2001) 281-287.
- [7] X. Deng, S. Xu, Solid mechanics simulation of friction stir welding process, Trans. NAMR–SME 29 (2001) 631–. 638.
- [8] P. Heurtier, C. Desrayaud, F. Montheillet, A thermomechanical analysis of the friction stir welding process, Mat. Sci. Forum. 396-402 (2002) 1537–1542.
- [9] S. Xu, X. Deng, Three-dimensional model for the friction-stir welding process. Theor. Appl. Mech. 21 (2002) 699-704.
- [10] C.M. Chen, R. Kovacevic, Finite element modeling of friction stir welding-thermal and thermomechanical analysis, J. Mach. Tools Manuf. 43 (2003) 1319-1326.
- [11] S. Guerdoux, L. Fourment, M. Miles, C. Sorensen, Numerical simulation of friction stir welding process using both Lagrangian and arbitrary Lagrangian Eulerian formulations, in: S. Ghosh, J.C. Castro, J.K. Lee (Eds.), Proceedings of Materials Processing and Design: Modeling, Simulation and Applications Conference, AIP, Columbus , 2004, pp. 1259-1264.
- [12] C. Chen, R. Kovacevic, Thermomechanical modelling and force analysis of friction stir welding by the finite element method. J. Mech. Eng. Sci. 218 (2004) 509-519.

- [13] L. Fourment, S. Guerdoux, M. Miles, T. Nelson, Numerical simulation of the friction stir welding process using both lagrangian and arbitrary lagrangian eulerian formulations, Proceedings of the Fifth International Conference on Friction Stir Welding, TWI, Metz, 2004.
- [14] R.W. McCune, H. Ou, C.G. Armstrong, M. Price, Modelling friction stir welding with the finite element method: A Comparative Study, Proceedings of the Fifth International Conference on Friction Stir Welding, TWI, Metz, 2004.
- [15] H. Schmidt, J. Hattel, Modelling thermomechanical conditions at the tool / matrix interface in Friction Stir Welding, Proceedings of the Fifth International Conference on Friction Stir Welding, TWI, Metz, 2004.
- [16] X.K. Zhu, Y.J. Chao, Numerical simulation of transient temperature and residual stresses in friction stir welding of 304L stainless steel, J. Mat. Process. Tech. 146 (2004) 263-272.
- [17] H.W. Zhang, Z. Zhang, J.T. Chen, The finite element simulation of the friction stir welding process, Mat. Sci. Eng.: A. 403 (2005) 340–348.
- [18] H. Schmidt, J. Hattel, A local model for the thermomechanical conditions in friction stir welding, Modelling Simul. Mat. Sci. Eng. 13 (2005) 77-93.
- [19] V. Soundararajan, S. Zekovic, R. Kovacevic, Thermo-mechanical model with adaptive boundary conditions for friction stir welding of Al 6061, Int. J. Mach. Tools Manuf. 45 (2005) 1577-1587.
- [20] Z. Zhang, J.T. Chen, H.W. Zhang, Modeling of the friction stir process under different pressures on the shoulder, J. Aeronaut. Mat. 25 (2005) 33-37.
- [21] D. Forrest, J. Nguyen, M. Posada, J. Deloach, D. Boyce, J. H. Cho, Simulation of HSLA-65 friction stir welding, Proceedings of the 7th International Conference on Trends in Welding Research, ASM, Pine Mountain, 2005.

- [22] J. Hua, R. Shivpuri, L. Fratini, A continuum based fem model for friction stir welding—model development, *Mat. Sci. Eng. A*, 419 (2006) 389-396.
- [23] H.W. Zhang, Z. Zhang, J. Bie, L. Zhou, J. Chen, Effect of viscosity on material behavior in friction stir welding process, *Trans. Nonferrous Met. SOC. China*. 16(2006) 1045-1052.
- [24] G. Buffa, L. Fratini, J. Hua, R. Shivpuri, Friction stir welding of tailored blanks: investigation on process feasibility, *Annals of the CIRP*. 55 (2006) 2-5.
- [25] G. Buffa, J. Hua, R. Shivpuri, L. Fratini, Design of the friction stir welding tool using the continuum based FEM model, *Mat. Sci. Eng. A*. 419 (2006) 381-388.
- [26] P. Heurtier, M.J. Jones, C. Desrayaud, J. H. Driver, F. Montheillet, D. Allehaux, Mechanical and thermal modelling of friction stir welding, *J. Mat. Proc. Technol*. 171 (2006) 348-357.
- [27] J.H. Cho, P.R. Dawson, Investigation on texture evolution during friction stir welding of stainless steel, *Metall. Mat. Trans. A*. 37(2006) 1147-1164.
- [28] Z. Zhang, H.W. Zhang, Material behaviors and mechanical features in friction stir welding process, *Inter. J. Adv. Manuf. Technol*. 35 (2007) 86-100.
- [29] H.W. Zhang, Z. Zhang, J.T. Chen, 3D modeling of material flow in friction stir welding under different process parameters, *J. Mat. Process. Technol*. 183 (2007).62-70.
- [30] Z. Zhang, H.W. Zhang, Numerical studies on effect of axial pressure in friction stir welding, *Sci. Technol. Weld. Join*. 12 (2007) 226-249.
- [31] D. Jacquin, C. Desrayaud, F. Montheillet, A thermo-fluid analysis of the friction stir welding process, *Mat. Sci. Forum*, 539-543 (2007) 3832-3837.
- [32] J.H. Cho, S.H. Kang, K. Hwan Oh., H.N.Han, S.B. Kang, Friction stir weld modeling of aluminum alloys, *Adv. Mat. Research*. 26-28 (2007) 999-1002.

- [33] Y. He, D.E. Boyce, P.R. Dawson, Three-dimensional modeling of void growth in friction stir welding of stainless steel, Proceedings of the Materials Processing and Design: Modeling, Simulation and Applications Conference, AIP, Porto, 2007.
- [34] J.H. Cho, H.W. Kim, S.B. Kang, Overview of modeling strength evolution during friction stir welding, *Mat. Sci. Forum.* 575-78 (2008) 805-810.
- [35] J.H. Cho, P.R. Dawson, Modeling texture evolution during friction stir welding of stainless steel with comparison to experiments, *J. Eng. Mat. Technol.* 130 (2008) 1-12.
- [36] Y. He, P.R. Dawson, D.E. Boyce, Modeling damage evolution in friction stir welding process, *J. Eng. Mat. Technol.* 130 (2008) 1-10.
- [37] A. Bastier, M.H. Maitournam, F. Roger, K.D. Van, Modelling of the residual state of friction stir welded plates, *J. Mat. Process. Technol.* 200 (2008) 25–37.
- [38] Z. Zhang, H.W. Zhang, Simulation of 3D material flow in friction stir welding of AA6061-T6, *China Weld.* 17 (2008) 57-63.
- [39] G. Buffa, L. Fratini, R. Shivpuri, Finite element studies on friction stir welding processes of tailored blanks, *Compu. Struct.* 86 (2008) 181-189.
- [40] H. Li, D. Mackenzie, Coupled thermo-mechanical modelling of friction stir welding, Proceedings of ASME Pressure Vessels and Piping Division Conference, ASME, San Antonio, 2008.
- [41] Z. Zhang, H.W. Zhang, A fully coupled thermo-mechanical model of friction stir welding, *Inter. J. Adv. Manuf. Technol.* 37(2008) 279-293.
- [42] H.B. Schmidt, J.H. Hattel, A thermal-pseudo-mechanical model for the heat generation in Friction Stir Welding, *Scrip. Mat.* 58 (2008) 332–337.

- [43] O. Lorrain, V. Favier, H. Zahrouni, M.E. Hadrouz, A critical analysis of FSW simulations, Proceedings of 7th International Friction Stir Welding Symposium, TWI, Awaji Island, 2008.
- [44] G. Buffa, L. Fratini, S. Pasta, R. Shivpuri, On the thermo-mechanical loads and the resultant residual stresses in friction stir processing operations, *Mat. Sci. Eng. A.* 57 (2008). 287-290.
- [45] L. Fratini, G. Buffa, Metallurgical phenomena modeling in friction stir welding of aluminium alloys: analytical versus neural network based approaches, *J. Eng. Mat. Technol.* 130 (2008) 1-6.
- [46] Z. Zhang, H.W. Zhang, Numerical studies on the effect of transverse speed in friction stir welding, *Mat. Design.* 30 (2009) 900-907.
- [47] G. Buffa, G. Campanile, L. Fratini, A. Prisco, Friction stir welding of lap joints: Influence of process parameters on the metallurgical and mechanical properties, *Mat. Sci. Eng. A.* 519 (2009) 19-26.
- [48] M. Grujicic, T. He, G. Arakere, , H.V. Yalavarthy, C.F. Yen, B.A. Cheeseman, Fully coupled thermomechanical finite element analysis of material evolution during friction-stir welding of AA5083, *J. Eng. Manuf.* 224 (2009) 609-625.
- [49] Z. Zhang, H.W. Zhang, Numerical studies on controlling of process parameters in friction stir welding, *J. Mat. Proc. Technol.* 209 (2009) 241-270.
- [50] L. Fratini, G. Buffa, D. Palmeri, Using a neural network for predicting the average grain size in friction stir welding, processes. *Comput. Struc.*, 87 (2009) 1166-1174.
- [51] J. Gagner, A. Ahadi, Finite element simulation of an AA2024-T3 friction stir weld, *Inter. Rev. Mech. Eng.* 3 (2009) 427-436.
- [52] G. Buffa, L. Fratini, B. Arregi, M. Penalva, A new friction stir welding based technique for corner fillet joints: experimental and numerical study, *Int. J. Mat. Form.* 3 (2010) 1039-1042.

- [53] R. Hamilton, D. MacKenzie, H. Li, Multi-physics simulation of friction stir welding process, *Int. J. Comp. Aid. Eng. Soft.* 27 (2010) 967-985.
- [54] S. Mukherjee, A. Ghosh, Flow visualization and estimation of strain and strain-rate during friction stir process, *Mat. Sci. Eng.: A.* 527(2010) 5130-5135.
- [55] F. Gemme, Y. Verreman, L. Dubourg, M. Jahazi, Numerical analysis of the dwell phase in friction stir welding and comparison with experimental data, *Mat. Sci. Eng. A.* 527 (2010) 4152-4160.
- [56] M. Assidi, L. Fourment, S. Guerdoux, T. Nelson, Friction model for friction stir welding process simulation : Calibrations from welding experiments, *Inter. J. Mach. Tool. Manuf.* 50 (2010) 143-155.
- [57] T. Azimzadegan, S. Serajzadeh, Thermo-mechanical modeling of friction stir welding, *Int. J. Mat. Res.* 101 (2010) 390-397.
- [58] G.A. Moraitis, G.N. Labeas, Investigation of friction stir welding process with emphasis on calculation of heat generated due to material stirring, *Sci. Technol. Weld. Join.* 15 (2010) 177-184.
- [59] P.F. Mendez, K.E. Tello, T.J. Lienert, Scaling of coupled heat transfer and plastic deformation around the pin in friction stir welding, *Act. Mat.* 58 (2010) 6012-6026.
- [60] C.C. Tutum, J.H. Hattel, A multi-objective optimization application in friction stir welding: considering thermo-mechanical aspects, *Proceedings of IEEE World Congress on Computational Intelligence and Congress on Evolutionary Computation*, IEEE, Barcelona, 2010.
- [61] K.L. Nielsen, T. Pardoen, V. Tvergaard, B. D. Meester, A. Simar, Modelling of plastic flow localisation and damage development in friction stir welded 6005A aluminium alloy using physics based strain hardening law, *Int. J. Solid. Struct.* 47 (2010) 2359-2370.

- [62] M. Grujicic, G. Arakere, H. V. Yalavarthy, T. He, C. Yen, B.A. Cheeseman, Modeling of AA5083 material-microstructure evolution during butt friction-stir welding, *J. Mat. Eng. Perform.* 19 (2010) 672-684.
- [63] H. Jamshidi Aval, S. Serajzadeh, A.H. Kokabi, Theoretical and experimental investigation into friction stir welding of AA 5086, *Int. J. Adv. Manuf. Technol.* 52 (2011) 531-544.
- [64] D. Jacquin, B.D. Meester, A. Simar, D. Deloison, F. Montheillet, C. Desrayaud, A simple Eulerian thermomechanical modeling of friction stir welding, *J. Mat. Process. Technol.* 211 (2011) 57-65.
- [65] G. Buffa, A. Ducato, L. Fratini, Numerical procedure for residual stresses prediction in friction stir welding, *Finit. Elem. Analy. Design.* 47 (2011) 470-476.
- [66] M. Grujicic, B. Pandurangan, C. Yen, B.A. Cheeseman, Modifications in the AA5083 Johnson-Cook material model for use in friction stir welding computational analyses, *J. Mat. Eng. Perform.* 21 (2012). 2207-2217.
- [67] A. Simar, Y. Bréchet, B. De Meester, A. Denquin, C. Gallais, T. Pardoën, Integrated modeling of friction stir welding of 6xxx series Al alloys: Process, microstructure and properties, *Progress Mat. Sci.* 57 (2012) 95-183.
- [68] G.J. Bendzsak, T. North, C. Smith, An experimentally validated 3D model for friction stir welding, *Proceedings of the 2nd International Symposium on Friction Stir Welding*, TWI, Gothenburg, 2000.
- [69] P.A. Colegrove, M. Painter, D. Graham, T. Miller, 3 dimensional flow and thermal modeling of the friction stir welding process, *Proceedings of the 2nd International Symposium on Friction Stir Welding*, TWI, Gothenburg, 2000.
- [70] P. Ulysse, Three-dimensional modeling of the friction stir-welding. *Process Int. J. Mach. Tools. Manuf.*, 42 (2002) 1549-1557.

- [71] H.R. Shercliff, P.A. Colegrove, Modelling of friction stir welding, Proceedings of the Mathematical Modeling of Weld Phenomenon 6 Conference, Maney, Graz, 2002.
- [72] A. P. Reynolds, K. Linder, W. Tang, T.U. Siedel, Weld efficiency and defect formation correlation between experiment and simple models, Proceedings of the 6th International Trends in Welding Research Conference, ASM, Pine Mountain, 2003.
- [73] A. P. Reynolds, M.Z.H. Khandkar, T. Long, W. Tang, J.A. Khan, Utility of relatively simple models for understanding process parameter effects on FSW, Mat. Sci. Forum. 426-432 (2003) 2959-2694
- [74] P.A. Colegrove, H.R. Shercliff, Experimental and numerical analysis of aluminium alloy 7075-T7351 friction stir welds, Sci. Technol. Weld. Join. 8 (2003) 360-368.
- [75] T.U. Seidel, A.P. Reynolds, Two-dimensional friction stir welding process model based on fluid mechanics, Sci. Technol. Weld. Join. 8 (2003). 175-183.
- [76] P.A. Colegrove, H.R. Shercliff, Development of Trivex friction stir welding tool part 1–two-dimensional flow modelling and experimental validation, Sci. Technol. Weld. Join. 9 (2004) 345-351.
- [77] P.A. Colegrove, H.R. Shercliff, Development of Trivex friction stir welding tool part 2 – three-dimensional flow modelling, Sci. Technol. Weld. Join. 9 (2004) 352-362.
- [78] D. Schmitter, I.M. Zylla, Modelling friction stir welding with thermally coupled fluid dynamics, J. Phys. 120 (2004) 677-680
- [79] P.A. Colegrove, Modeling and development of the Trivex friction stir welding tool, Weld. World. 48 (2004) 10-26.
- [80] P.A. Colegrove, H.R. Shercliff, 2-Dimensional CFD modelling of flow round profiled FSW tooling. Sci Technol. Weld. Join. 9 (2004) 483-492.

- [81] P.A. Colegrove, H.R. Shercliff, Modelling the friction stir welding of aerospace alloys, Proceedings of the 5th International Symposium on Friction Stir Welding, TWI, Metz, 2004.
- [82] S. Hirasawa, K. Okamoto, S. Hirano, T. Tomimura, Analysis of flow and temperature distribution during friction stir welding, Proceedings of ASME Heat Transfer/Fluids Engineering Summer Conference, ASME, Charlotte, 2004.
- [83] H. Schmidt, J. Hattel, CFD modelling of the shear layer around the tool probe in friction stir welding, Proceedings of Friction Stir Welding and Processing III, TMS, San Francisco, 2005.
- [84] P.A. Colegrove, H.R. Shercliff, 3-Dimensional CFD modelling of flow round a threaded friction stir welding tool profile, J. Mat. Process. Technol. 169 (2005) 320-327.
- [85] R. Nandan, G.G. Roy, T.J. Lienert, T. Debroy, Numerical modelling of 3D plastic flow and heat transfer during friction stir welding of stainless steel, Sci Technol. Weld. Join. 11 (2006) 526-537.
- [86] R. Nandan, G. Roy, Numerical simulation of three-dimensional heat transfer and plastic flow during friction stir welding, Metall. Mat. Trans. A. 37 (2006) 1247-1259.
- [87] A. Bastier, M.H. Maitournam, K.D. Van, F. Roger, Steady state thermomechanical modelling of friction stir welding, Sci Technol. Weld. Join. 11 (2006) 278-288.
- [88] R. Crawford, G.E. Cook, A.M. Strauss, A.C. Nunes, A mechanistic study of the friction stir welding process, Proceedings of the 57th International Astronautical Congress, IAF, Valencia, 2006
- [89] E. Foulvarcit, Y. Goroociturn, F. Boltout, 3D Modelling of Thermofluid Flow in Friction Stir Welding, Proceedings of the 7th International Conference on Trends in Welding Research, ASM, Pine Mountain, 2006.

- [90] R. Crawford, G.E. Cook, A.M. Strauss, D.A. Hartman, M.A. Stremmer, Experimental defect analysis and force prediction simulation of high weld pitch friction stir welding, *Sci Technol. Weld. Join.* 11 (2006) 657-665.
- [91] T. Long, A.P. Reynolds, Parametric studies of friction stir welding by commercial fluid dynamics simulation, *Sci Technol. Weld. Join.* 11 (2006) 200-208.
- [92] H. Schmidt, J. Hattel, Analysis of the velocity field in the shear layer in FSW: experimental and numerical modelling, *Proceedings of 6th International Friction Stir Welding Symposium*, TWI, Saint Sauveur, 2006.
- [93] T. Sato, D. Otsuka, Y. Watanabe, R.S. Division, N. Sharyo Designing of friction stir weld parameters with finite element flow simulation, *Proceedings of 6th International Friction Stir Welding Symposium*, TWI, Saint Sauveur, 2006.
- [94] C.B. Owen, Two dimensional friction stir welding model with experimental validation. Master's Thesis, Brigham Young University, 2006.
- [95] A.M. Tartakovsky, G. Grant, X. Sun, S.T. Hong, M. Khaleel, Smooth particle hydrodynamics (sph) model for friction stir welding (fsw) of dissimilar materials, *Proceedings of 6th International Friction Stir Welding Symposium*, TWI, Saint Sauveur, 2006.
- [96] P.A. Colegrove, H.R. Shercliff, CFD modelling of friction stir welding of thick plate 7449 aluminium alloy, *Sci Technol. Weld. Join.* 11(2006), 429-441.
- [97] R. Crawford, T. Bloodworth, G.E. Cook, A.M. Strauss, D.A. Hartman, High speed friction stir welding process modeling, *Proceedings of 6th International Friction Stir Welding Symposium*, TWI, Saint Sauveur, 2006.
- [98] T.D. Vuyst, O. Magotte, A. Robineau, J.C. Goussain, L. D'Alvise, Multi-physics simulation of the material flow and temperature field around FSW tool, *Proceedings of the Sixth International Conference on Friction Stir Welding*, TWI, Montreal, 2006.

- [99] I. Alfaro, L. Fratini, E. Cueto, F. Chinesta, F. Micari, Meshless simulation of friction stir welding. Proceedings of the Materials Processing and Design: Modeling, Simulation and Applications Conference, AIP, Porto, 2007.
- [100] T. De Vuyst, , & L.D. Alvisé, Material flow around a friction stir welding tool: development of a thermo-fluid code, *Weld. World.* 51 (2007) 37-43.
- [101] H. Chen, Y. Zhao, Y. Zhang, L. Wu, S. Lin, , Mechanistic study on friction stir welding of 2014 aluminium alloy, Proceeding of 58th International Astronautical Congress, IAF/IAA, Hyderabad, 2007.
- [102] H. Atharifar, D.C. Lin, , R. Kovacevic, Studying tunnel-like defect in friction stir welding process using computational fluid dynamics, Proceedings of Materials Science & Technology Conference and Exhibition: Exploring Structure, Processing, and Applications Across Multiple Materials Systems, Detroit, 2007
- [103] L. St-Georges, V. Dassyva-Raymond, L.I. Kiss, A.L. Perron, Transport phenomena in Friction Stir Welding, Proceedings of friction stir welding and processing IV, TMS, Orlando, 2007.
- [104] P.A. Colegrove, H.R. Shercliff, R. Zettler, Model for predicting heat generation and temperature in friction stir welding from the material properties, *Sci Technol. Weld. Join.* 12 (2007) 284-297.
- [105] T. Long, W. Tang, A.P. Reynolds, Process response parameter relationships in aluminium alloy friction stir welds, *Sci Technol. Weld. Join.* 12 (2007) 311-317.
- [106] R. Nandan, , G.G. Roy, T. J. Lienert, T. Debroy, Three-dimensional heat and material flow during friction stir welding of mild steel, *Acta Material.* 55 (2007) 883-895.
- [107] R. Nandan, B. Prabu, A. De, T. Debroy, Improving reliability of heat transfer and materials flow calculations during friction stir welding of dissimilar aluminum alloys, *Weld. Research.* 86 (2007) 313-322.

- [108] H. Atharifar, R. Kovacevic, Numerical study of the tool rake angle effect on the material flow in friction stir welding process, Proceedings of IMECE2007 ASME international Mechanical Engineering Congress and Exposition, ASME, Seattle, 2007.
- [109] S.M. Dörfler, Advanced modeling of friction stir welding – improved material model for aluminum alloys and modeling of different materials with different properties by using the level set method, Proceedings of the COMSOL 2008 Conference, COMSOL, Hannover, 2008.
- [110] L. St-georges, L.I. Kiss, V. Dassylva-Raymond, Mixing mechanism in friction stir welding of metallic composites, Proceedings of 7th International Friction Stir Welding Symposium, TWI, Awaji Island, 2008.
- [111] B.C. Liechty, B.W. Webb, Modeling the frictional boundary condition in friction stir welding., *Int. J. Mach. Tool. Manuf.* 48 (2008) 1474- 1485.
- [112] H. Schmidt, Thermal and material flow modelling of friction stir welding using Comsol, Proceedings of the COMSOL Conference, COMSOL, Hanover, 2008.
- [113] R. Nandan, T.J. Lienert, , T. Debroy, Toward reliable calculations of heat and plastic flow during friction stir welding of TI-6AL-4V alloy, *Int. J. Mat. Res.* 99 (2008) 434-444.
- [114] A. Kumar, D.P. Fairchild, S.J. Ford, Modeling of heat transfer and material flow during FSW of steel, Proceedings of 7th International Friction Stir Welding Symposium, TWI, Awaji Island, 2008.
- [115] D. Kim, H. Badarinarayan, K. Chung, Thermo-mechanical modeling of friction stir butt welding process of AA5083-H18- CFD modeling with steady state description, Proceedings of 7th International Friction Stir Welding Symposium, TWI, Awaji Island, 2008.
- [116] D.H. Lammlein, D.R. DeLapp, P.A. Fleming. A.M. Strauss, G.E. Cook, The application of shoulderless conical tools in friction stir welding: An experimental and theoretical study, *Mat. Design.* 30 (2009) 4012-4022.

- [117] H. Atharifar, D. Lin, R. Kovacevic, Numerical and Experimental Investigations on the Loads Carried by the Tool During Friction Stir Welding, *J. Mat. Eng. Perform.* 18 (2009) 339-350.
- [118] A. Arora, Z. Zhang, A. De, T. Debroy, Strains and strain rates during friction stir welding, *Scrip. Mat.* 61 (2009) 863-866.
- [119] D. Kim, H. Badarinarayan, J. Hoon, C. Kim, K. Okamoto, R.H. Wagoner, Numerical simulation of friction stir butt welding process for AA5083-H18 sheets. *Europ. J. Mech./A Solid.* 29 (2010) 204-215.
- [120] J. Hilgert, H. Schmidt, J.F. Santos, N. Huber, (2010). Moving geometry process model for bobbin Tool FSW, Proceedings of 8th International Friction Stir Welding Symposium, TWI, Timmendorfer Strand, 2010.
- [121] O.C. Zienkiewicz, P.C. Jain, E. Onate, Flow of solids during forming and extrusion- some aspects of numerical solutions, *Int. J. Solids. Struct.* 14 (1978) 15-38.
- [122] A. Bastier, M.H. Maitournam, K.D. Van, F. Roger, Steady state thermomechanical modelling of friction stir welding. *Sci. Technol. Weld. Join.* 11 (2006) 278-289.
- [123] A. Bastier, M.H. Maitournam, F. Roger, K.D. Van, Modelling of the residual state of friction stir welded plates, *J. Mat. Process. Technol.* 200 (2008) 25-37.
- [124] T. De Vuyst, V. Madhavan, B. Ducoeur, A. Simar, B.D. Meester, L.D. Alvisé, A thermo-fluid/ thermo-mechanical modelling approach computing temperature cycles and residual stresses in FSW, Proceedings of the 8th International Conference on Trends in Welding Research, ASM, Pine Mountain, 2008.
- [125] X. Qin, P. Michaleris, Thermo-elasto-viscoplastic modelling of friction stir welding, *Sci. Technol. Weld. Join.* 14 (2009) 640-649.
- [126] M. Nourani, A.S. Milani, S. Yannacopoulos, C.Y. Yan, Predicting residual stresses in friction stir welding of aluminum alloy 6061 using an integrated multiphysics model,

Proceedings of the 9th International Conference on Residual Stresses (ICRS 9), Garmisch-Partenkirchen , 2012.

- [127] B.A.B. Andersson, Thermal stress in a submerged-arc welded joint considering phase transformations, *J. Eng. Mater. Technol.* 100 (1978) 356-362
- [128] V.J. Papazoglou, K. Masubuchi, Numerical analysis of thermal stresses during welding including phase transformation effects, *J. Press. Vessel Technol.* 104 (1982) 198-203.
- [129] M. Nourani, A.S. Milani, S. Yannacopoulos, C. Yan, An integrated multiphysics model for friction stir welding of 6061 Aluminum alloy, *Int. J. of Multiphysics* (under final review), 2013.
- [130] M. Nourani, A.S. Milani, S. Yannacopoulos, C. Yan, Predicting grain size distribution in friction stir welded 6061 aluminum alloy, *Proceedings of 9th International Friction Stir Welding Symposium*, TWI, Huntsville, 2012.
- [131] R. Darby, *Chemical Engineering Fluid Dynamics*, second ed., CRC, New York, 2001.
- [132] F. Irgens, *Continuum Mechanics*, reprint, Springer, 2008.
- [133] P. Perzyna, Fundamental problems in visco-plasticity, in: *Recent Advances in Applied Mechanics*, Academic Press, New York, 1966.
- [134] O.C. Zienkiewicz, I.C. Corneau, Visco-plasticity. plasticity and creep in elastic solids: a unified numerical solution approach, *Int. J Num. Meth. Eng.* 8 (1974) 821-845.
- [135] K. Kuykendall, C. Sorensen, T. Nelson, (2011). A comparison of experimental data and model predictions with constitutive laws commonly used to model friction stir welding, *Proceedings of Friction Stir Welding and Processing V Conference*, John Wiley & Sons Inc., Hoboken, 2011.
- [136] P.J. Carreau, Rheological equations from molecular network theories, *Trans Soc Rheol.* 16 (1972) 99-127.

- [137] G.J. Bendzsak, T.H. North, Z. Li , Numerical model for steady state flow in friction welding, *Acta. Mater.* 45 (1997) 1735-1745.
- [138] G.J. Bendzsak, T.H. North, Numerical modelling of fluid dynamics and heat transfer in friction welding, *Proceedings of Mathematical Modelling of Weld Phenomena 4*, Institute of Materials, London, 1998.
- [139] T.C. Papanastasiou, Flows of materials with yield, *J. Rheo.* 31(1987) 385-390.
- [140] J.C. Simo, T.J.R. Hughes, *Computational inelasticity: Interdisciplinary Applied Mathematics*, Springer-Verlag, New York, 1998.
- [141] F. Humphreys, M. Hatherly, *Recrystallization and Related Annealing Phenomena*, second ed., Elsevier, Oxford, 2004.
- [142] C. Zener, J.H. Hollomon, Effect of strain rate upon plastic flow of steel, *J. App. Phys.* 15 (1944) 22-32.
- [143] C.M. Sellars, W.J.McG. Tegart, Hot workability, *Int. Met. Rev.*, 17 (1972) 1-24.
- [144] T. Sheppard, D.S. Wright, Determination of flow stress: Part 1 constitutive equation for aluminum alloys at elevated temperatures, *Met. Technol.* 6 (1979) 215-223.
- [145] K. Tello, A. Gerlich, P. Mendez, Constants for hot deformation constitutive models for recent experimental data, *Sci. Technol. Weld. Join.* 15(2010) 260–266.
- [146] R.G. Johnson, W. H. Cook, A constitutive model and data for metals subjected to large strains, high strain rates and high temperatures. *Proceedings of International Symposium on Ballistics*, ADPA, Hague, 1983.
- [147] J.L. Chenot, M. Bellet, The viscoplastic approach for the finite element modeling of metal forming processes, in: P Hartley, I Pillinger and C Sturgess (Eds.) *Numerical modelling of material deformation processes*, Springer-Verlag, 1992, 179-224.

- [148] R.H. Wagoner, J.L. Chenot, *Metal Forming Analysis*, Cambridge University Press, New York, 2001.
- [149] H. Mecking, U.F. Kocks, Kinetics of flow and strain-hardening, *Acta Metal.* 29 (1981) 1865–75.
- [150] Y. Estrin, H. Mecking A unified phenomenological description of work hardening and creep based on one-parameter models, *Acta Metal.* 32 (1984) 57–80.
- [151] U.F. Kocks, H. Mecking, Physics and phenomenology of strain hardening: the FCC case, *Prog. Mater. Sci.* 48 (203) 171–273.
- [152] E. Voce, Practical strain-hardening function, *Acta Metal.* 51 (1955) 219-26.
- [153] E.W. Hart, Constitutive relations for the nonelastic deformation of metals, *J. Eng. Mater. Technol.* 98 (1976) 193-202.
- [154] G. Eggert, P. Dawson, On the use of internal variable constitutive equations in transient forming processes, *Int. J. Mech. Sci.* 29 (1987) 95-113.
- [155] G. Eggert, P. Dawson, A viscoplastic formulation with elasticity for transient metal forming, *Comput. Meth. Appl. Mech. Eng.* 70 (1988) 165-90.
- [156] A. Garvus, Formulation of a new constitutive equation available simultaneously for static and dynamic loading. *Proceedings of the 9th International Conference on the Mechanical and Physical Behaviour of materials under Dynamic Loading, DYMAT, Brussels, 2009.*
- [157] F.J. Zerilli, R.W. Armstrong, Dislocation-mechanics-based constitutive relations for material dynamics calculations, *J. App. Phys.* 61 (1987)1816-1825.
- [158] P.S. Follansbee, U.F. Kocks, A constitutive description of the deformation of copper based on the use of the mechanical threshold, *Acta Metal.* 36 (1988) 81–93.

- [159] Private communication between Maekawa and Childs as appeared in Childs, T. H. C, Material Property Requirements for Modeling Metal Machining, 1997, Colloque C3, Journal de physique, III: XXI–XXXIV.
- [160] U.R. Andrade, M.A. Meyers, K.S. Vecchio, A.H. Chokshi, Dynamic recrystallization in high-strain, high-strain-rate plastic deformation of copper, *Acta Metal. et Mater.* 42 (1994) 3183–95.
- [161] K. Maekawa, T. Shirakashi, E. Usui, Flow stress of low carbon steel at high temperature and strain rate (Part 2), *Bull. Jap. Soc. Precis. Eng.* 17 (1983) 167-72.
- [162] D.J. Bammann, M.L. Chiesa, G.C. Johnson, Modeling large deformation and failure in manuf. processes, Proceedings of Theoretical and Applied Mechanics Conference, Kyoto, 1996.
- [163] S. Nemat-Nasser, J.B. Isaacs. Direct measurement of isothermal flow stress of metals at elevated temperatures and high strain rates with application to Ta and Ta–W alloys. *Acta Mater.* 45 (1997) 907-19.
- [164] N. Jones, *Structural Impact*. Cambridge University Press, Cambridge, 1989.
- [165] D.J. Steinberg, S.G. Cochran, M.W. Guinan, A constitutive model for metals applicable at high-strain rate, *J. Appl. Phys.* 51 (1980) 1498-1504.
- [166] D.J. Steinberg, C.M. Lund, A constitutive model for strain rates from 10^{-4} to 10^6 s⁻¹, *J. Phys. Colloq.* 49 (1988) 3-3.
- [167] D.L. Preston, D.L. Tonks, D.C. Wallace, Model of plastic deformation for extreme loading conditions, *J. Appl. Phys.* 93 (2003) 211-220.
- [168] H.J. Kleemola, M.A. Nieminen, On the strain-hardening parameters of metals, *Metall. Trans.* 5 (1974) 1863-1866.

- [169] P. Ludwik, *Elemente der Technologischen Mechanik*, Verlag von Julius, Springer, Berlin, 1909.
- [170] J.H. Hollomon, Tensile deformation, *Trans. AIME*, 162 (1945) 268-90.
- [171] H.W. Swift, Plastic instability under plane stress, *J. Mech. Phys. Solid.* 1 (1952) 1-18.
- [172] E. Voce, The relationship between stress and strain for homogeneous. deformation, *J. Inst. Metal.* 74 (1948) 537-62.
- [173] Z. Marciniak, J.L. Duncan, S.J. Hu, *Mechanics of Sheet Metal Forming*, Butterworth-Heinemann, London, 2002.
- [174] D.R. Lesuer, G. Kay, M. LeBlanc, Modeling large-strain, high-rate deformation in metals. Proceedings of the 3rd Biennial Tri-Laboratory Engineering Conference on Modeling and Simulation, Pleasanton, 1999.

References of Chapter 6

- [1] T.R. Mcnelley, J.Q. Su, Recrystallization mechanisms during friction stir welding/processing of aluminum alloys, *Scrip. Mater.*, 58 (2008) 349-354.
- [2] M.D. Fuller, S. Swaminathan, A.P. Zhilyaev, T.R. Mcnelley, Microstructural transformations and mechanical properties of cast nial bronze : effects of fusion welding and friction stir processing, *Mater. Sci. Eng. A*, 463 (2007) 128-137.
- [3] P.B. Prangnell, C.P. Heason, Grain structure formation during friction stir welding observed by the stop action technique, *Acta Mater.*, 53 (2005) 3179-3192.
- [4] K. Oh-ishi, A.P. Zhilyaev, T.R. Mcnelley, a microtexture investigation of recrystallization during friction stir processing of as-cast Ni Al bronze, *Metal. Mater. Trans. A*, 37 (2006) 2239-2251.
- [5] J. Su, T.W. Nelson, C.J. Sterling, Microstructure evolution during FSW / FSP of high strength aluminum alloys, *Mater. Sci. Eng. A*, 405 (2005) 277-286.

- [6] L.E. Murr, G. Liu, J.C. McClure, Dynamic recrystallization in friction-stir welding of aluminium alloy 1100, *J. Mater. Sci. Letter.*, 16 (1997) 1801-1803.
- [7] F.J. Humphreys, P.B. Prangnell, J.R. Bowen, A. Gholinia, C. Harris, Developing stable fine-grain microstructures by large strain deformation, *Philos. Trans. Royal Soci. A*, 357 (1999) 1663–1681.
- [8] H. Schmidt, J. Hattel, A local model for the thermomechanical conditions in friction stir welding, *Model. Sim. Mater. Sci. Eng.*, 13 (2005) 77-93.
- [9] G. Buffa, J. Hua, R. Shivpuri, L. Fratini, Design of the friction stir welding tool using the continuum based fem model, *Mater. Sci. Eng. A*, 419 (2006) 381-388.
- [10] P. Heurtier, M.J. Jones, C. Desrayaud, J.H. Driver, F. Montheillet, D. Allehaux, , et al., Mechanical and thermal modelling of friction stir welding, *J. Mater. Proc. Technol.*, 171 (2006) 348-357.
- [11] T. Long, W. Tang, A.P. Reynolds, Process response parameter relationships in aluminium alloy friction stir welds, *Sci. Tech. Weld. Join.*, 12 (2007) 311-318.
- [12] Z. Zhang, H.W. Zhang, Numerical studies on effect of axial pressure in friction stir welding, *Sci. Tech. Weld. Join.*, 12 (2007), pp. 226-249.
- [13] S. Xu, X. Deng, A study of texture patterns in friction stir welds, *Acta Mater.*, 56(2008) 1326-1341.
- [14] Z. Zhang, , and H.W. Zhang, Numerical Studies on the effect of transverse speed in friction stir welding, *Mater. Design*, 30 (2009) 900-907.
- [15] A. Arora, Z. Zhang, A. De, T. Debroy, Strains and strain rates during friction stir welding, *Scrip. Mater.*, 61 (2009), pp. 863-866.
- [16] L. Fratini, G. Buffa, D. Palmeri, Using a neural network for predicting the average grain size in friction stir welding processes, *Comp. Struc.*, 87 (2009) 1166-1174.
- [17] Z. Zhang, H.W. Zhang, Numerical studies on controlling of process parameters in friction stir welding, *J. Mater. Proc. Tech.*, 9 (2009) 241-270.
- [18] T. Azimzadegan, S. Serajzadeh, Thermo-mechanical modeling of friction stir welding, *Int. J. Mater. Research*, 101(2010) 390-397.
- [19] M. Assidi, L. Fourment, S. Guerdoux, T. Nelson, Friction model for friction stir welding process simulation: calibrations from welding experiments, *Inter. J. Mach. Tool. Manuf.*, 50 (2010) 143-155.

- [20] R. Hamilton, D. Mackenzie, H. Li, Multi-physics simulation of friction stir welding Process, *Eng. Comput.*, 27 (2010) 967-985.
- [21] H.J. Aval, S. Serajzadeh, A.H. Kokabi, Theoretical and experimental investigation into friction stir welding of AA 5086, *Inter. J. Adv. Manuf. Tech.*, 52 (2011) 531-544.
- [22] A. Reynolds, X. Deng, T. Seidel, S. Xu, Recent advances in fsw process physics, *Proc. from Joining of Advanced and Specialty Materials III*, M. Singh et al, eds., ASM International, St. Louis, 172–177, 2000.
- [23] S. Xu, X. Deng, A three-dimensional model for the friction-stir welding process, *Proc. of 21st Southeastern Conference on Theoretical And Applied Mechanics*, A. J. Kassab et al, eds., May Rivercross, Orlando, 699-704, 2002.
- [24] R.L. Goetz, , and K.V. Jata, Modelling friction stir welding of titanium and aluminum alloys, *Proc. of Friction Stir Welding and Processing I*, K. V. Jata, et al, eds., TMS, Warrendale, 35-42, 2001.
- [25] B. London, M. Mahoney, W. Bingel, M. Calabrese, D. Waldron, Experimental methods for determining material flow in friction stir welds, *Proc. 3rd International Symposium on Friction Stir Welding, TWI Ltd.*, Kobe, (CD-ROM) 2001.
- [26] D.G. Berghaus, H. B. Peacock, Deformation and strain analysis for high extrusion ratios and elevated temperatures, *Exper. Mech*, 25 (1985) 301-307.
- [27] K.E. Tello, A. Gerlich, P.F. Mendez, Constants for hot deformation constitutive models for recent experimental data, *Sci. Tech. Weld. Join.*, 15 (2010) 260-266.
- [28] M. Nourani, A.S. Milani, S. Yannacopoulos, C. Yan, An integrated multiphysics model for friction stir welding of 6061 Aluminum alloy, *Int. J. of Multiphysics* (under final review), 2013.
- [29] J.H. Hattel, H. Schmidt, C. Tutum, Thermomechanical modelling of friction stir welding, *Proc. 8th International Conference Trends in Welding Research* , S. A. David et al eds., ASM, Pine Mountain, 1-10, 2009.
- [30] P.A. Colegrove, H.R. Shercliff, 3-Dimensional CFD modeling of flow round a threaded friction stir welding tool profile, *J. Mater Process. Tech.*, 169 (2005) 320–327.
- [31] M.Z.H. Khandkar, J.A. Khan, A.P. Reynolds, Predictions of temperature distribution and thermal history during friction stir welding: input torque based model, *Sci. Tech. Weld. Join.*, 8 (2003) 165–174.

- [32] M. Assidi, L. Fourment, S. Guerdoux, T. Nelson, Friction model for friction stir welding process simulation: calibrations from welding experiments, *Inter. J. Mach. Tool. Manuf.*, 50 (2010) 143-155.

References of Chapter 7

- [1] S. Rajakumar, C. Muralidharan, V. Balasubramanian, Establishing empirical relationships to predict grain size and tensile strength of friction stir welded AA 6061-T6 aluminium alloy joints. *Transactions of Nonferrous Metals Society of China*, 20 (2010) 1863-1872.
- [2] A. Gerlich, M. Yamamoto, T.H. North, Local melting and tool slippage during friction stir spot welding of Al-alloys, *J Mater Sci*, 43 (2008) 2–11.
- [3] Y.S. Sato, M. Urata, H. Kokawa, Parameters controlling microstructure and hardness during friction-stir welding of precipitation-hardenable aluminum alloy 6063, *Metall Mater Trans A*, 33 (2002) 625-635.
- [4] W. Woo, Z. Feng, X.-L. Wang, D.W. Brown, B. Clausen, K. An, In situ neutron diffraction measurements of temperature and stresses during friction stir welding of 6061-T6 aluminium alloy. *Science and Technology of Welding & Joining*, 12 (2007) 298-303.
- [5] W. Woo, L. Balogh, T. Ungár, H. Choo, Z. Feng, Grain structure and dislocation density measurements in a friction-stir welded aluminum alloy using X-ray peak profile analysis. *Materials Science and Engineering A*, 498 (2008) 308-313.
- [6] W. Woo, T. Ungar, Z. Feng, E. Kenik, B. Clauen, X-Ray and neutron diffraction measurements of dislocation density and subgrain size in a friction-stir-welded aluminum alloy. *Metallurgical and Materials Transactions A*. 41 (2010) 1210-1216.
- [7] H. Atharifar, D. Lin, R. Kovacevic, Numerical and experimental investigations on the loads carried by the tool during friction stir welding, *J Mater Eng Perform*, 18 (2009), 339-350.
- [8] K. Tello, A. Gerlich, P. Mendez, Constants for hot deformation constitutive models for recent experimental data, *Sci Tech Weld Join*, 15 (2010), 260–266.
- [9] T. Long, A.P. Reynolds, Parametric studies of friction stir welding by commercial fluid dynamics simulation. *Science And Technology*, 11 (2006) 200-209.

- [10] M. Nourani, A.S. Milani, S. Yannacopoulos, Taguchi optimization of process parameters in friction stir welding of 6061 aluminum alloy: a review and case study, *Engineering*, 3 (2011) 144-155.
- [11] H.J. McQueen, M. Cabibbo, E. Evangelista, Piercing / Extrusion and FSW nugget microstructure formation in Al alloys, *Mater Sci Tech*, 23 (2007) 803-809.

References of Chapter 8

- [1] W. Woo, H. Choo, D.W. Brown, Z. Feng, P.K. Liaw, Angular distortion and through-thickness residual stress distribution in the friction-stir processed 6061-T6 aluminum alloy, *Mater. Sci. Eng. A*. 437 (2006) 64-69.
- [2] X. Qin, P. Michaleris, Thermo-elasto-viscoplastic modelling of friction stir welding, *Sci Tech Weld Join*. 14 (2009) 640-649.
- [3] Z. Feng, X.L. Wang, S.A. David, P.S. Sklad, Modeling of residual stress and property distribution in friction stir welds of aluminium ally 6061-T6, *J. Sci. Technol. Weld. Join*. 12 (2007), 348-356.
- [4] P. A. Colegrove, H. R. Shercliffa, 3-Dimensional CFD Modelling of flow round a threaded friction stir welding tool profile, *J. Mater. Process. Technol*. 169 (2005) 320-327.
- [5] X. Qin, P. Michaleris, Thermo-elasto-viscoplastic modelling of friction stir welding, *Sci Tech Weld Join*. 14 (2009) 640-649.
- [6] [5] W. Woo, H. Choo, D.W. Brown, Z. Feng, P.K. Liaw, Angular distortion and through-thickness residual stress distribution in the friction-stir processed 6061-T6 aluminum alloy, *Mater. Sci. Eng. A*. 437 (2006) 64-69.
- [7] S. Xu, X. Deng, A study of texture patterns in friction stir welds. *Acta Materialia*. 56 (2008) 1326-1341.
- [8] H. Atharifar, D. Lin, R. Kovacevic, Numerical and experimental investigations on the loads carried by the tool during friction stir welding, *J Mater Eng Perform*. 18 (2009) 339-350.

- [9] K. Tello, A. Gerlich, P. Mendez, Constants for hot deformation constitutive models for recent experimental data, *Sci Tech Weld Join.* 15 (2010) 260-266.
- [10] T. Long, A.P. Reynolds, Parametric studies of friction stir welding by commercial fluid dynamics simulation, *Sci Tech Weld Join.* 11 (2006) 200-209.
- [11] M. Riahi, H. Nazari,. Analysis of transient temperature and residual thermal stresses in friction stir welding of aluminum alloy 6061-T6 via numerical simulation. *Inter. J. Adv. Manuf. Tech.* 55 (2011) 143-152.
- [12] J. Simo, T. Hughes, *Computational Inelasticity*, Springer-Verlag, New York, 1998.
- [13] W. Woo, Z. Feng, X.L. Wang, D.W. Brown, B. Clausen, K. An, H. Choo, C.R. Hubbard, S.A. David, In situ neutron diffraction measurements of temperature and stresses during friction stir welding of 6061-T6 aluminium alloy, *Sci Tech Weld Join.* 12 (2007) 298-303.
- [14] X.L. Wang, Z. Feng, S.A. David, S. Spooner, C.R. Hubbard, Neutron diffraction study of residual stresses in friction stir welds. In: *Sixth international conference on residual stresses*. IOM Communications, London, (2000) 1408-1414.
- [15] C. Gallais, A. Simar, D. Fabregue, A. Denquin, G. Lapasset, Multiscale analysis of the strength and ductility of AA 6056 aluminum friction stir welds, *Metall. Mater. Trans. A.* 38A (2007) 964-981.

References of Chapter 9

- [1] J. Yan, M. Sutton, A. Reynolds, Process-structure-property relationships for nugget and heat affected zone regions of AA2524-T351 friction stir welds, *Sci. Technol. Weld. Joining*, 10 (2005) 725–736.
- [2] M. Mahoney, W. Harrigan, J. Wert, Friction stir welding sic discontinuously reinforced aluminum, *INALCO, Seventh Int. Conf. Joints in Aluminum (Cambridge, U.K.)*, 1998.

- [3] L. Commin, M. Dumont, J.-E. Masse, L. Barrallier, Friction stir welding of AZ31 magnesium alloy rolled sheets: Influence of processing parameters. *Acta Materialia*, 57 (2009) 326-334.
- [4] W.-B. Lee, S.-B. Jung, The Joint properties of copper by friction stir welding, *Mater. Lett.*, 58 (2004) 1041–1046.
- [5] P.J. Konkol, J.A. Mathers, R. Johnson, J.R. Pickens, Friction stir welding of HSLA-65 steel for shipbuilding, *J. Ship Prod.*, 19 (2003) 159–164.
- [6] C.D. Sorensen, T.W. Nelson, Sigma phase formation in friction stirring of Iron-Nickel-Chromium alloys, *Trends in Welding Research, Proceedings of the Seventh International Conference*, ASM International, 2005.
- [7] R. Nandan, T. J. Lienert, T. DebRoy, Toward reliable calculations of heat and plastic flow during friction stir welding of Ti-6Al-4V Alloy, *International Journal of Materials Research*, 99 (2008) 434-444.
- [8] T. Luijendijk, Welding of dissimilar aluminium alloys, *Journal of Materials Processing Technology*, 103 (2000) 29–35.
- [9] W.B. Lee, Y.M. Yeon, D.U. Kim, S.B. Jung, Effect of friction welding parameters on mechanical and metallurgical properties of aluminium alloy 5052–A36 steel joint. *Materials Science and Technology*, 19 (2003) 773-778.
- [10] H. Kroninger, A. Reynolds, R-curve behavior of friction stir welds in aluminum- lithium alloy 2195, *Fatigue Fract. Eng. Mater. Struct.*, 25 (2002) 283–290.
- [11] A.A. McLean, G.L F. Powell, I.H. Brown, V. M. Linton, Friction stir welding of magnesium alloy AZ31B to aluminium alloy 5083. *Science and Technology of Welding & Joining*, 8 (2003) 462-464.
- [12] U.K. Mudali, B.M.A. Rao, K. Shanmugam, R. Natarajan, B. Raj, Corrosion and microstructural aspects of dissimilar joints of titanium and type 304L stainless steel. *Journal of Nuclear Materials*, 321 (2003) 40-48.

- [13] H. Uzun, C. Dalle Donne, A. Argagnotto, T. Ghidini, C. Gambaro, Friction stir welding of dissimilar Al 6013-T4 To X5CrNi18-10 stainless steel. *Materials & Design*, 26 (2005) 41-46.
- [14] J. Ouyang, E. Yarrapareddy, R. Kovacevic, Microstructural evolution in the friction stir welded 6061 aluminum alloy (T6-temper condition) to copper. *Journal of Materials Processing Technology*, 172 (2006), 110-122.
- [15] U. Dressler, G. Biallas, U. A. Mercado, Friction stir welding of titanium alloy TiAl6V4 to aluminium alloy AA2024-T3. *Materials Science and Engineering A*, 526 (2009) 113-117.
- [16] Y.D. Chung, H. Fujii, H. Tanigawa, Dissimilar friction stir welding of F82H steel and austenite stainless steels without transformation. 8th international FSW symposium TWI Timmendorfer Strand, Germany, 2010.
- [17] Friction Stir Welding and Processing. Editors. Rajiv S. Mishra. Murray W. Mahoney. ASM International®. Materials Park, Ohio.
- [18] W. Woo, H. Choo, Texture analysis of a friction stir processed 6061-T6 aluminum alloy using neutron diffraction. *Acta Materialia*, 54 (2006) 3871-3882.
- [19] G. Frankel, Z. Xia, Localized corrosion and stress corrosion cracking resistance of friction stir welded aluminum alloy 5454, *Corrosion*, 55 (1999) 139-150.

Appendix A

Polynomial functions tested for calculation of the adjusted maximum UTS

$$1- Y = b*X1+c*X2+d*X3$$

$$2- Y = a+b*X1+c*X2+d*X3$$

$$3- Y = a+b*X1^2+c*X2^2+d*X3^2$$

$$4- Y = a+e*X1*X2+f*X1*X3+g*X2*X3$$

$$5- Y = a+b*X1+c*X2+d*X3+e*X1^2+f*X2^2+g*X3^2$$

$$6- Y = a+b*X1+c*X2+d*X3+b*X1^2+c*X2^2+d*X3^2$$

$$7- Y = a+b*X1+c*X2+d*X3+e*X1*X2+f*X1*X3+g*X2*X3$$

$$8- Y = a+b*X1+c*X2+d*X3+b*X1*X2+c*X2*X3+d*X1*X3$$

$$9- Y = b*X1^2+c*X2^2+d*X3^2+e*X1*X2+f*X1*X3+g*X2*X3$$

$$10- Y = a+e*X1^2+f*X2^2+g*X3^2+e*X1*X2+f*X1*X3+g*X2*X3$$

$$11- Y = a+e*X1^2+f*X2^2+g*X3^2+e*X1*X2+f*X2*X3+g*X1*X3$$

$$12- Y = a+b*X1*X2+c*X2*X3+d*X3*X1+e*X1^2+f*X2^2+g*X3^2$$

$$13- Y = a+b*X1*X2+c*X2*X3+d*X3*X1+e*X1^2+f*X2^2+g*X3^2+i*X1*X2*X3$$

$$14- Y = a+b*X1+c*X2+d*X3+e*X1^2+f*X2^2+g*X3^2+e*X1*X2+f*X1*X3+g*X2*X3$$

$$15- Y = a+b*X1+c*X2+d*X3+e*X1^2+f*X2^2+g*X3^2+e*X1*X2+f*X2*X3+g*X1*X3$$

$$16- Y = a+b*X1+c*X2+d*X3+e*X1^2+f*X2^2+g*X3^2+g*X1*X2+f*X1*X3+e*X2*X3$$

$$17- Y = a+b*X1+c*X2+d*X3+e*X1^2+f*X2^2+g*X3^2+g*X1*X2+e*X1*X3+f*X2*X3$$

$$18- Y = a+b*X1+c*X2+d*X3+e*X1^2+f*X2^2+g*X3^2+f*X1*X2+e*X1*X3+g*X2*X3$$

$$19- Y = a+b*X1+c*X2+d*X3+e*X1^2+f*X2^2+g*X3^2+f*X1*X2+g*X1*X3+e*X2*X3$$

$$20- Y = a+b*X1+c*X2+d*X3+b*X1^2+c*X2^2+d*X3^2+e*X1*X2+f*X1*X3+g*X2*X3$$

$$21- Y = a+b*X1+c*X2+d*X3+b*X1^2+c*X2^2+d*X3^2+e*X1*X2+f*X2*X3+g*X1*X3$$

$$22- Y = a+b*X1+c*X2+d*X3+e*X1^2+f*X2^2+g*X3^2+b*X1*X2+c*X1*X3+d*X2*X3$$

$$23- Y = a+b*X1+c*X2+d*X3+e*X1^2+f*X2^2+g*X3^2+b*X1*X2+c*X2*X3+d*X1*X3$$

$$24- Y = a+b*X1+c*X2+d*X3+e*X1^2+f*X2^2+g*X3^2+d*X1*X2+c*X1*X3+b*X2*X3$$

$$25- Y = a+b*X1+c*X2+d*X3+e*X1^2+f*X2^2+g*X3^2+d*X1*X2+b*X1*X3+c*X2*X3$$

$$26- Y = a+b*X1+c*X2+d*X3+e*X1^2+f*X2^2+g*X3^2+c*X1*X2+b*X1*X3+d*X2*X3$$

$$27- Y = a+b*X1+c*X2+d*X3+e*X1^2+f*X2^2+g*X3^2+c*X1*X2+d*X1*X3+b*X2*X3$$